NOTICE

The quality of this microform is heavily dependent upon the quality of the original thesis submitted for microfilming. Every effort has been made to ensure the highest quality of reproduction possible.

If pages are missing, contact the university which granted the degree.

Some pages may have indistinct print especially if the original pages were typed with a poor typewriter ribbon or if the university sent us an inferior photocopy.

Reproduction in full or in part of this microform is governed by the Canadian Copyright Act, R.S.C. 1970, c. C-30, and subsequent amendments.

AVIS

La qualité de cette microforme dépend grandement de la qualité de la thèse soumise au microfilmage. Nous avons tout fait pour assurer une qualité supérieure de reproduction.

S'il manque des pages, veuillez communiquer avec l'université qui a conféré le grade.

La qualité d'impression de certaines pages peut laisser à désirer, surtout si les pages originales ont été dactylographiées à l'aide d'un ruban usé ou si l'université nous a fait parvenir une photocopie de qualité inférieure.

La reproduction, même partielle, de cette microforme est soumise à la Loi canadienne sur le droit d'auteur, SRC 1970, c. C-30, et ses amendements subséquents.

MAGMATIC-HYDROTHERMAL AND WALL ROCK ALTERATION AT THE LAKE SHORE GOLD DEPOSIT, KIRKLAND LAKE, ONTARIO

By

Kevin Douglas Hicks

A thesis submitted to the School of Graduate Studies in partial fulfillment of the requirements for the degree of Master of Science in Geology

UNIVERSITY OF OTTAWA

ISBN 0-315-62319-5

UNIVERSITÉ D'OTTAWA
UNIVERSITY OF OTTAWA

ABSTRACT

The Lake Shore Au deposit lies in the Kirkland Lake Au camp, the second largest Archean camp in North America. The deposit is hosted in an alkaline to sub-alkaline intrusive complex composed of augite syenite, syenite, feldspar porphyry and quartz-feldspar porphyry. Feldspar and quartz-feldspar porphyry are the latest of the intrusive phases within the Lake Shore property and host over two-thirds of the Au in the camp. Detailed petrography and geochemistry of the feldspar porphyry indicate that it is predominantly a quartz-monzodiorite. The primary mineralogy of this unit consists of plagioclase, orthoclase, biotite, and hornblende, with accessory magnetite, apatite, titanite, monazite, and zircon. Miarolitic cavities within this unit suggest a relatively shallow level of emplacement as well as an H_2O-rich nature for the magma.

Four successive alteration facies are recognized within the feldspar porphyry. The hydrothermal biotite facies is characterized by the replacement and/or overgrowth of primary biotite and hornblende by Mg-rich hydrothermal biotite. It is accompanied by minor titanitization and hematitization of primary magnetite and the development of fine disseminated grains of the sulphate barian celestine. This alteration assemblage, coupled with the occurrence of miarolitic cavities containing a similar mineralogical assemblage, suggests that

oxidized magmatic-hydrothermal activity took place during the intrusion of the feldspar porphyry phase of the intrusive complex.

Following the magmatic-hydrothermal event, these rocks were subsequently overprinted by alteration associated with auriferous hydrothermal activity, resulting in three concentric alteration zones adjacent to the auriferous vein system. The outermost alteration zone, the chlorite facies, is characterized by the replacement of all ferromagnesian minerals by chlorite as well as the development of minor sericite and carbonate alteration.

Alteration intensity increases as the ore veins are approached and the chlorite facies grades into the phlogopite-hematite facies. This facies is characterized by the replacement of chlorite by phlogopite, the hematitization of primary and secondary magnetite, and the occurrence of fine-grained hematite in the groundmass.

Immediately adjacent to the ore veins fuchsite, sericite, and pyrite replace phlogopite and hematite, respectively. Plagioclase exhibits pervasive sericitization and increased amounts of carbonate are also noted. The footwall rocks are generally highly deformed and the porphyritic texture is commonly obliterated by the development of a fine shear foliation.

Major element geochemical trends show relatively little variation amongst the facies, with the exception of K_2O and

Na_2O which are exchanged during sericitization of plagioclase. Marked losses of Sr and Ba indicate the leaching of sulphate formed during the magmatic-hydrothermal event from the more intensely altered wall rocks.

The concentric nature of the later three alteration facies as zones about the auriferous veins may be the result of several overprinting, chemically distinct hydrothermal events, each of which penetrated the wall rocks to subsequent decreasing depths. A second possibility is that they are the result of a fluid which evolved as it penetrated the wall rocks. While the lack of encroachment of the latter two facies upon the earlier facies, coupled with consistent successive mineralogical changes observed in the alteration assemblages, favours the second theory of formation, no definite conclusion as to the origin of the hydrothermal alteration facies may be drawn at this time. These observed changes indicate decreasing activities for K_2O, CO_2, S, and increasing activities for MgO, Fe_2O_3 as the fluids permeated outward from the veins. The hematitization and titanitization of magnetite indicate a highly oxidized nature throughout the auriferous hydrothermal event.

ACKNOWLEDGEMENTS

The author is indebted to Dr. Keiko Hattori of the University of Ottawa for proposing the Lake Shore project. Her constant enthusiasm for the project, moral support, and suggestions were instrumental in its completion. Thanks are also extended to Drs. André Lalonde (University of Ottawa) and François Robert (Geological Survey of Canada) who, as members of the advisory committee, supplied countless suggestions throughout the project.

Thanks are also extended to Lac Minerals and the management at Lake Shore for permission to carry out the project and for supplying office space throughout the field work. Special thanks are extended to Frank Ploeger (project geologist) and Jim Gray (geologist) for their assistance during the initial bewildering stages.

Thin and polished sections were prepared by George Mrazek and Jean-François Tardif. XRF analyses were completed by Ron Hartree and Kelly Sears. Wet geochemical analyses were carried out with the assistance of John Loop. Figures, photographs, and photomicrographs were improved by assistance given by E. Hearn. Dan Byron and Derrick Watson prepared samples for geochemical analyses.

Electron microprobe analyses were completed with the assistance of Dr. Scott Ercit (National Museum of Natural Sciences, Mineral Science Division) and Dave Kempson (Queens

University).

Thanks are also extended to Len Cunningham of L.J. Cunningham and Associates for his advice, suggestions, and the samples he provided during the project.

Special thanks are expressed to Mike White of M.V.W. White and Associates Limited for the use of computer drafting facilities and the encouragement to get the job done.

Most of all I would like to thank my parents, Doug and Ruby Hicks, whose continued encouragement for a higher education provided much needed enthusiasm throughout my university career.

Financial support for the project was provided by an operating grant from the National Science and Engineering Research Council of Canada and an Ontario Geoscience Research Grant (#313) awarded to Dr. K. Hattori and an Ontario Graduate Scholarship (1987/88) awarded to the author.

TABLE OF CONTENTS

LIST OF FIGURES

LIST OF PLATES

LIST OF TABLES

Chapter 1

Introduction

The Lake Shore deposit is an Archean lode Au deposit located in the Kirkland Lake Au camp. The camp is situated in the southern portion of the Abitibi Greenstone Belt of the Superior province. Kirkland Lake is the second largest Archean Au camp in North America with more than 710,000 kg (23,000,000 oz) of Au produced (Ploeger and Crocket, 1982). The Kirkland Lake camp lies along the Kirkland Lake Main Break, a splay structure off the major Kirkland Lake-Larder Lake Break, a structure long known for its association with Au deposits.

The Lake Shore deposit is located in the centre of the camp and is the largest Au producer to date. The deposit is hosted primarily within an elongate, composite subalkaline to alkaline intrusive suite that has intruded volcanic, sedimentary, and pyroclastic rocks of the Timiskaming Group. The host intrusion is comprised principally of augite syenite, felsic syenite, and feldspar porphyry.

The spatial association between Au deposits and felsic

intrusive rocks, particularly porphyritic rocks, has long been appreciated by prospectors and exploration geologists alike. Hodgson and MacGeehan (1982) have estimated that over 90% of the Au deposits in the Superior province with more than one million ounces of Au produced are hosted by, or are spatially related to, felsic porphyritic rocks. In the Kirkland Lake-Larder Lake and Porcupine areas, Cherry (1983) estimates that more than 60% of the Au deposits display spatial associations with felsic intrusive rocks. Despite these numerous occurrences a genetic model for Au deposits hosted within or associated with felsic intrusions has yet to be accepted.

Au mineralization at the Lake Shore deposit occurs predominantly along two parallel fault-veins developed within the Kirkland Lake Main Break and secondary, parallel and branching structures. These fault-veins are primarily hosted within the feldspar porphyry, especially in the eastern portion and lower levels of the mine. At Lake Shore, as well as throughout the Kirkland Lake camp, more than two-thirds of the Au mineralization is hosted within the feldspar porphyry.

1.1 Location and Access

The Lake Shore Au mine is located in the town of Kirkland Lake, Teck Township, District of Timiskaming, in northeastern Ontario (Figs. 1.1, 1.2). Kirkland Lake is located at approximately 48°05'N latitude and 80°03'W longitude.

The area is easily accessed via provincial highways 11,

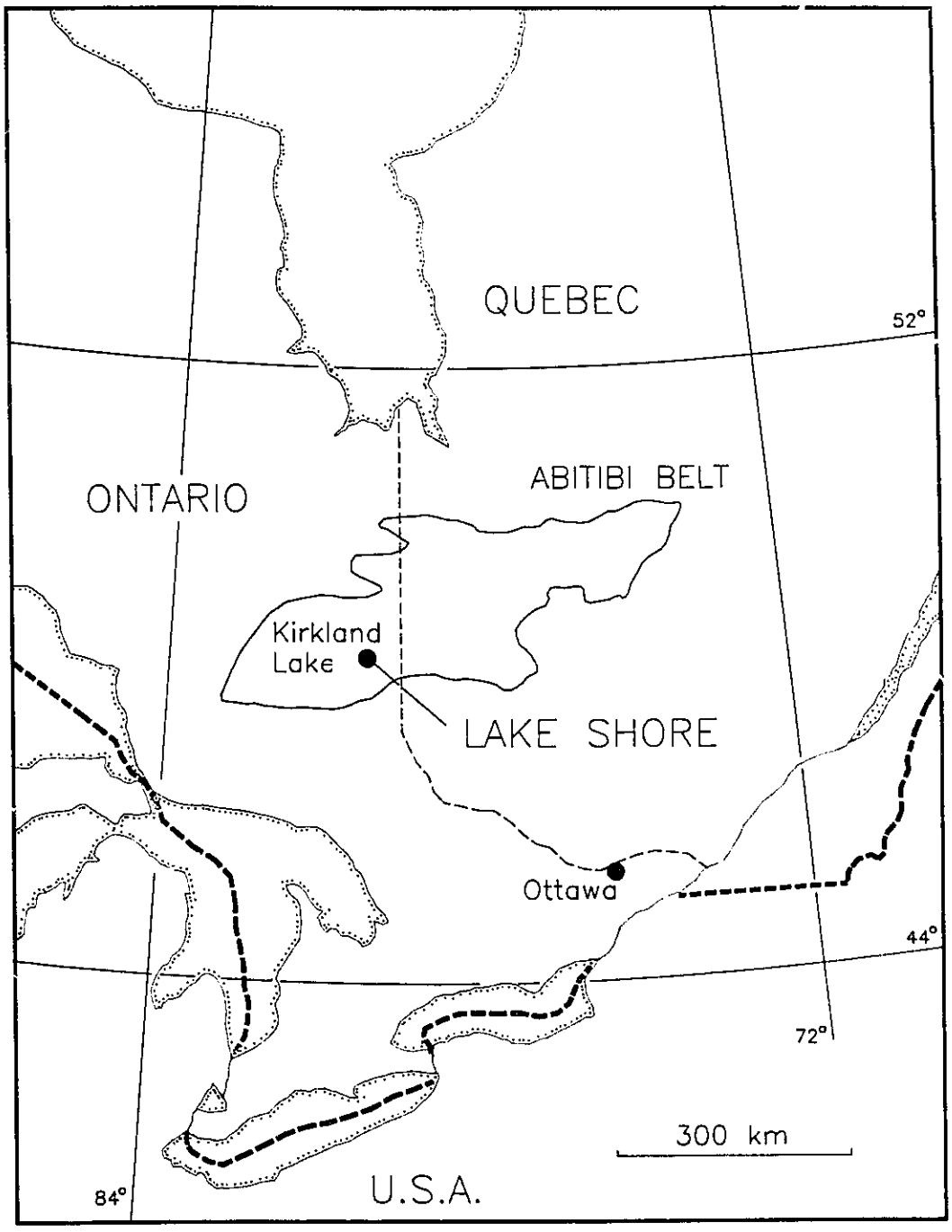

Fig. 1.1. Map showing the location of the Lake Shore Gold Mine

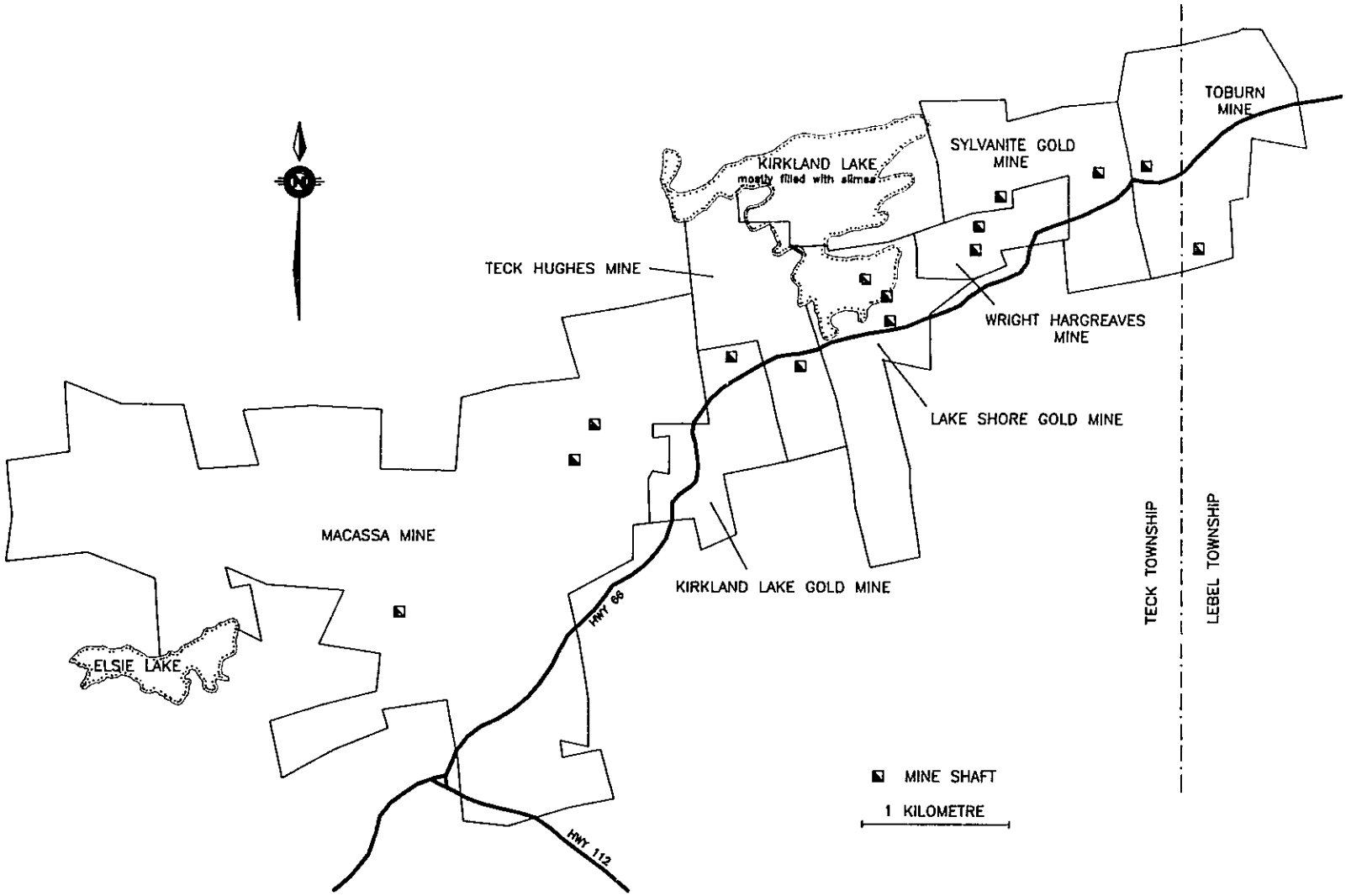

Fig. 1.2. Major mining properties in the Kirkland Lake gold camp

66, 112, and 624. The Ontario Northland Railway passes about ten kilometers to the southwest in Swastika, Ontario. A small commercial airport lies north of the Kirkland Lake town limits.

1.2 History of the Kirkland Lake Au Camp

Au exploration around the Kirkland Lake area was brought about as the result of the Larder Lake Au rush in 1906. At this time many claims were staked around the Kirkland Lake-Swastika area, however, most of the claims reverted to the crown due to insignificant findings early on. The discovery of several Au-bearing veins near Swastika, and the success at the Porcupine camp led to a renewed interest in the Kirkland Lake area.

Au was first discovered near Kirkland Lake by W. H. Wright in the fall of 1911 on what is now the old Wright-Hargreaves mine site. A year later, a high-grade discovery three-quarters of a mile northeast of the lake on the Tough-Oakes property (later Toburn) led to the Au rush of 1913.

Following the prospecting rush, the mines in the camp were gradually developed until 1933, when seven mines, all straddling the Kirkland Lake Main Break, were in production. The seven mines, from west to east, were Macassa, Kirkland Lake Gold, Teck-Hughes, Lake Shore, Wright-Hargreaves, Sylvanite, and Toburn (Fig. 1.2). Currently, only Macassa remains in production.

The Lake Shore mine commenced production in 1918 and continued uninterrupted until 1965. During that time 264,350 kg (8,499,050 oz.) of Au and 60,500 kg (1,945,120 oz.) of silver were produced (Ploeger and Crocket, 1982). In 1983 the mine was reopened and operated by Lac Minerals to remove the crown pillar and several of the higher grade boundary pillar sections. Production continued up to May 1987, during which time more than 2020 kg (65,000 oz.) of Au were recovered (Frank Ploeger, Chief Mine Geologist, pers. comm., 1987).

1.3 Objectives

Magmatic-hydrothermal activity has been well documented in Phanerozoic epizonal felsic intrusions where pressure reduction during magma ascent causes the release of a vapour phase and subsequent high-temperature hydrothermal activity. Porphyry-type mineralization and alteration are considered results of this type of hydrothermal activity (e.g., Beane and Titley, 1981).

In Archean terrains, it is generally believed that magmatic-hydrothermal events have been obscured by later overprinting events such as metamorphism, deformation, and possibly later hydrothermal activity. However, at Lake Shore, later hydrothermal and other overprinting events are not observed at a distance from the ore veins, thus the products of earlier magmatic-hydrothermal activity are still preserved.

In contrast, (hydrothermal) wall rock alteration

associated with Archean lode Au deposits has been well documented (e.g., Robert and Brown, 1984, Kerrich and Watson, 1984). Archean Au deposits commonly display multiple stages of hydrothermal activity along major dilatant zones (e.g. Robert and Brown, 1984). The Au deposits of the Kirkland Lake camp demonstrate this type of alteration.

At the Lake Shore deposit, preliminary petrographic studies by the author indicated the presence of magmatic hydrothermal components within the host feldspar porphyry intrusive rocks. Adjacent to the auriferous veins, these same rocks have undergone intense hydrothermal alteration associated with auriferous hydrothermal activity. The different styles of these two alterations, as well as the overprinting relationships observed between the two, allow them to be easily distinguished.

The objective of this investigation was to outline the petrography and geochemistry of the two hydrothermal alteration events in the porphyritic phase. Studies were restricted to the porphyry due to the mining operations during the initial field work. The information attained in this study may aid in the understanding of the overall geological processes which occurred in the area, as well as assisting in further determining the role of felsic intrusions in Au mineralization. In addition, information on the paragenesis of the alteration mineralogy may provide a better understanding of changes that occur in hydrothermal fluids during

mineralization.

1.4 Previous Work

Previous geological investigations have been carried out in the Kirkland Lake area intermittently since Au was first discovered in the area in 1911. The earliest geological studies of the Kirkland Lake area were carried out by Burrows and Hopkins (1914, 1920, 1923), Tyrrell and Hore (1926) and Todd (1928). The earliest major studies of the Kirkland Lake area including the main ore zone were by Thomson (1950), Thomson et al. (1950) and Hawley (1950), with a follow up study of the deeper levels by Charlewood (1964).

Other investigations in the Kirkland Lake area include; studies of the Timiskaming group by Hewitt (1963), Cooke (1966), Cooke and Moorehouse (1969), Hyde and Walker (1977) and Hyde (1980); regional reconnaissance studies by Ridler (1970), Jensen (1976, 1978, 1981), Jensen and Langford (1985), Pyke and Jensen (1976); studies of the Au mineralization by Ploeger (1980), Ploeger and Crocket (1982), Watson (1984), Kerrich and Watson (1984), Roberts (1987); and structural studies by Toogood and Hodgson (1985, 1986) and Hodgson et al. (1988).

Recent investigations at Lake Shore on the mineralogy of the ore veins and wall rock alteration have been carried out by McInnes (1985) and Theriault (1988). A fluid inclusion study has been completed by Gallimore (1988).

1.5 Sampling and Methodology

Field work and sampling for the project were carried out over a cumulative period of 5 weeks during the summers of 1986 and 1987. A total of 153 samples were collected along drifts, crosscuts, working stopes, and from drill core. Of the samples collected, 146 were from the Lake Shore mine. The remaining 7 samples were obtained from the Teck-Hughes property immediately northwest of Lake Shore.

All samples collected and analyzed from Lake Shore are from the upper portions of the mine. These areas include the crown pillar section (surface to 400 foot level), the east boundary pillar between the Lake Shore and Wright-Hargreaves properties between the 600 and 1200 foot levels, and the number 1 shaft pillar from the 800 foot level. Approximately 80% of the samples collected were from the feldspar porphyry.

Several samples of augite syenite and feldspar porphyry were collected from the Teck-Hughes property for comparison. One sample of syenite was examined from the Macassa Mine 1.5 km to the west, as none could be obtained from Lake Shore.

Samples for wall rock alteration studies were collected along crosscuts and from horizontal drill holes from the east crown pillar section and east boundary pillar sections. Four suites of samples roughly perpendicular to the North and South Veins were collected in order to observe the spatial variation of alteration. Detailed locations of these samples are given in Appendix IV.

Samples used in the description of the auriferous veins were collected from the North and South Veins from the previously mentioned areas of the mine. Metallic mineralogical studies of vein samples relied heavily upon samples from the North Vein on the 1200 foot level.

From the samples collected, a total of 136 thin sections and 5 polished sections were cut for petrographic examination. An additional 17 polished thin sections were cut from previously sectioned rocks for microprobe analyses. Seventy-eight samples were analyzed for major and selected trace elements and are listed in Table A1.2 along with their corresponding CIPW norm calculations (excluding vein samples).

Host rock samples selected for major and trace element analyses were chosen so as not to include any vein material, in order to obtain quantitative analyses of the alteration. Least altered samples were chosen after petrographic examination. Samples were crushed in a Chipmunk jaw crusher and subsequently powdered in a Spex Industries Shatterbox.

Geochemical analyses were performed at the Department of Geology, University of Ottawa, and at Technical Service Laboratories in Mississauga. Analytical methods, elements analyzed, and the precision of recorded values are given in Appendix I.

Electron microprobe analyses were completed at the National Museum of Natural Sciences (Mineral Science Division) in Ottawa, and at Queens University, Kingston, Ontario.

Procedures and equipment used are given in Appendix II.

Chapter 2

Regional Geology

2.1 Geology of the Abitibi Greenstone Belt

The Lake Shore Au deposit lies within the Abitibi Greenstone Belt, the largest and best preserved Archean greenstone terrain in the Canadian Shield. In addition to Au, other significant mineral deposits found within the Abitibi belt include Au-Ag, Cu-Zn-Au-Ag, Ni-Cu, Fe, Mo-Bi, Li, and asbestos (Goodwin and Ridler, 1970).

The Abitibi Greenstone belt lies in the southeast part of the Superior tectonic province. It is an east-northeast trending belt approximately 760 km long and 200 km wide (Fig. 2.1). The belt is truncated to the east and west by northeast trending crystalline rocks of the Grenville province and the Kapuskasing Gneiss Belt, respectively (Fig. 2.1).

The lithic assemblage of the Abitibi belt is characteristic of many Archean greenstone terrains in the Canadian shield. Older supracrustal and intrusive rocks, which have been deformed and are generally of greenschist facies

Fig. 2.1. Generalized geology of the Abitibi Greenstone Belt (modified after Goodwin and Ridler, 1970).

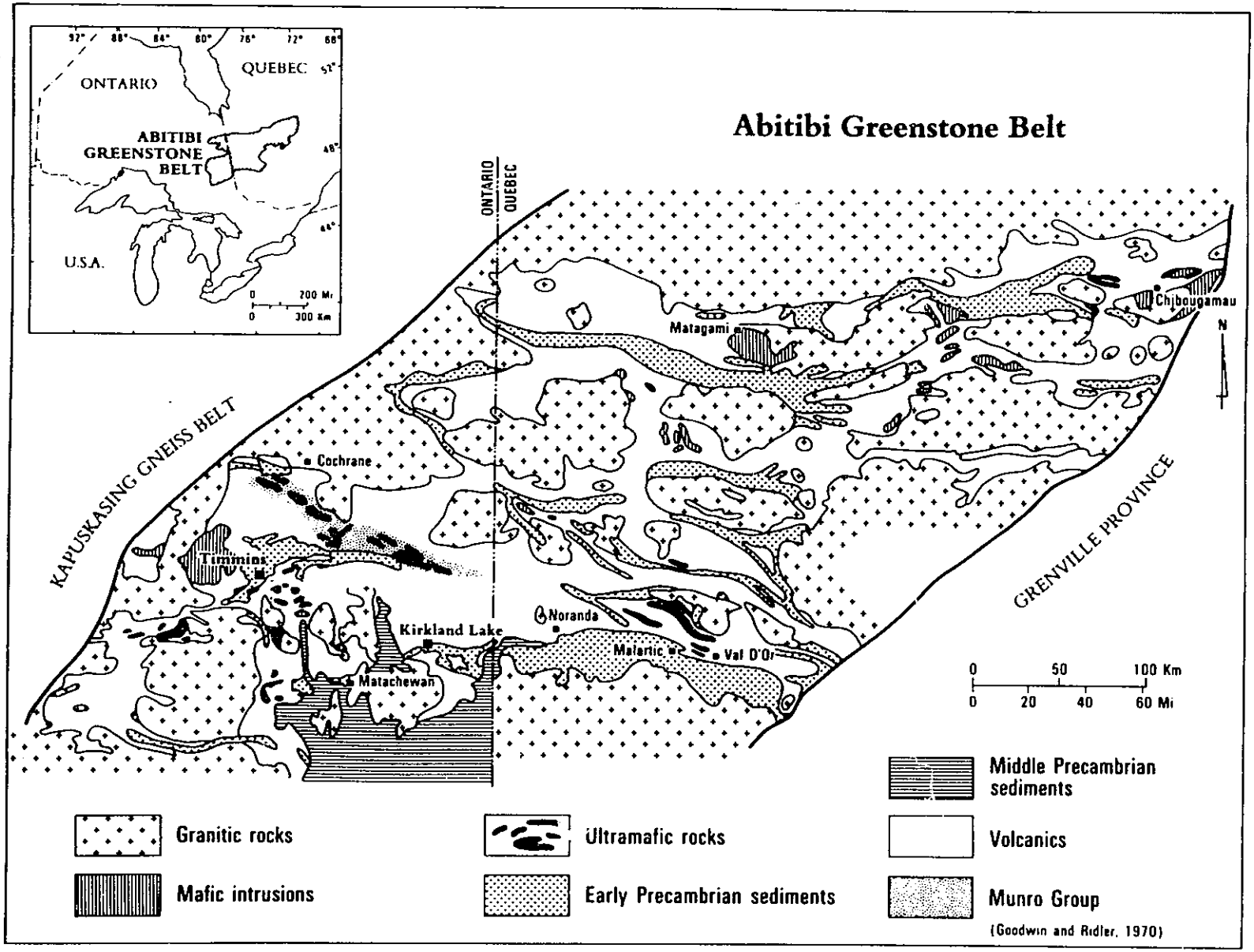
Abitibi Greenstone Belt
ONTARIO
QUEBEC
ABITIBI GREENSTONE BELT
U.S.A.
ONTARIO
QUEBEC
KAPUSKASING GNEISS BELT
GRENVILLE PROVINCE
Cochrane
Timmins
Kirkland Lake
Noranda
Malartic
Val D'Or
Matachewan
Matagami
Chibougamau
N
0 50 100 Km
0 20 40 60 Mi
Granitic rocks
Mafic intrusions
Ultramafic rocks
Early Precambrian sediments
Middle Precambrian sediments
Volcanics
Munro Group
(Goodwin and Ridler, 1970)

regional metamorphic grade, have been intruded by late Archean mafic to felsic stocks and batholiths. Diabase dykes of the Matachewan and Keweenawan swarms transect most of the belt. Flat-lying Proterozoic and Paleozoic rocks, extending northward from the south, overlie some of the older supracrustal rocks. A simplified geological map of the Abitibi Greenstone Belt is shown in Figure 2.1.

The older supracrustal rocks are dominantly volcanic. They include ultramafic flows and mafic to felsic flows and pyroclastic rocks. The mafic to felsic assemblages vary from tholeiitic to calc-alkaline affinities. Thick mafic packages are typically overlain by felsic volcanic rocks, with each felsic concentration generally representing an eruptive centre (Fig. 2.2).

Sedimentary rocks in the Abitibi belt range from thin discontinuous interflow units to broad regional east-trending belts (e.g., Timiskaming Group). Sediments are predominantly turbiditic, suggesting rapid accumulation in tectonically unstable environments. Two principal sedimentary facies are identified; volcanogenic and flyschoid (Goodwin and Ridler, 1970). Volcanogenic sediments include greywacke, shale, lithic sandstone, conglomerate, breccia, and iron formation (Goodwin and Ridler, 1970). Flyschoid sediments are typically composed of rhythmically bedded greywacke/argillite sequences (Goodwin and Ridler, 1970).

Numerous ultramafic to mafic sheets, dykes, and sills lie

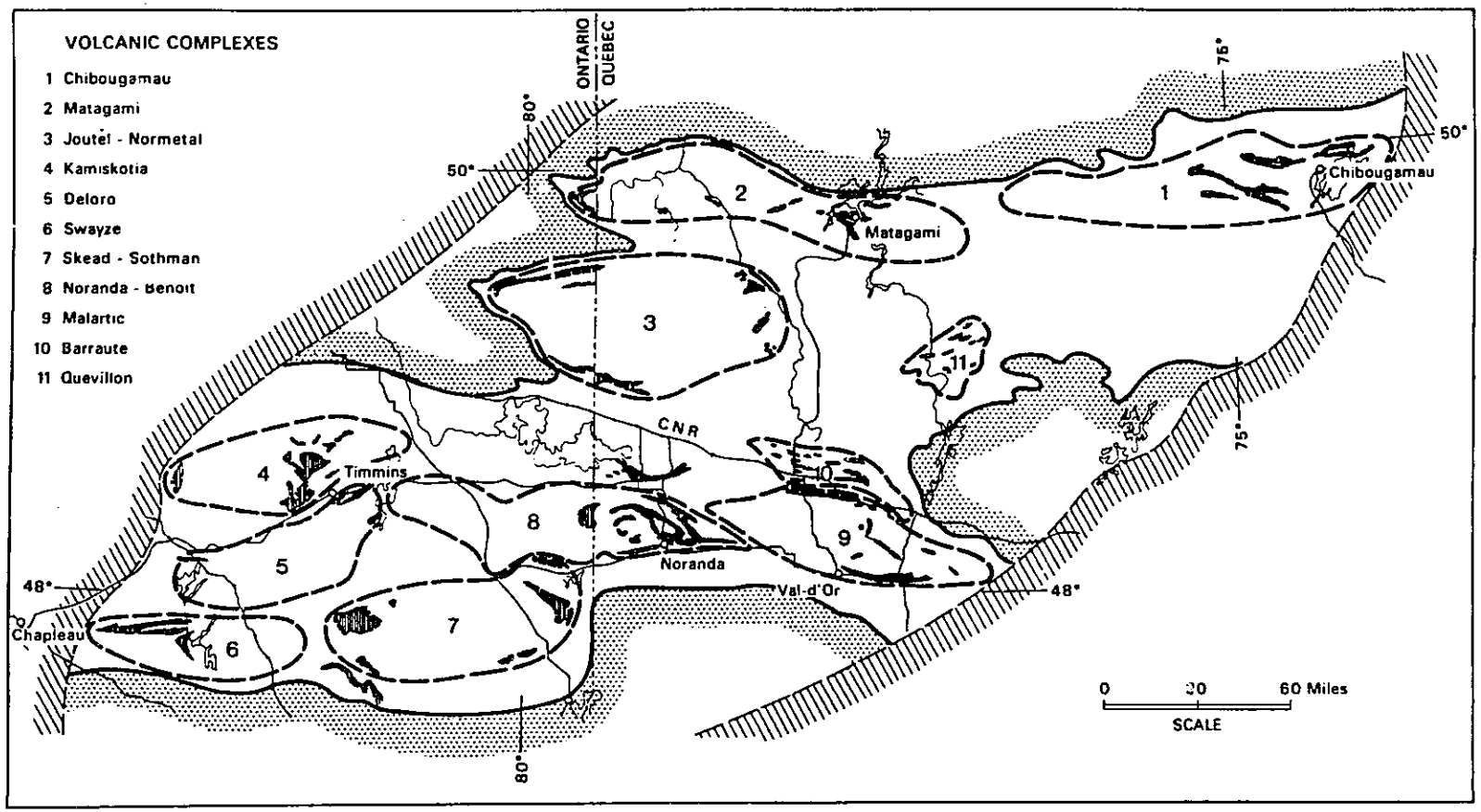

Fig. 2.2. Distribution of volcanic complexes in the Abitibi Greenstone Belt. Felsic volcanic rocks are indicated by vertical line hatching. Boundaries of the complexes are indicated by heavy dashed lines (after Goodwin and Ridler, 1970).

within the mafic volcanic rocks. A variety of massive to foliated granitic rocks underlies the margins of the regions. Granitic plutons are also abundant within the belt. Nine major plutons, 65-160 km in diameter, lie within the belt, most of them in the northern parts. These bodies generally post-date the volcanic and sedimentary rocks in their emplacement (Goodwin and Ridler, 1970).

The S-shape of the Abitibi belt reflects severe structural deformation marked by internal east-trending tight isoclinal folds (Goodwin and Ridler, 1970)(Fig. 2.3). Several steeply dipping, east-trending shear zones have been identified in the southern portion of the belt (Fig. 2.3). These include the Destor-Porcupine Break and the Kirkland Lake-Larder Lake Break, which extends eastward into Quebec as the Cadillac-Malartic Break.

2.2 Geology of the Kirkland Lake Area

The first geological investigations in the Kirkland Lake area by the Ontario Department of Mines resulted in the development of three simple stratigraphic series for the area: the Keewatin, Timiskaming, and Algoman series (e.g., Burrows and Hopkins, 1923).

The first detailed mapping projects of the Kirkland Lake area were by Thomson during the 1940's (Fig. 2.4). Thomson (1946, 1950) recognized an angular unconformity between the Keewatin volcanic rocks and the overlying sedimentary rocks in

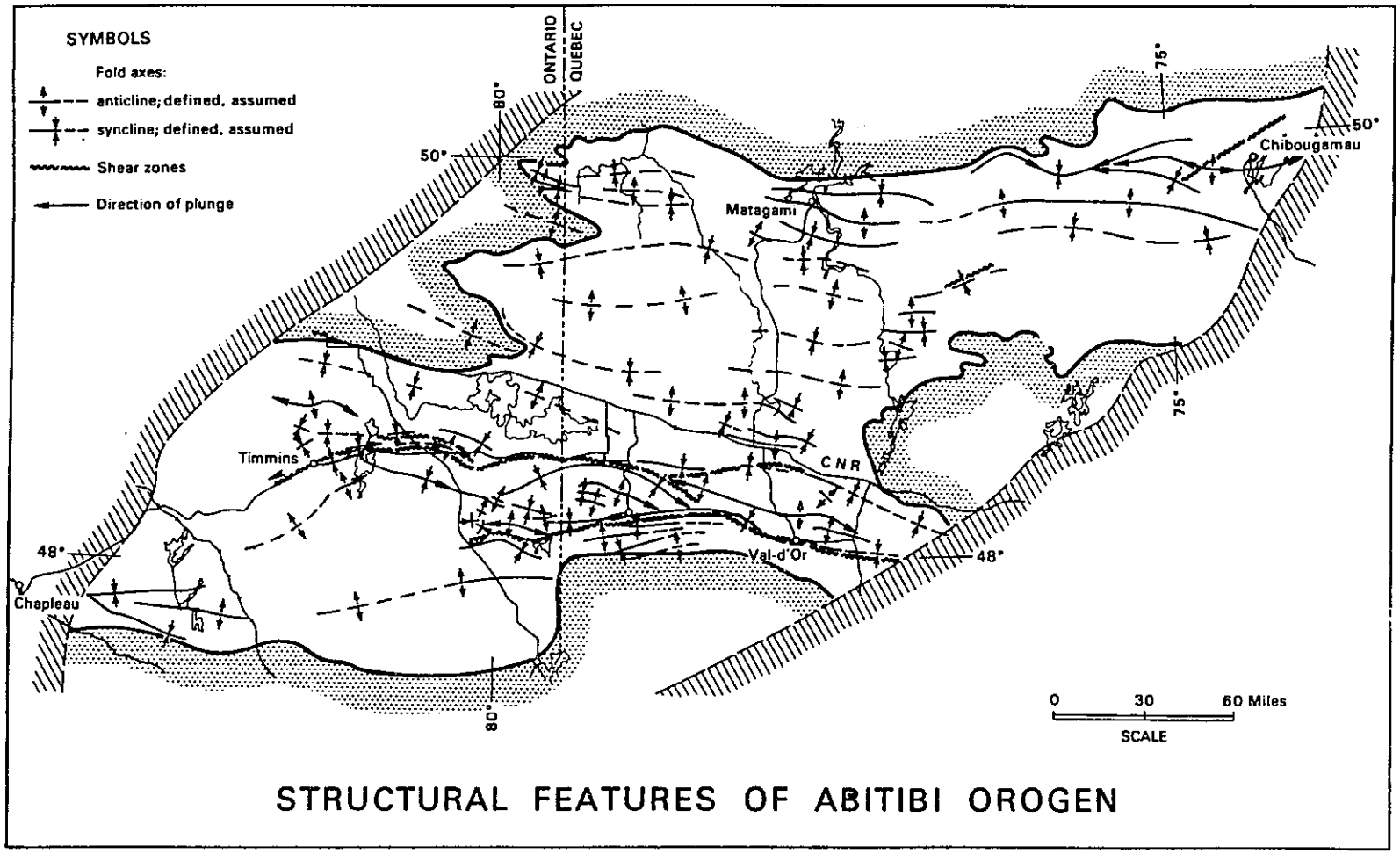

Fig. 2.3. Structural features of the Abitibi Greenstone Belt (after Goodwin and Ridler, 1970).

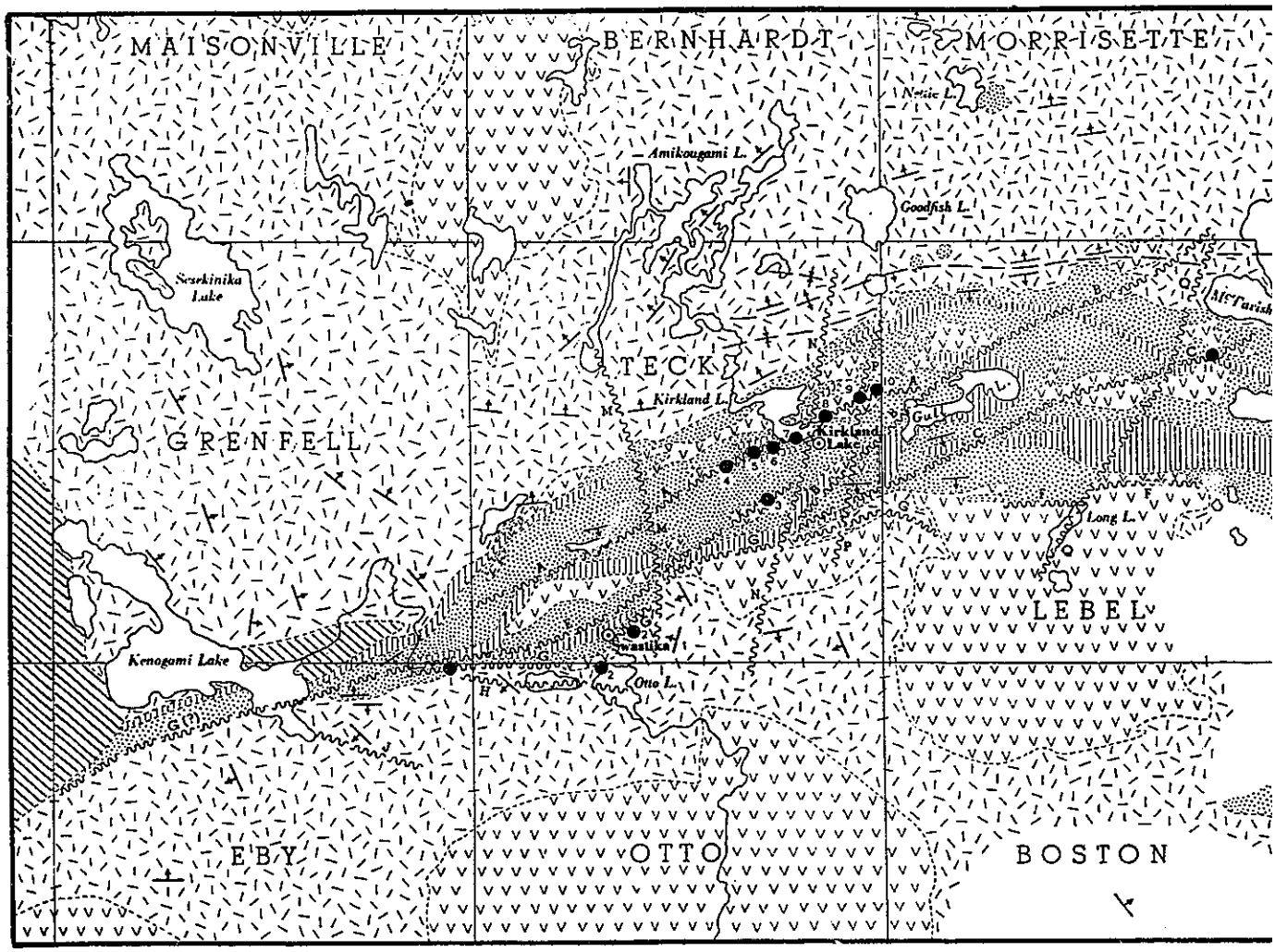

List of Properties

1. Baldwin Consolidated
2. Golden Gate
3. Amalgamated Kirkland
4. Macassa
5. Kirkland Lake Gold
6. Teck-Hughes
7. Lake Shore
8. Wright-Hargreaves
9. Sylvanite
10. Toburn
11. Bidgood Kirkland
12. Upper Canada
13. Anoki
14. Queenston
15. Ritoria
16. Beaverhouse Lake (Argonaut)
17. Laguerre
18. Omega
19. Amalgamated Larder (Fernland)
20. Amalgamated Larder (Cheminis)
21. Amalgamated Larder (Barber Larder)
22. Kerr-Addison
23. Chesterville
24. Martin-Bird

List of Faults

A. Kirkland Lake Fault
B. Murdock Creek Fault
C. Bidgood Fault
D. Upper Canada Fault
E. Amalgamated Kirkland-Blanche River Fault
F. Turtle Lake Fault
G. Larder Lake Fault
H. Vigrass Lake Fault
J. South Bay Fault
K. Northeast Arm Benson Creek Fault
L. Milky Creek Fault
M. Amikougami Creek Fault
N. Lake Shore Fault
P. Sylvanite Fault
Q. Long Lake Fault
R. Misema River Fault
S. Sharp Creek Fault

Fig. 2.4 Generalized geology of the Kirkland

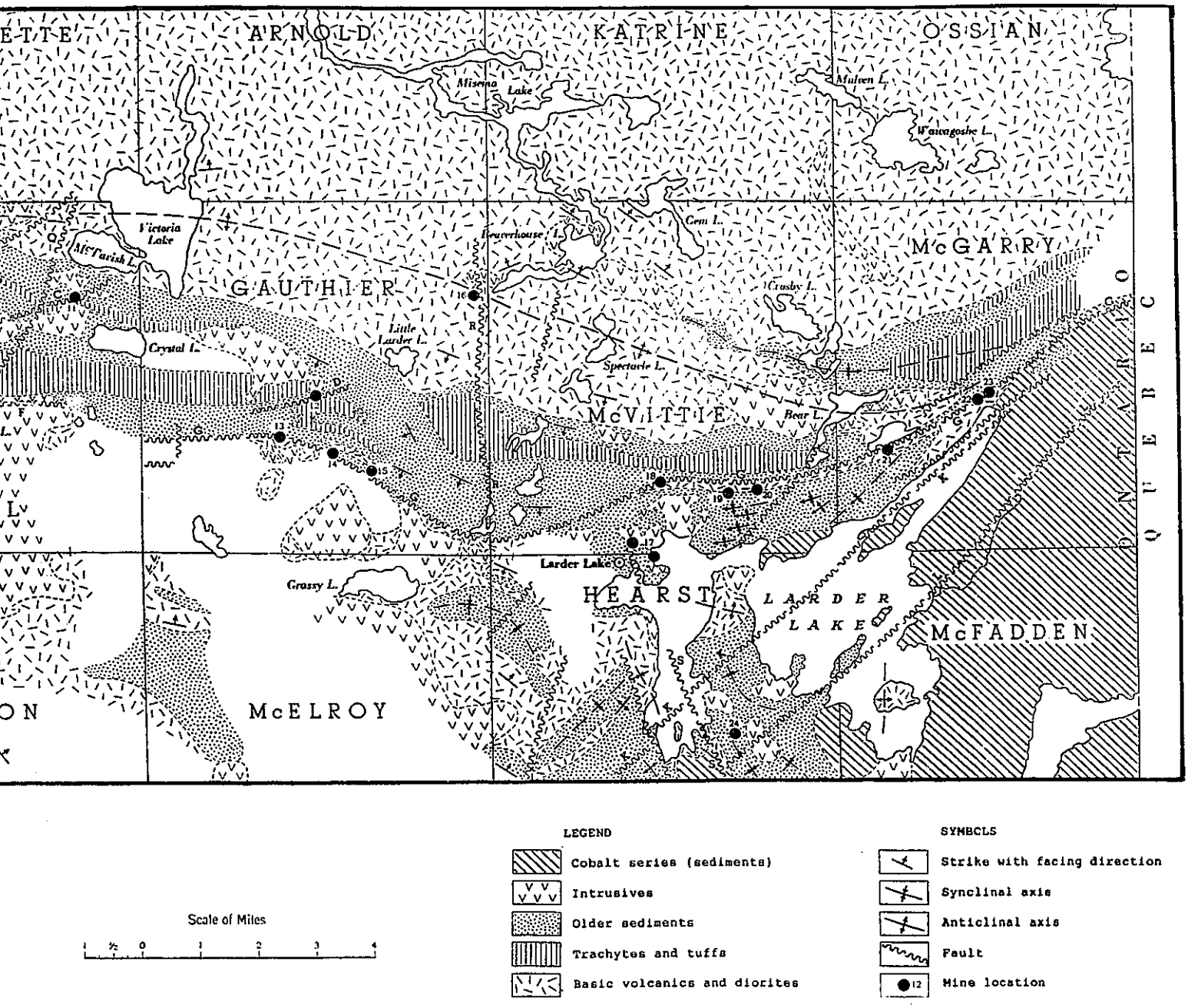

Kirkland Lake-Larder Lake Area (after Thomson, 1950).

Lebel township and further west. To the east, however, the contact was conformable. Thomson (1946) correlated the sedimentary rocks with the Timiskaming series and suggested that they were separated from the volcanic rocks by a major break, termed the Larder Lake Break (Fig. 2.4). The evidence for the break was a broad zone of intense shearing and carbonate alteration. Thomson (1946) further suggested that the break was probably continuous with the Cadillac Break to the east in Quebec.

In the early 1970's, L.S. Jensen and D.R. Pyke of the Ontario Department of Mines began a systematic stratigraphic study of the Timmins-Kirkland Lake area. Using whole rock geochemical data of the volcanic rocks, they defined two volcanic cycles with associated sedimentation and plutonism similar to those recognized by Goodwin (1965) (Fig. 2.5). These cycles, referred to as Upper and Lower Supergroups, each consisted of komatiitic volcanism followed by tholeiitic and calc-alkaline volcanism.

2.2.1 Stratigraphy

In the Kirkland Lake area, the volcanic rocks of the Abitibi Greenstone Belt are interpreted to form the large east-plunging Blake River Synclinorium lying between the Lake Abitibi and Round Lake Batholiths (Jensen, 1979)(Fig. 2.5). These batholiths have U-Pb zircon ages of 2690±4 m.y. and 2703±2 m.y. respectively (Jim Mortensen, Geological Survey of

Fig. 2.5. Generalized geology of the Kirkland Lake-Timmins area (modified after Jensen and Langford, 1985).

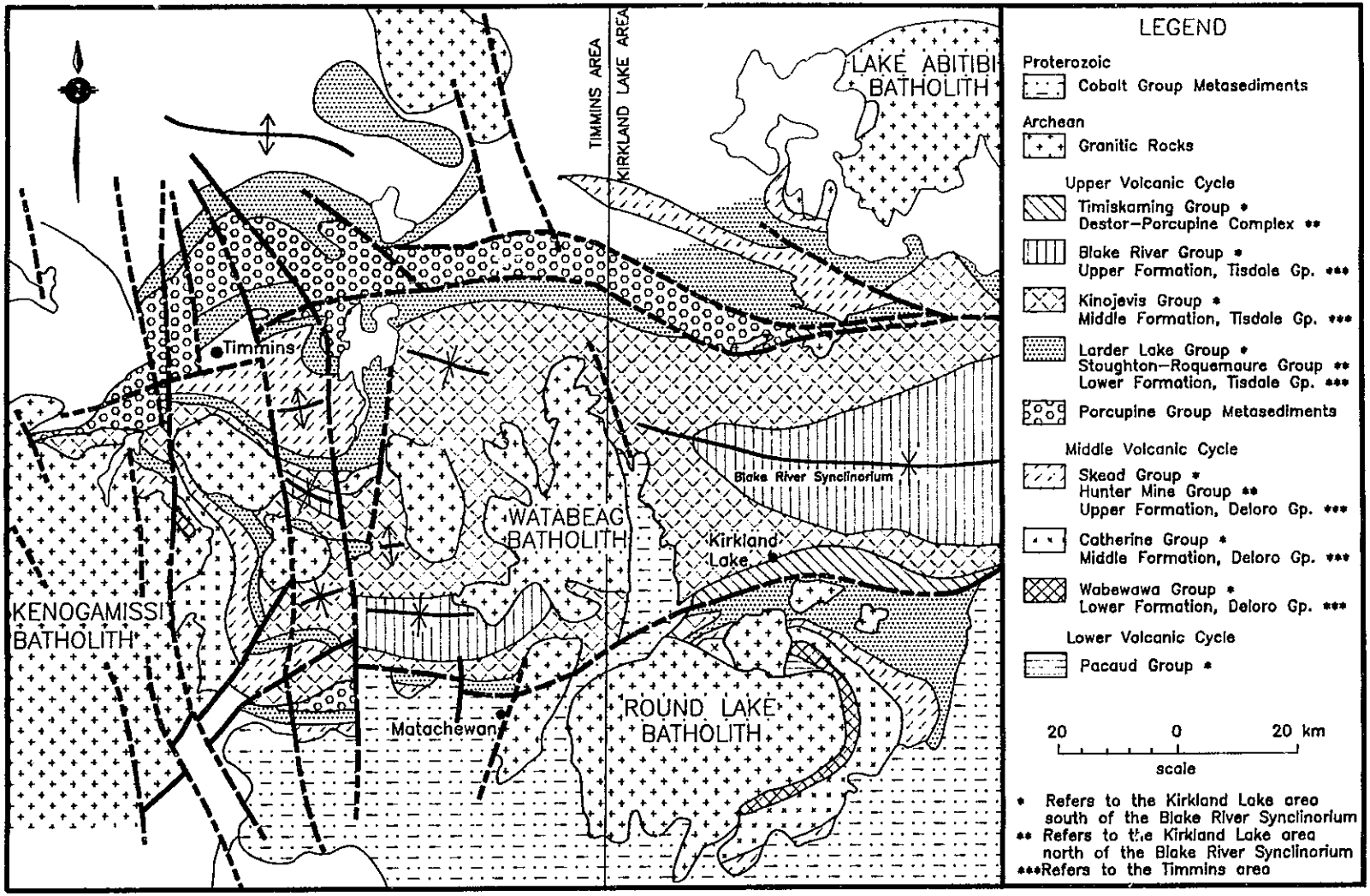
TIMMINS AREA
KIRKLAND LAKE AREA
LAKE ABITIBI BATHOLITH
Timmins
Blake River Synclinorium
WATABEAG BATHOLITH
Kirkland Lake
KENOGAMISSI BATHOLITH
Matachewan
ROUND LAKE BATHOLITH
LEGEND
Proterozoic
Cobalt Group Metasediments
Archean
Granitic Rocks
Upper Volcanic Cycle
Timiskaming Group *
Destor–Porcupine Complex **
Blake River Group *
Upper Formation, Tisdale Gp. ***
Kinojevis Group *
Middle Formation, Tisdale Gp. ***
Larder Lake Group *
Stoughton–Roquemaure Group **
Lower Formation, Tisdale Gp. ***
Porcupine Group Metasediments
Middle Volcanic Cycle
Skead Group *
Hunter Mine Group **
Upper Formation, Deloro Gp. ***
Catherine Group *
Middle Formation, Deloro Gp. ***
Wabewawa Group *
Lower Formation, Deloro Gp. ***
Lower Volcanic Cycle
Pacaud Group *
20 0 20 km
scale
* Refers to the Kirkland Lake area south of the Blake River Synclinorium
** Refers to the Kirkland Lake area north of the Blake River Synclinorium
***Refers to the Timmins area

Canada, pers. comm., 1987). The north and south limbs of the synclinorium are cut by two major east-west striking breaks, the Destor-Porcupine Break, and the Kirkland Lake-Larder Lake Break, respectively.

Within this area, Jensen (1981) has recognized two complete cycles (supergroups) of komatiitic to calc-alkaline supracrustal sequences as well as the uppermost unit of an older, third cycle. In the Kirkland Lake area, the top of the upper volcanic cycle is overlain by shallow water sedimentary and alkalic volcanic rocks of the Timiskaming Group, which lie along the Kirkland Lake-Larder Lake Break (Fig. 2.5).

However, recent radiometric age determinations by Marmont and Corfu (1988a, b) suggest that Jensen's temporal distinction for the upper volcanic cycle in the Kirkland Lake area is invalid. While temporal distinctions for each of the rock groups within the cycle may be invalid, their general descriptions and spatial distributions appear correct.

The Pacaud Group, a series of calc-alkaline tuffs and tuff breccias, comprises the oldest rocks in the Kirkland Lake area. The group is thought to represent the top of an older volcanic cycle (Jensen, 1981) which is consistent with its U-Pb zircon age of 2747±2 m.y. (Jim Mortensen, Geological Survey of Canada, pers. comm., 1987).

Unconformably overlying the Pacaud Group is the Wabewawa Group, the basal komatiitic unit of the middle volcanic cycle. This group is comprised of peridotitic and basaltic

komatiites, Mg-rich tholeiitic basalts and minor rhyolite tuffs, and sedimentary rocks.

The Wabewawa Group is conformably overlain by the Catherine Group, a series of Mg-Fe-rich tholeiitic basalts approximately 8000 m thick (Jensen, 1978). Fe tholeiitic basalts predominate towards the top of the section. This group is in turn overlain by the Skead Group, the uppermost division of the middle cycle. This group is comprised predominantly of calc-alkaline fragmental rocks of basalt, andesite, dacite, and rhyolite composition. A calc-alkaline rhyolite tuff from this group has been dated at 2701±3/2 m.y. by Marmont and Corfu (1988a).

A trachyte-pebble conglomerate, which separates the Skead Group from the upper volcanic cycle, suggests that alkalic volcanism may have occurred at the end of the second volcanic cycle.

The rocks of the middle volcanic cycle are unconformably overlain by rocks of the upper volcanic cycle. The basal komatiitic division of the upper cycle is comprised of the Larder Lake Group. This group lies south of the Kirkland Lake-Larder Lake area and is comprised of calc-alkaline rhyolite tuff-breccias, crystal and cherty tuffs, ultramafic and basaltic komatiite flows, and Mg-rich tholeiitic basalt flows. Most of the komatiitic rocks are metamorphosed and/or metasomatized to talc-serpentine-chlorite schists and green and grey carbonate-rich rocks respectively. The sedimentary

rocks are comprised of conglomerate, wacke, argillite, and carbonate rocks. The thickness of the Larder Lake Group is thought to be about 5000-6000 m (Jensen, 1979). An interflow rhyolite has been dated at 2705±3/2 m.y. (Marmont and Corfu, 1988a).

Overlying the Larder Lake Group is the Kinojevis Group, a sequence of Mg-Fe-rich tholeiitic basalt flows with minor tholeiitic andesite, dacite and rhyolite. On the north limb of the Blake River synclinorium, the Kinojevis Group conformably overlies the komatiitic rocks of the Stoughton-Roquemaure Group. However, in the Kirkland Lake-Larder Lake area, the Kinojevis Group is spatially separated from the Larder Lake Group by the Timiskaming Group. Further to the west in Eby township, a sequence of Mg-Fe-rich tholeiitic basalts conformably overlies the komatiitic rocks. This tholeiitic sequence extends further west and appears to be part of the Kinojevis Group, suggesting that the Kinojevis Group conformably overlies the Larder Lake Group. The thickness of the Kinojevis Group is about 10,000 m (Jensen, 1979).

The Kinojevis Group is conformably overlain by the Blake River Group. This group is comprised of calc-alkaline basalt, andesite, dacite and rhyolite flows, and pyroclastic rocks. Exposure of the group is restricted to the centre of the Blake River synclinorium, where it reaches a thickness of 10,000 m (Jensen, 1980). Nunes and Jensen (1980) obtained ages of 2701±2 and 2703±1.5 m.y. from two samples on opposite sides of

the Blake River Syncline, which folds the Blake River Group.

The upper volcanic cycle is overlain by the Timiskaming Group, a series of K-rich alkaline to calc-alkaline volcanic rocks (Cooke, 1966) interbedded with sedimentary rocks (Hyde, 1978). On its northern contact, the Timiskaming Group unconformably overlies the Kinojevis Group and, in places, the Blake River Group (Thomson, 1946). On its southern contact, the top of the Timiskaming has been faulted against the Larder Lake Group; this contact likely representing the surface expression of the Kirkland Lake-Larder Lake Break (Jensen, 1978). In several places, blocks of the Timiskaming Group have been faulted into the Larder Lake Group. The Timiskaming Group is discussed in further detail in chapter 3.

2.2.2 Geochronology

Recent age dates from the Kirkland Lake area indicate that two episodes of volcanic activity peaked at approximately 2750 and 2700 m.y. These age dates are in accordance with the lower two volcanic cycles outlined by Jensen (1981).

While Jensen's stratigraphic sequence involving volcanic cycles is predominantly based upon field observations and whole-rock data, recent age dates obtained for the middle and upper volcanic cycles (Marmont and Corfu, 1988a, b) suggest a temporal distinction for the upper volcanic cycle may not be valid. Conflicting age dates between the Blake River (2703±2 m.y.) and Skead Groups (2701±3/2 m.y.), which represent the

tops of the upper and middle volcanic cycles respectively, suggest that the two groups can not be part of the same stratigraphic sequence as Jensen has defined them.

This age discrepancy led Marmont and Corfu (1988a) to suggest that the observed thickness of the supracrustal rocks in the area may be due to repetition of tectonic slices or juxtaposition of allochthonous terrains, rather than accumulation of volcanic successions. These conflicting age dates indicate a much more complex stratigraphy than previously interpreted, and a further need for continuing studies of the regional geology of the Kirkland Lake area.

2.2.3 Structure

The most prominent structural features in the greater Kirkland Lake area are the Blake River Synclinorium, and two main east-west-striking break structures; the Destor-Porcupine Break and the Kirkland Lake-Larder Lake Break (Fig. 2.6). These break structures for the most part follow lithofacies boundaries, particularly volcanic-sedimentary interfaces. They are steeply dipping structures, generally of uncertain displacement. Their relationship with Au mineralization is illustrated by the numerous past and present producers with which they are associated, making them prime targets for present day exploration activities (Fig. 2.6).

The Kirkland Lake-Larder Lake Break extends from Matachewan in the west to the Rouyn-Noranda area, where it is

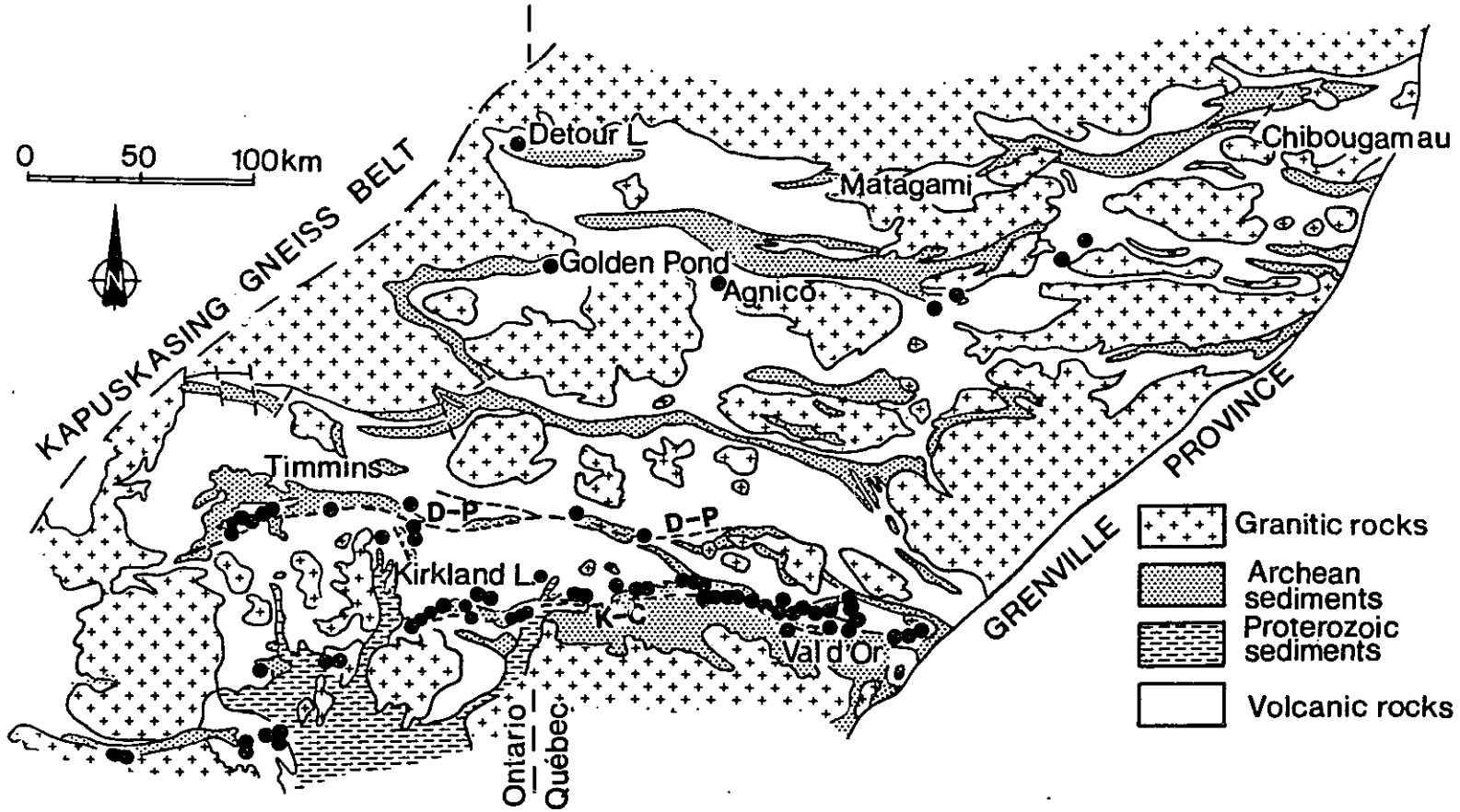

Fig. 2.6. Map showing the spatial relationships between gold deposits (solid circles) and major structural breaks in the Abitibi Greenstone Belt. D-P: the Destor-Porcupine Break; K-C: the Kirkland Lake-Larder Lake-Cadillac Break (after Roberts, 1987).

known as the Cadillac-Malartic Break (Fig. 2.6). The break may be traced as far eastward as the Grenville Front (Pyke, 1981; Hodgson, 1982; Roberts, 1987). Between Kenogami Lake and Matachewan, the break is overlain by flat-lying Proterozoic sediments of the Cobalt Group.

The Destor-Porcupine Break extends from approximately 25 km southwest of Timmins to about 60 km east of Duparquet where it merges with the Cadillac-Malartic Break, a total distance of about 250 km (Fig. 2.6).

Jolly (1978) has concluded that the development of these three main structures took place throughout the deposition of the volcanic and sedimentary rocks. More recent tectonic investigations on the Abitibi belt suggest the two major breaks developed as normal-slip growth faults (Dimroth et al., 1983), or as part of wrench-fault system (Hubert et al., 1984). Subsequent reactivation of these structures, predominantly as reverse faults, during the late stages of deformation resulted in the emplacement of late alkaline plutons and the development of Au-quartz vein systems within complex structural zones (Sibson et al., 1988).

In addition to the two main break structures, numerous northwest- to northeast-trending faults transect the area. Numerous diabase dykes of the Matachewan and Keeweenawan swarms have intruded along these northerly trending faults.

2.2.4 Metamorphism

Jolly (1974, 1978), in a regional study of metamorphism of the Abitibi Greenstone Belt, concluded that the majority of the pre-Timiskaming rocks of the Kirkland Lake area were metamorphosed to sub-greenschist and greenschist facies regional metamorphic grade.

In areas adjacent to the Lake Abitibi and Round Lake Batholiths, the metamorphic grade increases from sub-greenschist through lower, middle and upper greenschist facies. Rocks at the contacts of both batholiths reach the amphibolite facies. Adjacent to the numerous alkali intrusions, metamorphic aureoles as high as the pyroxene hornfels facies are common. Alkali metasomatism is often associated with these intrusions, particularly in highly sheared areas along the Destor-Porcupine and Kirkland Lake-Larder Lake Breaks (Jensen and Langford, 1985).

Chapter 3

Local and Mine Geology

3.1 Timiskaming Group

The town of Kirkland Lake and the immediate surrounding area is underlain by rocks of the Timiskaming Group. The Timiskaming Group forms a narrow continuous belt ranging from 0.8 to 5 km in width and approximately 60 km in length. The belt extends from Kenogami Lake in Eby township in the west through Teck township eastward to the Quebec border, where it is overlain by Huronian sediments of the Cobalt Group (Fig. 2.4).

The Timiskaming Group consists of fluvial and shallow marine sedimentary rocks, including argillite, greywacke, and conglomerate (Hyde, 1978), interlayered with K-rich alkalic and calc-alkaline flows, tuffs, and tuff breccias of trachyte composition (Cooke, 1966). The group forms a south-facing homoclinal sequence with a general eastward strike, and dips 30-60° south (Cooke and Moorhouse, 1969). The stratigraphic thickness of the Timiskaming ranges from 2100 to 4600 m (Cooke

and Moorhouse, 1969).

In areas where the Timiskaming Group is flat-lying, such as near its base, the basalts of the underlying Kinojevis Group are steeply dipping and face north, indicating the deposition of the Timiskaming following major tectonic activity (Jensen and Langford, 1985). Hodgson (1983) suggests that sedimentation of the Timiskaming Group was influenced by fault activity along the Kirkland Lake-Larder Lake Break. Jolly (1978) concluded that the Timiskaming Group had undergone little erosion, based on its low metamorphic grade, and suggested that it may have been formed and preserved in a narrow graben structure.

Hyde (1978) has suggested that the Timiskaming sediments from Kenogami Lake to Kirkland Lake are fluviatile sediments deposited in river channels flowing east. Jensen (1976) indicated that the three main sedimentary lithologies, conglomerate, greywacke, and argillite, contain clasts that were derived from three main environments. These include a komatiitic volcanic source, a carbonate-rich environment, and a composite source comprised of trachytic volcanic rocks interlayered with the sedimentary rocks. Jensen and Langford (1985) further noted that the conglomerates contain clasts of alkalic volcanic rocks, and syenite and monzonite clasts of local derivation, as well as clasts of komatiite, tholeiite, iron formation, and chert which appear to have been derived from the south. They also indicated that rocks from the Kino-

jevis and Blake River Groups to the north appear to be absent.

Throughout the deposition of the sedimentary rocks, four episodes of volcanic activity were produced by two volcanic centres located in Gauthier and Lebel townships (Cooke and Moorhouse, 1969). Each of the episodes usually began with the deposition of tuffaceous rocks, which were followed by flows with minor tuffs and finally by a variety of pyroclastic rocks. Flows are more common in the east in McVittie and Gauthier townships, while tuffs predominate to the west in Teck and Lebel townships (Fig. 3.1). The early Timiskaming lavas are calc-alkaline andesites with minor basalts and trachytes that are likely transitional from the underlying Blake River Group (Cooke and Moorhouse, 1969). The second and third episodes of volcanic activity were comprised of trachyte and leucitic flows and tuffs. The final episode, centred around Lebel and Gauthier townships, was comprised of trachyte flows followed by leucitic pyroclastic rocks and sedimentary rocks (Fig. 3.1).

3.2 Kirkland Lake Intrusive Complex

The Kirkland Lake Au Camp is hosted predominantly within a composite subalkaline to alkaline intrusive complex that is centred on the western town limits of Kirkland Lake (Fig. 3.2). The long axis of the intrusive complex strikes 060-080°, roughly parallel to the strike of the sedimentary and volcanic rocks of the Timiskaming Group. On surface the complex is

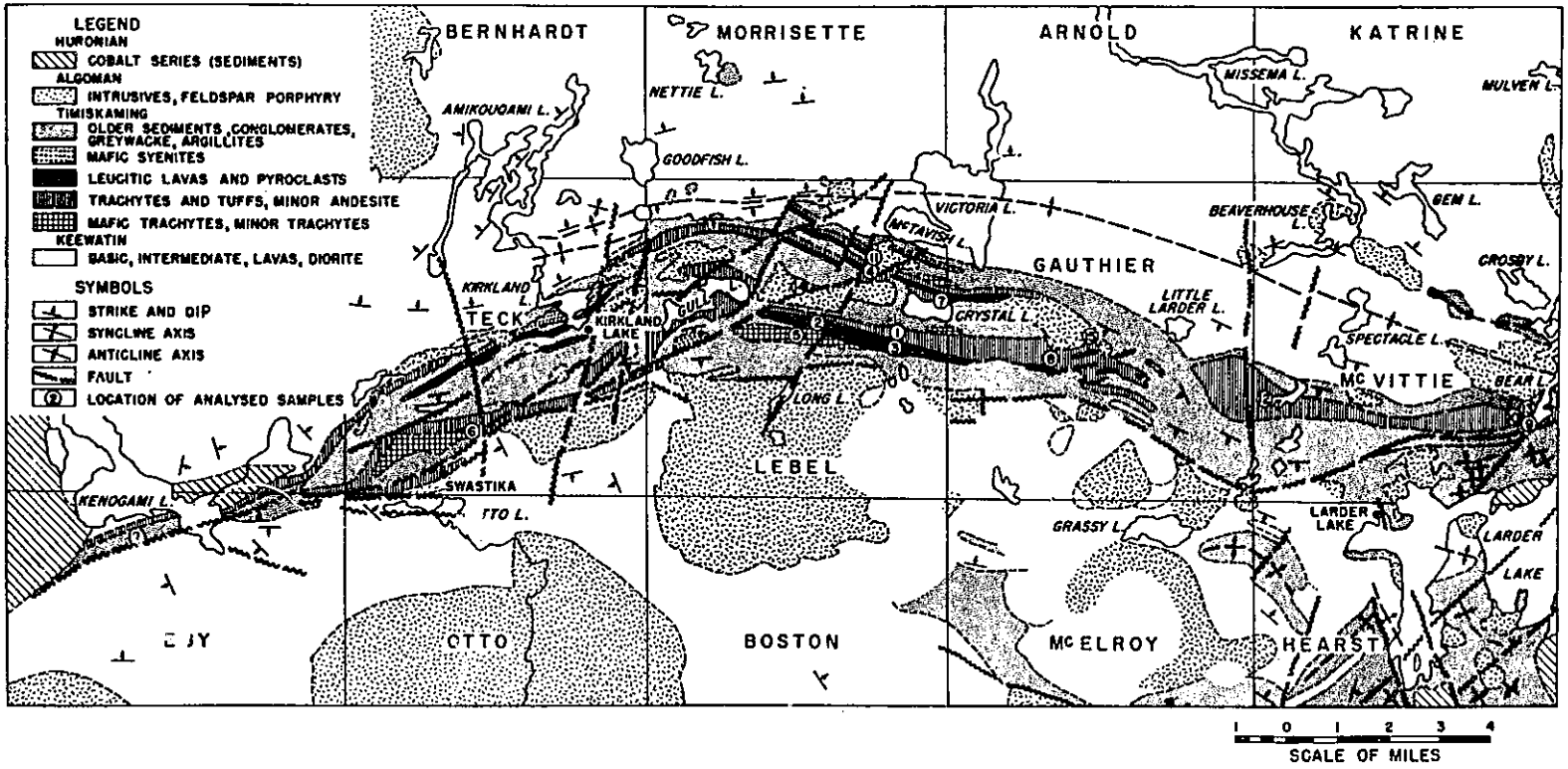

Fig. 3.1. Detailed geology of the Timiskaming Group (after Cooke and Moorhouse, 1968).

Fig. 3.2. Generalized geology of the Kirkland Lake gold camp (modified after Ploeger and Crocket, 1982).

GEOLOGICAL CROSS SECTIONS

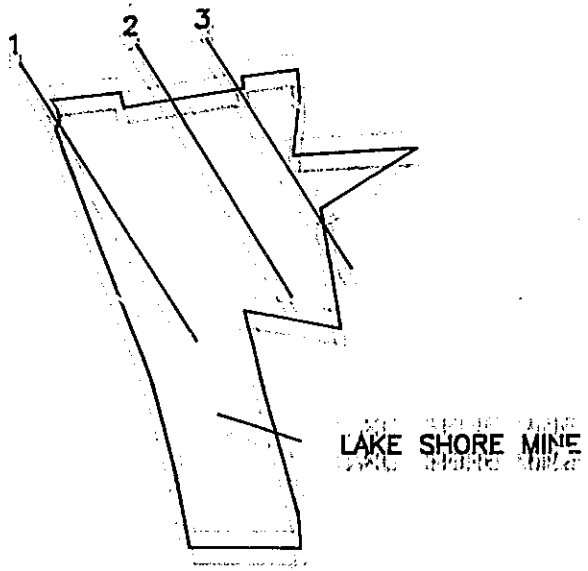

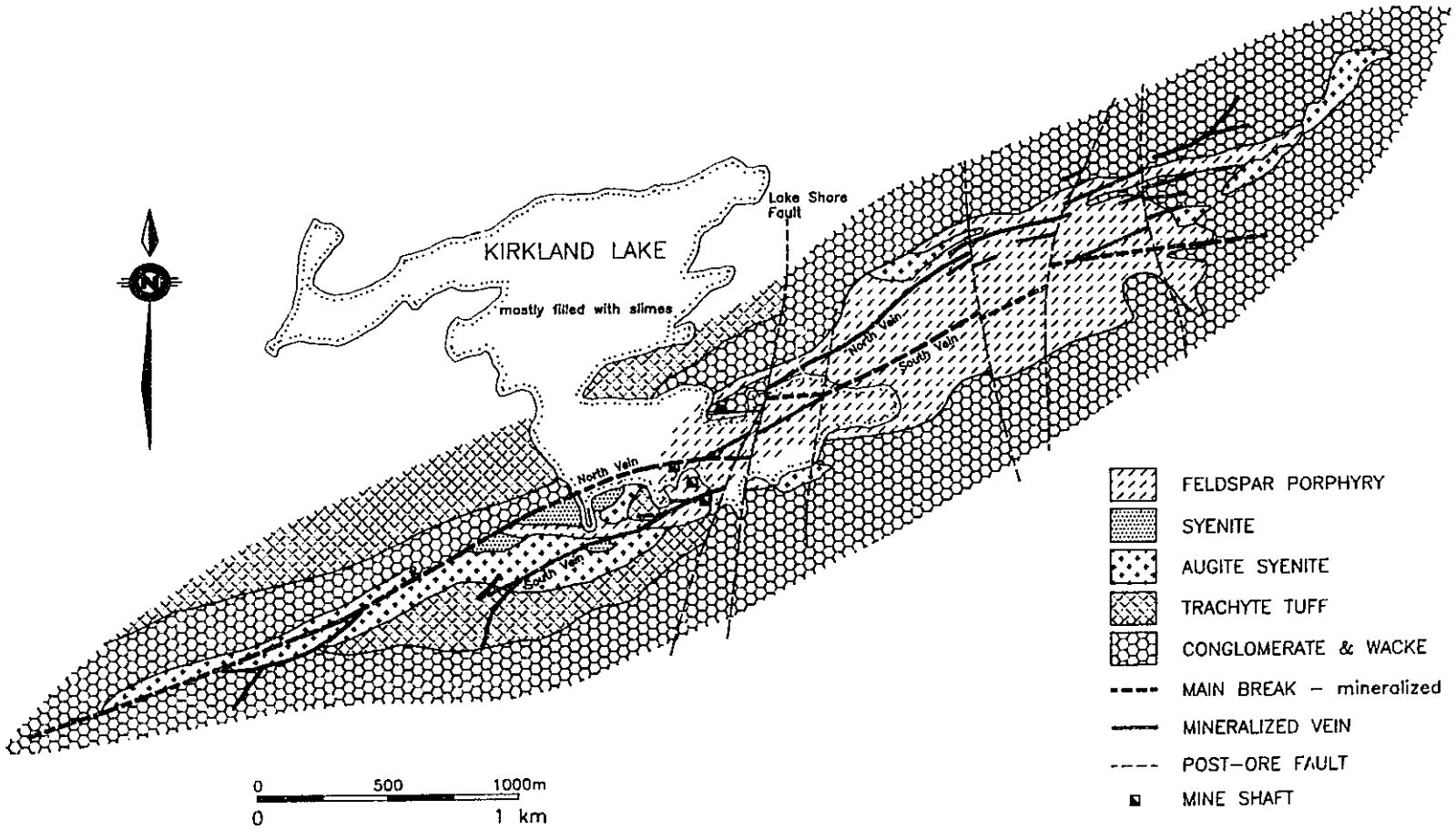
KIRKLAND LAKE
mostly filled with slimes
Lake Shore Fault
North Vein
South Vein
North Vein
South Vein
0 500 1000m
0 1 km
FELDSPAR PORPHYRY
SYENITE
AUGITE SYENITE
TRACHYTE TUFF
CONGLOMERATE & WACKE
MAIN BREAK – mineralized
MINERALIZED VEIN
POST–ORE FAULT
MINE SHAFT

slightly wedged-shaped, widening to the east (Fig. 3.2). The southern contact of the intrusive complex has a flatter dip than the northern; thus, the intrusion widens with depth. The entire complex dips steeply to the south and has an overall steep pitch to the west (Fig. 3.3).

The intrusive complex is comprised of three principal phases; augite syenite, syenite, and feldspar porphyry, with intrusion occurring in that order. Previously, the feldspar porphyry has been referred to as syenite porphyry (e.g. Todd, 1928; Hawley, 1950; Thomson, 1950). However, detailed petrography and geochemistry by the author suggest that the porphyry is not a syenite (according to IUGS classification) and hence the more physically descriptive name of feldspar porphyry has been applied. Quartz-feldspar porphyry, a minor phase within the Lake Shore property, is believed to be a late differentiate of the feldspar porphyry phase because of its mineralogical and textural similarities. Augite syenite was the earliest of the intrusive phases and forms irregular tabular lenses and dyke-like bodies (Thomson, 1950). The syenite phase forms pipe-like bodies that plunge to the west (Watson, 1984). Both well-defined intrusive contacts and transitional contacts between these two phases have been observed in drill core and in the underground workings (Frank Ploeger, Chief Mine Geologist, pers. comm., 1987).

Feldspar porphyry crosscuts both the augite syenite and the syenite phases with well defined intrusive contacts

Fig. 3.3. Diagrammatic longitudinal section along the hangingwall of the Kirkland Lake Main Break, showing the principal rock types (after Thomson, 1950).

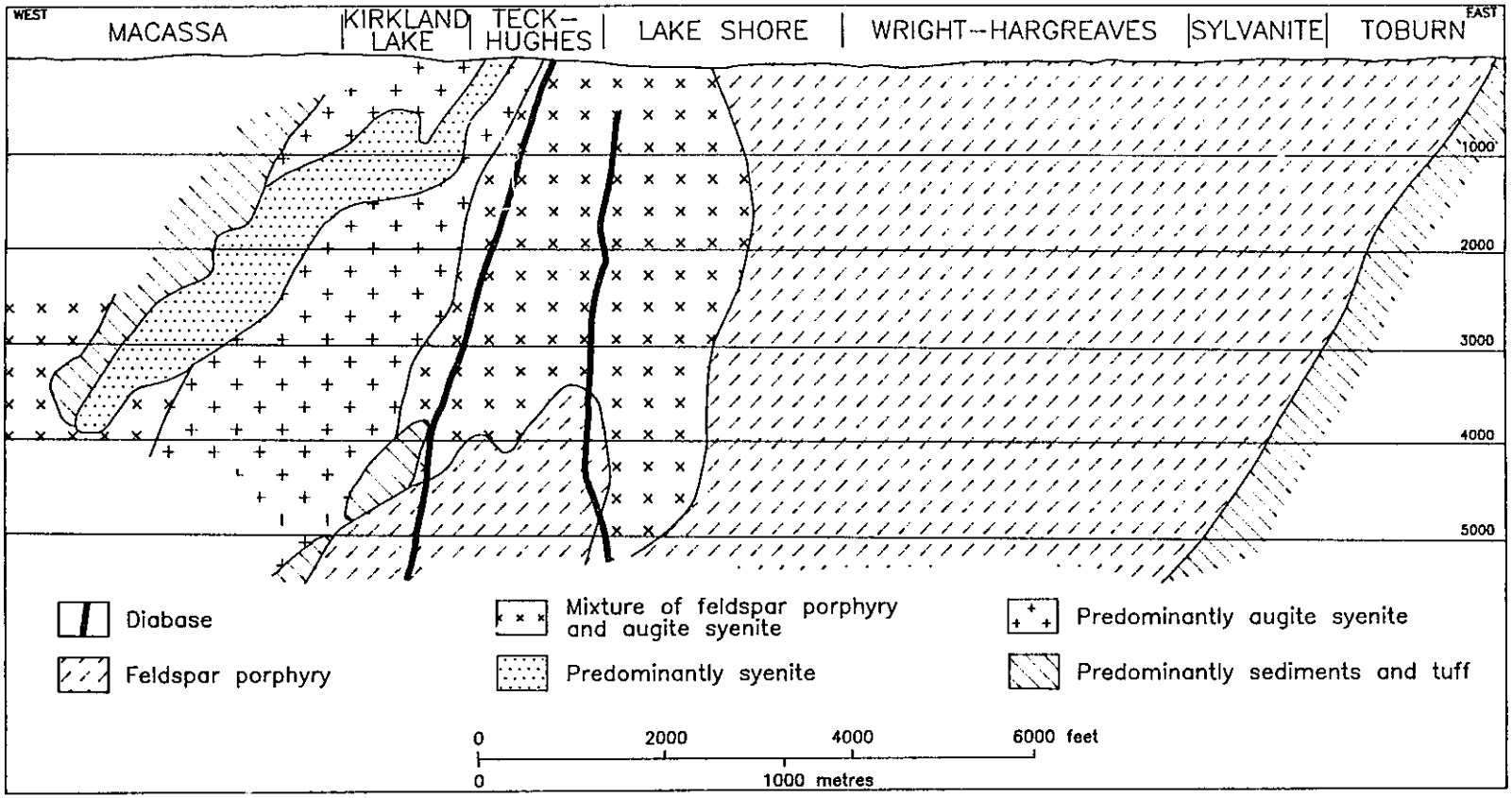
WEST
MACASSA
KIRKLAND LAKE
TECK–HUGHES
LAKE SHORE
WRIGHT–HARGREAVES
SYLVANITE
TOBURN
EAST
1000
2000
3000
4000
5000
Diabase
Feldspar porphyry
Mixture of feldspar porphyry and augite syenite
Predominantly syenite
Predominantly augite syenite
Predominantly sediments and tuff
0
2000
4000
6000 feet
0
1000 metres

indicating it to be the youngest of the three main phases. Contacts between the augite syenite and the feldspar porphyry are commonly irregular and often interfingered. The main composite body of the feldspar porphyry phase extends from the centre of the Lake Shore property eastward to the eastern limit of the complex. This body forms a central elongate plug that plunges steeply to the west (Fig. 3.3). Within this main body, well-defined porphyry-porphyry contacts indicate a composite intrusive nature for the porphyritic phases. At the west end of the camp, the feldspar porphyry occurs as dykes and small irregular-shaped bodies that cut the augite syenite and syenite phases with well-defined intrusive contacts (Thomson, 1950, Watson, 1984).

All phases of the intrusive complex as well as the Timiskaming Group are cut by diabase and minette dykes. The minette dykes are generally biotite lamprophyres and typically small in nature. Their exact relationship with the auriferous veins is uncertain. Hopkins (1946) suggests they are a late differentiate of the intrusive complex and therefore pre-ore in nature. Thomson (1950) suggests they were intruded after the main intrusive event but is uncertain of their relationship with the auriferous veins. Rare angular to rounded lamprophyre xenoliths within the feldspar porphyry indicate the onset of lamprophyre emplacement prior to the completion of feldspar porphyry intrusive activity.

Diabase ranges from small dykelets to dykes with a

maximum width of about 25 m. Two such larger dykes cut the area trending approximately north-south and dipping slightly west to near vertical (Fig. 3.3). These dykes cut the auriferous veins, substantiating a post-ore nature.

3.3 Rock Types in the Mine

The rock types present at the Lake Shore Mine include; 1) the older sediments and pyroclastic rocks of the Timiskaming Group, 2) augite syenite, syenite and porphyritic rocks of the Kirkland Lake intrusive complex, and, 3) later crosscutting diabase and minette dykes. Almost all of the mine workings lie within the intrusive complex; however, some of the drifts and crosscuts cut the sediments and pyroclastic rocks of the Timiskaming Group (Fig. 3.4). West of the shaft section, Timiskaming conglomerates and trachyte tuffs are in fault contact with the North Vein from the surface to the 800 foot level.

Lying to the north of the intrusive complex is an interbedded sequence of conglomerate, greywacke and bedded tuff. Drifting to the south of the intrusion reveals that tuffs flank the intrusive complex, followed in turn by conglomerate.

The intrusive complex trends 067°, roughly parallel to the Main Break and vein system (Fig. 3.2). East of the shaft section all of the Au-bearing veins lie within the feldspar porphyry phase (Figs. 3.3, 3.4). West of the shaft section,

Fig. 3.4. North-south cross sections through the Lake Shore mine. The locations of the sections are given in Figure 3.2. All sections looking east. After Thomson, 1950.

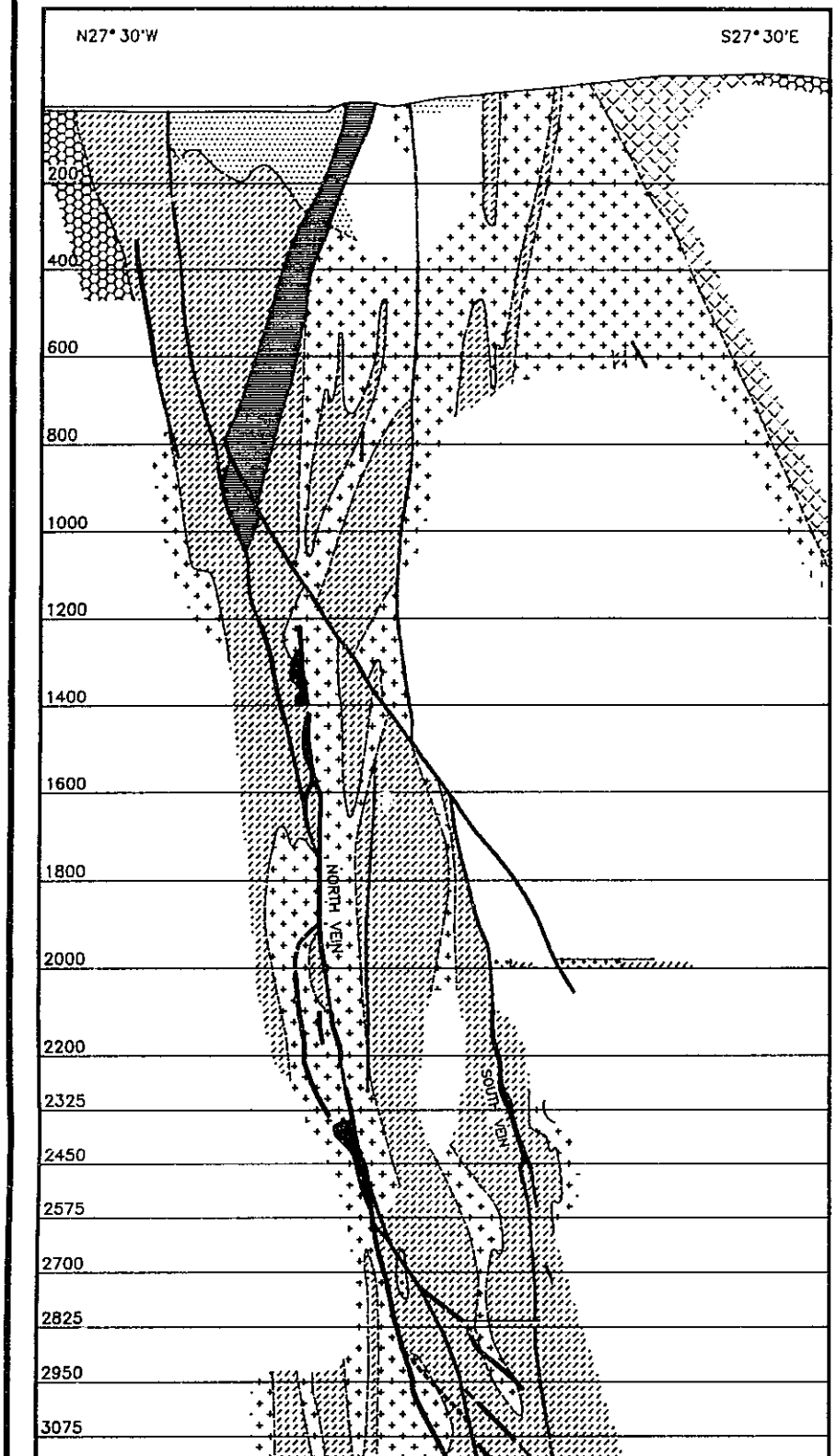
N27° 30'W
S27° 30'E
200
400
600
800
1000
1200
1400
1600
1800
2000
2200
2325
2450
2575
2700
2825
2950
3075
NORTH VEIN
SOUTH VEIN

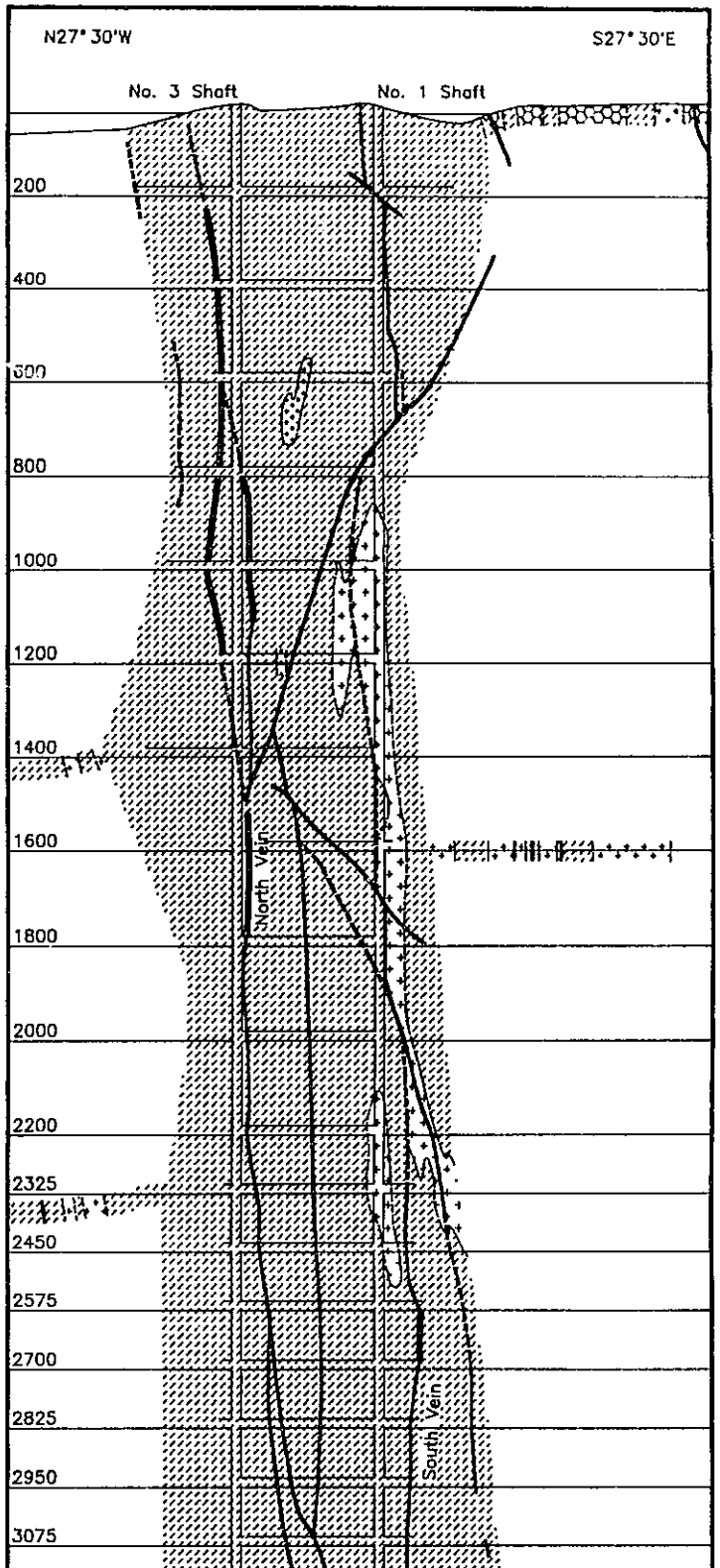
N27° 30'W
S27° 30'E
No. 3 Shaft
No. 1 Shaft
200
400
600
800
1000
1200
1400
1600
1800
2000
2200
2325
2450
2575
2700
2825
2950
3075
North Vein
South Vein

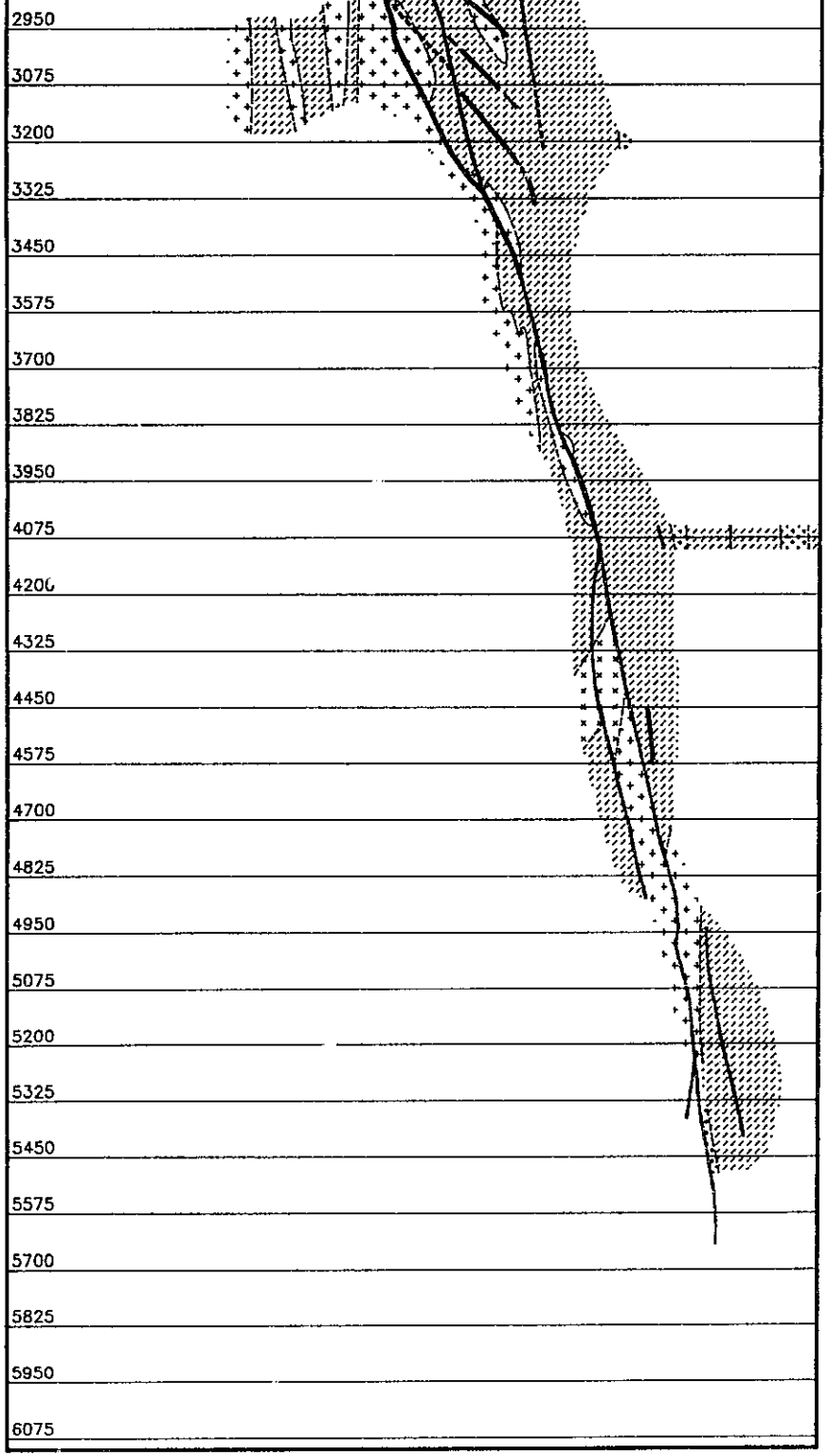

SECTION No. 1

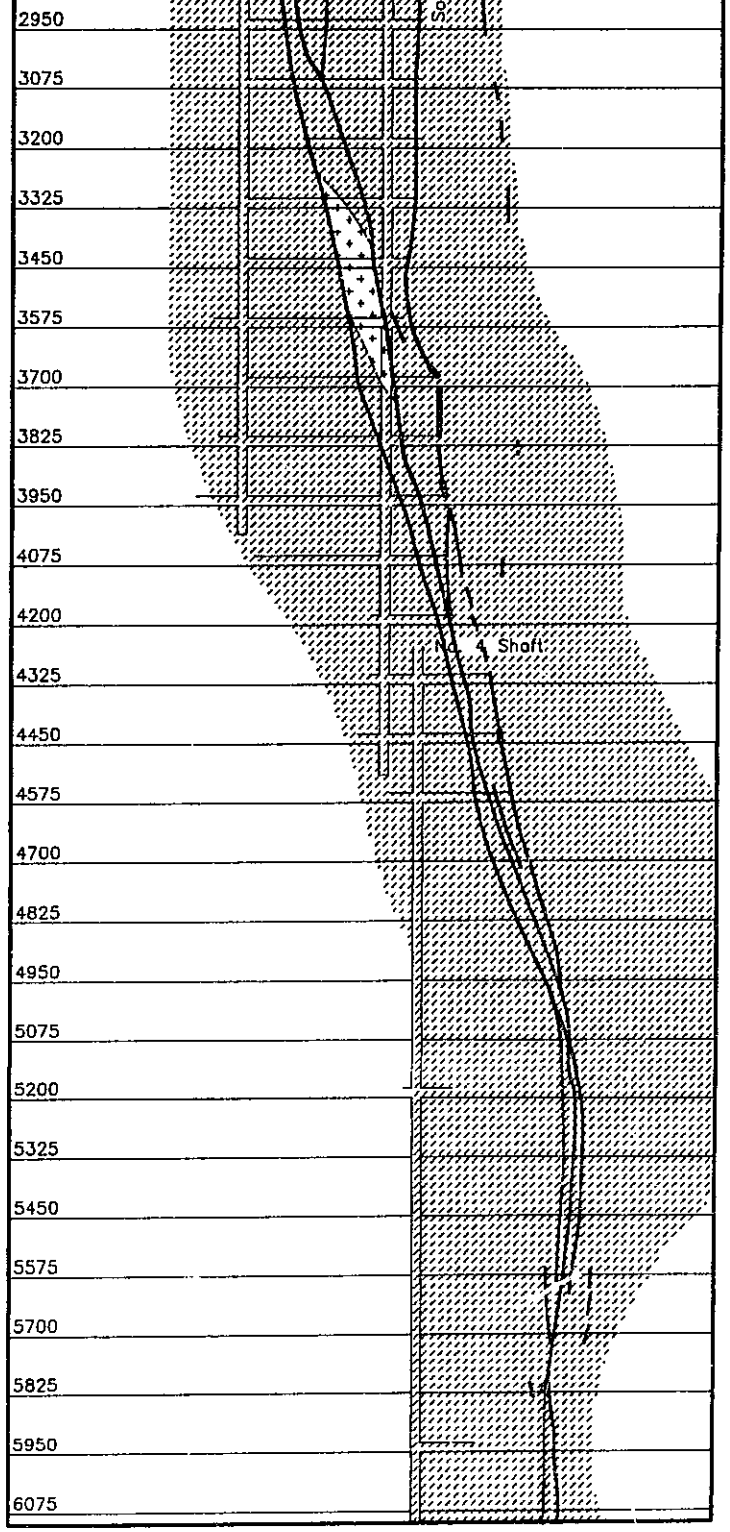

SECTION No. 2

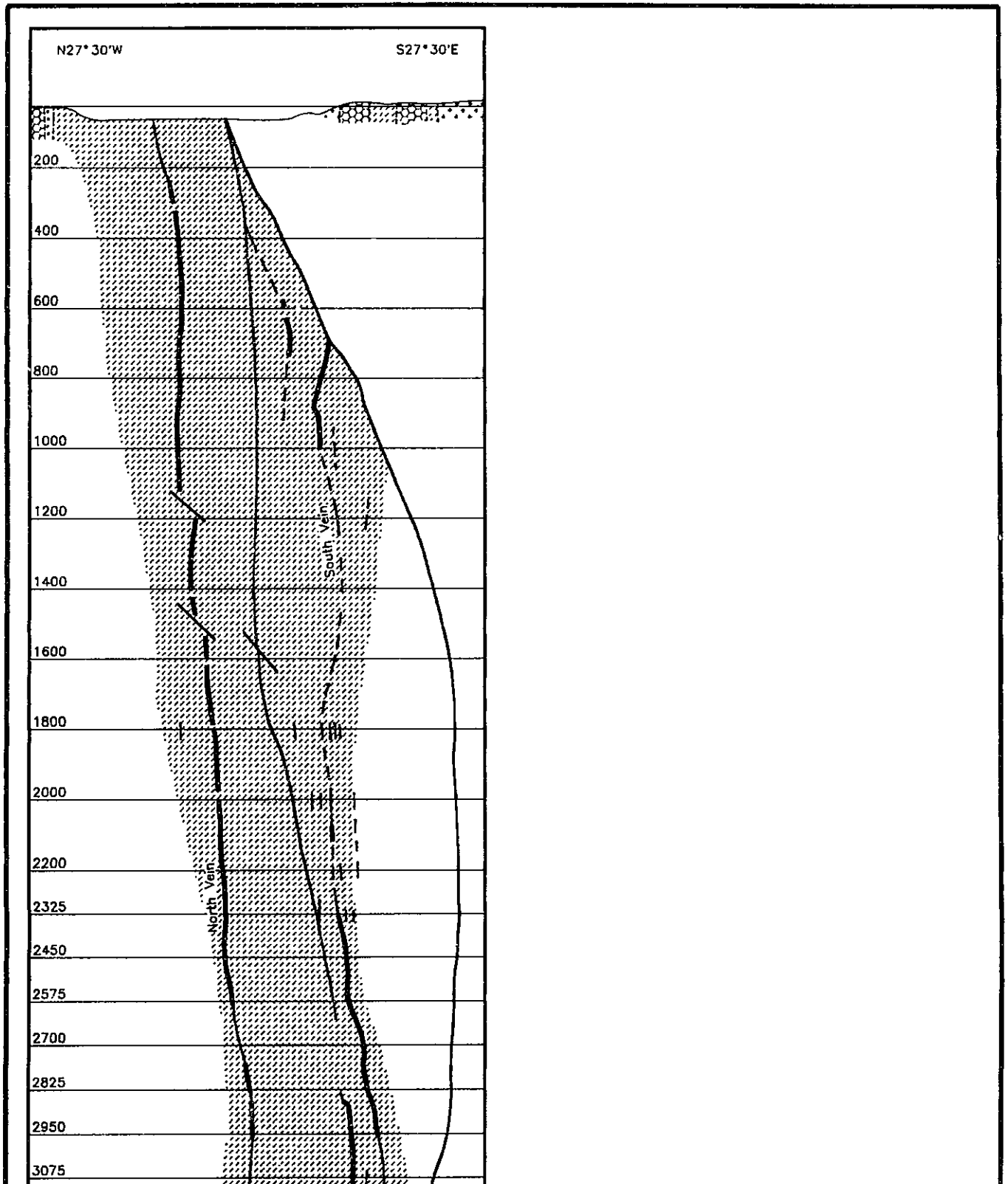
N27°30'W
S27°30'E
200
400
600
800
1000
1200
1400
1600
1800
2000
2200
2325
2450
2575
2700
2825
2950
3075
South Vein
North Vein

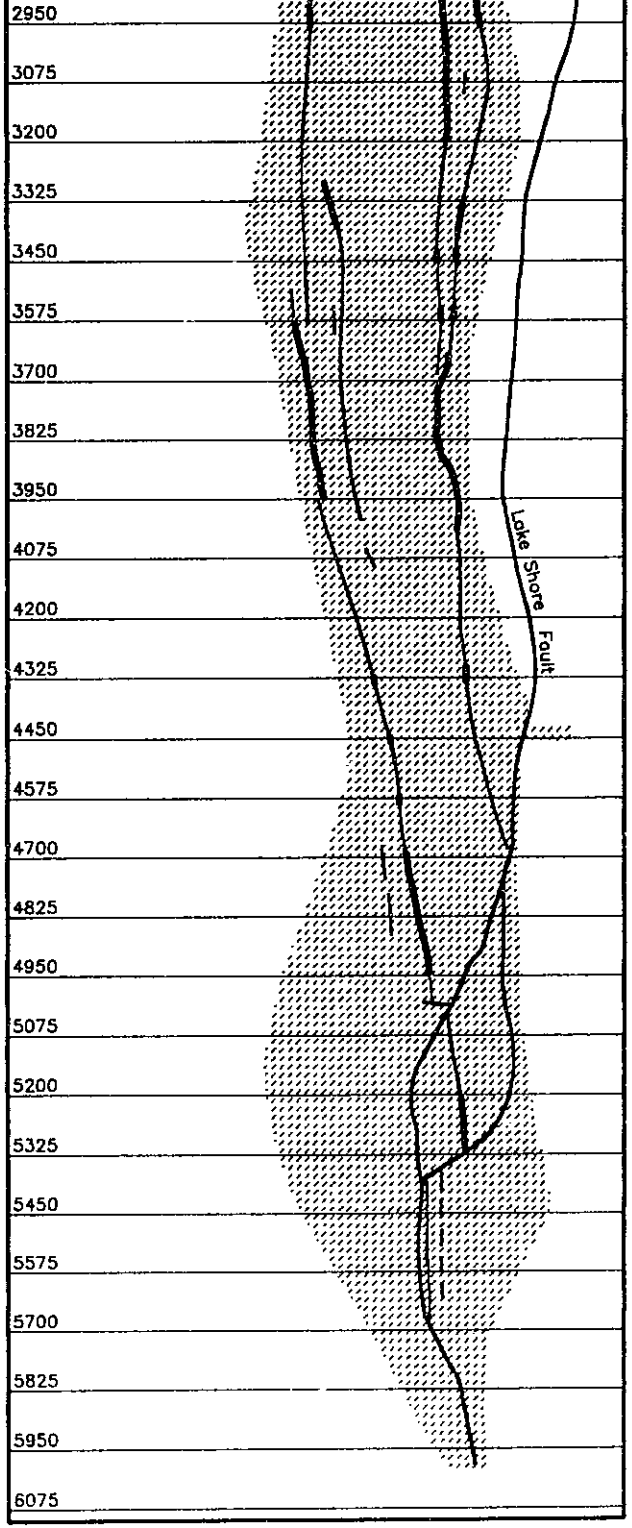

SECTION NO. 3

LEGEND

- Diabase
- Feldspar Porphyry
- Quartz–Feldspar Porphyry
- Syenite
- Augite Syenite
- Conglomerate
- Tuff

SYMBOLS

- Post–Ore Fault
- Stoped Ore
- Vein–Fault, Vein Fracture, Vein

400 0 400 800

Scale: 1 inch to 400 feet

augite syenite is interfingered with the porphyry and, to a lesser extent, the syenite. With increasing depth the amount of augite syenite decreases, until it is relatively scarce below the 5000 foot level (Figs. 3.3, 3.4). Small bodies of syenite occur in the upper portions of the west end of the Lake Shore property.

All rock types in the mine are cut by a subvertical north-south-trending diabase dyke that lies at the west end of the Lake Shore property. The average width of the dyke is about 15 m, although it does widen up to as much as 20 m in places. Minor offsets within the dykes are observed in the upper levels of the eastern limit of the mine where they cross the Kirkland Lake Main Break, indicating recurrent movement along the break.

3.4 Structure

The main structural feature of the immediate Kirkland Lake area is the Kirkland Lake-Larder Lake Break. The break passes just south of the town of Kirkland Lake, striking approximately 080° and dipping steeply to the south (Thomson, 1946, 1950). It is a brittle-ductile shear zone that ranges from 20 m to more than 100 m in width (Hodgson et al., in press). Generally this zone is comprised of chlorite, talc-chlorite, and chlorite-sericite schists associated with carbonate alteration (Hodgson et al., in press).

The Kirkland Lake Main Break, a splay structure off the

Kirkland Lake-Larder Lake Break, is the predominant pre-ore structure within the camp. The Main Break and its associated splay structures are a system of brittle to brittle-ductile faults which host virtually all of the significant Au ore in the Kirkland Lake camp (Hodgson et al., in press)(Fig. 3.2).

The Main Break is a reverse fault that can be traced across Teck township and a short distance into Lebel township (Thomson, 1950). The break is parallel to the long axis of the Kirkland Lake intrusive complex as well as to the general trend of the sedimentary units in the Timiskaming Group. The fault has a steep dip to the south and has been traced to a depth of more than 2400 m. Tyrrell and Hore (1926) estimated the vertical displacement at the west end of the camp to be about 570 m with the south or hangingwall moving upwards with respect to the north or footwall. Thomson (1950) calculated a vertical displacement of 460 m at Lake Shore by measuring the displacement between similar bodies of quartz-feldspar porphyry exposed on the north and south sides of the Main Break. At the east end of the camp, the offset in the porphyry-greywacke contact along the main plane suggests a vertical displacement of 110 m (Thomson, 1950). This suggests a rotational movement along the main plane, with the west end being thrust upward approximately 460 m more than the east end. Alternatively, the unequal displacement across the Main Break may also be attributed to a complex system of discontinuous, interconnecting faults (Thomson, 1950). In the

west, the Main Break is represented by a single or double plane of movement. Moving eastward, the fault system divides into more and more branches with decreasing amounts of displacement.

The temporal relationships between the Main Break and intrusive activity are uncertain. The elongate shape and parallel nature of the intrusive complex to the break suggest that it acted as a conduit for the intrusions. Subsequent movement along the break after solidification of the intrusions would provide a conduit for auriferous hydrothermal fluids.

The Kirkland Lake Main Break traverses east-west across the Lake Shore property, covering a distance of about 850 m (Fig. 3.2). Two prominent branching structures are developed near the centre of the property, giving the fault system the appearance of two parallel faults connected by a diagonal crossover structure (Fig. 3.2).

In addition to the break structures, numerous fractures are developed throughout the camp, most of which are subsidiary to the larger breaks. The majority of these smaller structures are tensional features that developed complementary to the larger structures (Thomson, 1950).

Numerous post-ore faults and fractures occur throughout the camp; however, they are generally more common at the east end. These structures include faults parallel to the Main Break and vein system, as well as cross faults that generally

have a north to northeast strike. Post-ore faults parallel to the Main Break and vein system generally have flatter dips than the main break and related faults.

The Lake Shore Fault is the best developed and most important of the post-ore cross faults. It generally contains one or more well developed planes of chloritic gouge as well as minor fault breccia. The fault strikes north-northeast and dips steeply to the east. It crosses the eastern portion of the Lake Shore property and the western portion of the Wright-Hargreaves property, transecting the Au-bearing vein system (Fig. 3.2). Thomson (1950) estimated a horizontal displacement of 180-230 m and vertical component of about 100 m, with the east side being downthrown and moved northwards with respect to the west side.

3.5 Metamorphism

The regional metamorphic grade of the Kirkland Lake camp is very low. Within the conglomerates of the Timiskaming Group, the clasts contain mineral assemblages indicative of prehnite-pumpellyite facies metamorphism, whereas the matrix is unmetamorphosed (Jolly, 1974). This suggests that sedimentation of the Timiskaming Group post-dated regional metamorphism. It further suggests that the intrusive rocks hosting the Kirkland Lake camp are unmetamorphosed.

Chapter 4

Veining and Mineralization

Veining and mineralization at the Lake Shore Deposit, as well as throughout the Kirkland Lake Au camp, occurs along the previously mentioned pre- and post-ore fault and fracture systems. Thomson (1950) termed these vein-bearing structures as vein faults where displacement was apparent, and vein fractures if there was no apparent displacement.

The veins at Lake Shore may be divided into three principal groups; 1) auriferous veins, 2) post-ore veins, and, 3) veins of uncertain timing.

4.1 Auriferous Veins

Au-bearing veins occur along the aforementioned pre-ore fault and fracture system. They are found in all of the previously mentioned rock types with the exception of the late diabase and minette dykes. The best developed and most productive veins at Lake Shore are the North and South Veins, two subparallel veins separated by a distance of about 150 m

on surface (Fig. 4.1). Both veins are continuous across the east-west extent of the Lake Shore property.

4.1.1 North Vein

The North Vein is the best developed and most productive structure at Lake Shore. It extends across the Lake Shore property between the Teck-Hughes and Wright-Hargreaves boundaries, covering a distance of about 850 m (Fig. 4.1). The vein is as equally persistent vertically, extending below the 7000 foot level (Charlewood, 1964)(Fig. 3.4). Shearing is commonly associated with the North Vein and where present is generally stronger on the footwall or north side. West of the Mud Break, a diagonal cross structure between the North and South Veins towards the east end of the property, the North Vein lies within the Main Break. East of this structure the vein lies within a branching structure off the Main Break (Fig. 4.1).

4.1.2 South Vein

On surface the South Vein parallels the North Vein, and lies roughly 150 m to the south (Fig. 4.1). East of the Mud Break the South Vein lies within the Main Break, while west of the Mud Break it lies within a parallel branching structure. The South Vein is not as continuous as the North Vein, both vertically and horizontally. The dip of the South Vein is somewhat steeper than the North Vein, and as a result the two

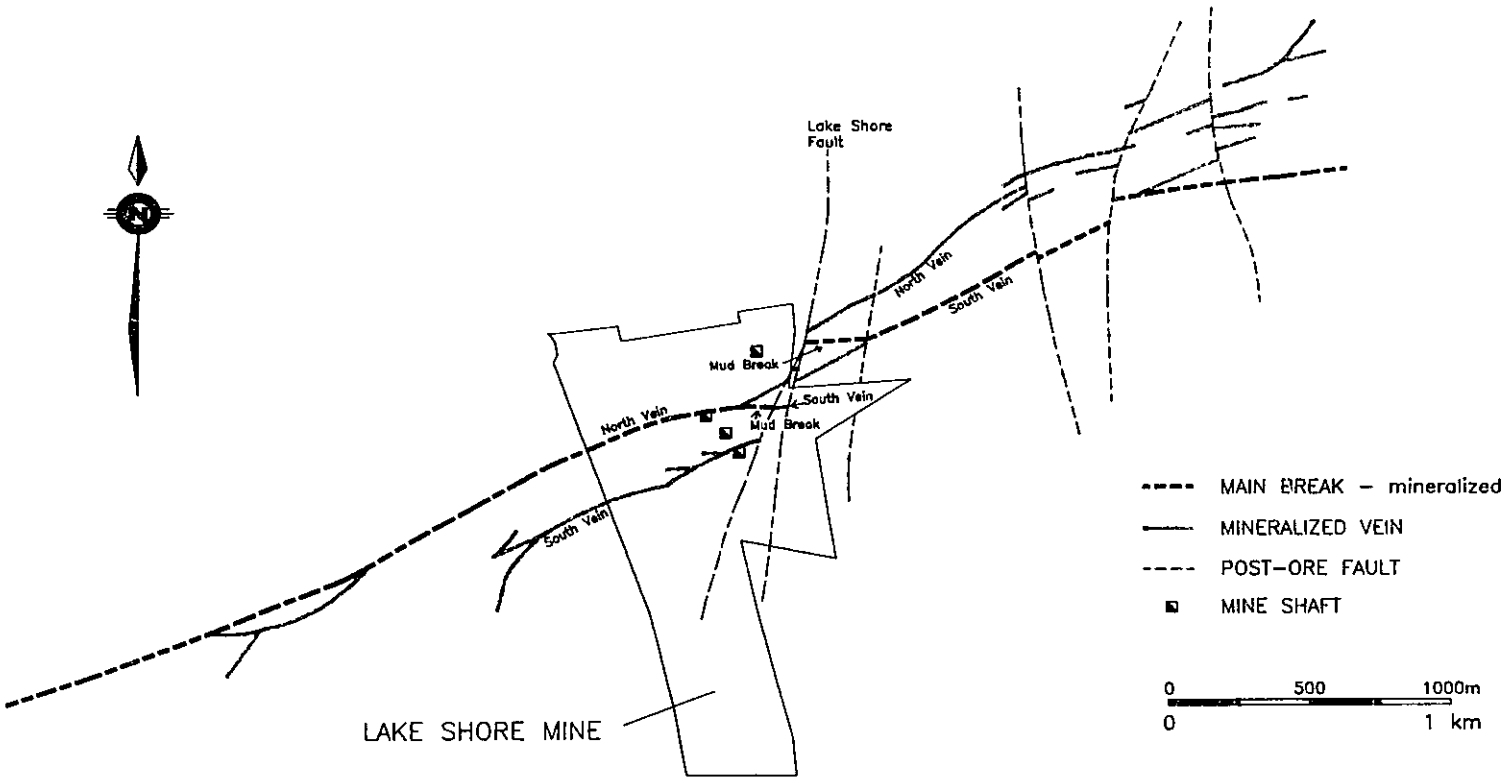

Fig. 4.1. The main vein system at Kirkland Lake (modified after Ploeger and Crocket, 1982).

coalesce at about the 4000 foot level (Fig. 3.4)

4.1.3 Mud Break

The Mud Break lies between the North and South Veins at the east end of the property (Fig. 4.1). It has generally been considered as the continuation of the Kirkland Lake Main Break between the North and South Veins; however, Thomson (1950) suggested this may not be the case. While the Mud Break is well developed in the upper levels of the mine, Thomson argued that between the 1200 and 2450 foot levels, it broke up into several weak fractures, and that between the 2450 and 4000 foot levels it consisted of two weak slips near the junction with the North Vein. Inaccessibility during this study negated the possibility of further assessment.

The Mud Break displays a different type of mineralization than the North and South Veins. Veining is relatively minor along this structure and, as a result, the term "gouge ore" has been applied. This ore is characterized by the occurrence of Au, as well as sulphides and tellurides (?), in chloritic fault gouge or in quartz lenses within the major fault system (Jim Gray, mine geologist, pers comm., 1986). Au grades are erratic and generally lower than those associated with the quartz vein system.

4.1.4 Vein Classification and Description

The veins may be classified as single fissure veins,

breccia veins, stockworks, and sheeted veins. Single fissure veins (Plate 4.1) are by far the most common in the upper portions of the Lake Shore mine. Single fissure veins generally lie within the main break or within several of the parallel and/or branching faults and fractures. These veins vary in width from 3 cm up to 1.5 m, and are commonly separated from the wall rocks on one or both sides by seams of chloritic fault gouge up to 2 cm in width (Plate 4.1). The gouge is a cataclastic mixture of fine grained chlorite, quartz, pyrite and rock fragments. Its lack of recrystallization suggests formation during recurrent fault movement after the main-stage hydrothermal activity associated with Au mineralization. Generally, where fault gouge appears only on one side of a vein, fracturing of the wall rock has led to the formation of irregular quartz stringers on the opposite side of the vein which emanate into the wall rocks.

Quartz stockworks (Plate 4.2), breccia veins, and sheeted veins are less common. They generally lie adjacent to the main fault systems and form ore zones up to 20 m in width (Thomson, 1950).

Vein fillings are comprised predominantly of quartz and lesser amounts of angular to brecciated inclusions of altered and mineralized wall rock. Narrower veins are commonly filled only with quartz. Breccia veins are formed where large amounts of wall rock have been incorporated into the veins.

Plate 4.1. Photograph of a typical single fissure vein from the 1200 foot level, east boundary pillar. Note the development of chloritic gouge (Cg) along the foot wall of the vein indicating recurrent movement along the host fault. The lens cap for scale is approximately 5.5 cm in diameter.

Plate 4.2. Photograph of the stockwork vein system. Note the abundance of the molybdenite/graphite slip material which commonly lines the wall rock fragments. The lens cap for scale is approximately 5.5 cm in diameter.

Plate 4.3. Photograph of a single fissure vein with molybdenite/graphite line fracture surfaces ("moly slips") and inclusions of wall rock fragments (Wf). The sample represents the whole width of the North Vein from the east boundary pillar, 1200 level. The extreme narrowness is not typical as widths up to 2m are also observed. The white scale bar is 2 cm.

4.1

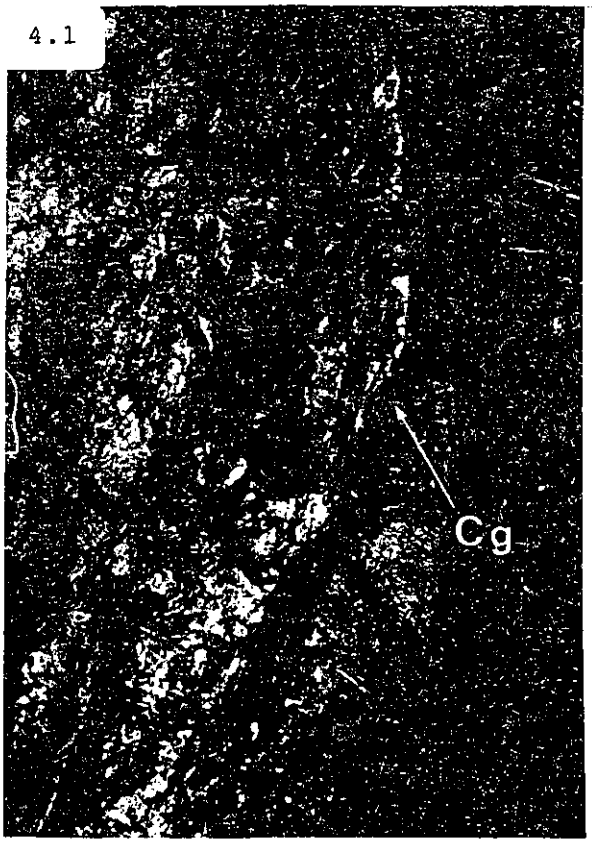

4.3

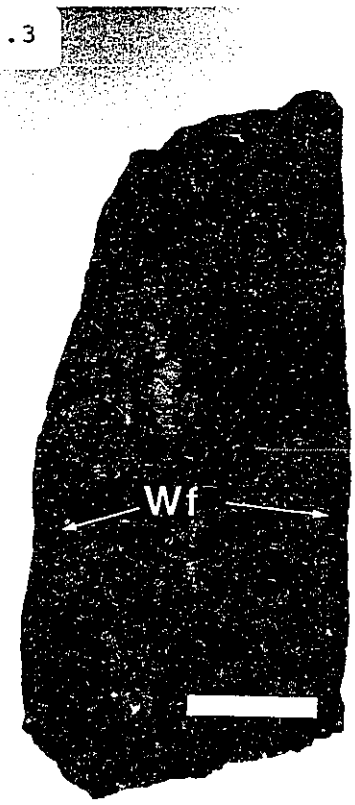

4.2

4.1.5 Vein Petrology, Mineralogy, and Paragenesis

Vein quartz varies from dark greasy grey to white glassy varieties. Petrographic studies of the vein quartz indicate that multiple stages of hydrothermal activity occurred synchronously with brittle-ductile deformation (this study, Theriault, 1988). White quartz appears to have been the primary vein filling. Grey quartz generally fills fractures transecting the earlier quartz, its darker colour being due to the presence of numerous fluid inclusions. A fluid inclusion study by Gallimore (1988) at the Macassa Mine indicates a minimum filling temperature of 335°C for the main ore veins there. These results may also be applied to Lake Shore as it is part of the same vein system.

In thin section the quartz is generally anhedral; however, there are rare euhedral crystals indicating minor open-space filling. Undulatory extinction, small 2V axial angles, jagged grain boundaries, microfaults, and displacements due to pressure solution are very common in the earlier generations of quartz. In some sections of the South Vein, the quartz has a chert-like appearance, and ranges in colour from buff to light brown. In thin section it displays a "mylonitic-like" texture characterized by minor amounts of relatively undeformed grains set in a fine grained, crushed matrix.

The auriferous veins are generally highly fractured, resulting from brittle deformation of the quartz due to recurrent movement along the fault and fracture planes.

Fracture and slip surfaces within the veins are commonly lined with a dark bluish-grey greasy material ("moly-slips")(Plate 4.3). These surfaces often display slickensides, a further indication of recurrent fault movement. Analyses by Todd (1928) indicate the "moly-slip" material to be comprised of 90% sericite and chlorite, 6.5% molybdenite, and 3.5% pyrite. Theriault (1988) confirmed the presence of molybdenite in some of the "moly-slips" by utilizing X-ray camera techniques. Graphite may or may not be associated with these slip surfaces (Theriault, 1988). In narrower sections of the veins these slip surfaces are generally parallel to the veins, while in wider sections they often have a braided appearance.

Carbonates, chlorite, and sericite are also present in the veins. Carbonate minerals include calcite and ankerite, the majority of which appears to have been introduced after Au mineralization (see post-ore veins).

Pyrite is the most abundant sulphide mineral in the veins, averaging approximately 2% by volume. It is more commonly found (up to 10% by volume) in the altered and mineralized wall rocks adjacent to the veins or in wall rock fragments within the veins. Within the veins, it is predominantly found in fractures and along the bluish-grey "moly-slips". Within the slips, pyrite occurs as a fine grained cataclastic material due to its brittle nature and grinding action associated with movement along the slips.

Euhedral pyrite crystals are most often found within the

massive quartz gangue. They are locally observed in association with altaite (PbTe) in fractures where they often display replacement by altaite (Plate 4.4). Rare inclusions of altaite (Plate 4.5) and gangue minerals suggest syn-deposition or recrystallization of pyrite. Grain sizes are generally less than 0.5 mm for all types of pyrite.

Chalcopyrite is the second most abundant sulphide mineral occurring predominantly within fractures in quartz. It is commonly overgrown or replaced by altaite (Plate 4.6), Au, calaverite ($AuTe_2$), and coloradoite (HgTe), suggesting it was formed early in the paragenetic sequence. Chalcopyrite is also common in the post-ore carbonate veins.

The occurrence of galena and sphalerite in the Kirkland Lake camp is very rare (Todd, 1928; Hawley, 1950). McInnes (1985) noted veining or replacement of sphalerite by chalcopyrite, altaite, calaverite, coloradoite, and Au, suggesting it occurs relatively early in the paragenetic sequence. Neither of these minerals were observed in this study.

Altaite is the most abundant telluride in the auriferous veins at Lake Shore (this study) as well as throughout the Kirkland Lake camp (Hawley, 1950). It is frequently observed overgrowing and replacing coloradoite, pyrite, chalcopyrite (Plate 4.6), and Au (Plate 4.7) suggesting it occurs very late in the paragenetic sequence.

The occurrence of coloradoite at Lake Shore is quite

Plate 4.4. Photomicrograph showing altaite (Al) invading and replacing euhedral fractured pyrite (Py) cubes. Reflected light.

Plate 4.5. Photomicrograph showing inclusions of altaite (Al) in euhedral pyrite (Py) suggesting either the recrystallization of pyrite or continual or repeated introduction of pyrite during the later stages of hydrothermal activity. Reflected light.

Plate 4.6 Photomicrograph showing altaite (Al) replacing/overgrowing chalcopyrite (Cp). Reflected light.

Plate 4.7. Photomicrograph showing altaite (Al) overgrowing/replacing coloradoite (Co) and gold (Au) and replacing pyrite (Py). The relationship between gold and coloradoite appears to simply be an overgrowth. Reflected light.

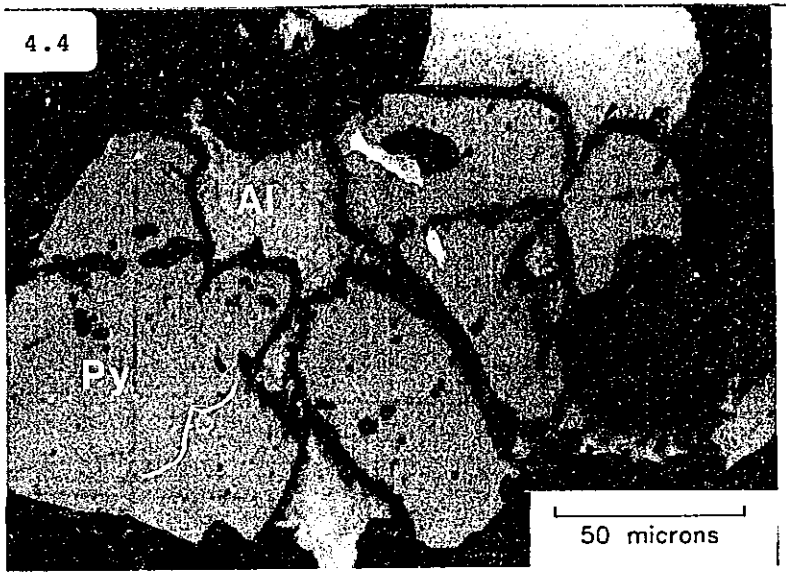
4.4
Al
Py
50 microns

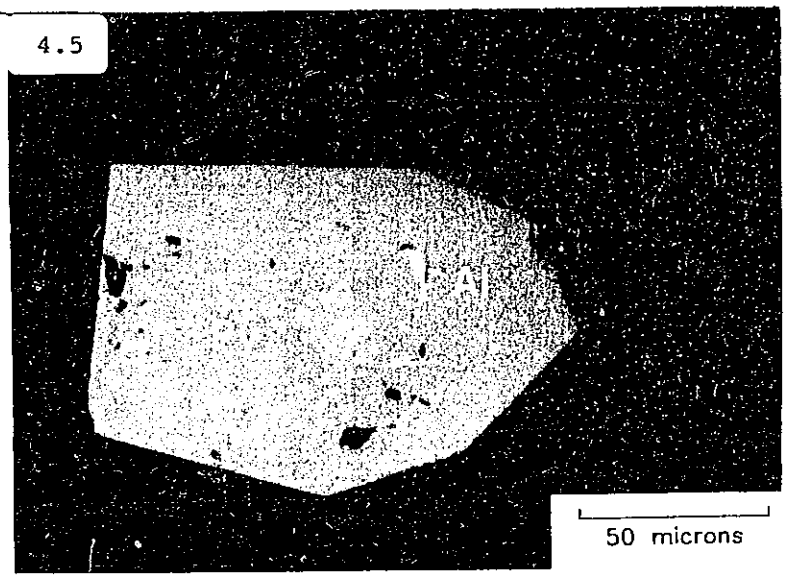
4.5
Al
50 microns

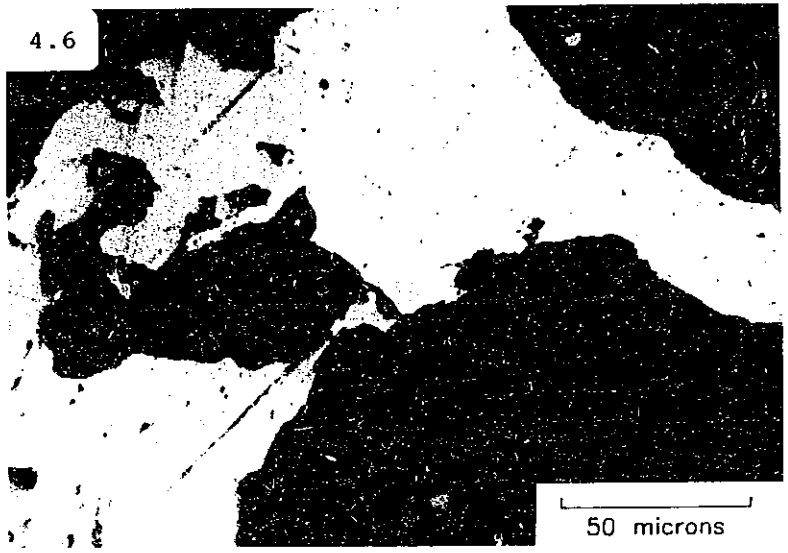
4.6
50 microns


4.7
50 microns

common. It is generally associated with altaite, calaverite, Au, or varying assemblages of the three as rounded inclusions. More rarely, it is observed overgrowing or replacing altaite (Plate 4.8).

Calaverite, although rare in this study, was reported to have accounted for up to 17% of the Au ore mined during the early days of the Kirkland Lake camp (Todd, 1928). It is most commonly associated with altaite, or with altaite, coloradoite, and Au as inclusions.

Native Au occurs as fracture fillings in quartz or as smears formed due to recurrent fault movement along the "moly-slips". More commonly it is associated with tellurides, particularly altaite, as rounded to amoeboid inclusions (Plate 4.7). Au rims most of the previously described minerals, suggesting that most of it was precipitated late in the paragenetic sequence (Plate 4.8). Hawley (1950) reported the presence of fine inclusions of Au in pyrite throughout the camp, however, none were observed in this study. Native Au also occurs in the altered wall rocks and in altered wall rock fragments within the veins (Hawley, 1950). Relationships between Au and other metallic minerals are unknown in these occurrences as none were observed in this study.

The paragenetic sequence of the Kirkland Lake and Lake Shore ores has been described by Hawley (1950), McInnes (1985) and Theriault (1988). All three studies are in general agreement with each other, as well as with this study.

Plate 4.8. Photomicrograph depicting altaite (Al) being overgrown/replaced by coloradoite (Co), which is in turn being overgrown/replaced by gold (Au). Reflected light.

Plate 4.9. Photograph showing post-ore carbonate veins (CV) crosscutting the quartz fracture filling (QV) in a typical breccia vein. The sample has been rotated 90 degrees from true attitude and represents the whole width of the North Vein.

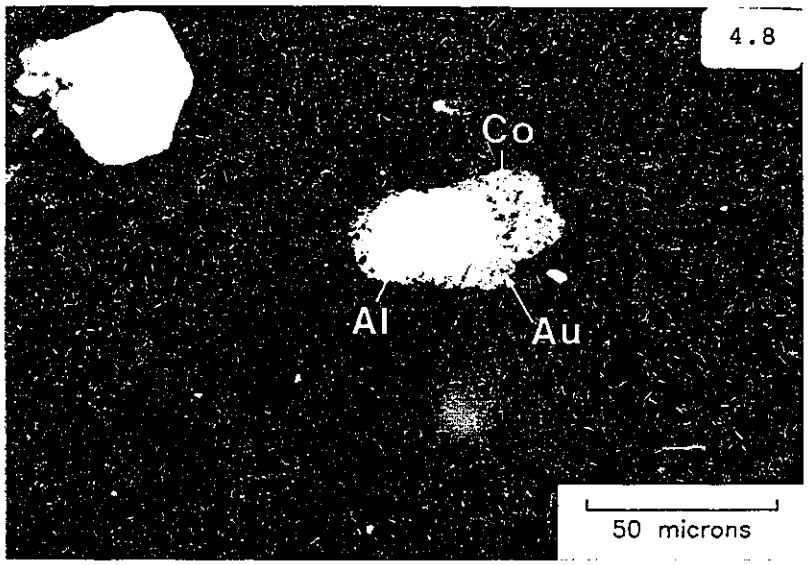

4.9

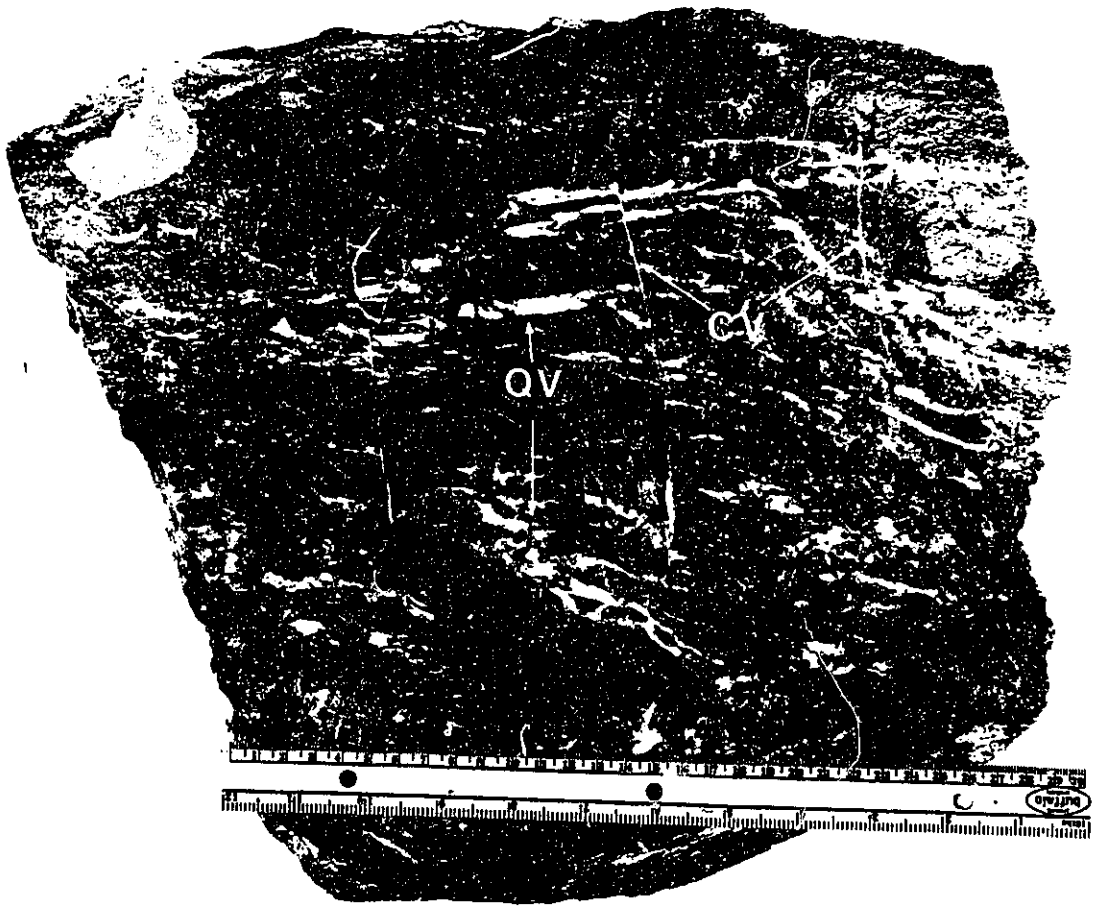

The development of the auriferous vein system began with the precipitation of massive white quartz. Subsequent brittle-ductile deformation and recrystallization of the quartz formed an intricate fracture system within the veins, providing fluid conduits and allowing the introduction and deposition of metallic minerals including Au.

Pyrite appears to have been the first mineral deposited, followed by chalcopyrite. Replacement of sphalerite by chalcopyrite led McInnes (1985) to place sphalerite deposition prior to chalcopyrite, while Hawley (1950) suggests they are coeval.

Deposition of sulphides was followed by tellurides and Au. Calaverite, coloradoite, altaite, and Au appears to have been the order of deposition; however, local variations in this order suggest overlapping of the depositional periods. Inclusions of altaite in pyrite suggest either the recrystallization of pyrite or deposition over a long period of time.

4.2 Post-Ore Veins

Several types of post-ore veins are recognized at Lake Shore. Late stage fractures within the ore veins and adjacent altered wall rocks, formed by post-ore movement along the vein faults, are filled with quartz or carbonate and varying amounts of quartz, barite, gypsum, chlorite, sericite, and chalcopyrite. These veins are generally parallel to

subparallel to the main auriferous veins. Where hosted in the auriferous veins, they are generally discontinuous. Quartz is generally white to glassy while calcite is commonly pinkish.

Small carbonate stringers cutting the ore veins at right angles are fairly common (Plate 4.9). Carbonates within the post-ore veins and veinlets are occasionally euhedral, possibly indicating open-space filling. Pressure twinning is generally present, indicating minor degrees of strain. Fluid inclusion studies by Gallimore at Macassa (1988) indicate a minimum filling temperature for these veins of 270°C, suggesting deposition during the waning stages of hydrothermal activity. Carbonate deposition was likely brought about by post-ore faulting which resulted in pressure reduction, allowing the precipitation of carbonate (Gallimore, 1988).

The post-ore quartz veins appear to pre-date the post-ore carbonate veins as evidenced by cross cutting relationships. Furthermore, fluid inclusion studies by Gallimore (1988) at Macassa indicate a minimum filling temperature of 325°C for these veins, suggesting they may have precipitated from the cooling fluids responsible for the auriferous veins. These findings may also be applied to Lake Shore, which is part of the same system.

Post-ore veining is also associated with the Lake Shore Fault. Filling by quartz and carbonate is fairly common for this structure as well. In areas where vein filling is absent, the fractures are characterized by chloritic fault gouge.

4.3 Veins of Uncertain Timing

These veins are dominated by hematite and quartz-hematite stringers and veinlets and are confined within the composite intrusive complex. They are abundant in areas proximal to the North Vein (<15 m) on the 600 foot level, however, their full distribution is unknown. They are never present in the rocks adjacent to the auriferous veins where sulphide mineralization has taken place, suggesting pre-ore emplacement; however, the exact time of emplacement of these veins is uncertain, as crosscutting relationships with other veins are not observed. As a result of this, their timing relationship with the fault and fracture systems is also uncertain.

Chapter 5

Petrology and Geochemistry of the Intrusive Rocks

5.1 Petrology

5.1.1 Augite Syenite

Augite syenite is the earliest of the intrusive phases in the Kirkland Lake complex. Samples collected from the Lake Shore and Tech-Hughes properties show strong similarities both mineralogically and texturally. In hand specimen, the rock is typically dark, varying from dark grey to dark greyish black, and is generally medium to coarse-grained with a hypidiomorphic granular texture (Plate 5.1). Coarser grained portions often have a black and white mottled appearance (Plate 5.1).

The primary mineralogical constituents consist dominantly of augite (25-45% by volume), and K-feldspar (40-60% by volume) with minor amounts of titaniferous magnetite (up to 5% by volume), biotite (<5% by volume), hornblende (<3% by volume), apatite (<2% by volume), and titanite (<1% by volume). According to the IUGS classification system for

Plate 5.1. Photograph showing the typical nature of the augite syenite. The dominant mineralogy of this rock is comprised of augite and potassium feldspar. The white scale bar is 2 cm.

Plate 5.2. Photomicrograph of an actinolite pseudomorph (after augite) in the augite syenite. Minor remnant augite (A) is still present within the pseudomorph. Plane polarized light.

Plate 5.3. Photomicrograph showing the alteration of primary magnetite (Mt) to titanite (Ti) along grain margins and fractures in the augite syenite. Reflected light.

Plate 5.4. Photograph of relatively unaltered feldspar porphyry displaying a unimodal size distribution of plagioclase phenocrysts. The white scale bar is 2 cm.

5.1

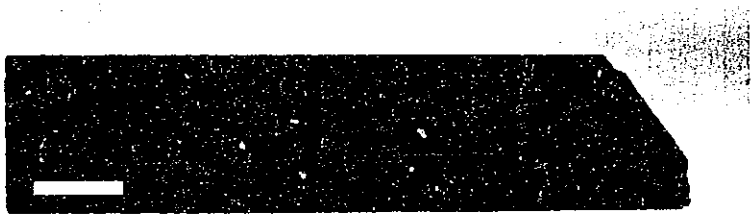

5.2

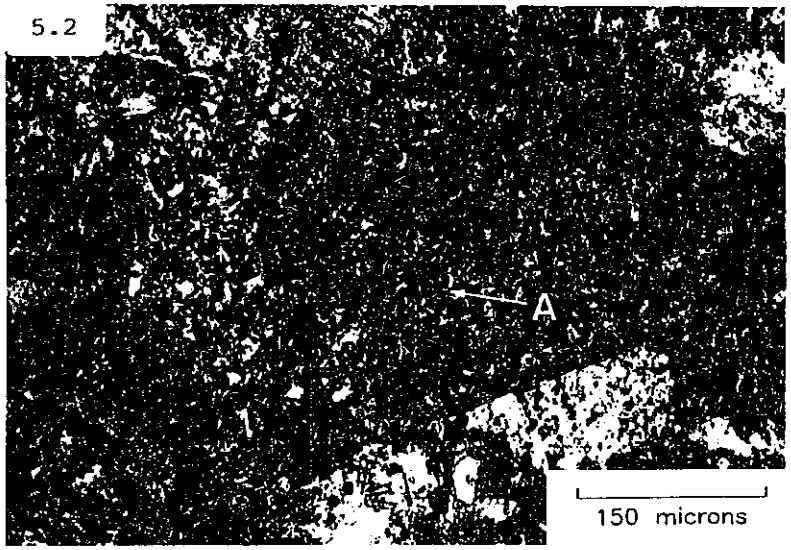

5.3

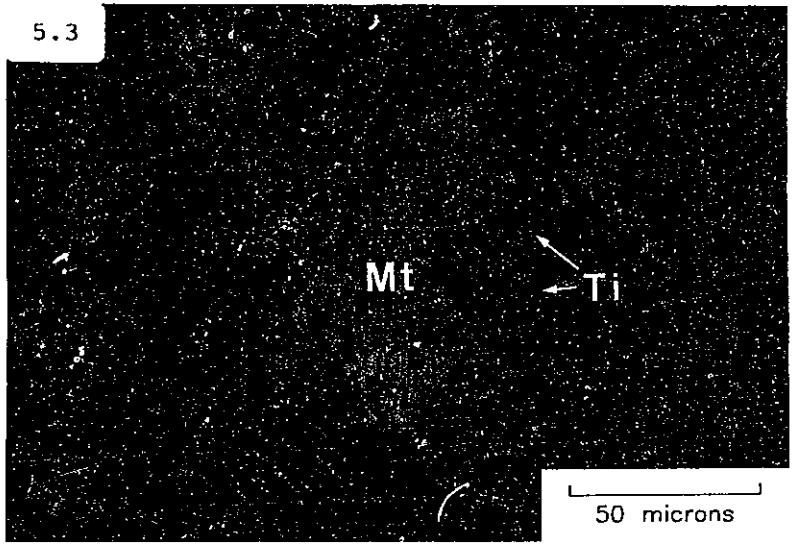

5.4

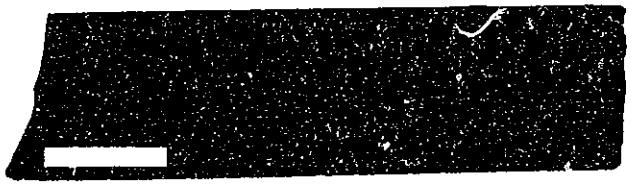

plutonic rocks (after Streckeisen, 1973), this rock would be classified as alkali-feldspar syenite.

Augite is generally euhedral, averages 3-5 mm in length, and commonly contains euhedral inclusions of apatite. It typically displays various degrees of alteration to pale green actinolite, chlorite, magnetite, and carbonate. Actinolite pseudomorphs (Plate 5.2) are common in the more altered rocks.

K-feldspar is generally orthoclase. Perthitic to microperthitic intergrowths with albite are rarely observed in the larger grains. Sericite and carbonate alteration of the K-feldspar is ubiquitous, while albite alteration is more rarely observed. Inclusions of fine grained actinolite are common in the K-feldspar, particularly adjacent to actinolite pseudomorphs.

Deep reddish-brown biotite occurs as fine elongate grains up to 1 mm in length within the K-feldspar. Primary hornblende is relatively rare. It is generally pseudomorphed by chlorite and easily identified where the characteristic basal diamond shape is preserved.

Magnetite displays variable degrees of hematite and titanite alteration along grain edges and fractures (Plate 5.3), indicative of subsolidus oxidation (Carmichael and Nicholls, 1967). Although relatively minor in the unaltered augite syenite, magnetite accounts for as much as 10% by volume in the altered rock due to its formation as a by-product during the breakdown of augite.

5.1.2 Syenite

Syenite is the least abundant of the three main intrusive phases at Lake Shore as well as throughout the Kirkland Lake camp (Figs. 3.2, 3.3). In hand specimen, the unaltered rock is medium grey. With increasing alteration, this rock takes on an orange or pinkish red colour. It is typically medium grained with an hypidiomorphic granular texture. Overall, it shows mineralogical and textural similarities to the augite syenite, the major differences being grain size and the amount of ferromagnesian minerals, particularly augite, present.

The primary mineralogy of this rock consists mainly of orthoclase with lesser intergrown plagioclase (perthite?), and augite. Accessory minerals include biotite, magnetite and apatite. Secondary minerals include chlorite, carbonate, leucoxene, and sericite. Like the augite syenite, this rock type is also classified as an alkali-feldspar syenite (IUGS classification).

Syenite is generally finer grained than the augite syenite. Feldspar grains range in size up to a maximum of about 2 mm. Sericite alteration of the feldspars is ubiquitous throughout the syenite.

Biotite is common in the least altered rocks, displaying pleochroism from brown to dark green. More commonly it has been altered to chlorite or assemblages of chlorite, calcite, K-feldspar and magnetite.

5.1.3 Feldspar Porphyry

Feldspar porphyry is the most abundant of the intrusive phases at Lake Shore as well as throughout the Kirkland Lake camp. In hand specimen, relatively unaltered feldspar porphyry varies from dark grey to olive black. It has a distinct porphyritic texture with lighter coloured phenocrysts of plagioclase, orthoclase, and more rarely quartz, contrasting with the darker, aphanitic to fine grained groundmass (Plate 5.4).

Angular to subround xenoliths of mafic rock up to 5 cm in diameter are common in the porphyry. They are typically darker in colour than the porphyry and are generally composed of varying assemblages of hornblende, actinolite, chlorite, and carbonate.

On the basis of phenocryst mineralogy, the feldspar porphyry intrusions may be divided into 4 distinct phases. These are, in decreasing order of abundance; 1) plagioclase-biotite porphyry, 2) plagioclase-orthoclase ± biotite porphyry, 3) plagioclase-hornblende-biotite porphyry, and 4) plagioclase-quartz ± orthoclase-biotite-hornblende porphyry (previously identified as quartz feldspar porphyry). Well defined intrusive contacts as well as gradational contacts are observed between these phases. The distribution of these phases throughout the intrusive complex appears to be random although it has not been fully documented.

Plagioclase is the most dominant phenocryst among all

phases of the feldspar porphyry, often accounting for up to 60% of the rock by volume. Well developed albite twins (Plate 5.6) are common, with rarer Carlsbad and pericline twins. Grains vary in size up to 3 mm in length and are generally euhedral. They are commonly white to cream coloured and more rarely are pinkish. Zonal growth is common with compositional variations ranging from oligoclase ($Ab_{81.2}$ $An_{13.2}$ $Or_{5.6}$) to albite ($Ab_{98.9}$ $An_{0.6}$ $Or_{0.5}$) (Table A2.1).

Orthoclase phenocrysts in the orthoclase-bearing phases of the porphyry account for less than 10% by volume of the rock. These grains show a strong variation in size, ranging up to 15 mm, and are generally subhedral to euhedral. They are generally much larger than plagioclase, thus resulting in a bimodal size distribution of the feldspars (Plate 5.5), and are commonly pinkish. Microprobe analyses indicate compositions ranging from Or_{72} Ab_{27} $An_{<1}$ to Or_{89} Ab_{11} (Table A2.1). The high TiO_2 contents (up to 1.14 wt.%) are atypical of orthoclase and may possibly be due to small inclusions of titanite or rutile, although none were observed. Inclusions of plagioclase are common in the larger orthoclases. Mild sericite and carbonate alteration of the feldspar phenocrysts is ubiquitous.

Biotite is the most common ferromagnesian mineral in all phases of the porphyry. Primary biotite occurs predominantly as phenocrysts up to 2 mm in length, with an average of about 1 mm. Several generations of biotite are commonly observed, as

Plate 5.5. Photograph of relatively unaltered feldspar porphyry displaying a bimodal size distribution of smaller plagioclase (Pl) and larger orthoclase (Or) phenocrysts in the orthoclase phenocryst-bearing varieties. The white scale bar is 2 cm.

Plate 5.6. Photomicrograph showing several partially resorbed, oval quartz phenocrysts (Q) and albite twinned plagioclase (Pl) typical of the quartz phenocryst- bearing varieties of the feldspar porphyry. Crossed nicols.

Plate 5.7. Photomicrograph of a euhedral titanite (Ti) grain inside a plagioclase (Pl) phenocryst substantiating a primary origin for the titanite and a highly oxidized nature for the intrusion. Crossed nicols.

Plate 5.8. Photomicrograph of a typical miarolitic cavity in the feldspar porphyry. The cavities display a zoned nature with hydrothermal biotite (Bh) lining the walls, followed by magnetite/hematite (Mt). The interiors are filled with quartz (Q), biotite (Bh), apatite (Ap), and sulphate (S). Plane polarized light.

5.5

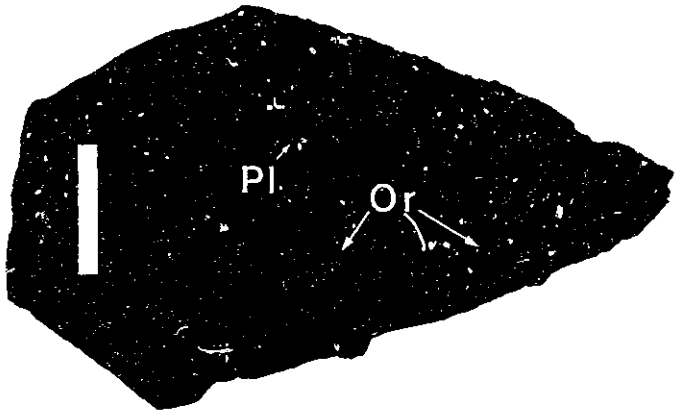

5.6

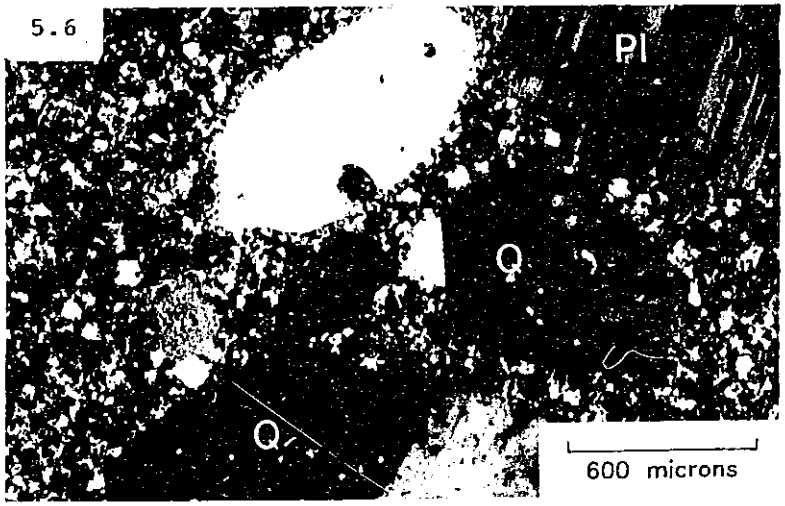

5.7

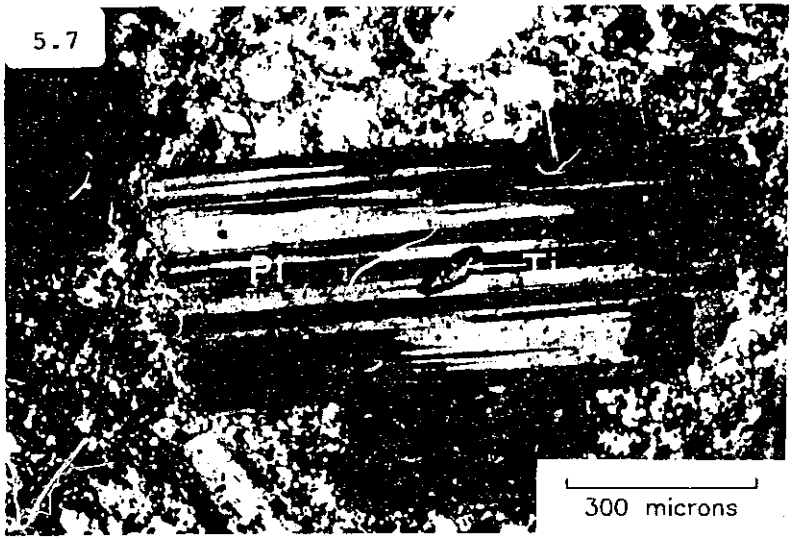

5.8

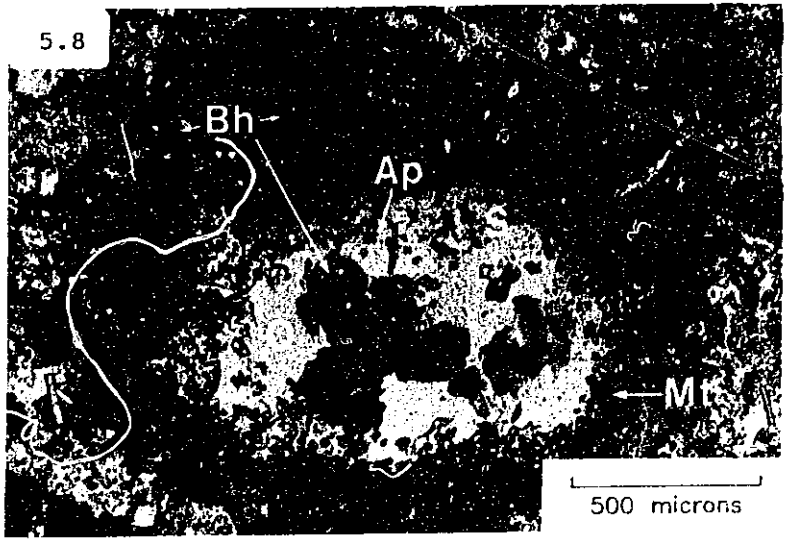

indicated by overgrowth and replacement textures (see sections 6.1, 6.2). Primary magmatic biotite is pleochroic from deep reddish brown to dark greenish brown. As with biotite in the augite syenite, the dark colours reflect the high Fe and Ti contents of the biotites (Table A2.2). Chloritization of grain margins is rare in the least altered samples. Rare inclusions of biotite in plagioclase substantiate their primary magmatic origin.

Quartz phenocryst-bearing phases of the porphyry are relatively rare at Lake Shore. Within these phases, the phenocrysts never exceed 5% by volume. When present, they occur as partially resorbed oval to round grains averaging about 1 mm in size (Plate 5.6). Quartz-feldspar porphyry samples examined from the Vindicator stock 0.6 km to the north show overall similar mineralogy and textures as the feldspar porphyry, the only difference being a slightly greater volume of quartz phenocrysts.

Green hornblende (edenite, after Hawthorne's classification, 1983) constitutes less than 7% by volume in the hornblende-bearing phases of the porphyry. Grains are generally small (< 1 mm) and display well developed euhedral shapes. Microprobe analyses of hornblende inclusions in plagioclase show higher SiO_2, Na_2O, and lower Al_2O_3 contents than common hornblende (Table A2.3).

Accessory minerals common to all phases of the porphyry include magnetite, apatite, rutile, titanite, monazite, and

zircon. Cameron and Carrigan (1987), utilizing electron backscattered images, have shown that Ti is present as a small scale, discrete phase within the magnetite rather than as a solid solution impurity.

Titanite generally forms euhedral crystals within the groundmass, and more rarely occurs as inclusions in plagioclase (Plate 5.7). Partial coronas of secondary titanite on magnetite are not as common as in the augite syenite.

Apatite, zircon, and monazite occur as minute grains in the groundmass. The groundmass is comprised primarily of plagioclase with variable amounts of orthoclase and quartz. Mild sericite and carbonate alteration of the groundmass is ubiquitous in all phases of the porphyry.

Miarolitic cavities are locally observed in the porphyry (Plate 5.8). These cavities vary from 1 to 4 mm in diameter, average about 1.5 mm, and are evidence of the release of a fluid phase from the cooling magma (Jahns and Burnham, 1969) which has resulted in subsequent magmatic-hydrothermal alteration. These cavities are generally confined to the biotite-bearing phases of the porphyry that do not contain hornblende. They are most often zoned: light to medium green biotite lines the cavity walls, followed by a layer of magnetite/hematite. The cores are filled with varying assemblages of quartz, biotite, orthoclase, apatite, and sulphates (Plate 5.8).

5.1.4 Diabase

In hand specimen, the diabase is dark greenish black in colour. It has a typical diabasic texture. Dykes have fine grained chill margins and coarser grained central portions.

The bulk of the mineralogy of the diabase is made up of subhedral to euhedral, lath-shaped plagioclase (55-65% by volume) and interstitial augite (35-45% by volume). Grain sizes attain a maximum of about 4 mm in the central portion of the dykes.

Primary quartz is rare, never exceeding 1% by volume. It is more commonly found in myrmekitic intergrowths with plagioclase (up to 2% by volume). Accessory minerals include apatite and magnetite.

In areas proximal to the Main Break, plagioclase in diabase is completely replaced by sericite, carbonate, epidote, and minor amounts of chlorite, while augite shows only mild alteration to actinolite, chlorite, and carbonate. Diabase dykes crosscut the ore veins, suggesting that the observed alteration is a result of fluids associated with post-ore movements along the Main Break, rather than with auriferous hydrothermal activity.

5.2 Geochemistry

Major oxide, selected trace element, and corresponding CIPW norm calculations for the least altered augite syenite, syenite (from Thomson, 1950, average of 2 analyses), feldspar

porphyry, and diabase are included in Table A1.2.

The whole rock analyses of augite syenite and syenite are atypical of syenites. Augite syenite contains lower SiO_2 and Al_2O_3 and higher Fe_2O_3, FeO, MgO, CaO, K_2O, and P_2O_5 abundances while the syenite is lower in SiO_2, Fe_2O_3, FeO, MgO, CaO, and K_2O and higher in Al_2O_3, K_2O, and TiO_2 than typical syenites (comparison with average composition of syenites from McBirney, 1984, Table 2-2, p 34). These differences are predominantly reflected in the amount of ferromagnesian minerals present in the augite syenite and the large amounts of K-feldspar in the syenite.

The three main phases of the Kirkland Lake intrusive complex constitute distinct populations in terms of their major element geochemistry (Table A1.2). Augite syenite and syenite plot well within the alkaline field on an alkali-silica diagram (Fig. 5.1). In contrast, the feldspar porphyry lies close to the alkaline-subalkaline dividing line, with 5 of the 11 samples lying within the alkaline field.

Similar distinctions can also be observed when the samples are plotted on a Harker diagram with SiO_2 on the x-axis (Fig. 5.2). Minor deviations from typical fractionation trends for Al_2O_3, Fe_2O_3, MgO, and CaO suggest that the feldspar porphyry may not be comagmatic with the augite syenite and syenite phases. This is further suggested by the marked differences in the trends of the average slopes between augite syenite and syenite and the porphyry for all oxides

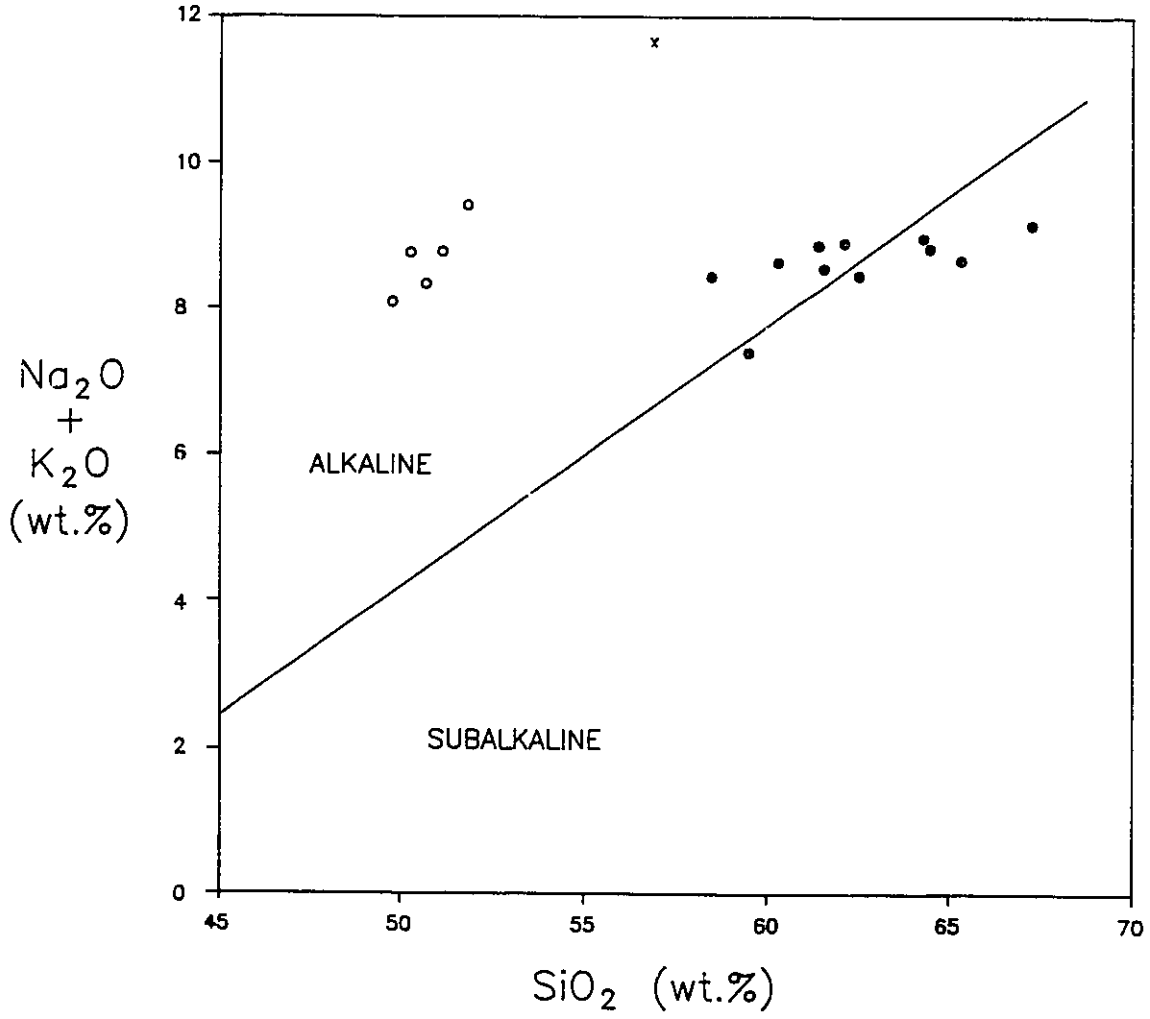

Fig. 5.1. Alkali-silica diagram for the main phases of the Kirkland Lake intrusive complex from the Lake Shore mine and area. Open circles = augite syenite; crosses = syenite (from Thomson, 1950); filled circles = feldspar porphyry. Data from Table A1.2 (Appendix I). Subalkaline-alkaline dividing line after Irvine and Baragar, 1971.

Fig. 5.2. Harker diagram for the main phases of the Kirkland Lake intrusive complex from the Lake Shore mine and area. Open circles = augite syenite; crosses = syenite; closed circles = feldspar porphyry. Data from Table A1.2 (Appendix I). Syenite value represents an average of two analyses from Thomson, 1950. Trend lines determined by best visual fit.

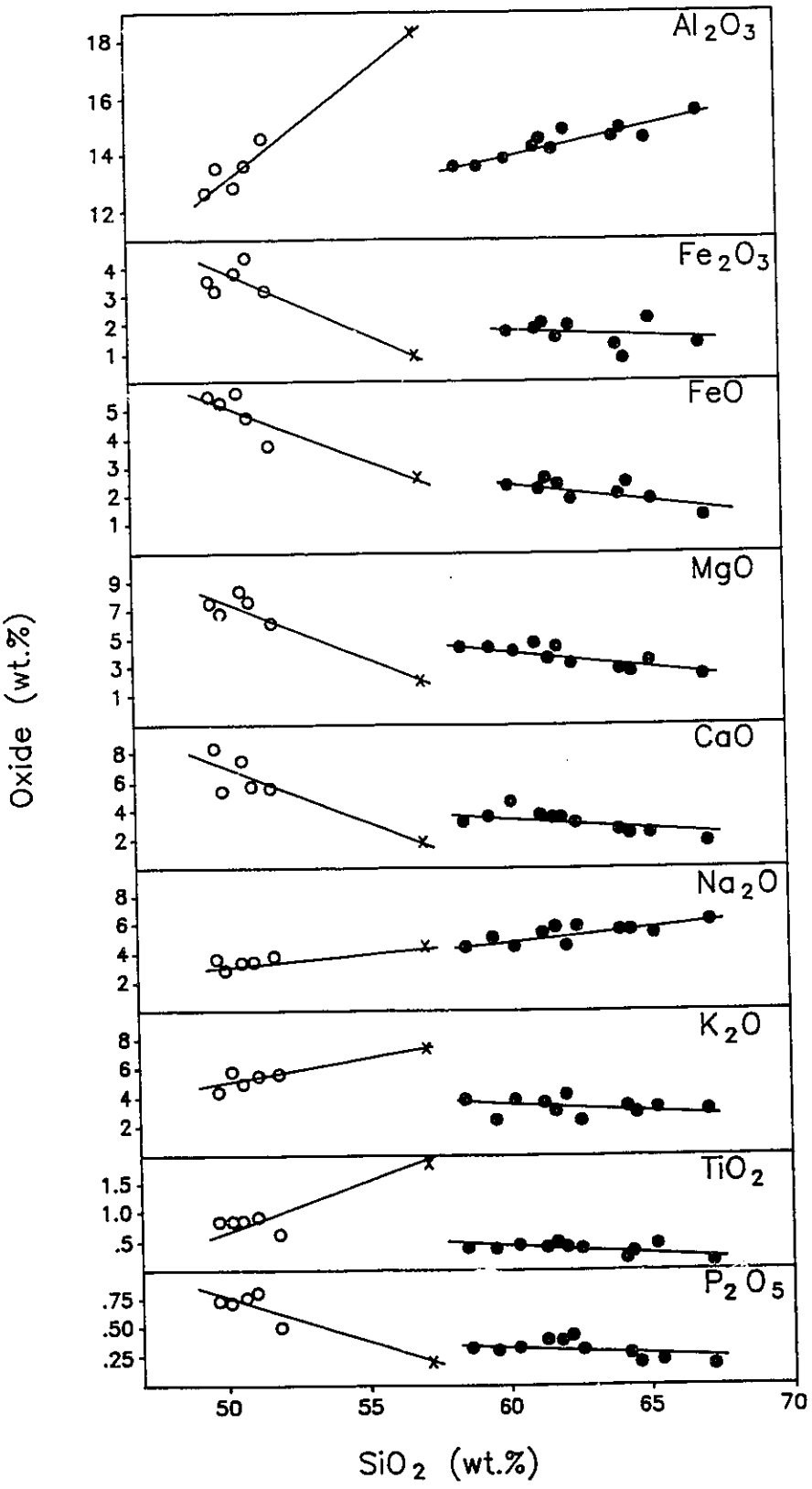
Al2O3
Fe2O3
FeO
MgO
CaO
Na2O
K2O
TiO2
P2O5
Oxide (wt.%)
SiO2 (wt.%)
50
55
60
65
70

except Na_2O (Fig. 5.2). It is also supported by the subsolvus nature of the feldspar porphyry and contrasting hypersolvus nature of the augite syenite and syenite. Similar observations by Cooke and Moorhouse (1969) led them to conclude that the porphyritic rocks in the Kirkland Lake area were compositionally distinct from the syenites. However, on the basis of similar REE trends, Watson (1984) described the three units as being comagmatic.

Although only one analysis of syenite is included (from Thomson, 1950), the mineralogical similarity and local gradational contacts between the augite syenite and syenite suggest them to be comagmatic. Linear variations for the major oxide contents within the feldspar porphyry itself suggest a common magma source for the different phases of the porphyry.

The CIPW norms for the augite syenite and syenite (Table A1.2) show normative Ne and Ol, which strongly contrasts with the observed mineralogy. These variations are likely due to the excessive amounts of K-feldspar in both rock types and the large amount of augite in the augite syenite. The occurrence of Ne and Ol in the norm is indicative of silica undersaturation while the presence of Ne confirms an alkaline affinity.

CIPW normative calculations for the porphyry show normative Q, indicative of silica saturation. While the contrasting degrees of silica saturation displayed by the augite syenite and syenite, and the porphyry agree with a non-

comagmatic origin, the occurrence of both Ne and Q normative rocks is common in anorogenic syenitic complexes (e.g. Size, 1972). Furthermore, where associated with more silicic rocks, alkaline intrusions commonly occur as small stocks and dykes. This is similar to the relationships displayed by the three main intrusive units in the Kirkland Lake complex.

CIPW normative values for Or, Q, An, and Ab from the least altered feldspar porphyry samples were recalculated to modal percent and plotted on a Streckeisen diagram (Fig. 5.3) (after Streckeisen, 1973). Normative values for An and Ab were combined to form normative plagioclase. Samples for the porphyry plot within the quartz-monzodiorite field and along the quartz-monzonite - quartz-monzodiorite dividing line.

The Streckeisen plot for the feldspar porphyry agrees very well with the observed mineralogy. Combining normative values for Ab and An to give normative plagioclase results in compositions varying from Ab85.1 An14.9 to Ab91.1 An8.9, which fall within the compositional range determined by microprobe analyses (section 5.1.3, Table A2.1). These similarities in composition, as well as the large amount of modal plagioclase phenocrysts and relatively minor amounts of primary K-feldspar, further substantiate the results of the Streckeisen plot.

Feldspar porphyry samples plotted on a normative Ab-An-Or diagram lie within the trondhjemite and granite fields (Fig. 5.4). Samples of the augite syenite and syenite plot within

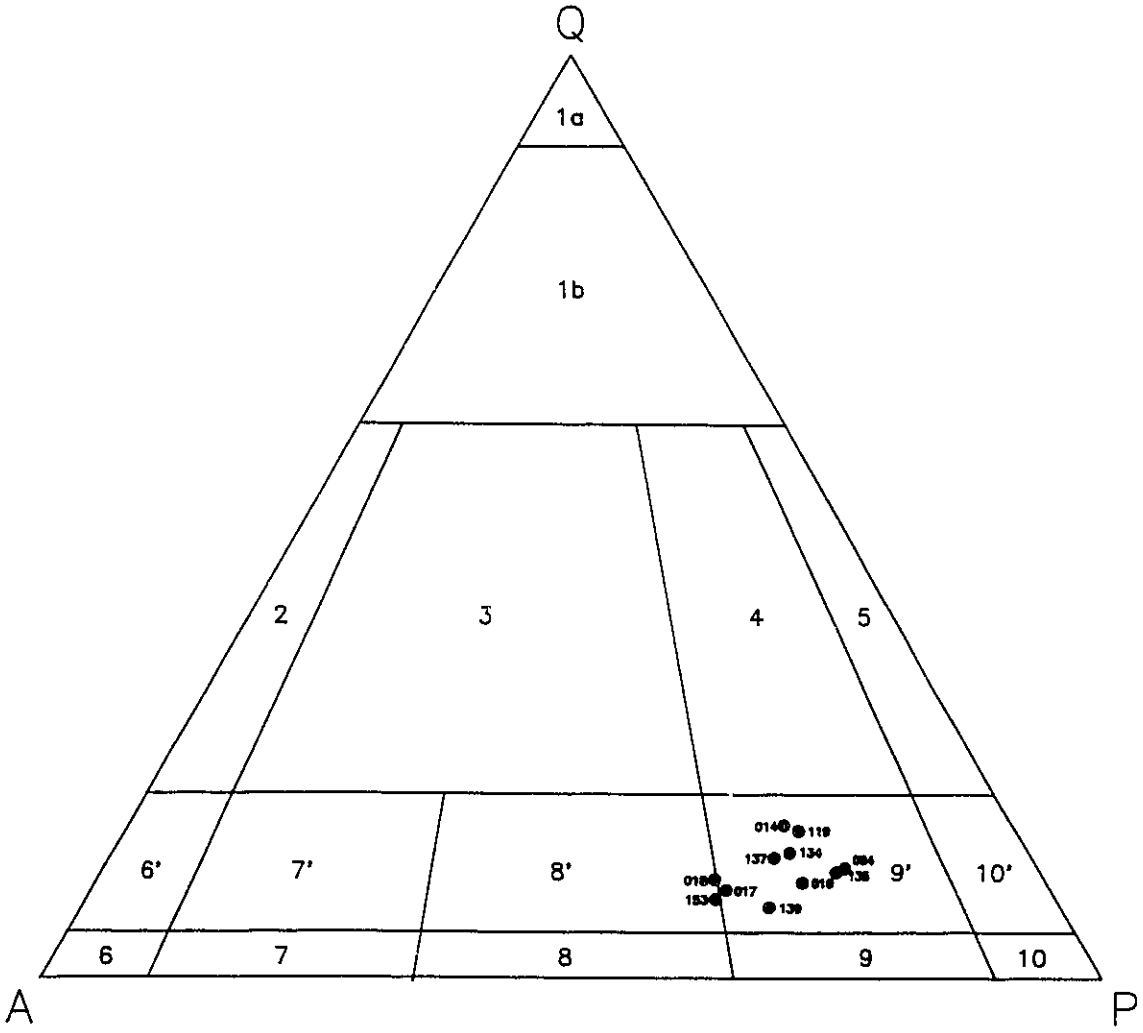

Fig. 5.3. Quartz (Q) - alkali feldspar (A) - plagioclase (P) diagram (CIPW normative values converted to percent by volume) for the feldspar porphyry unit. Plagioclase component was formed by combining normative albite (Ab) and anorthite (Ar) because plagioclase in the rocks has compositions of albite (>An 5) and oligoclase compositions for plagioclase (See Table A2.1 in Appendix II). The classification of igneous plutonic rocks according to Streckeisen (1973) is indicated as follows: 1a = quartzolite; 1b = quartz-rich granitoids; 2 = alkali-feldspar granite; 3 = granite; 4 = granodiorite; 5 = tonalite; 6' = alakli-feldspar quartz syenite; 7' = quartz syenite; 8' quartz monzonite; 9' quartz monzodiorite; 10' = quartz diorite; 6 = alkali-feldspar syenite; 7 = syenite; 8 = monzonite; 9 = monzodiorite; 10 = diorite/gabbro. Note that most samples lie within the quartz-monzodiorite field. Data from Table A2.1 (Appendix II).

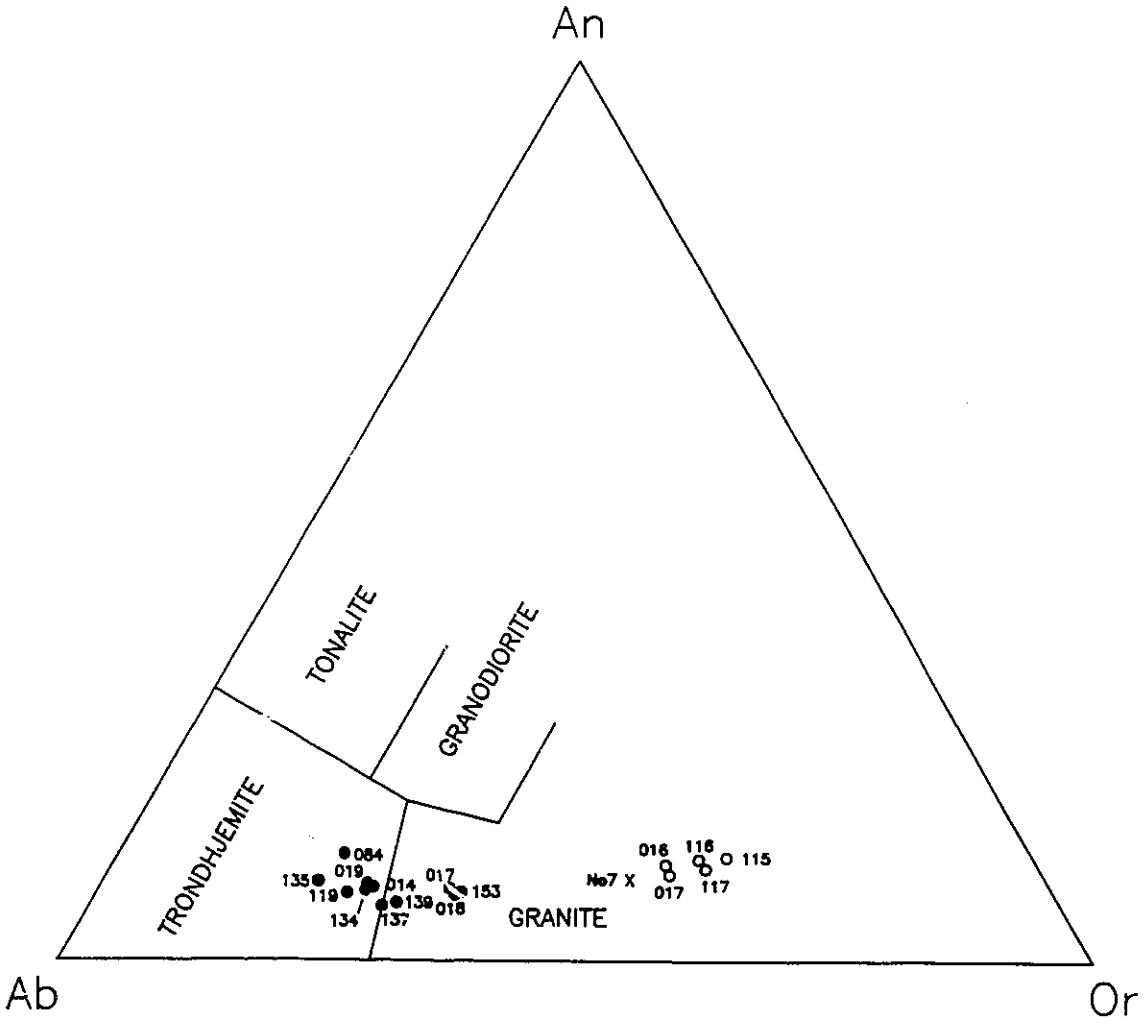

Fig. 5.4. Normative Ab-An-Or diagram for the main phases of the Kirkland Lake intrusive complex from the Lake Shore mine and surrounding area. Open circles = augite syenite; crosses = syenite, filled circles = feldspar porphyry. Data from Table A2.1 (Appendix II). After Barker, 1979; modified after O'Connor, 1965.

the granite field (Fig. 5.4).

Whole rock analyses for the diabase are typical of a magnesium tholeiite. High values for K_2O (1.21 - 3.55 wt.%) reflect moderate to pervasive sericitization of plagioclase. Elevated levels of Ba and Sr also reflect the higher amounts of K_2O. CIPW norm calculations are indicative of an olivine tholeiite (Table A1.2).

Chapter 6

Hydrothermal Alteration

Hydrothermal alteration studies completed on the feldspar porphyry from the upper levels (above 1200 level) of the eastern portion of the mine reveal four distinct alteration, facies based on alteration mineralogy. These facies include, from the least to most altered; 1)hydrothermal (secondary) biotite facies, 2) chlorite facies, 3) phlogopite-hematite facies, and 4) fuchsite-sericite-pyrite facies. No apparent relationship exists between the various phases of the feldspar porphyry and the alteration facies.

The spatial distribution of the latter two facies as concentric zones relative to the auriferous veins (Fig. 6.1) suggests that they are the result of hydrothermal alteration associated with main stage veining. The broad distribution and mineralogical assemblage of the hydrothermal biotite facies suggest that it is not associated with the above alteration, but rather with hydrothermal fluids related to the intrusive activity. This is further suggested by the occurrence of

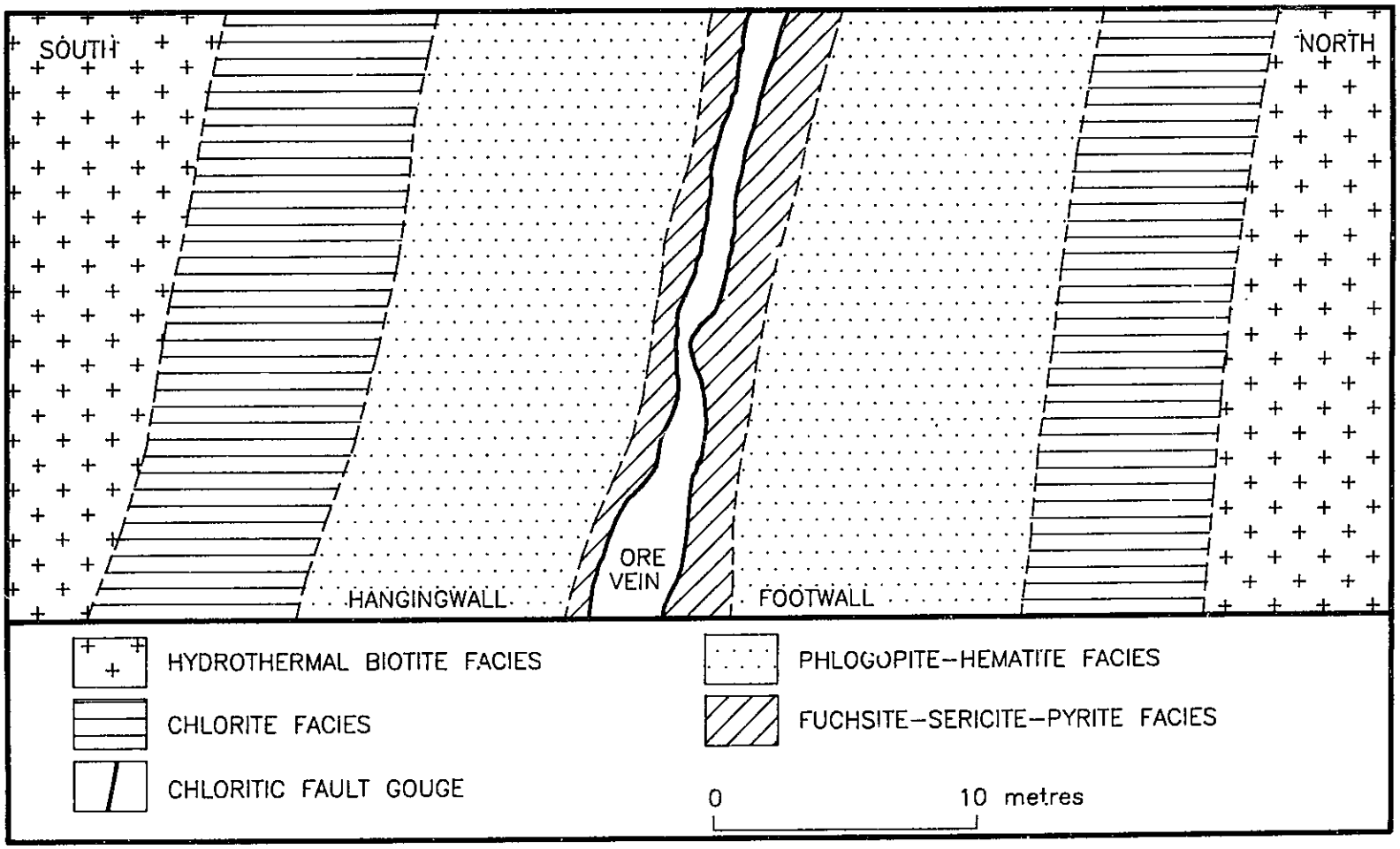

Fig. 6.1. Diagrammatic sketch showing the spatial distribution of the four hydrothermal alteration facies for the feldspar porphyry about the ore veins in the upper levels of the eastern portion of the Lake Shore Mine. Actual widths of the alteration zones and ore veins may vary.

miarolitic cavities which contain biotite with optical and chemical properties similar to those of the secondary biotite within the rock.

The chlorite facies is always found between the phlogopite-hematite facies and either the hydrothermal biotite facies or relatively unaltered porphyry (Fig. 6.1). Its position in the alteration sequence suggests that it likely represents the zone of alteration most distant from the main stage veins, rather than alteration associated with igneous hydrothermal activity.

The locations of critical samples used in the hydrothermal alteration study are given in Appendix iv.

6.1 Magmatic-Hydrothermal Alteration

6.1.1 Hydrothermal Biotite Facies

The hydrothermal or secondary biotite facies constitutes most of the least altered feldspar porphyry at Lake Shore. The rocks of this facies are generally found at distances greater than 20 m from the auriferous veins. While their distribution has not been fully documented in this study, almost all of the porphyry samples collected at Lake Shore and the local vicinity that are not affected by visible alteration associated with Au mineralization display this type of cryptic alteration. In hand specimen, the rocks of this facies are indistinguishable from the relatively unaltered feldspar porphyry.

This facies is characterized by the replacement and/or overgrowth of magmatic biotite and hornblende by hydrothermal biotite, as well as by the development of phenocrystic and fine grained, sucrosic biotite (after Jambor, 1976) in the groundmass.

Hydrothermal biotite may be differentiated from magmatic biotite by its lighter colours and its replacement and overgrowth textures. Overgrowths of hydrothermal biotite on magmatic biotite are revealed in cores of deep reddish brown biotite (magmatic) surrounded by successive rims of light to medium green biotite (hydrothermal) (Plate 6.1). Grain edges have a flaky appearance, typical of hydrothermal biotite (e.g. Jambor, 1976; Jacobs and Parry, 1976)(Plate 6.1).

Where magmatic biotite is replaced by hydrothermal biotite, star-shaped asters comprised of acicular rutile (sagenite texture) are developed in the biotite (Plate 6.2). These asters are similar to those found in the partially chloritized magmatic biotite (see chapter 5.3). However, greater quantities of rutile are typically developed in the hydrothermally replaced magmatic biotite. Large, rutile-free phenocrysts of hydrothermal biotite suggest direct precipitation from fluid rather than replacement of magmatic biotite.

The replacement of hornblende by hydrothermal biotite is marked by the presence of biotite pseudomorphs after hornblende (Plate 6.3). Hornblende is typically replaced by

Plate 6.1. Photomicrograph of hydrothermal biotite (Bh) overgrowing primary magmatic biotite (Bm) in the hydrothermal biotite facies. Plane polarized light.

Plate 6.2. Photomicrograph of microphenocrysts of hydrothermal biotite in the hydrothermal biotite facies. The abundant magnetite (Mt) and rutile (Ru) asters (sagenite texture) within the biotite suggests these phenocrysts may have criginally been magmatic biotites which were replaced by hydrothermal biotite. Tnis theory is based upon the low Fe and Ti contents of the hydrothermal biotite compared to magmatic biotite. Plane polarized light.

Plate 6.3. Photomicrograph of a biotite pseudomorph (after hornblende) as suggested by the characteristic basal diamond shape of amphiboles. Note that the replacement occurs by felted aggregates of biotite rather than by an individual grain. Plane polarized light.

Plate 6.4. Photomicrograph of late hydrothermal biotite (Bh2) overgrowing earlier hydrothermal biotite (Bh1) in the hydrothermal biotite facies. Note the trails of fluid inclusions (FI) separating the two generations of hydrothermal biotite. Also note the presence of small inclusions of sulphate (S). Plane polarized light.

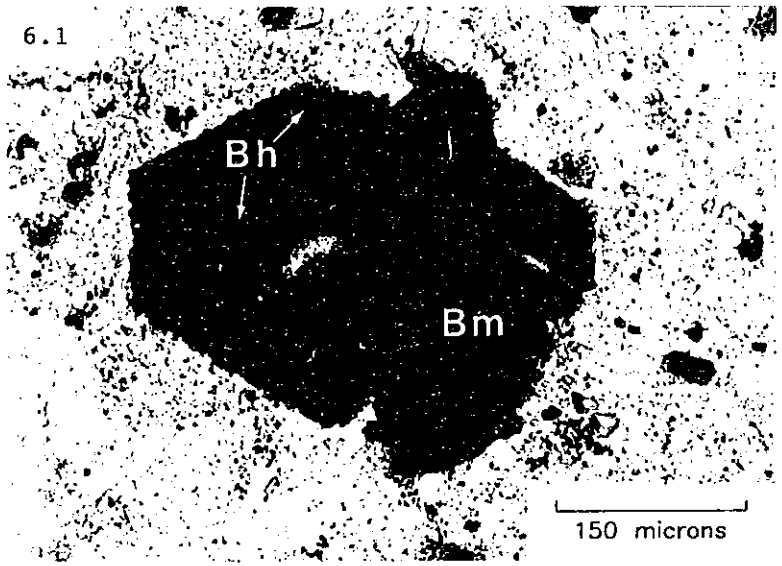
6.1
Bh
Bm
150 microns

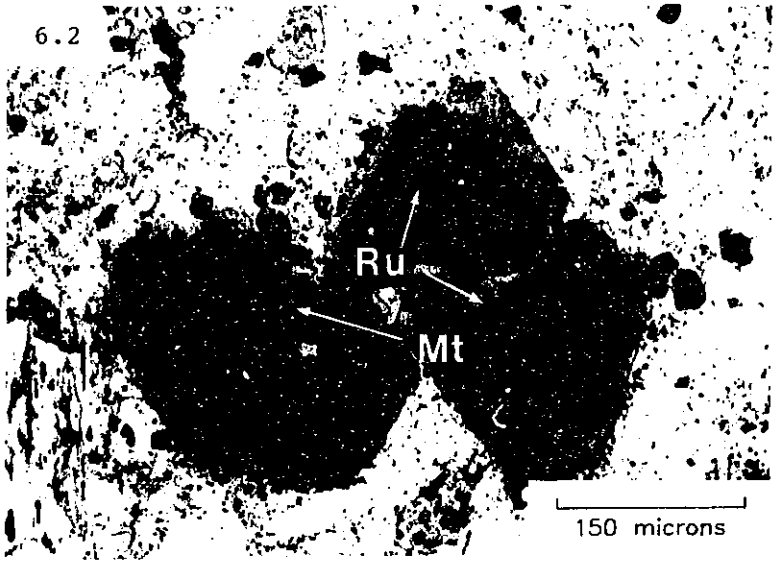
6.2
Ru
Mt
150 microns

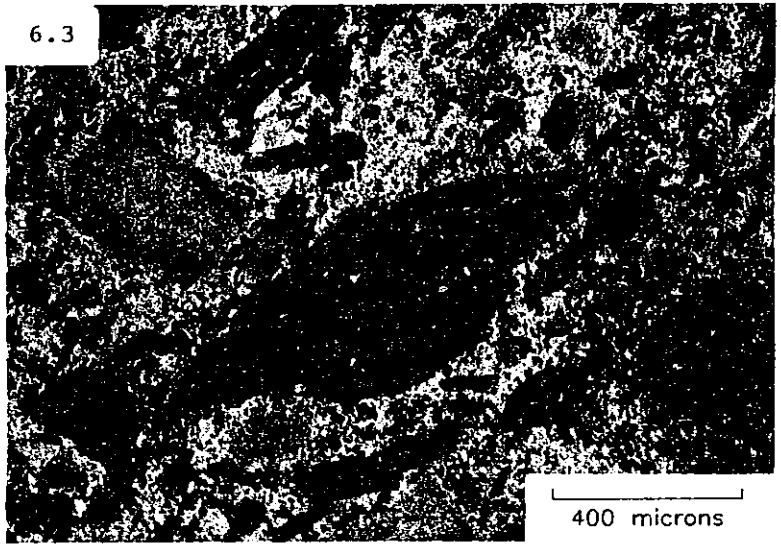
6.3
400 microns

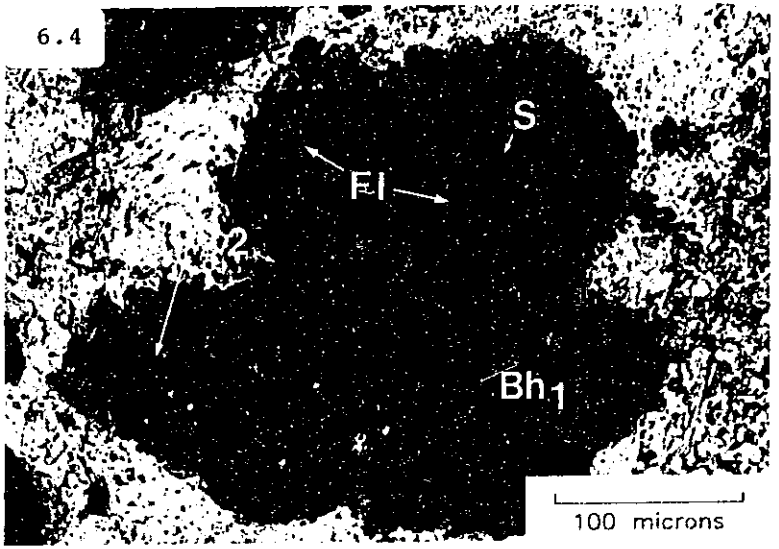
6.4
S
Fl
Bh1
100 microns

aggregates of fine grained biotite rather than by individual grains. The pseudomorphs are best identified where the characteristic basal diamond shape of the amphibole has been preserved.

Two generations of hydrothermal biotite can be distinguished by their different colours and overgrowth textures (Plate 6.4). Earlier formed hydrothermal biotite displays concentric pleochroic colours ranging from colourless through pale green to medium green, moving from the interior to the exterior of the grains (Plate 6.4). Distinct colour changes are common at overgrowth boundaries. Later hydrothermal biotite is pleochroic from medium green to greenish brown. The earlier formed, lighter coloured (colourless to pale green), hydrothermal biotites occasionally display a mottled or patchy colouring. This may be indicative of inhomogeneity within individual biotite grains, or it may be the result of welding of biotite aggregates. As the early hydrothermal biotites become greener, the colour becomes more homogeneous suggesting, a more homogeneous fluid source. Later formed hydrothermal biotite generally displays a homogeneous colouring suggesting a more homogeneous composition. Where distinct overgrowths of later hydrothermal biotite on earlier hydrothermal occur, the two generations of biotite are often separated from each other by a plane of fluid inclusions (Plate 6.4).

Plagioclase grains in this facies display variable

alteration, on the rims of individual grains, to albite and orthoclase. This alteration forms a fine grained mosaic (Plate 6.5) which is easily observed upon staining with sodium cobaltinitrate solution. These secondary rims are generally sericite free, or contain very little sericite compared to the grain interiors, suggesting growth after sericitization. Electron microprobe analyses indicate near end member compositions, suggesting a hydrothermal origin (Table A2.1, sample 153-1c).

Fine grains of sulphate are commonly developed in this facies. They are typically small (<10 μm) and occur disseminated in the groundmass, as inclusions in the secondary biotite, or as inclusions in the altered plagioclase rims (Plate 6.5). Microprobe analyses (Table A2.4) indicate bulk compositions of the sulphate barian-celestine. Since there is an immiscibility gap in the series barite-celestine at low temperatures (Malinin and Urusov, 1983), this bulk composition indicates that these sulphates were formed at relatively high temperatures.

Electron back scattered images suggest that small scale inhomogeneities are present within the individual grains. This may be the result of the low temperature exsolution of the barite component at a μm scale. Apatite (hydrothermal?) inclusions within the sulphate generally show elevated SO_4^{2-} abundances compared to magmatic apatites (Table A2.4).

Magnetite within this facies displays weak hematite and

Plate 6.5. Photomicrograph of altered plagioclase rims in the hydrothermal biotite facies. The rims are composed of a fine grained mosaic of albite, orthoclase, and sulphate. Crossed nicols.

Plate 6.6. Photomicrograph showing the alteration of biotite (Bi) to chlorite (Ch) in the chlorite facies. Replacement occurs along grain boundaries and the (001) cleavage planes. Secondary magnetite (Mt) and rutile (Ru) are formed due to excess Fe and Ti. Plane polarized light.

Plate 6.7. Photomicrograph of a chlorite (Ch) pseudomorph (after hornblende) as suggested by the characteristic basal diamond shape of amphiboles. Note that abundant carbonate (Ca) is also formed as a by-product during the alteration. Crossed nicols.

Plate 6.8. Photomicrograph of a chlorite (Ch) phenocryst (after biotite?) showing the extensive development of magnetite (Mt) and rutile (Ru) (sagenite texture) along the (001) plane in the chlorite facies. Plane polarized light.

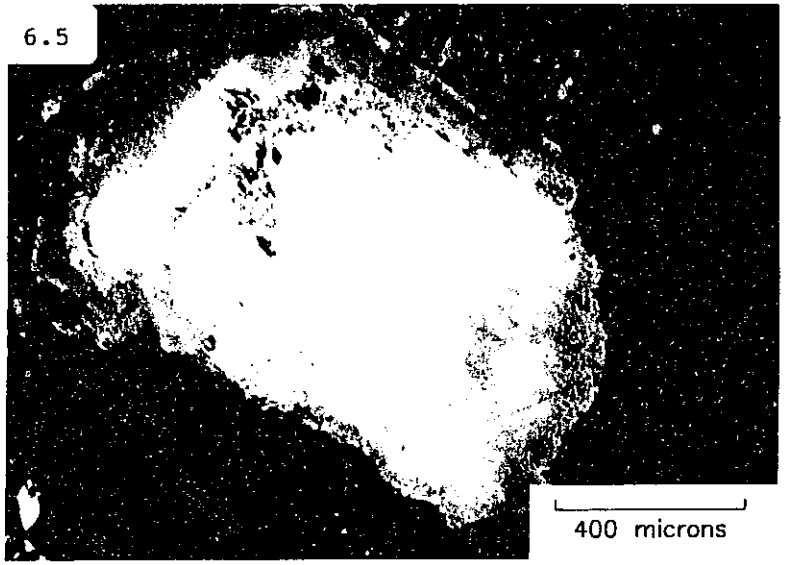
6.5
400 microns

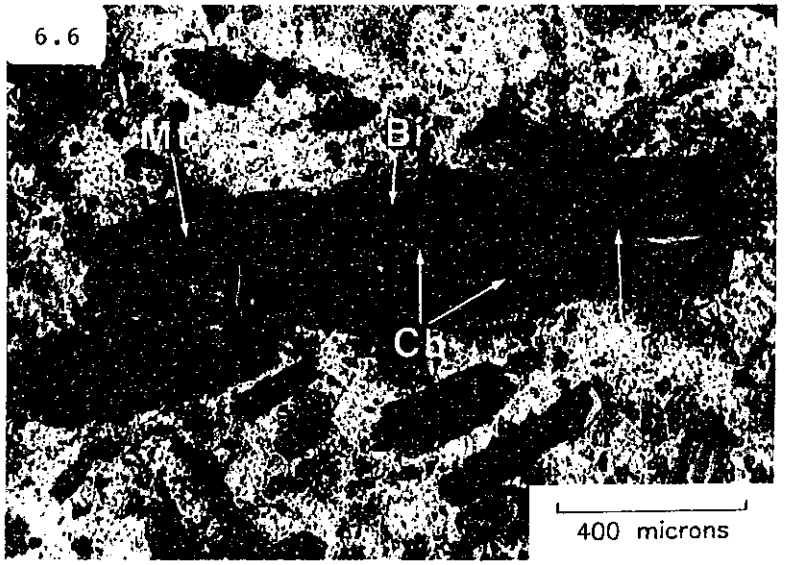
6.6
Mt
Bi
Ch
400 microns

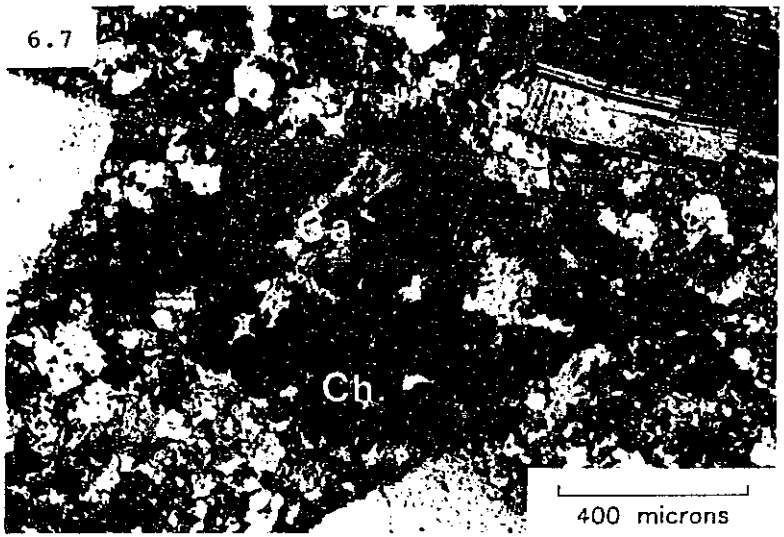
6.7
Ca
Ch
400 microns

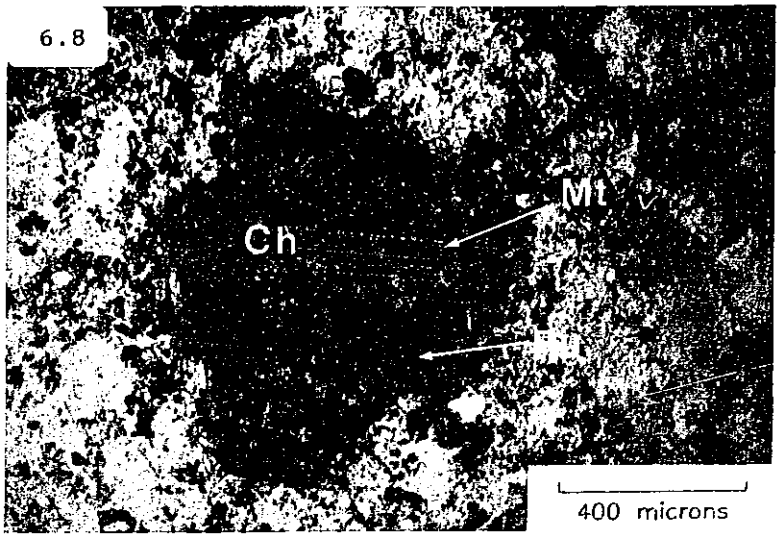
6.8
Ch
Mt
400 microns

titanite alteration. These replacements occur along grain margins and fractures and are evidence of late oxidation.

Mild sericite and carbonate alteration of plagioclase and the groundmass is ubiquitous throughout this facies.

6.1.2 Biotite Compositions

In addition to colour and textural differences, the magmatic and hydrothermal biotites may be differentiated on the basis of mineral chemistry (Table A2.2, Figs. 6.2, 6.3). Magmatic biotites are characterized by higher Fe/Mg ratios and TiO_2 contents. Annite contents range from 33-38 mole %, thus the biotites are true biotites.

The hydrothermal biotites are characterized by lower TiO_2 contents and lower Fe/Mg ratios (Figs. 6.2-6.4a). Annite contents range from 8-33 mole % and thus actually lie within the phlogopite compositional field (Fig. 6.3); however, they are referred to as biotites because of their green colours as well as to avoid confusion with later phlogopitic alteration associated with auriferous hydrothermal activity.

Similar characteristics in hydrothermal biotites have been observed by Jacobs and Parry (1976) for several quartz monzonite to granodiorite stocks in the Basin and Range province of the western United States. In addition, the hydrothermal biotites in this study also show elevated Cr_2O_3 contents, which are uncharacteristic of magmatic biotites (Fig. 6.4b). Furthermore, the total number of octahedrally

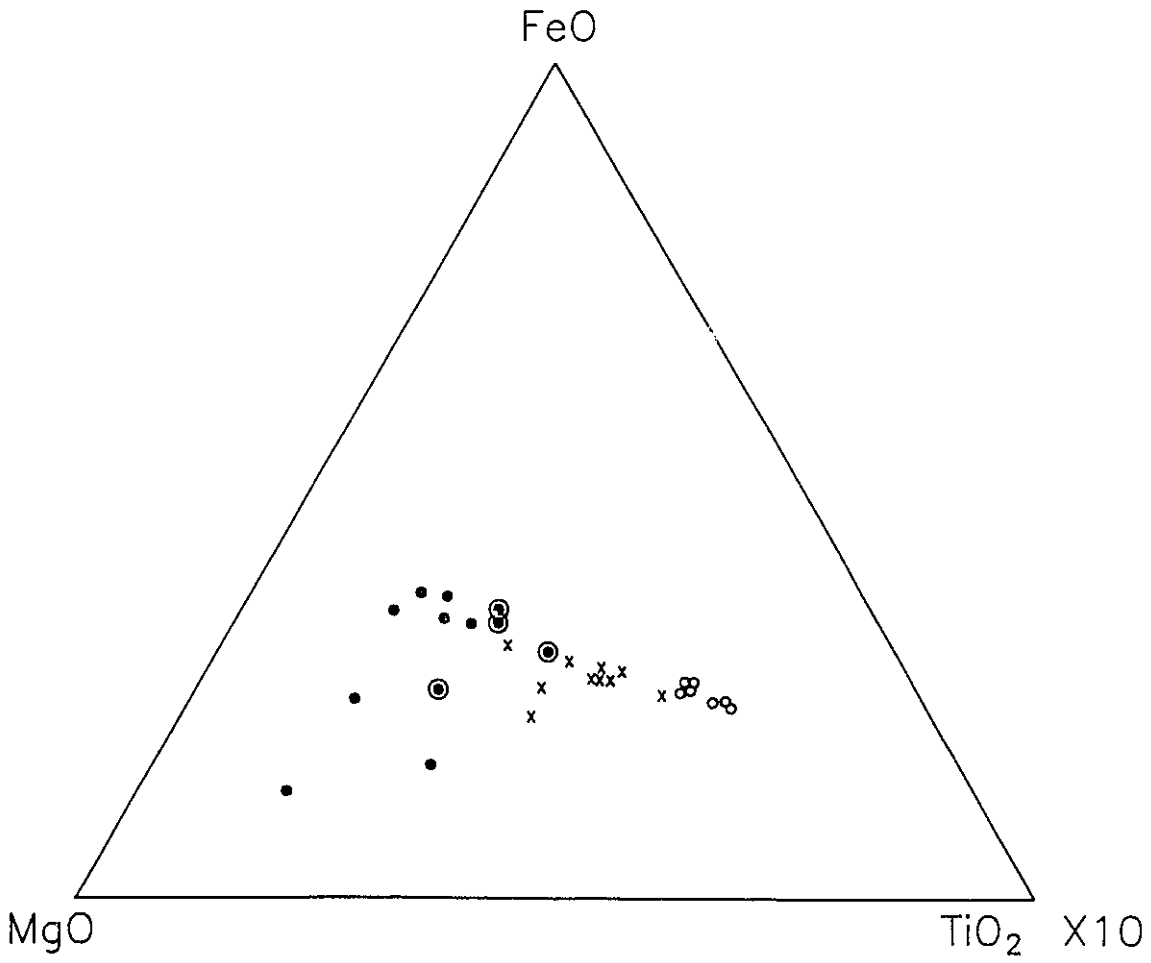

Fig. 6.2. FeO-MgO-TiO_2 (x10) ternary diagram (wt. %) displaying compositional variations for the multiple generations of biotite at Lake Shore. Open circles = magmatic biotite; filled circles = pale green early hydrothermal biotite; crosses = late hydrothermal biotite; ringed filled circles = medium green early hydrothermal biotites. Note the greater compositional ranges displayed by the hydrothermal biotites compared to the magmatic biotite. Total Fe expressed as FeO. Data from Table A2.2 (Appendix II).

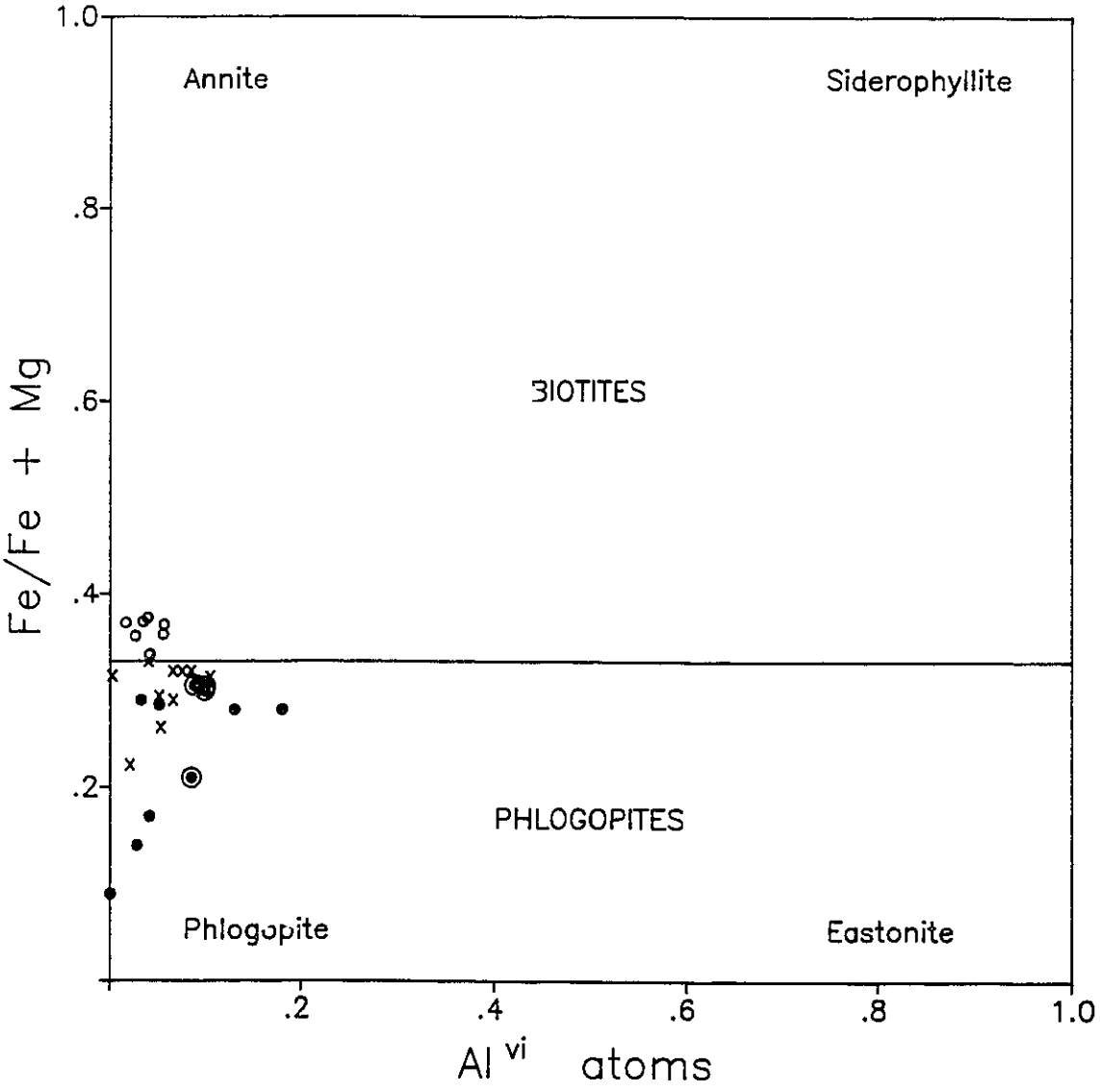

Fig. 6.3. Compositional fields for biotites, plotted in the annite-phlogopite-eastonite-siderophyllite quadrilateral (after Deer et al., 1963). Open circles = magmatic biotite; filled circles = pale green early hydrothermal biotite; crosses = late hydrothermal biotite; ringed filled circles = medium green early hydrothermal biotite.

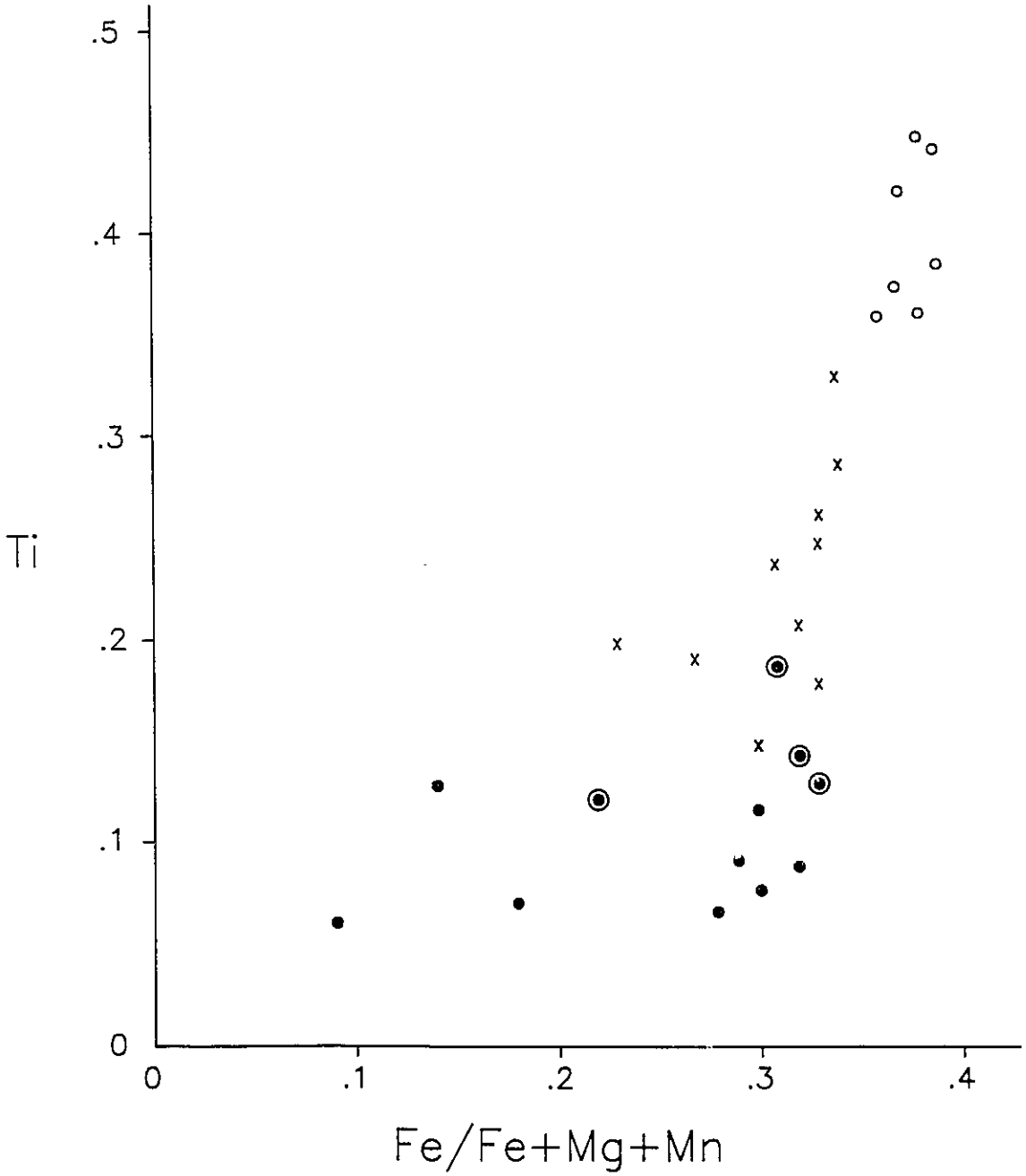

Fig. 6.4a. Plot of Ti versus Fe/Fe+Mg+Mn for the multiple generations of biotite from Lake Shore. Open circles = magmatic biotite; filled circles = pale green early hydrothermal biotite; ringed filled circles = medium green early hydrothermal biotite; crosses = late hydrothermal biotite. Values are number of cations based microprobe analyses calculated to 22 oxygens. Note the greater compositional ranges for hydrothermal biotites compared to magmatic biotite. Data from Table A2.2 (Appendix II).

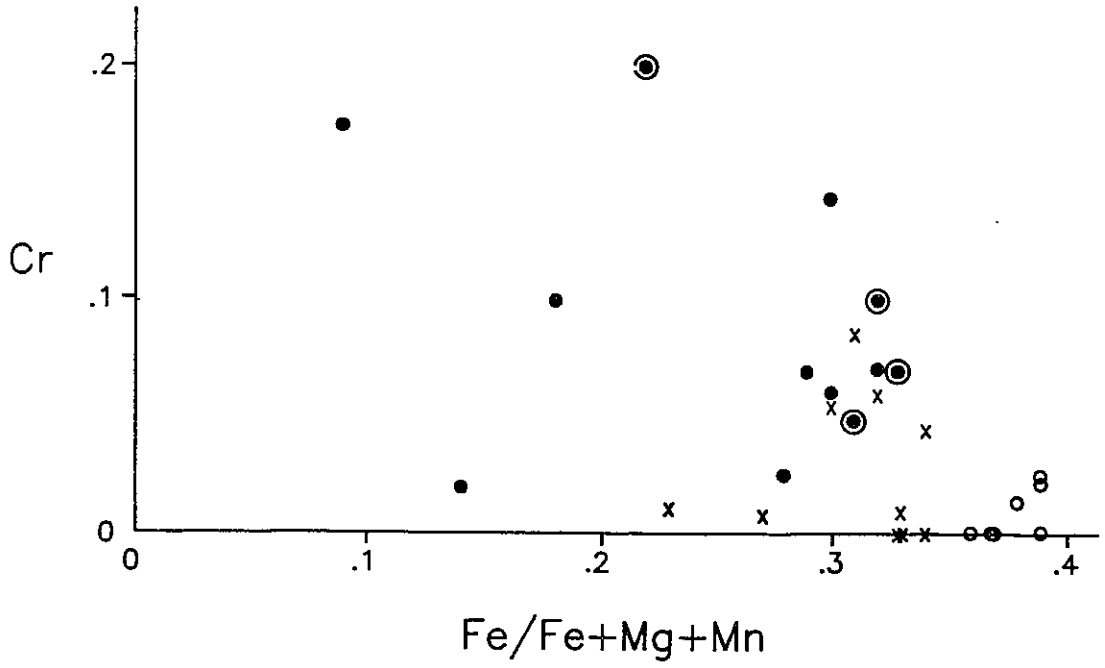

Fig. 6.4b. Plot of Cr versus Fe/Fe+Mg+Mn for the multiple generations of biotite from Lake Shore. Open circles = magmatic biotite; filled circles = pale green early hydrothermal biotite; ringed filled circles = medium green early hydrothermal biotite; crosses = late hydrothermal biotite. Values are number of cations based microprobe analyses calculated to 22 oxygens. Note the greater compositional ranges for hydrothermal biotites compared to magmatic biotite. Data from Table A2.2 (Appendix II).

coordinated cations in hydrothermal biotites is commonly greater than 6.000 (Σ6.016), compared to less than 6.000 (Σ5.865) for magmatic biotites. This suggests some of the Fe to be present as Fe^{3+} implies higher Fe^{3+}/Fe^{2+} ratios in the hydrothermal biotites.

The lower TiO_2 and higher Cr_2O_3 contents of the hydrothermal biotites help to further substantiate their origin. Furthermore, the hydrothermal biotites typically display a much wider range of compositions than do the magmatic biotites (Figs. 6.2-6.4a). It is very unlikely that biotites of such varied compositions could be formed from a melt. The high TiO_2 content of the feldspar porphyry suggests a magmatic origin for the high TiO_2 biotite.

Chemical variations are also observed among the hydrothermal biotites themselves. The earlier formed hydrothermal biotites display the lowest TiO_2 contents, lowest Fe/Mg ratios, highest Cr_2O_3 contents, and widest range of compositions (Figs. 6.2-6.4a). Chemically, the later generations of hydrothermal biotite lie between the magmatic and early hydrothermal biotites and display a more restricted compositional range than the early hydrothermal biotite (Figs. 6.2-6.4). The medium green coloured varieties of the early hydrothermal biotites have intermediate compositions between the colourless to pale green varieties of early hydrothermal biotite and later hydrothermal biotite (Figs. 6.2-6.4). The variation in Ti and Cr contents within the early hydrothermal

biotites suggests an initial high Cr content for the fluid, which gradually evolved into a Ti-rich fluid. The overlapping of Cr and Ti contents (Fig. 6.5) for the medium green coloured varieties of early hydrothermal biotite suggests fluid evolution was responsible for the variation.

The complex overgrowth nature of biotite, as well as minor chlorite contamination, make it impossible to obtain Fe^{3+} analyses for individual biotite types. Despite this, estimates of fO_2 may still be made on the basis of experimental work by Wones and Eugster (1965). The stability of biotite as a function of fO_2 and temperature at 2070 bars total pressure, as determined by Wones and Eugster (1965), is shown in figure 6.6. Biotites with compositions similar to the magmatic biotite from Lake Shore ($0.33 < X_{Fe} > 0.38$) imply an fO_2 in the approximate range of 10^{-12} - 10^{-8} bars. Increasing X_{Fe} values for hydrothermal biotites from Lake Shore indicate decreasing fO_2 with time and infer a minimum fO_2 of 10^{-8} bars during formation of the later hydrothermal biotites.

6.2 Wall Rock Alteration

6.2.1 Chlorite Facies

The chlorite facies is characterized by the replacement of all ferromagnesian minerals by chlorite. The rocks are similar in colour and texture to those of the unaltered and secondary biotite facies and are generally only recognized in thin section. They are generally found at distances greater

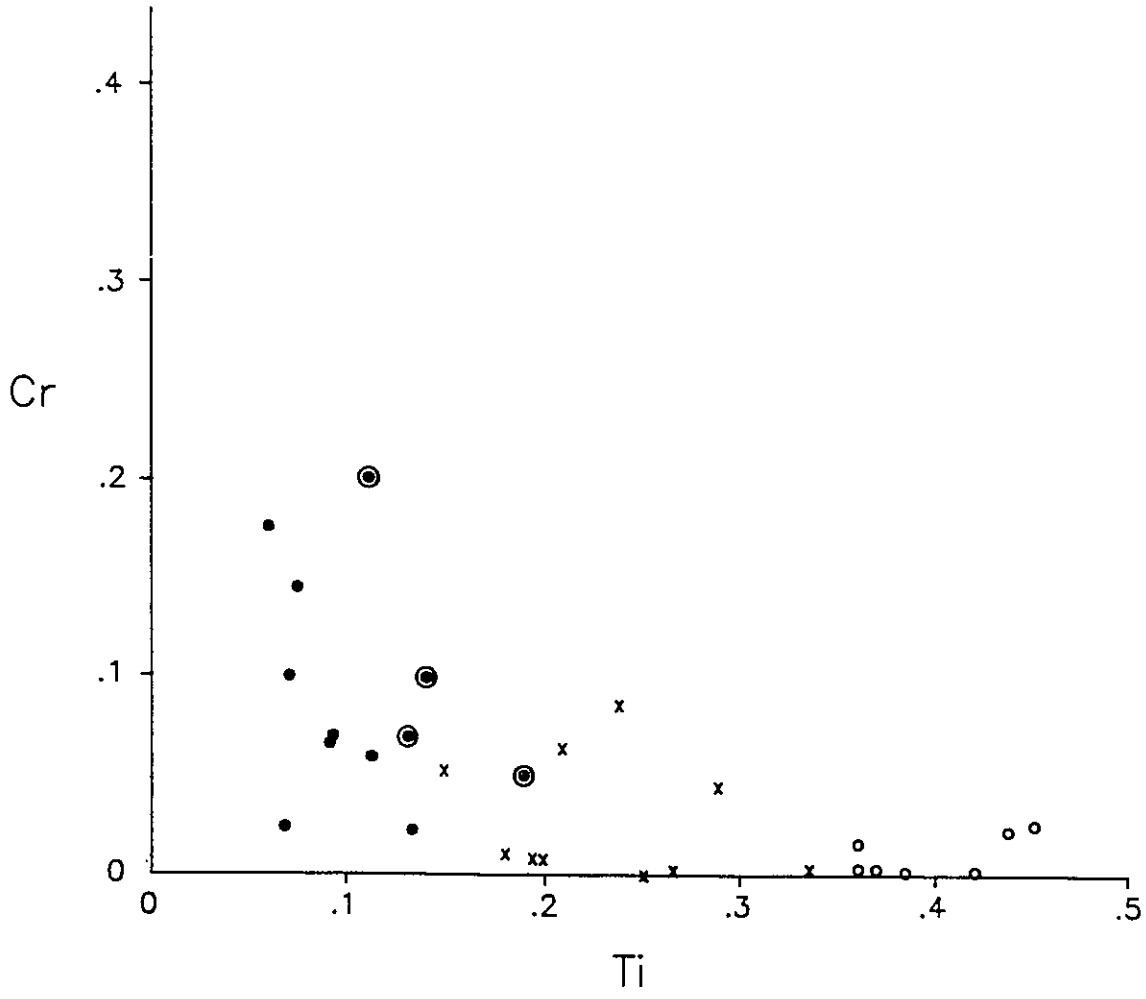

Fig. 6.5. Plot of Cr versus Ti for the multiple generations of biotite from Lake Shore. Open circles = magmatic biotite; filled circles = pale green early hydrothermal biotite; ringed filled circles = medium green early hydrothermal biotite; crosses = late hydrothermal biotite. Values are number of cations based microprobe analyses calculated to 22 oxygens. Note the greater compositional ranges for hydrothermal biotites compared to magmatic biotite. Data from Table A2.2 (Appendix II).

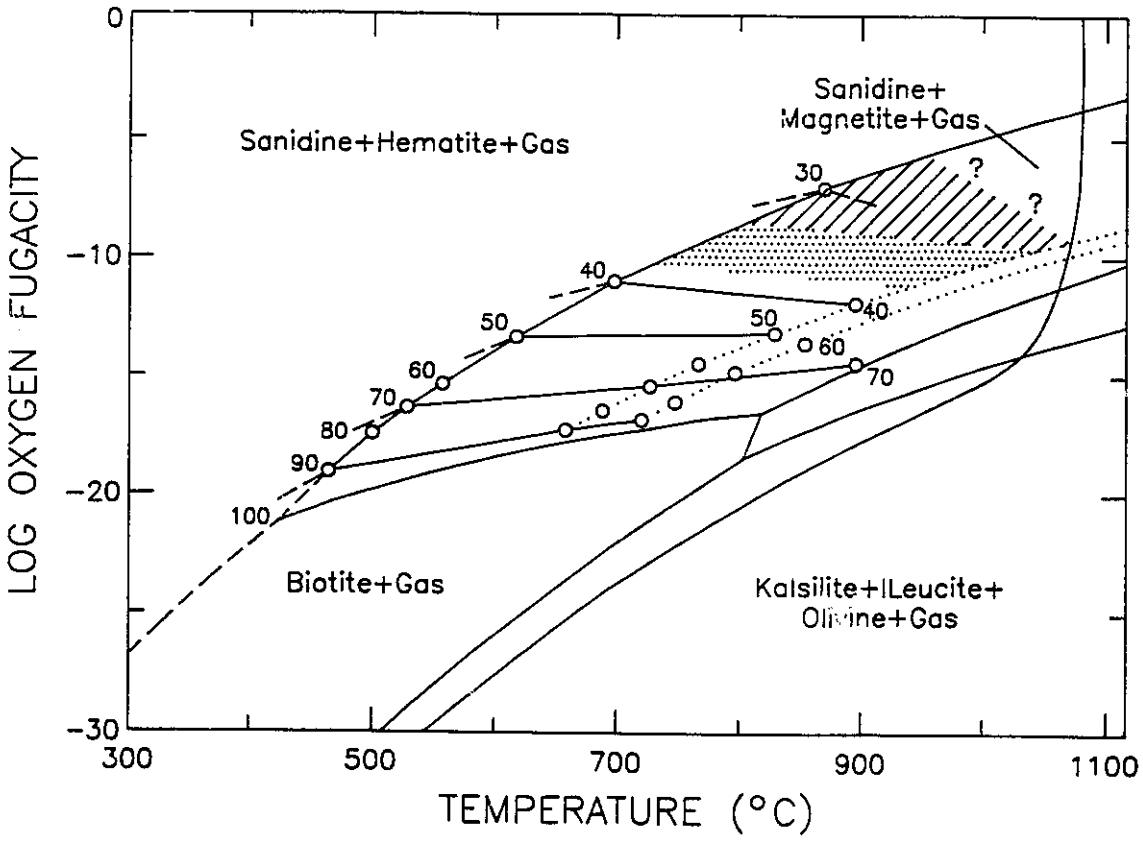

Fig. 6.6. Stability of biotite as a function of oxygen fugacity and temperature at 2070 bars total pressure (after Wones and Eugster, 1965). Stippled area - projected area of stability for magmatic biotite; ruled area - projected area of stability for hydrothermal biotites. While temperature estimates have not been determined, the consistency in biotite compositions with X_{Fe} <0.50 with varying temperature allows an estimate of fO_2 to be made. Contours and corresponding numbers represent Fe/Fe+Mg X 100 values for biotites.

than 12 m and less than 20 m from the auriferous veins (Fig. 6.1). Towards the veins, these rocks grade into rocks of the phlogopite-hematite facies. Away from the auriferous veins, they are in contact with either the unaltered feldspar porphyry or rocks of the hydrothermal biotite facies.

The alteration of biotite, either magmatic or hydrothermal, takes place along grain margins and the {001} cleavage plane (Plate 6.6). The amount of sagenite (rutile) within the chloritized biotite increases with chlorite alteration, a reflection of the inability of the chlorite to incorporate all of the TiO_2 from the biotite (Plates 6.6, 6.8). Basal sections commonly show well developed rutile asters (Plate 6.8). Small grains of secondary magnetite, K-feldspar, and carbonate are also developed along the cleavage planes, indicating a minor reduction in volume during the alteration of biotite to chlorite. Magnetite and K-feldspar are formed due to the inability of chlorite to incorporate all of the Fe and K released during the breakdown of biotite.

Chlorite pseudomorphs after hornblende are identified by aggregates of fine grained chlorite with a characteristic basal amphibole shape (Plate 6.7). The replacement of hornblende by chlorite may be direct, or hornblende may be first replaced by hydrothermal biotite, which is followed by chlorite.

Increased sericite and carbonate alteration of the plagioclase and groundmass also accompany this alteration. The

albite-orthoclase-celestine overgrowths on plagioclase, common in the hydrothermal biotite facies, generally begin to show signs of minor sericite alteration, particularly in the more altered samples. Primary magnetite shows increased alteration to hematite, and titanite coronas become abundant. Siderite, identified by its high relief and rusty stain, is frequently associated with the magnetite/ hematite assemblages.

6.2.2 Phlogopite-Hematite Facies

The phlogopite-hematite facies begins 1 to 2 m away from the auriferous veins and extends up to 12 m from the veins. The facies is characterized by the replacement of chlorite (after biotite and hornblende) by phlogopite, the hematitization of primary and secondary magnetite, and the development of fine-grained hematite in the groundmass. As a result of the hematite alteration, the rocks in this facies vary from pinkish red to brick red in colour while still retaining their porphyritic texture (Plate 6.9). In more altered samples, plagioclase phenocrysts take on a mild red colouration. Narrow (<2mm) hematite and quartz-hematite stringers and veinlets are commonly observed in these rocks. The rocks are highly fractured, as evidenced by the numerous chlorite slips.

The replacement of chlorite by phlogopite occurs along grain boundaries and the {001} cleavage (Plate 6.10). Early replacement is marked by a mottled or "salt and pepper"

Plate 6.9. Photograph showing the highly fractured nature and red colour of the feldspar porphyry from the phlogopite-hematite facies. The white scale bar is 2 cm.

Plate 6.10. Photomicrograph of phlogopite (P) replacing chlorite (Ch) in the phlogopite-hematite facies. Replacement occurs along grain boundaries and the 001 cleavage plane. Note the secondary magnetite (Mt) and rutile (Ru) retained from the chlorite facies. Plane polarized light.

Plate 6.11. Photomicrograph showing the extensive development of the rutile (Ru) asters (sagenite texture) along the 001 plane in the phlogopite-hematite facies. Plane polarized light.

6.9

6.10

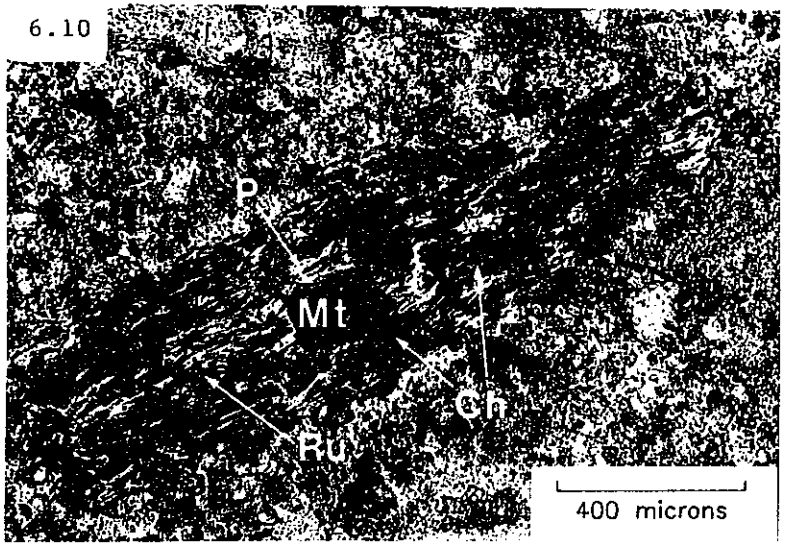

6.11

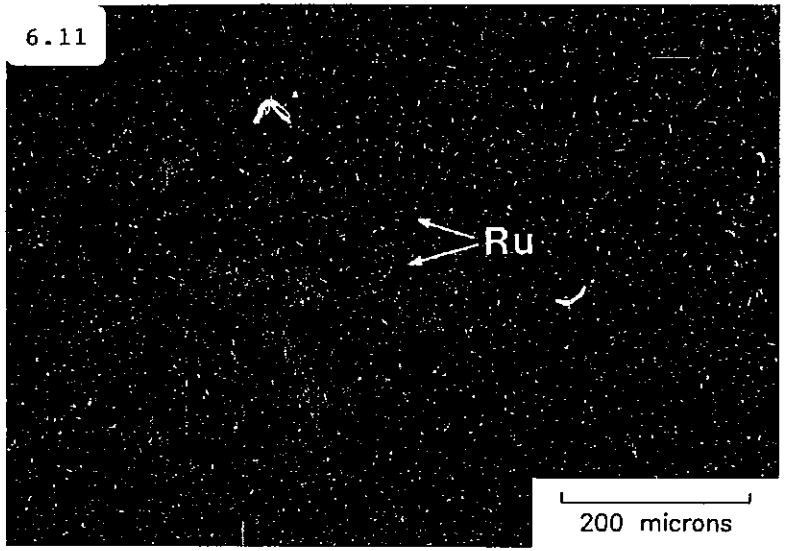

texture as the chlorite is gradually replaced by phlogopite (Plate 6.10). Rutile (sagenite) and magnetite inclusions within the grains generally increase in abundance with alteration as Fe and Ti are released during the breakdown of chlorite (Plates 6.10, 6.11). However, actual contents are related to the original amount of Ti and Fe present. As in the chlorite facies, basal sections show well developed rutile asters (Plate 6.11). In the most altered samples in this facies, the acicular grains of rutile display a marked reduction in size due to partial hydration to leucoxene.

Primary and secondary magnetite is variably replaced by hematite along grain boundaries and fractures (Plate 6.12). Small round grains of hematite are developed in the groundmass, imparting a red colour to the rocks (Plate 6.13). Inclusions in the plagioclase lined with submicroscopic flakes of iron oxide become more apparent with increasing alteration (Plate 6.14). Iron released during the alteration of chlorite to phlogopite is the likely source for hematite formation as relatively little change is observed in Fe contents between the two facies (Table A1.2). This alteration imparts the mild red colour to the plagioclase as seen in hand specimen.

The breakdown of titanite to rutile and carbonate is occasionally observed. Increased sericite and carbonate alteration of the plagioclase and groundmass, compared to similar alteration in the chlorite facies, also accompanies this alteration.

Plate 6.12. Photomicrograph showing the replacement of magnetite (Mt) by hematite (Hm) in the phlogopite-hematite facies. Reflected light.

Plate 6.13. Photomicrograph showing the extensive development of fine-grained hematite (Hm) in the groundmass of the feldspar porphyry from the phlogopite-hematite facies. Reflected light.

Plate 6.14. Photomicrograph of a turbid red plagioclase phenocryst in the feldspar porphyry from the phlogopite-hematite facies. The turbid red colour is due to the presence of Fe-oxides along the walls of fluid inclusions in the plagioclase. Plane polarized light.

Plate 6.15. Photograph showing the highly altered nature of the feldspar porphyry from the fuchsite-sericite-pyrite facies. Note the distinctly faded porphyritic texture. The white scale bar is 2 cm.

6.12

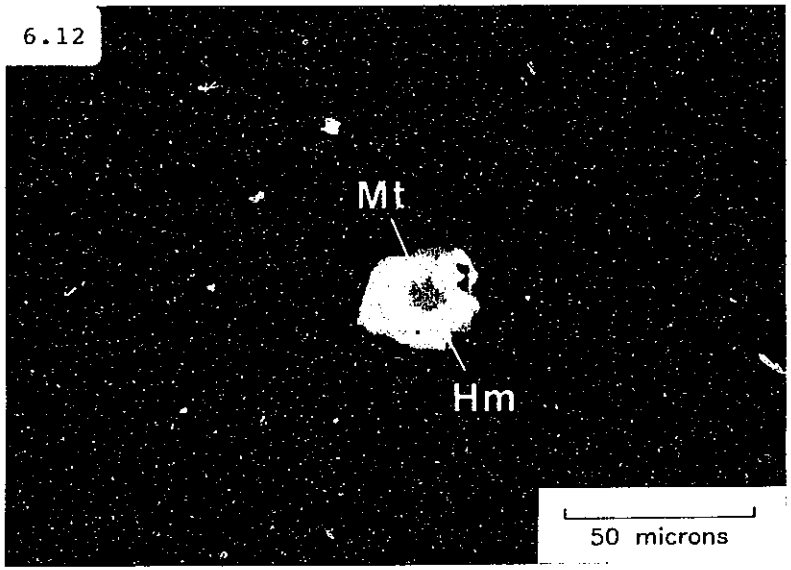

6.13

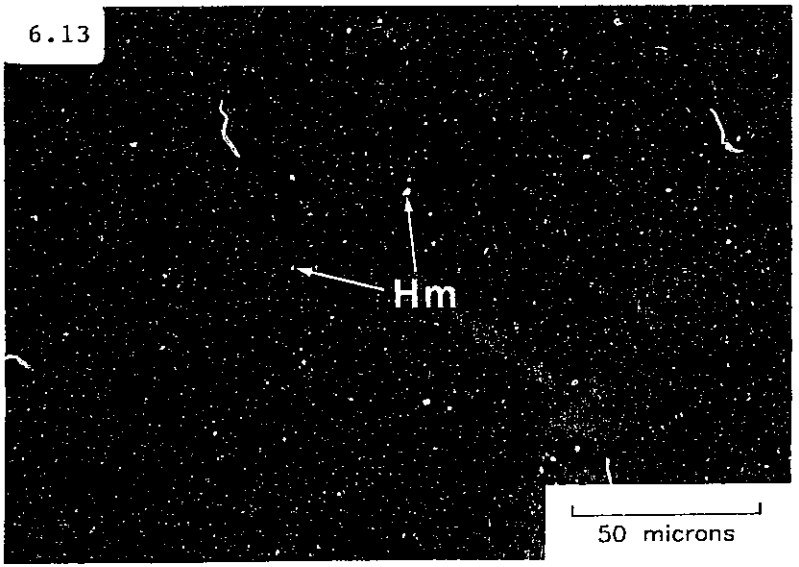

6.14

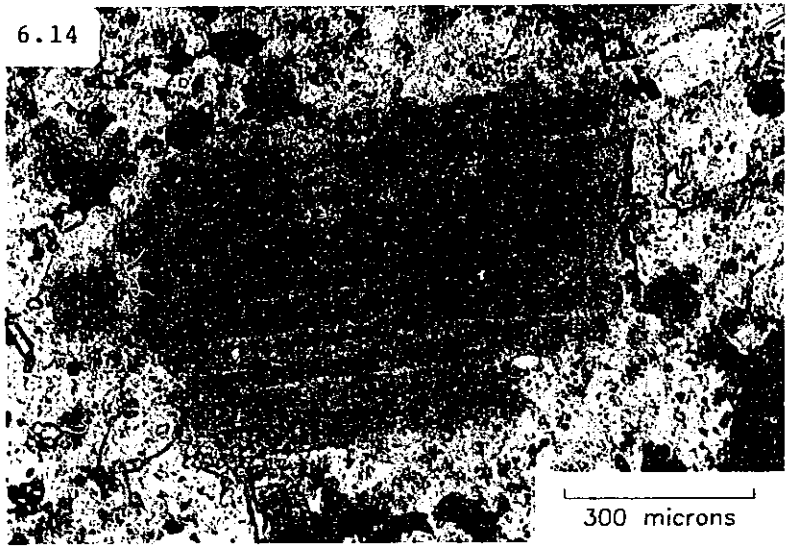

6.15

6.2.3 Fuchsite-Sericite-Pyrite Facies

This facies constitutes the immediate wall rocks of the auriferous veins, extending outward 1 to 2 m from them. In hand specimen these rocks vary in colour, with increasing alteration, from orangy pink to light olive green in the most highly sericitized samples (Plate 6.15). They are highly fractured to moderately sheared, particularly the footwall rocks, which in turn generally display a higher alteration intensity. The increased intensity is probably brought about by the greater permeability, and hence fluid access, in the more deformed footwall rocks. In these rocks the alteration and deformation is so intense that the porphyritic texture is obliterated and replaced by a weak foliation.

The fuchsite-sericite-pyrite facies is characterized by the replacement of phlogopite (after chlorite) by fuchsite or sericite, pervasive sericite alteration of the feldspars and groundmass, and the replacement of hematite and magnetite by pyrite.

The replacement of phlogopite by fuchsite is characterized by the change from colourless phlogopite to pale blue-green fuchsite. The amount of fuchsite present is very minor, commonly less than 5% by volume, relative to the amount of mica in the chlorite and phlogopite-hematite facies. Furthermore, it appears that not all of the phlogopite (after chlorite, in turn after biotite) is converted to fuchsite. Rather, the formation of fuchsite appears to be controlled by

the amount of Cr_2O_3 in the original biotite prior to alteration, rather than by the introduction of Cr from the hydrothermal fluids. Biotites high in Cr_2O_3, such as early hydrothermal biotite, are apparently altered to chlorite, then phlogopite, and finally to fuchsite, with Cr_2O_3 being retained throughout the sequence. Biotites low in or lacking Cr_2O_3 are altered to sericite, rather than fuchsite, as an end product. Electron microprobe analyses of optically similar white mica within this facies, i.e. those containing sagenite and therefore assumed to have been biotite originally, show a range of Cr_2O_3 contents from nil (sericite) to just above the 1% threshold for fuchsite (Table A2.2), substantiating this hypothesis.

Rutile asters formed in the chlorite and phlogopite-hematite facies are variably replaced by leucoxene (Plate 6.16). The degree of replacement increases as the auriferous veins are approached. As a result, the star-shaped aster appearance has been destroyed and replaced with a wispy, or powdery, texture typical of leucoxene.

In the more deformed footwall rocks, the long axis of fuchsite (or sericite) is realigned parallel to the foliation plane (Plate 6.17). With increased shearing, fuchsite is gradually removed until all that remains are thin, dark seams of leucoxene parallel to the foliation (Plate 6.18).

Pyrite is formed in this facies at the expense of hematite and magnetite. This hypothesis is supported by minor

Plate 6.16. Photomicrograph of fuchsite (F) in the fuchsite-sericite-pyrite facies. As alteration progresses, the secondary magnetite and rutile developed during the previous hydrothermal alteration events is hydrated to leucoxene (L). Plane polarized light.

Plate 6.17. Photomicrograph showing the early stages of deformation in the fuchsite-sericite-pyrite facies. The photomicrograph shows fuchsite (F) being realigned parallel to the foliation planes by gliding along cleavages of mica due to shear deformation. All secondary magnetite and rutile has been replaced by leucoxene (L). Plane polarized light.

Plate 6.18. Photomicrograph showing the later stages of deformation in the fuchsite-sericite-pyrite facies. The photomicrograph shows thin black seams of leucoxene (L) formed by the realignment due to shear deformation. Plane polarized light.

Plate 6.19. Photomicrograph showing the development of post-ore albite alteration associated with quartz-carbonate veining. Where the quartz carbonate vein (QC) cuts a pervasively sericitized plagioclase (Pl) grain, the fracture filling within the grain is near end member albite (Ab) similar to analysis 153-1c in Table A2.1 which is optically oriented with the host plagioclase grain. Crossed nicols.

6.16

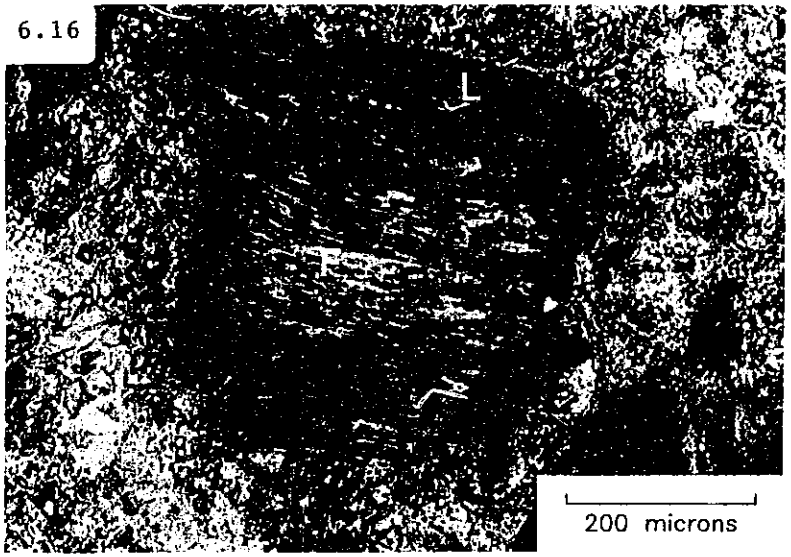

6.17

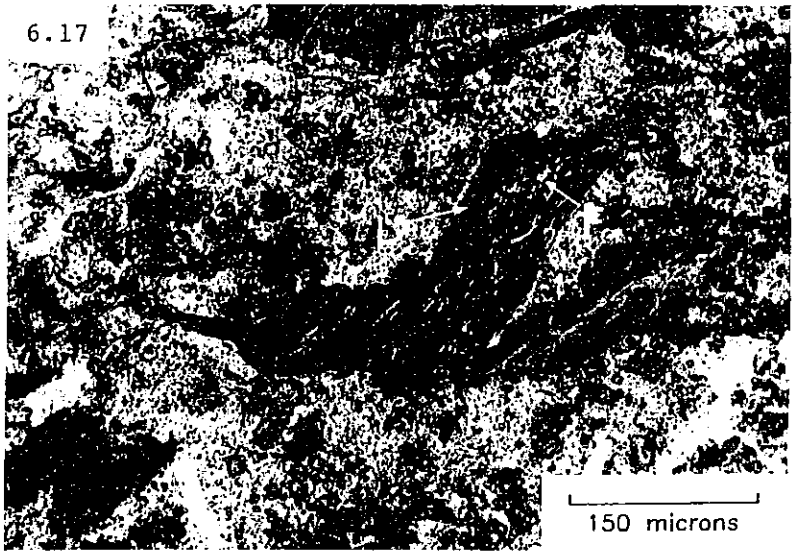

6.18

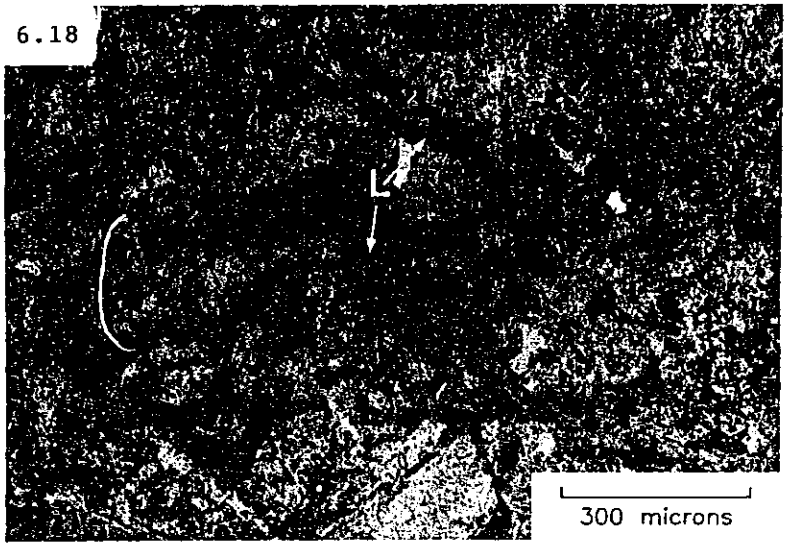

6.19

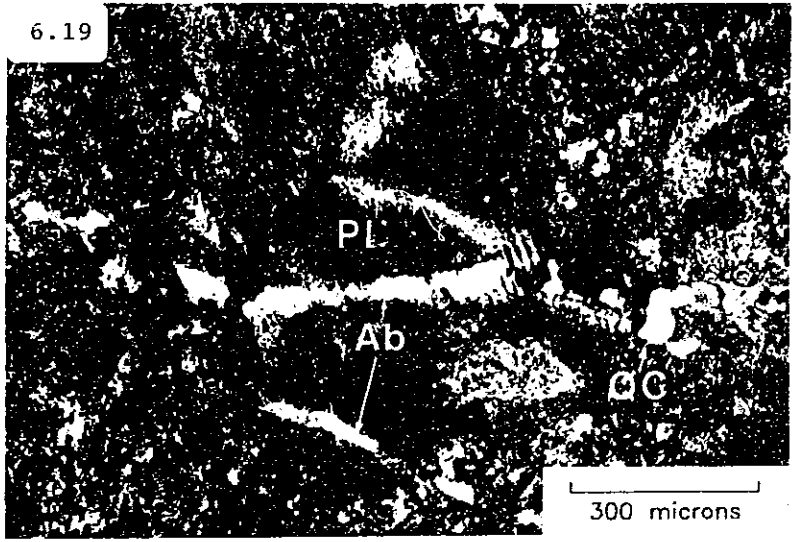

reductions in the amount of Fe within this facies. Pyrite occurs up to distances of about 1 m from the ore veins, and often extends farther into the more deformed footwall rocks, thereby substantiating their increased permeability due to deformation. In the less deformed rocks of this facies, pyrite inclusions in fuchsite are common, replacing secondary magnetite and hematite.

Minor silicification and the development of secondary K-feldspar also accompany this alteration. Minor amounts of sericite are observed in the K-feldspar, suggesting either the incorporation of existing sericite or alteration during a post-ore hydrothermal event.

Primary and secondary titanite and rutile are absent from this facies, having been completely replaced by leucoxene. Carbonate alteration is more prevalent in the less deformed hangingwall rocks.

6.3 Post-Ore Alteration

Several types of post-ore alteration are recognized at Lake Shore, including the formation of sericite, albite, and carbonate. Timing relationships among the three are uncertain as cross cutting relationships are absent.

Post-ore sericite alteration is best demonstrated where the post-ore diabase dyke at the western end of the property cuts the North Vein. Here, the diabase displays moderate to pervasive sericite alteration of plagioclase. This type of

alteration is not recognized in the feldspar porphyry, possibly due to the pervasive sericite alteration associated with the main stage ore forming fluids.

Small fracture fillings of quartz and quartz-carbonate are common throughout all alteration facies of the porphyry, including the highly altered wall rocks. Where these veinlets cut pervasively sericitized plagioclase phenocrysts, fracture fillings within the plagioclase grains consist of albite, of near end-member composition, in optical continuity with the host grains (Plate 6.19). In addition, optically clear, phenocryst-sized albite grains up to 0.5mm are developed with veins of quartz or quartz-carbonate trailing from them. Both types of albite show no signs of sericite alteration, further suggesting formation after main stage hydrothermal activity.

Post-ore carbonate alteration is associated with the Lake Shore cross fault. It is recognized solely by an increase in the amount of carbonate in the groundmass of the porphyry in areas adjacent to the fault. It was impossible to tell from this study if any other alteration is associated with this structure, as all samples collected were proximal to the auriferous veins and have been affected by previous hydrothermal activity.

6.4 Whole Rock Geochemistry

Major oxide and selected trace element analyses of samples from the four hydrothermal alteration facies are given

in Table A1.2 (Appendix I). Distribution plots of major elements versus distance from the ore veins indicate moderate degrees of chemical variation within these alteration facies (Fig. 6.7). However, plots for the hydrothermal biotite facies (least altered) also show moderate degrees of variation within the porphyry unit itself, which may assist in "hiding" chemical variations brought about as a result of alteration (Fig. 6.7).

The most prominent change observed is variable gains in K_2O for the fuchsite-sericite-pyrite facies (Fig. 6.7). Increase in K_2O and loss of CaO and Na_2O as the veins are approached reflect increasing sericite alteration. Direct replacement of Na_2O in plagioclase by K_2O in sericite (or orthoclase) is reflected in Figure 6.8. Highly deformed samples immediately adjacent to the ore veins display the highest K_2O (Figs. 6.7, 6.8) contents, reflecting the complete replacement of all plagioclase by sericite. While obliteration of primary textures suggests large changes in volume, the lack of Na_2O (Na_2O = 0.00%) in several samples substantiates the observed increases in K_2O. Furthermore, the relatively large degree of heterogeneity (Fig. 6.7) observed among the least altered samples makes it difficult to assign a parent chemistry upon which losses and gains could be calculated.

Moderate variations are also noted for Fe_2O_3 (total), MgO, and P_2O_5 (Fig. 6.7). Losses of Fe and Mg are the result of biotite breakdown, while loss of P suggests the removal of

Fig. 6.7. Distribution trends of major oxides and selected trace elements across the North and South Veins. The sample suites represented were collected from the 1246 crosscut (solid line), drill hole 04-42 (dashed line), and the 643 crosscut (dotted line). The 11 samples plotted to the farthest right of the diagrams represent the least altered samples. The following designations apply for the three suites: 1) For the 1246 crosscut; 0 represents the position of the North Vein. 2) For drill hole 04-42; 0 represents the position of the South Vein. 3) For the 643 crosscut; 0 represents the position of the North Vein while the South Vein is located at 17 m to the right. The three samples located at 8 m to the right are adjacent to the Lake Shore cross fault. Data taken from Table A1.2. Specific sample locations and distributions with respect to a given alteration facies are given in A4.1 through A4.4.

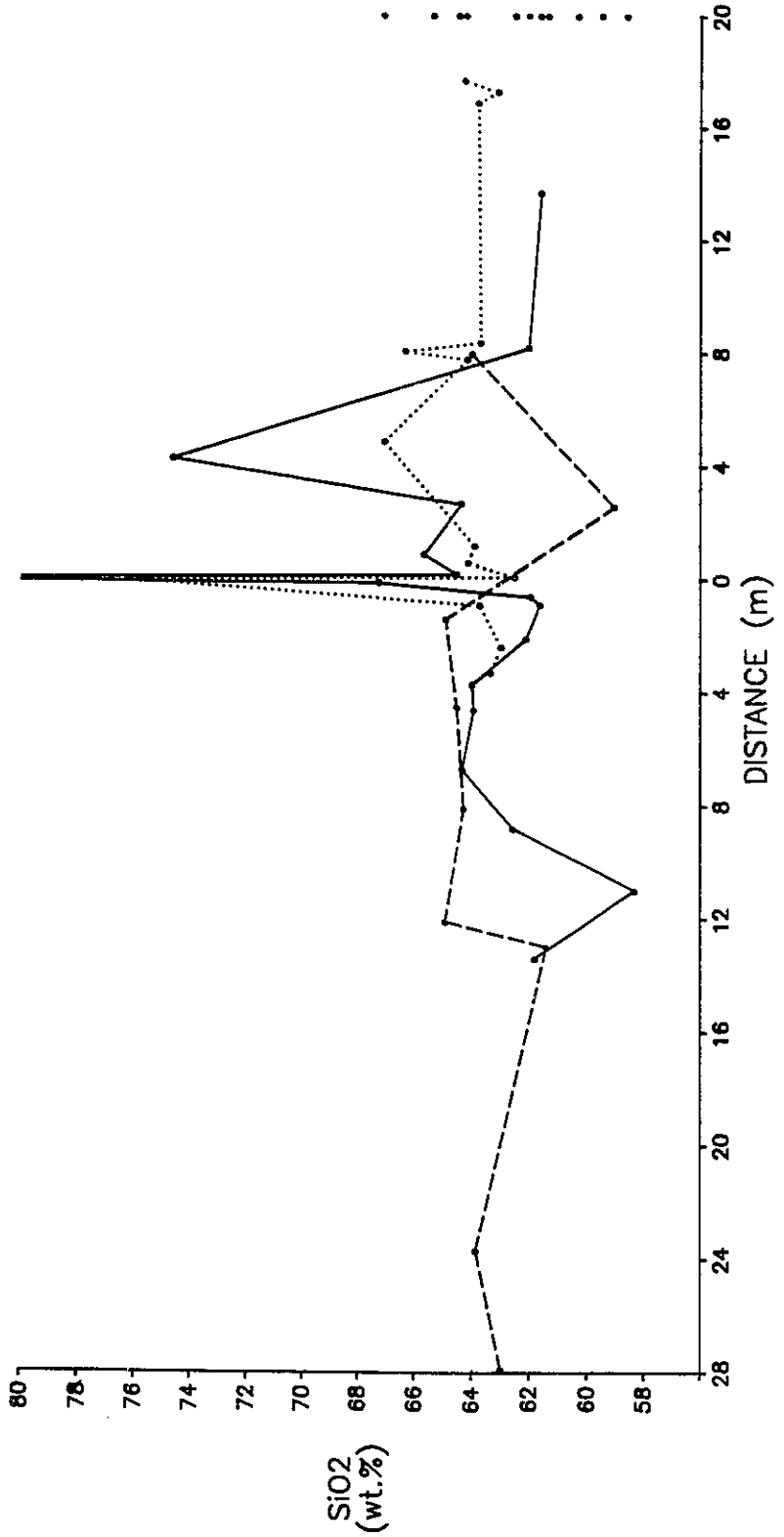
SiO2
(wt.%)
80
78
76
74
72
70
68
66
64
62
60
58
28
24
20
16
12
8
4
0
4
8
12
16
20
DISTANCE (m)

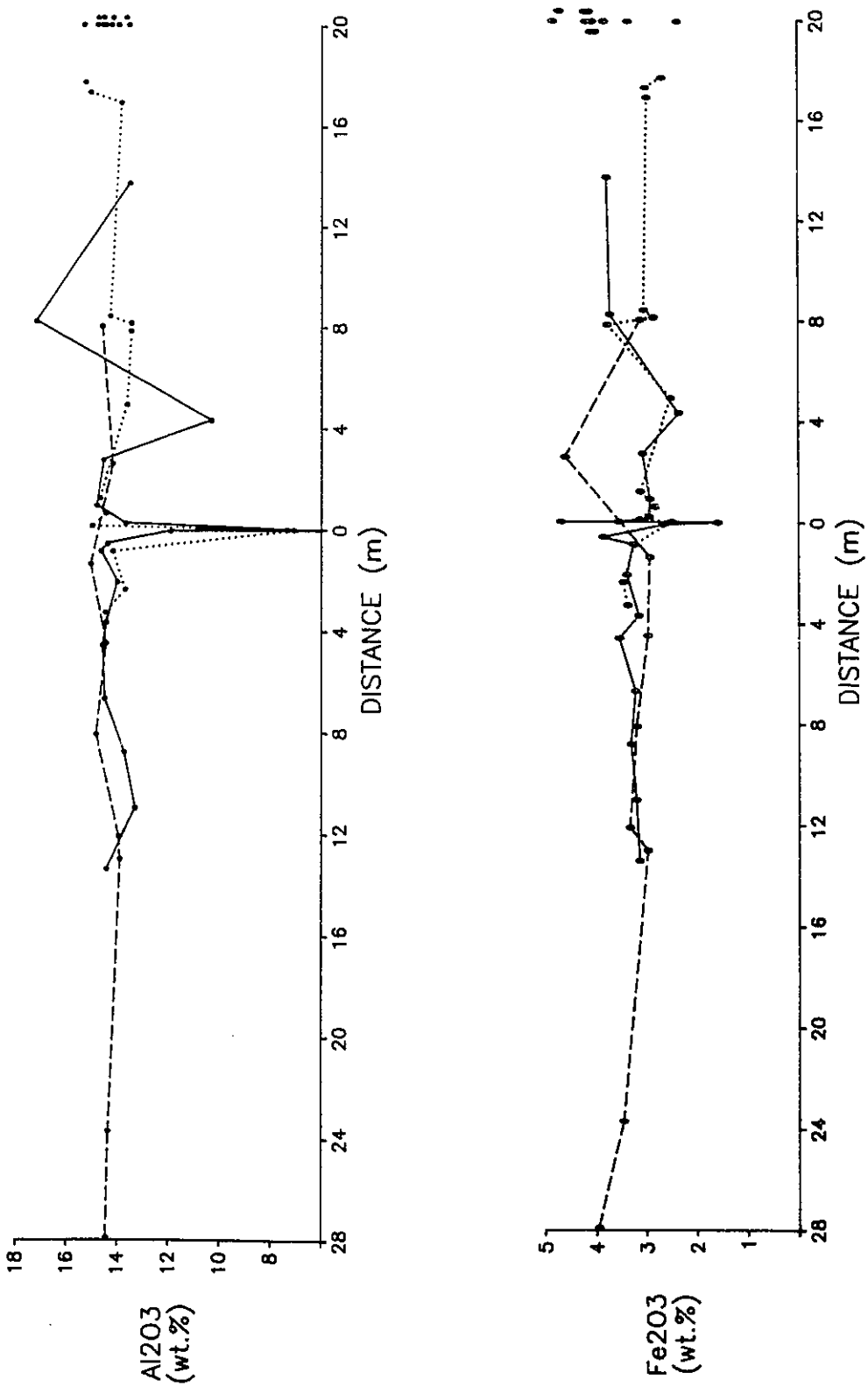
Al2O3 (wt.%)
18
16
14
12
10
8
28
24
20
16
12
8
4
0
4
8
12
16
20
DISTANCE (m)
Fe2O3 (wt.%)
5
4
3
2
1
28
24
20
16
12
8
4
0
4
8
12
16
20
DISTANCE (m)

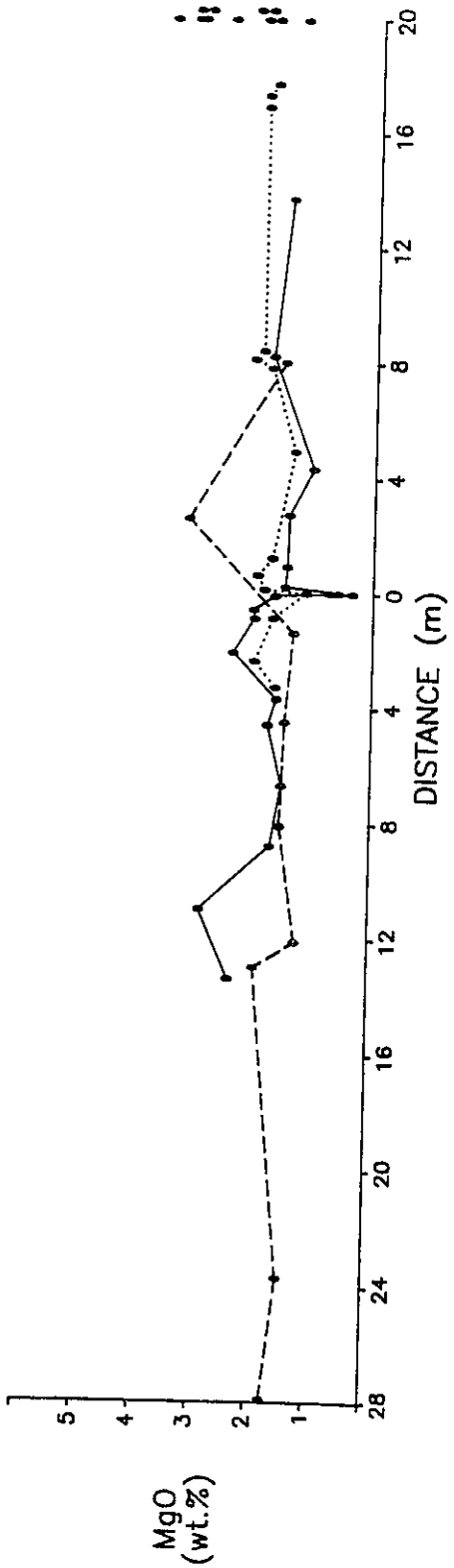
MgO
(wt.%)
DISTANCE (m)

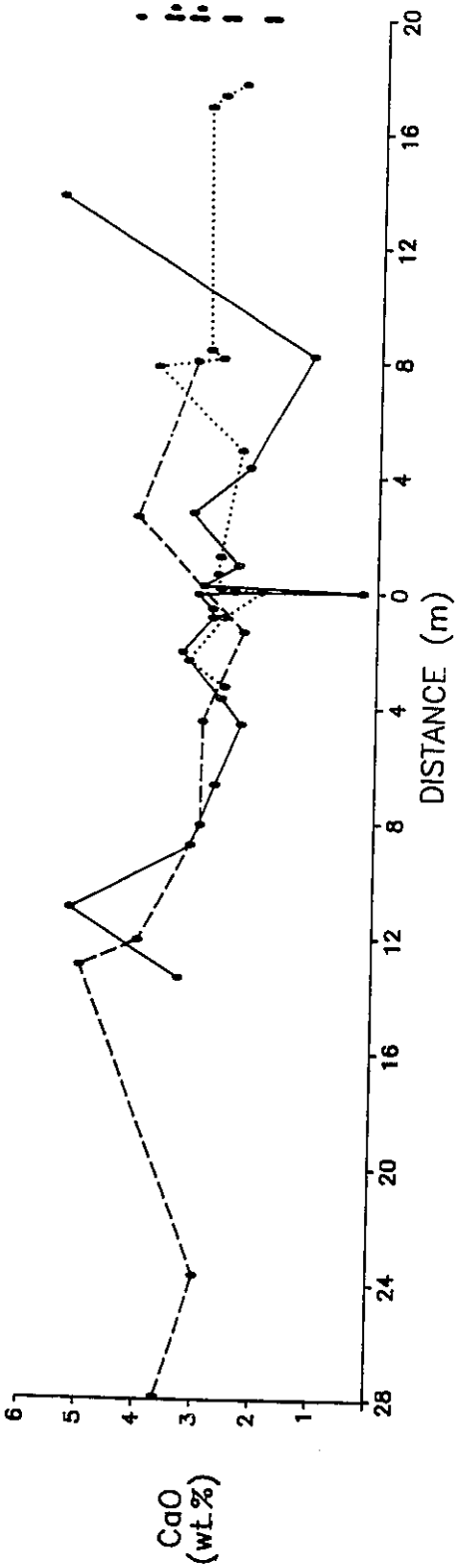
CaO
(wt.%)
DISTANCE (m)

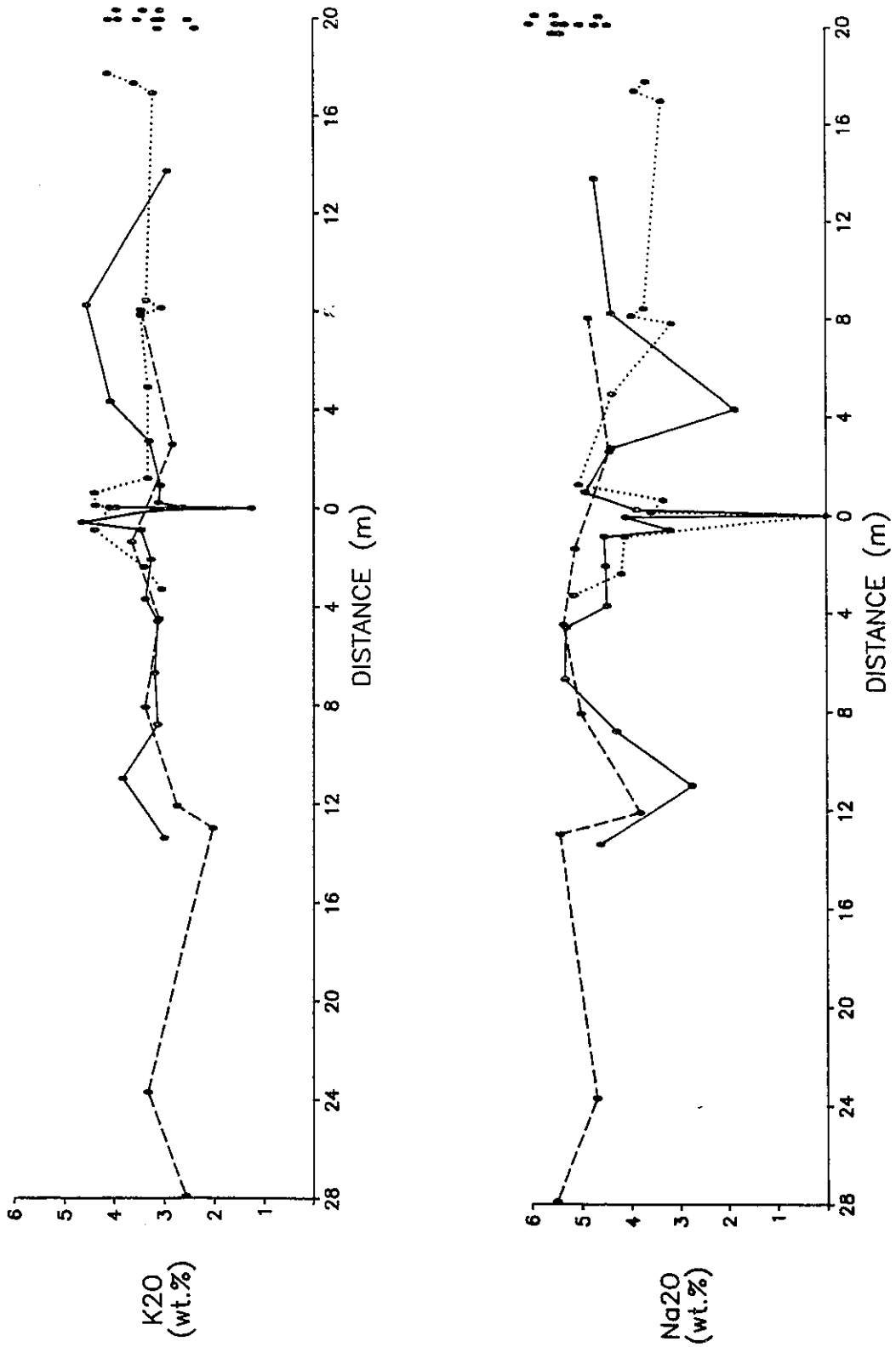
K2O
(wt.%)
6
5
4
3
2
1
28
24
20
16
12
8
4
0
4
8
12
16
20
DISTANCE (m)
Na2O
(wt.%)
6
5
4
3
2
1
28
24
20
16
12
8
4
0
4
8
12
16
20
DISTANCE (m)

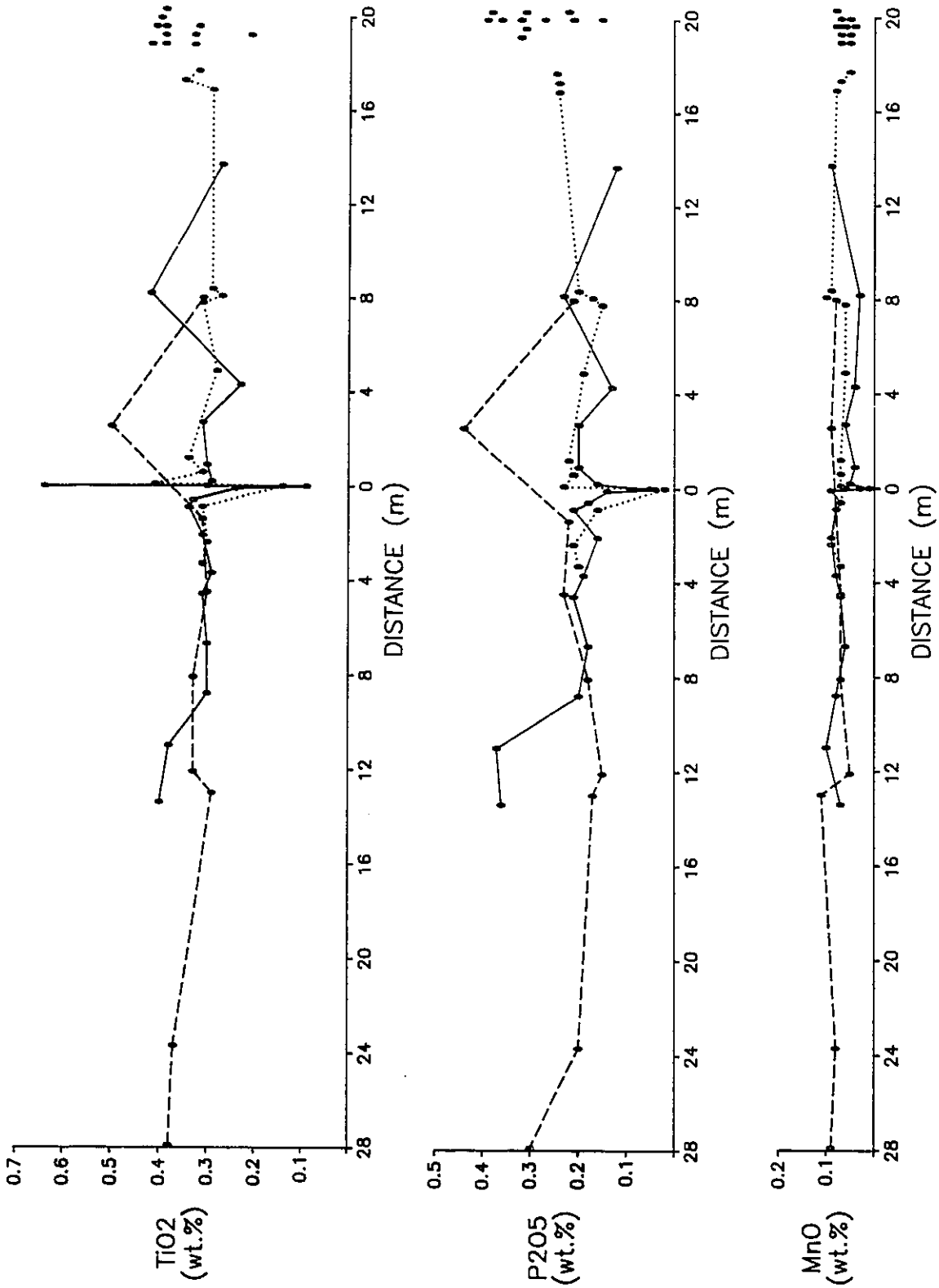
TiO2 (wt.%)
0.7
0.6
0.5
0.4
0.3
0.2
0.1
28 24 20 16 12 8 4 0 4 8 12 16 20
DISTANCE (m)
P2O5 (wt.%)
0.5
0.4
0.3
0.2
0.1
28 24 20 16 12 8 4 0 4 8 12 16 20
DISTANCE (m)
MnO (wt.%)
0.2
0.1
28 24 20 16 12 8 4 0 4 8 12 16 20
DISTANCE (m)

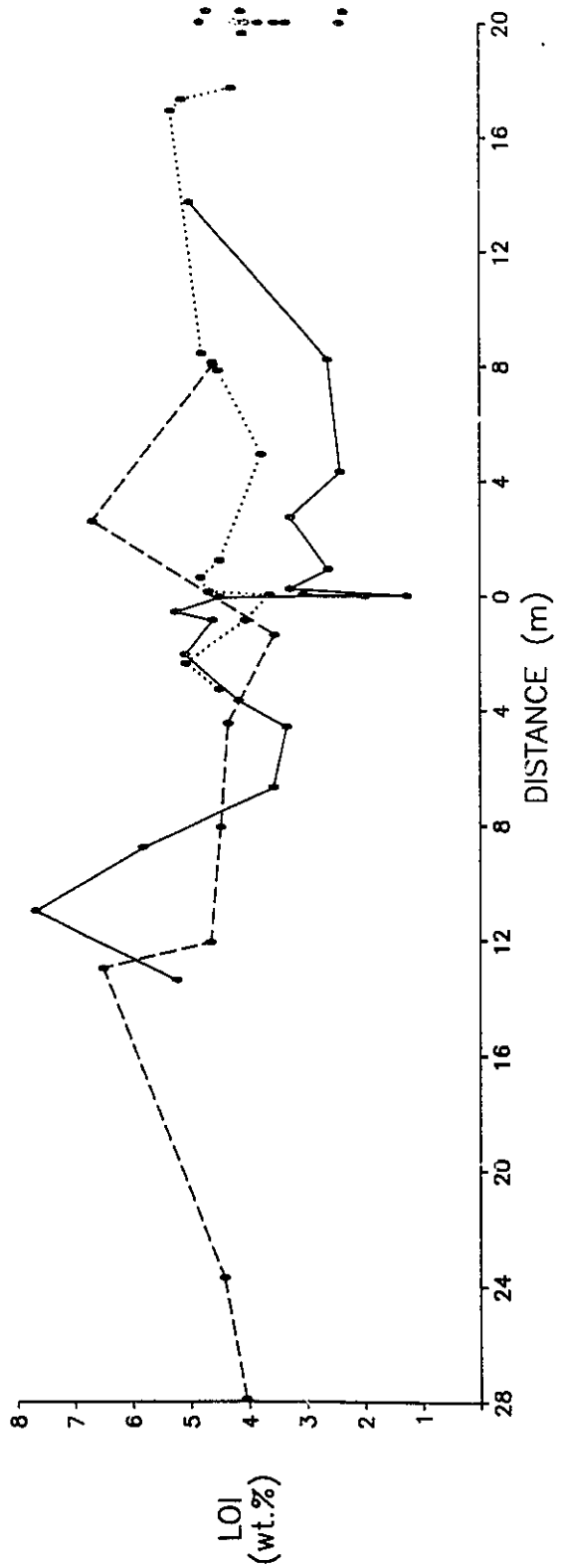
LOI
(wt.%)
8
7
6
5
4
3
2
1
28
24
20
16
12
8
4
0
4
8
12
16
20
DISTANCE (m)

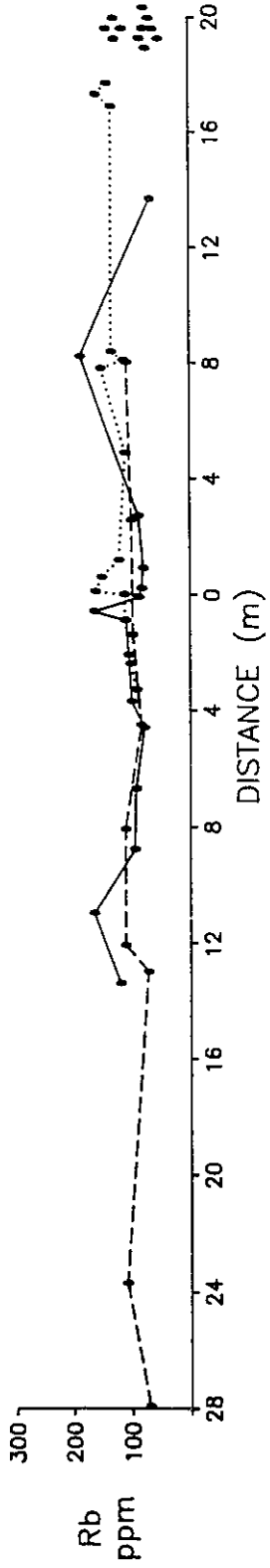
Rb
ppm
300
200
100
28
24
20
16
12
8
4
0
4
8
12
16
20
DISTANCE (m)

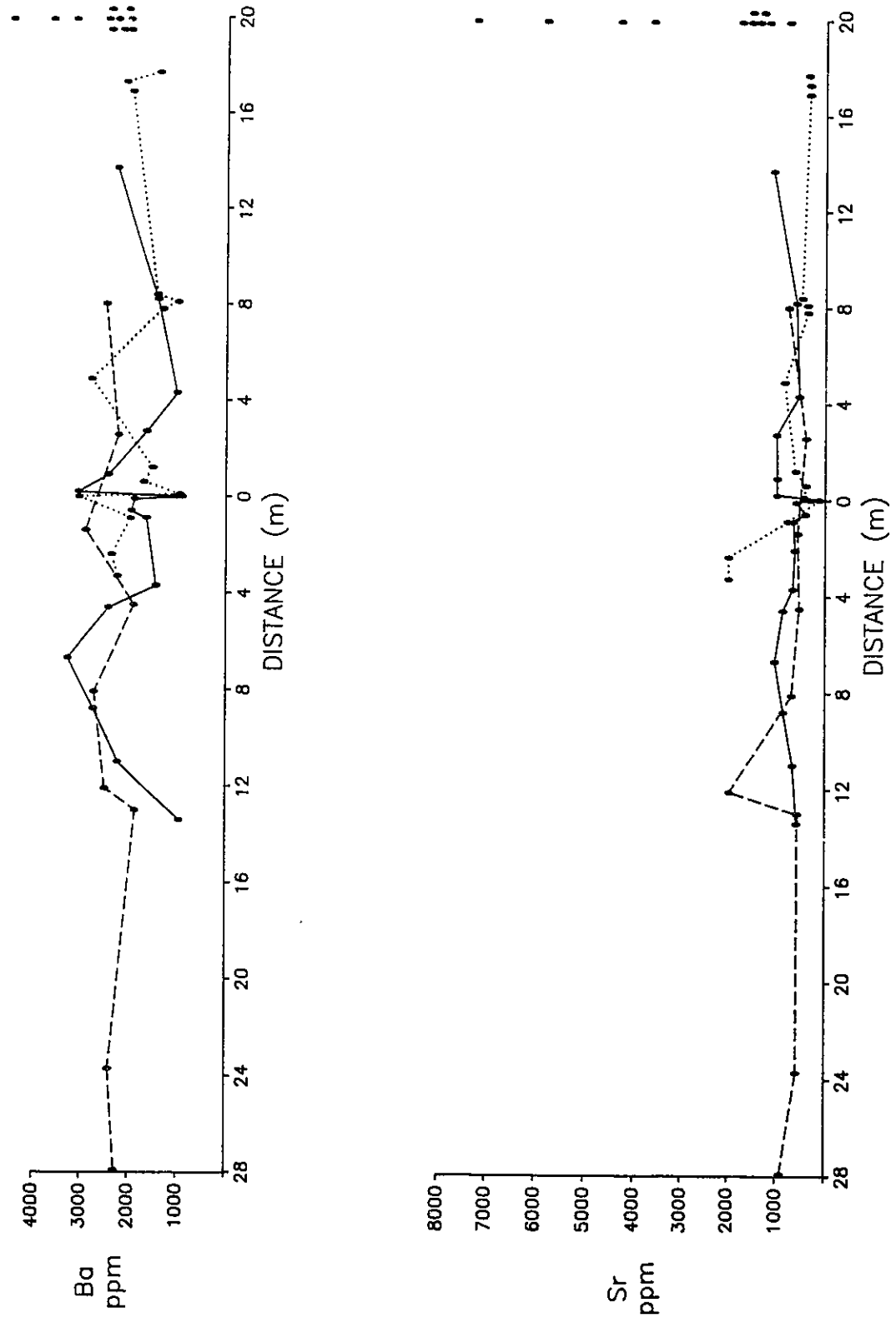
Ba
ppm
4000
3000
2000
1000
28
24
20
16
12
8
4
0
4
8
12
16
20
DISTANCE (m)
Sr
ppm
8000
7000
6000
5000
4000
3000
2000
1000
28
24
20
16
12
8
4
0
4
8
12
16
20
DISTANCE (m)

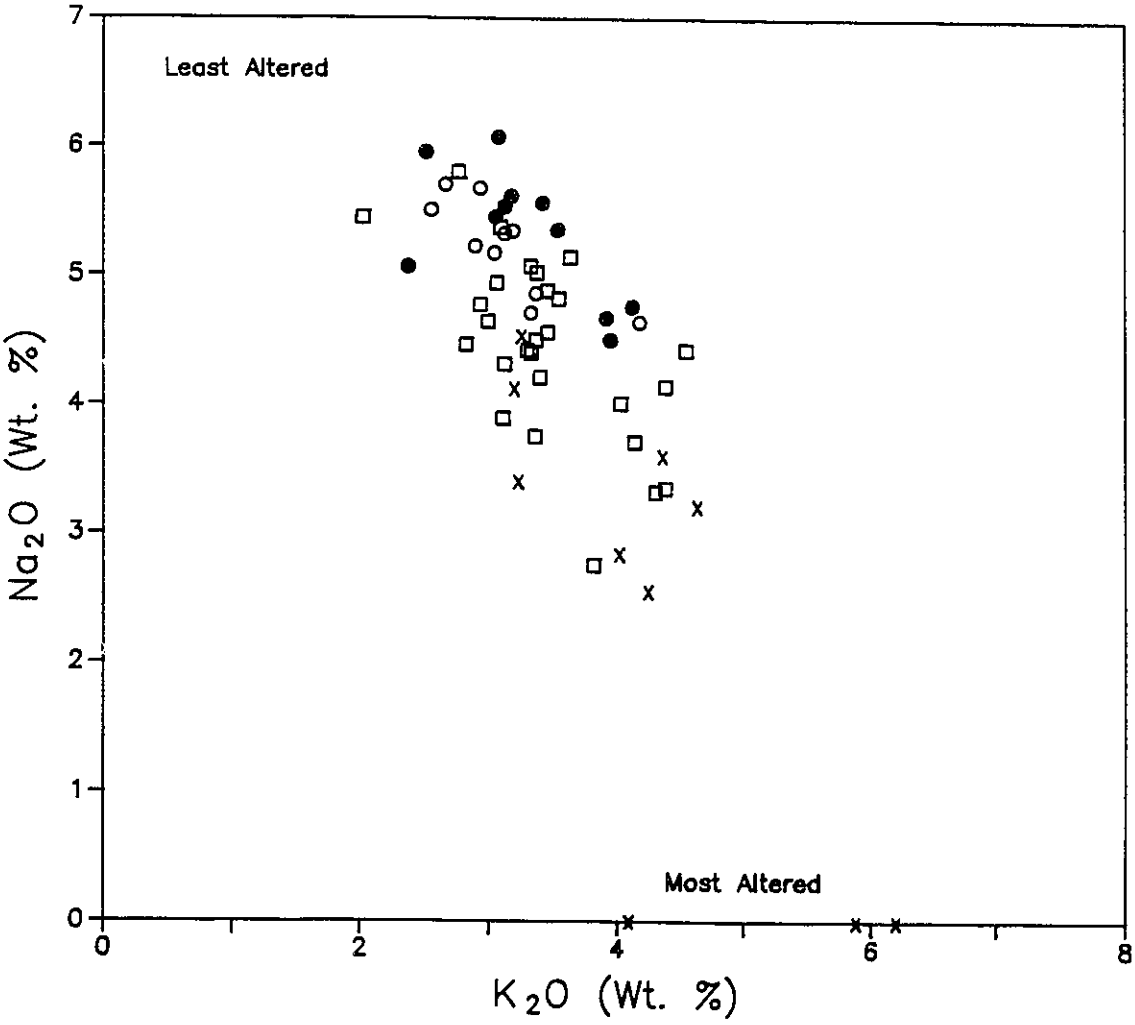

Fig. 6.8. Plot of Na_2O versus K_2O for the four hydrothermal alteration facies. The strong antithetic nature reflects the replacement of Na_2O by K_2O during the alteration of plagioclase to sericite or K-feldspar. Solid circles = hydrothermal biotite facies; open circles = chlorite facies; boxes = phlogopite-hematite facies; crosses = fuchsite-sericite-pyrite facies. Data from Table A1.2 (Appendix I).

apatite. These variations may also be representative of parent chemical compositions prior to alteration.

Marked differences are also observed in Sr, Ba, and Rb for the four facies (Fig. 6.7). The lesser altered hydrothermal biotite and chlorite facies contain generally higher contents of Sr (Table A1.2). The higher levels of Sr can be attributed to the formation of barian-celestine during the magmatic-hydrothermal event. This hypothesis is further substantiated by the lack of any correlation between Sr and K_2O, the normal element (K) for which Sr substitutes, implying Sr to be present in a discrete phase (Fig. 6.9a). A lack of, or possible weak correlation between Ba and K_2O contents suggests some of the Ba may also be tied up in a discrete phase (Fig. 6.9b). A positive correlation between Sr and Ba helps to further establish their co-existence (Fig. 6.10). Electron microprobe analyses of sulphate minerals in the hydrothermal biotite facies show the bulk composition of barian-celestine (6.82-15.13% BaO, Table A2.4), substantiating the observed geochemistry.

Lower levels of Sr, and to some extent Ba, in the phlogopite-hematite and fuchsite-sericite-pyrite facies likely reflect the leaching of sulphate during alteration associated with main-stage hydrothermal activity.

Elevated levels of Rb parallel increasing sericite alteration and are reflected in the strong correlation between Rb and K_2O (Fig. 6.11).

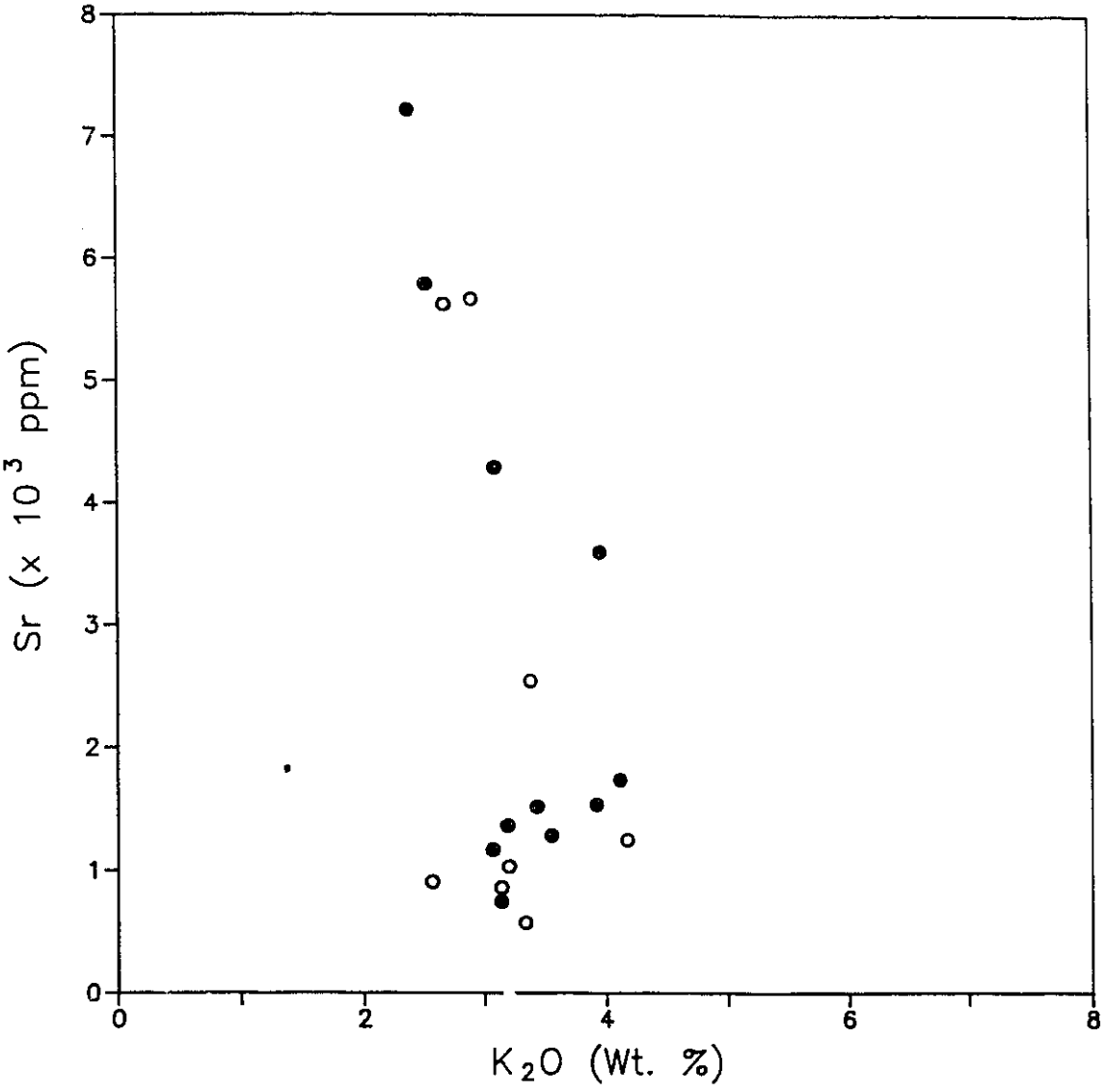

Fig. 6.9a. Plot of Sr versus K_2O for the hydrothermal biotite and chlorite facies. The distinct lack of correlation between the two suggests that Sr may be present within a discrete phase. Solid circles = hydrothermal biotite facies; open circles = chlorite facies. Data from Table A1.2 (Appendix I).

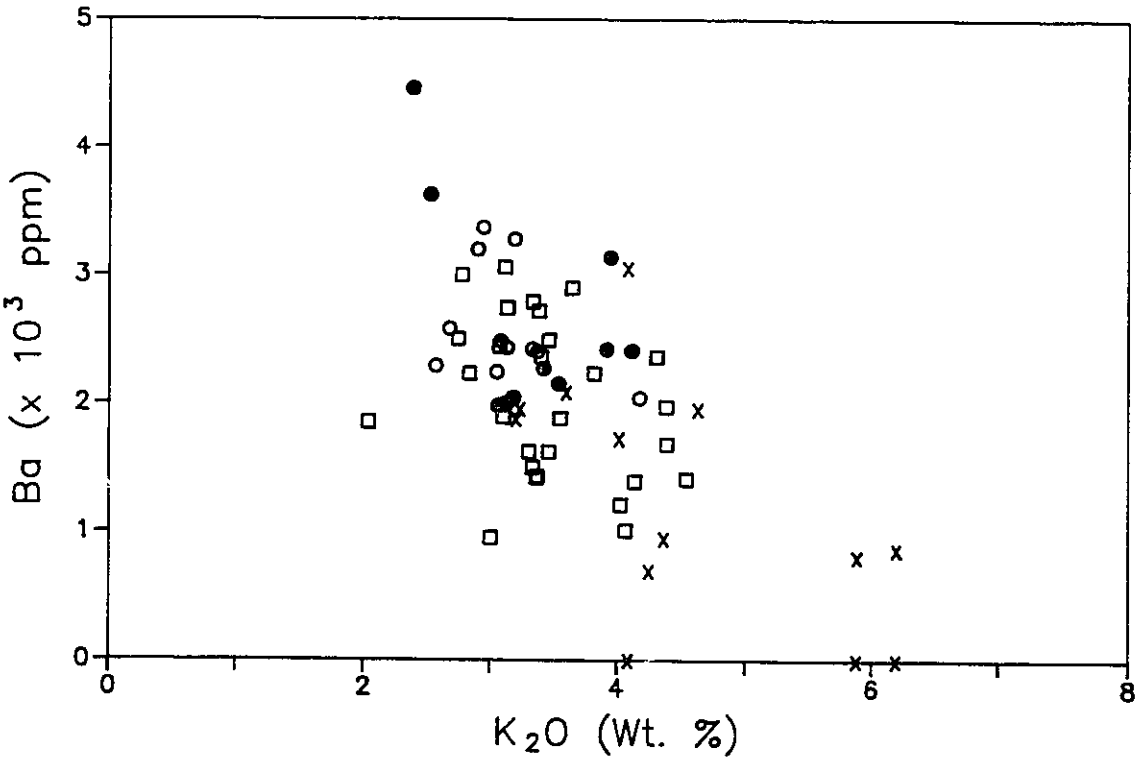

Fig. 6.9b. Plot of Ba versus K_2O for the four hydrothermal alteration facies. The lack of, or weak correlation between the two suggests that some of the Ba may be present within a discrete phase. Solid circles = hydrothermal biotite facies; open circles = chlorite facies; boxes = phlogopite-hematite facies; crosses = fuchsite-sericite-pyrite facies. Data from Table A1.2 (Appendix I).

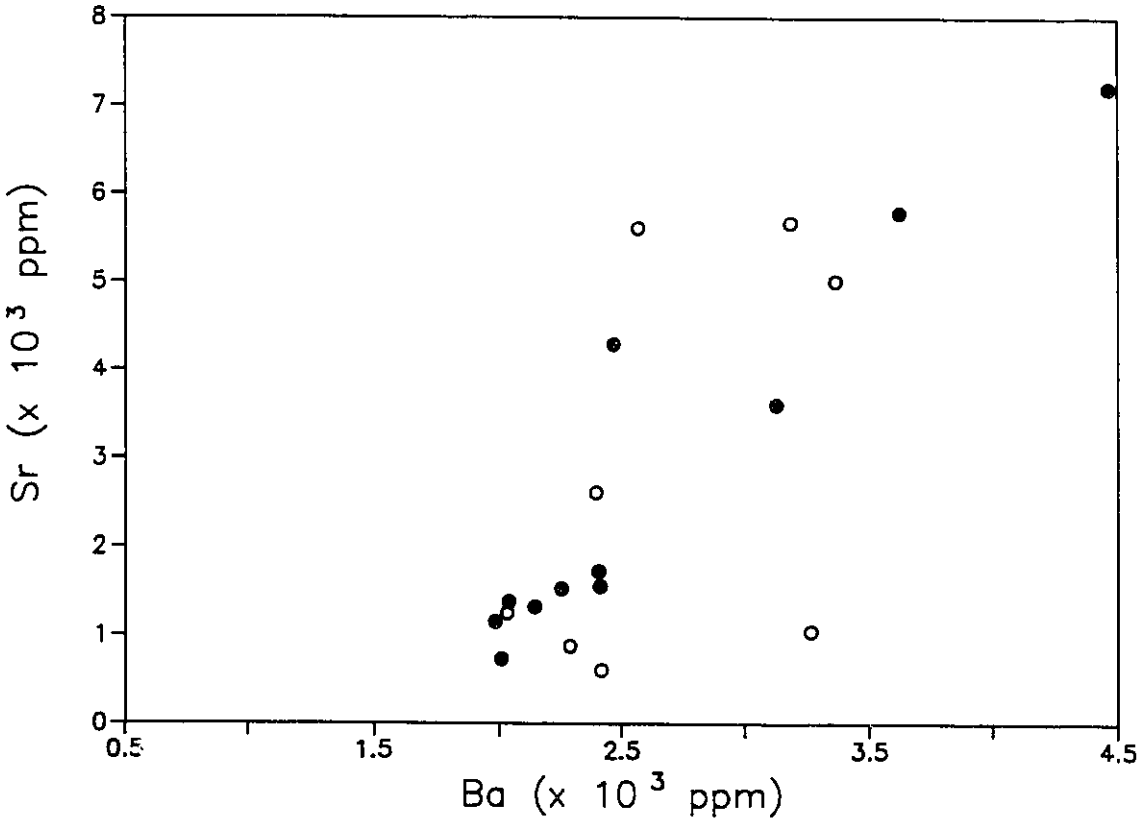

Fig. 6.10. Plot of Sr versus Ba for the lesser altered hydrothermal biotite and chlorite facies. The positive correlation suggests that the two may co-exist within a single phase. Solid circles = hydrothermal biotite facies; open circles = chlorite facies. Data from Table A1.2 (Appendix I).

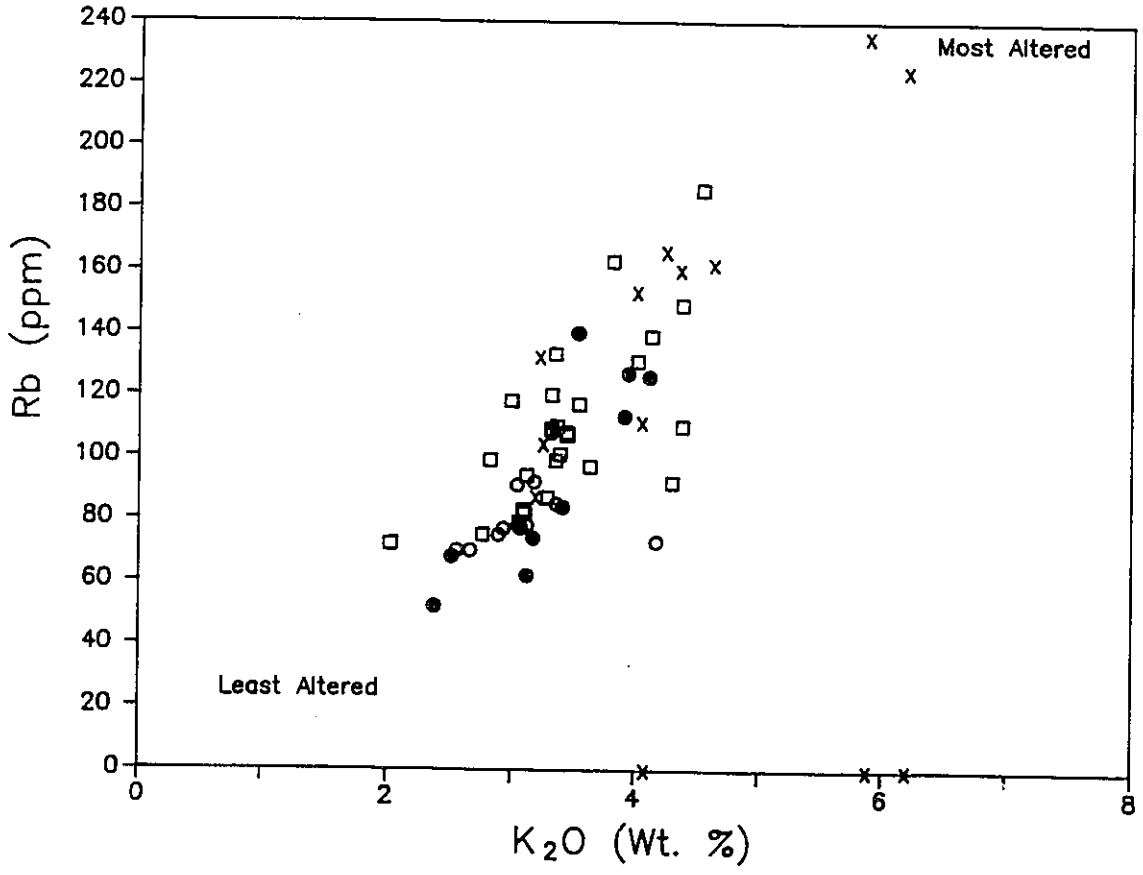

Fig. 6.11. Plot of Rb versus K_2O for the four hydrothermal alteration facies. The strong correlation reflects the substitution of Rb for K. Overall increases in Rb are therefore attributed to increased sericite or K-feldspar alteration. Solid circles = hydrothermal biotite facies; open circles = chlorite facies; boxes = phlogopite-hematite facies; crosses = fuchsite-sericite-pyrite facies. Data from Table A1.2 (Appendix I).

Chapter 7

Discussion

Detailed petrological and geochemical studies of the porphyritic intrusive rocks at the Lake Shore deposit indicate they were subjected to at least three periods of hydrothermal activity. Two of these events, a magmatic-hydrothermal event associated with intrusive activity and hydrothermal activity associated with Au mineralization, may be considered as major events. Later post-ore alteration may be considered as minor in intensity and spatial distribution relative to the other alteration events.

The occurrence of secondary hydrothermal biotite in miarolitic cavities within the porphyry unit, as well as the overgrowth and/or replacement of magmatic biotite by the former, imply that the hydrothermal biotite facies was a direct result of alteration caused by high temperature magmatic-hydrothermal fluids released by the cooling intrusions. Because the area has undergone sub-greenschist facies regional metamorphism (Jolly, 1974), biotite could not

have been formed as a result of metamorphism.

Both textural features and geochemistry indicate the formation of two generations of hydrothermal biotite. The earlier formed varieties are typified by their lighter green colours, high Mg/Fe ratios, higher Cr, and lower Ti contents. The later formed varieties are typically darker green and possess lower Mg/Fe ratios, higher Ti and lower Cr contents. The observed overgrowth textures between these two generations imply the formation of the lighter coloured varieties prior to the dark varieties. The compositions of early hydrothermal biotites are consistent with those found associated with porphyry-Cu deposits (eg. Jacobs and Parry, 1976; Mason, 1978).

While distinct colour differences are noted between the two varieties at overgrowth contacts, gradual changes in chemical composition between the two generations of hydrothermal biotite (Fig. 6.2) suggest more of a temporal evolution, as opposed to overprinting of two independent hydrothermal events. However, observed geochemical trends for the later varieties of hydrothermal biotite, i.e. decreasing Mg/Fe and increasing TiO_2 content, contradict those of usual hydrothermal biotites. The observed "evolution" between these two generations of hydrothermal biotite implies changing fluid chemistries from Cr- to Ti-rich. The occurrence of fluid inclusion trails at overgrowth boundaries suggests the later hydrothermal biotite to have formed by direct precipitation

rather than by replacement of the early hydrothermal biotite.

Recent investigations by Hattori and Levesque (1989) relate the formation of light green Cr-rich micas to lamprophyric intrusions within the Kirkland Lake camp. The widespread nature of the hydrothermal biotite facies, coupled with the insignificant amount of lamprophyre observed, suggests this is unlikely. Further difficulties are presented by the uncertain time of emplacement of the lamprophyre magma, which occurs as dykes crosscutting the porphyry and as inclusions within the porphyry

The occurrence of sulphate minerals in igneous rocks may be the result of two processes; oxidation of primary sulphide, or hydrolysis of SO_2 gas in magmatic-hydrothermal fluids. SO_2 gas dissolved in an aqueous fluid at high temperatures will undergo hydrolysis to form magmatic-hydrothermal sulphate by the following reaction;

$$SO_2(gas) + 2H_2O = H_2SO_4 + H_2(gas)$$

with loss of H_2 gas causing the reaction to move to the right (Hattori and Cameron, 1986). The formation of sulphate in epizonal intrusions commonly occurs in this manner. The occurrence of sulphate in miarolitic cavities within the feldspar porphyry, as well as inclusions of sulphate in hydrothermal biotite, imply a similar origin for sulphate at Lake Shore. In addition, hydrothermal apatites associated with the sulphate commonly display elevated SO_4^{2-} contents, substantiating a magmatic-hydrothermal origin.

Sulphur isotope values of samples from the hydrothermal biotite facies range from +5.2 to +6.7 per mil and are consistent with sulphates formed through oxidized magmatic-hydrothermal activity (Hattori, unpublished data).

The spatial relationship of the chlorite, phlogopite-hematite, and fuchsite-sericite-pyrite facies as concentric zones about the auriferous veins suggests they are the result of alteration associated with main stage veining and mineralization. The mineralogy and alteration sequences characteristic of each facies are summarized in Figure 7.1. The development of these three facies may have occurred in several ways. One possibility is that each facies is representative of different depths to which chemically distinct hydrothermal fluids penetrated the wall rocks. These fluids may be representative of successive individual hydrothermal events, each penetrating the host rocks to a lesser depth and subsequently overprinting the previous alteration facies (e.g. Robert and Brown, 1984). Under such a hypothesis, all rocks up to approximately 20 m from the main veins would have first undergone chlorite facies alteration. During a second hydrothermal event, wall rocks altered to the chlorite facies would be overprinted by the phlogopite-hematite facies up to 12 m from the main veins. During the final hydrothermal event the rocks immediately adjacent (up to 2 m) to the veins, previously altered to phlogopite-hematite facies, would be overprinted by the fuchsite-sericite-pyrite

Fig. 7.1. Schematic diagram summarizing the hydrothermal alteration for the feldspar porphyry unit from the upper levels of the eastern portion of the Lake Shore Mine. Increasing relative quantities are represented by changes from short dashed to solid lines. Blue lines = magmatic-hydrothermal alteration; black lines = hydrothermal alteration associated with main-stage veining; red lines = post-ore alteration. Alteration associated with the Lake Shore fault has been omitted.

HYDROTHERMAL ALTERATION FACIES DIAGRAM

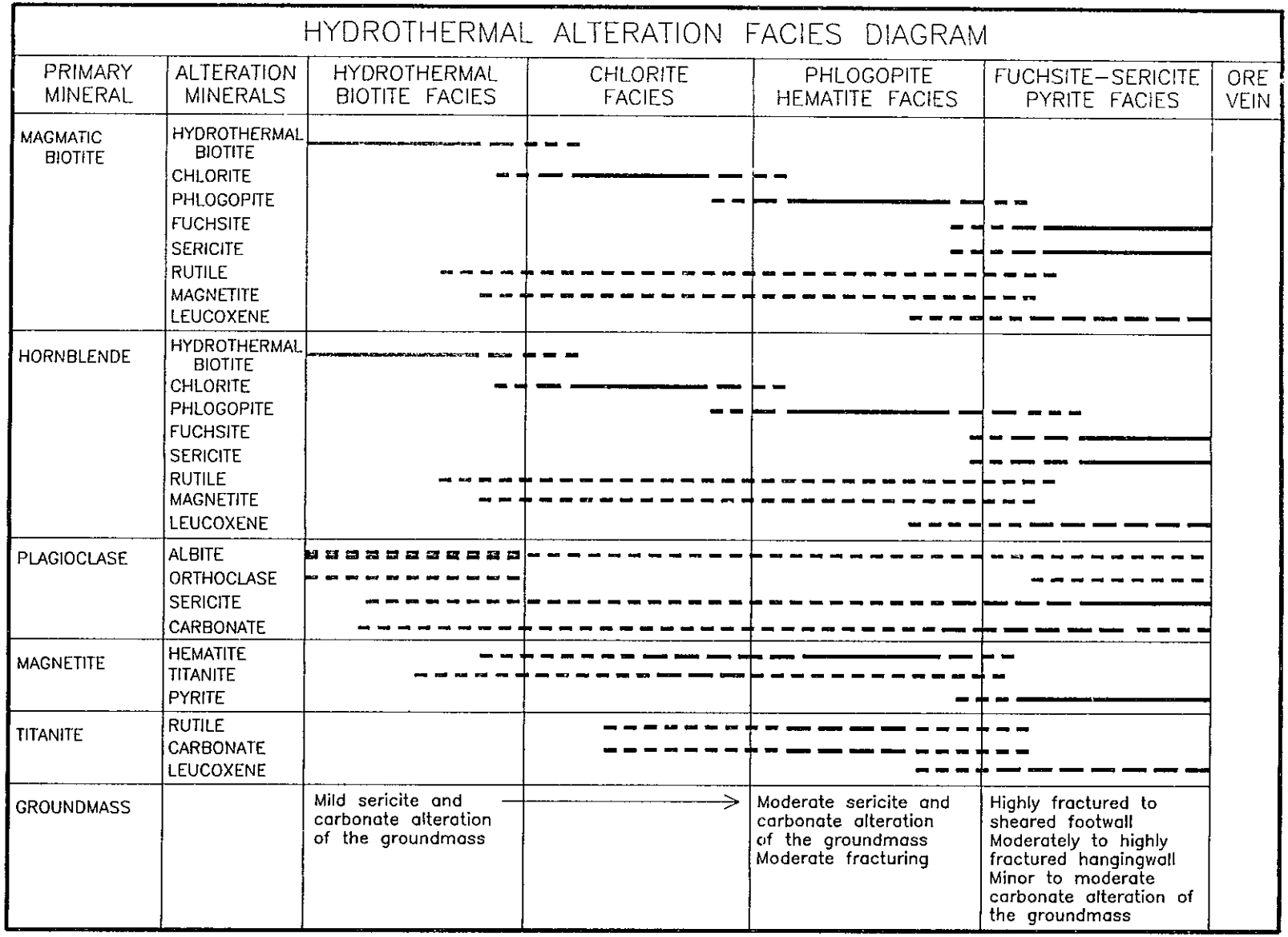

facies.

The occurrence of pyrite, the principal sulphide within the main veins, as well as the occurrence of Au within the fuchsite-sericite-pyrite facies (Hawley, 1950), suggests the hydrothermal event responsible for this alteration event to be responsible for Au mineralization. Deposition of quartz as the primary vein filling likely occurred during the earlier hydrothermal alteration events and may have resulted in partial silica sealing of the wall rocks, subsequently limiting the depth of penetration of each hydrothermal event. A similar theory has been put forward by Robert and Brown (1984) for the overprinting nature of cryptic and visible alteration zones at the Sigma mine in Val d'Or, Quebec. Sibson et al. (1988) have proposed a model in which high-angle reverse faults (such as the Kirkland Lake Main Break) act as fluid-activated fault-valves on hydrothermal reservoirs resulting in periodic discharges of hydrothermal fluid. Such discharges, if chemically distinct, may result in the production of distinct alteration zones such as observed at Lake Shore.

A second possible origin for the concentric nature for the hydrothermal alteration facies is that they resulted from a single fluid, which evolved as it penetrated and reacted with the surrounding wall rocks. The reaction of the fluid with various mineral constituents in the wall rocks would result in changes in fluid chemistry and therefore variations

in alteration products as the fluids migrated from the fault conduits into the wall rocks.

If such an hypothesis is correct, the rocks immediately adjacent to the veins would best reflect the parent chemistry of the hydrothermal fluids. Petrology and geochemistry of these rocks at Lake Shore indicate the fluids were enriched in K_2O, CO_2, and S, a common feature observed among many Au-quartz vein deposits. (eg. Golding and Wilson (1983), Roberts (1987), and Colvine et al. (1988)).

Decreasing amounts of sericite moving further into the wall rocks indicate decreasing activity for K_2O as it permeated the wall rocks. The occurrence of near-end member albite as overgrowths on albite-oligoclase phenocrysts, as well as its occurrence in quartz-carbonate microveinlets away from the veins, indicate increasing activity for Na_2O as the fluids migrated from the veins. These changes are consistent with the exchange of K_2O for Na_2O during sericite alteration of plagioclase in the fuchsite-sericite-pyrite facies. Similar trends are also observed for Fe_2O_3 and MgO. The alteration of biotite to chlorite to phlogopite to fuchsite/sericite indicates increasing activity of MgO away from the veins. While Fe released during the breakdown of biotite and/or chlorite is generally converted to magnetite, geochemical trends indicate the loss of some Fe during alteration.

Increasing carbonate content as the veins are approached indicates the fluids to be highly CO_2 charged. Continual

reaction between the host rocks and hydrothermal fluid decreased the activity of CO_2, and hence restricted carbonate development away from the veins.

The confinement of pyrite to the immediate wall rocks may also be explained by the fluid evolution process. As fluids permeated the first few metres of the wall rocks, sulphur would be removed from the fluid through the formation of pyrite at the expense of magnetite and/or hematite, leaving a sulphur-free fluid to react with the outer wall rocks. Although the increasing development of hematite towards the veins implies a highly oxidized environment, Cameron and Hattori (1987) have shown that pyrite may be stabilized in an oxidizing environment if the partial pressure of sulphur is high.

Alternatively, the confinement of pyrite to the immediate wall rocks may have been due to late introduction of sulphur. The occurrence of pyrite along vein fractures and slip surfaces implies a relatively late introduction. Such a theory is consistent with the aforementioned overprinting alteration patterns, whereby pyrite is deposited during a later hydrothermal event.

The successive change from biotite through chlorite and phlogopite to fuchsite or sericite developed in the facies, along with increasing degrees of carbonate, sericite, and hematite towards the main veins tend to support the evolution theory for hydrothermal alteration at Lake Shore. Furthermore,

if the first hypothesis is correct, the inner alteration zones (phlogopite-hematite and fuchsite-sericite-pyrite facies) should be observed encroaching on, or crosscutting, the outer zones (chlorite or hydrothermal biotite facies). This feature is never observed; however, it may be a function of the relatively simple mineralogy, both primary and secondary, as well as of the open framework of the micas and chlorite which has prevented the preservation of crosscutting textures. In addition, the development of Au and related sulphides along fractures within the quartz veins suggests multiple stages of hydrothermal activity.

The evidence presented in this study is inconclusive in determining the origin of the hydrothermal alteration facies, and hence Au mineralization, at the Lake Shore Deposit. Despite this, it has indicated a complex nature for hydrothermal activity that occurred at the Lake Shore deposit, as well as throughout the Kirkland Lake Au camp.

Chapter 8

Conclusions

1) Detailed petrography and geochemistry establish the feldspar porphyry unit of the Kirkland Lake intrusive complex predominantly as a quartz monzodiorite (IUGS classification). Previously this unit has been referred to as syenite porphyry. Minor deviations from typical fractionation trends as well as a subsolvus nature for the porphyry indicate that it is not comagmatic with the associated hypersolvus augite syenite and syenite.
2) Primary phenocryst mineralogy allows the division of the porphyry into four distinct phases including;
   - plagioclase-biotite porphyry
   - plagioclase-orthoclase ± biotite porphyry
   - plagioclase-hornblende-biotite porphyry
   - plagioclase-quartz ± orthoclase-biotite-hornblende porphyry

   Contact relationships among these four phases are

gradational as well as sharp. Their distribution within the intrusive complex is unknown at this time.

3) Miarolitic cavities within the porphyry indicate a relatively shallow level of emplacement and an H_2O-rich nature for the magma.

4) High temperature hydrothermal fluids released from the cooling porphyry phases resulted in subsequent alteration of the feldspar porphyry to the hydrothermal biotite facies. This alteration includes; i) the replacement and/or overgrowth of primary ferromagnesian by hydrothermal biotite, ii) the development of phenocrystic and fine-grained "sucrosic" hydrothermal biotite, iii) minor titanitization and hematitization of primary magnetite, iv) formation of albite and orthoclase on plagioclase rims, and v) the development of fine-grained barian-celestine within the groundmass, as inclusions in hydrothermal biotite, and within the altered plagioclase rims.

5) Magmatic biotite compositions indicate an fO_2 in the range of 10^{-12} - 10^{-8} bars during magma crystallization. Hydrothermal biotite compositions indicate a minimum fO2 of 10^{-8} bars.

6) Following the magmatic-hydrothermal event, the rocks in the vicinity of the auriferous veins were overprinted by alteration associated with auriferous hydrothermal activity. Three concentric alteration facies were formed

about the auriferous veins. The outermost facies, the chlorite facies, extends up to 12 to 20 m away from the vein system. Towards the veins, this facies grades into the phlogopite-hematite facies. Immediately adjacent to the veins, the rocks are altered to the fuchsite-sericite-pyrite facies.

7) Major element geochemical trends indicate gains in K_2O, CO_2, and S, with losses in Na_2O, Fe_2O_3, and MgO. K_2O and Na_2O are exchanged during sericitization of plagioclase. Marked losses of Sr and Ba indicate leaching of barian celestine during alteration to the phlogopite-hematite and fuchsite-sericite-pyrite facies. Increasing carbonate alteration and the development of pyrite in the wall rocks adjacent to the veins indicate the addition of CO_2 and S to the wall rocks.

8) The origin of the hydrothermal alteration facies is uncertain. Development of the facies may be the result of fluid evolution due to interaction with the wall rocks, or due to periodic hydrothermal events, each successively overprinting the earlier ones.

9) Detailed petrographic examination indicates that highly oxidized conditions were maintained throughout the emplacement and cooling of the Kirkland Lake intrusive complex. These conditions were further maintained during magmatic-hydrothermal activity while the intrusions cooled. The extensive development of hematite and presence

of turbid red feldspars indicate that these conditions were also achieved during post-magmatic auriferous hydrothermal activity.

10) Although the spatial relationships between Au deposits and felsic intrusions has received much attention in the past decade, crosscutting relationships indicate that the host Kirkland Lake intrusive complex was not the source of these fluids. However, related intrusions at depth may have provided the fluid and/or heat source required to drive the hydrothermal system.

References

Barker, F., 1979. Trondhjemites: definition, environment, and hypotheses of origin; p. 1-12 in Trondhjemites, Dacites, and Related Rocks, edited by F. Barker, Elsevier, Amsterdam, 659p.

Beane, R.E., and Titley, S.R., 1981. Porphyry copper deposits; part II, hydrothermal alteration and mineralization; Economic Geology, 75th Anniversary Volume, p. 235-269.

Burrows, A.G., and Hopkins, P.E., 1914. The Kirkland Lake and Swastika gold areas; Ontario Bureau of Mines, vol. 23, pt. 2.

_____, 1920. The Kirkland Lake gold area (second report); Ontario Department of Mines, vol. 29, pt.4, p. 1-48.

_____, 1923. Kirkland Lake gold area; Ontario Department of Mines, vol. 32, pt. 4, p. 1-52.

Cameron, E.M., and Carrigan, W.J., 1987. Oxygen fugacity of Archean felsic magmas: relationship to gold mineralization; Geological Survey of Canada, Paper 87-1A, p. 281-298.

Cameron, E.M., and Hattori, K., 1987. Archean gold mineralization and oxidized hydrothermal fluids; Economic Geology, vol. 82, p. 1177-1191.

Carmichael, I.S.E., and Nicholls, J., 1967. Iron-titanium oxides and oxygen fugacities in volcanic rocks; Journal of Geophysical Research, vol. 72, p. 4665-4687.

Cherry, M.E., 1983. The association of gold and felsic intrusions - examples from the Abitibi belt; p. 48-55, in the Geology of Gold in Ontario, edited by A.C. Colvine, Ontario Geological Survey, Miscellaneous Paper 110, 278p.

Charlewood, G.H., 1964. Geology and deep developments on the main ore zone at Kirkland Lake; Ontario Department of Mines, Geological Circular 11, 49p.

Colvine, A.C., Fyon, J.A., Heather, K.B., Marmont, S., Smith, P.M., and Troop, D.G., 1988. Archean lode gold deposits in Ontario; Ontario Geological Survey, Miscellaneous Paper 139, 136p.

Cooke, D.L., 1966. The Timiskaming volcanics and associated sediments of the Kirkland Lake area; unpublished Ph.D. thesis, University of Toronto, 147p.

Cooke, D.L., and Moorhouse, W.W., 1969. Timiskaming volcanism in the Kirkland Lake area, Ontario, Canada; Canadian Journal of Earth Science, vol. 6, p. 117-132.

Deer, W.A., Howie, R.A., and Zussman, J., 1963. Rock-Forming Minerals, vol. 2, Chain Silicates: London, Longmans, 379p.

Dimroth, E., Imreh, L., Goulet, N., and Rocheleau, M., 1983. Evolution of the south-central segment of the Archean Abitibi Belt, Quebec. Part II: Tectonic evolution and geomechanical model; Canadian Journal of Earth Science, vol. 20, p. 1355-1373.

Gallimore, N., 1988. Fluid inclusion geochemistry of hydrothermal solutions responsible for the Kirkland Lake gold deposits; unpublished B.Sc thesis, University of Ottawa, Ottawa, 79p.

Golding, S.D., and Wilson, A.F., 1983. Geochemical and stable isotope studies of the No. 4 lode, Kalgoorlie, Western Australia; Economic Geology, vol. 78, p. 438-450.

Goodwin, A.M., and Ridler, R.H., 1970. The Abitibi orogenic belt: in Symposium on Basins and Geosynclines of the Canadian Shield; Geological Survey of Canada, paper 70-40, p. 1-30.

Hattori, K., and Cameron, E.M., 1986. Archean magmatic sulphate; Nature, vol. 319, p. 45-47.

Hattori, K., and Levesque, G., 1989. Hydrothermal activity in the Kirkland Lake intrusive complex; p.59-67 in Geoscience Research Grant Program, Summary of Research 1988-1989, Ontario Geological Survey, Miscellaneous Paper 143, 189p.

Hawley, J.E., 1950. Mineralogy of the Kirkland Lake ores; p. 108-124 in geology of the main ore zone of Kirkland Lake. Ontario Department of Mines, annual report for 1948, vol. 57, pt. 5. 188p.

Hawthorne, F.C., 1983. The crystal chemistry of amphiboles; Canadian Mineralogist, vol. 21, p. 173-480.

Hewitt, D.F., 1963. The Timiskaming Series of the Kirkland Lake area; Canadian Mineralogist, vol. 7, p. 497-523.

Hodgson, C.J., 1982. Gold deposits of the Abitibi Belt, Ontario: p. 192-197 in Summary of Field Work by the Ontario Geological Survey, edited by John Wood, Owen I. White, R.B. Barlow, and A.C. Colvine, Ontario Geological Survey, Miscellaneous Paper 106, 235p.

_____, 1983. Preliminary report on the Timmins-Kirkland Lake area; Ontario Geological Survey Open File Report 5467, 197p.

Hodgson, C.J., Hamilton, J.V., and Guimond, R.P., In press. Final Report, Grant 227 relationship between gold deposits and the tectonic framework of the Abitibi Greenstone Belt in the Kirkland Lake-Larder Lake area; Ontario Geological Survey, Open File Report.

Hodgson, C.J., and MacGeehan, P.J., 1982. A review of the geological characteristics of "gold only" deposits in the Superior Province of the Canadian Shield; Canadian Institute Mining and Metallurgy, Special Volume 24, p. 211-229.

Hopkins, H., 1946. Geology of the gold mines of Kirkland Lake; unpublished report, Ministry of Northern Development and Mines.

Hubert, C., Trudel, P., and Gélinas, L., 1984. Archean wrench fault tectonics and structural evolution of the Blake River Group, Abitibi Belt, Quebec; Canadian Journal of Earth Science, vol. 21, p. 1024-1032.

Hyde, R.S., 1978. Sedimentology, volcanology, stratigraphy and tectonic setting of the Archean Timiskaming Group, Abitibi Greenstone Belt, northeastern Ontario, Canada; unpublished Ph.D. thesis, McMaster University, Hamilton, 422p.

_____, 1980. Sedimentary facies in the Archean Timiskaming Group and their tectonic implications, Abitibi Greenstone Belt, northeastern Ontario, Canada; Precambrian Research, vol. 12, p. 161-195.

Hyde, R.S., and Walker, R.G., 1977. Sedimentary environments and the evolution of the Archean Greenstone Belt in the Kirkland Lake area, Ontario; Geological Survey of Canada, Paper 77-1A, p. 185-190.

Jacobs, D.C., and Parry, W.T., 1976. A comparison of the geochemistry of biotite from some basin and range stocks; Economic Geology, vol. 71, p. 1029-1035.

Jahns, R.H., and Burnham, W.C., 1969. Experimental studies of pegmatite genesis: I. a model for the derivation and crystallization of granitic pegmatites; Economic Geology, vol. 64, p. 843-864.

Jambor, J.L., 1976. Geology and hydrothermal alteration at the Maggie porphyry copper-molybdenum deposit, south central, British Columbia; Geological Survey of Canada, paper 75-17, 41p.

Jensen, L.S., 1976. Regional stratigraphy and structure of the Timmins-Kirkland Lake area, districts of Cochrane and Timiskaming and the Kirkland Lake-Larder Lake area, district of Timiskaming; p. 82-95, in Summary of Field Work, 1976, edited by V.G. Milne, K.D. Card, and J.A. Robertson, Ontario Geological Survey, Miscellaneous Paper 67, 183p.

_____, 1978. Regional stratigraphy and structure of the Timmins-Kirkland Lake area, districts of Cochrane and Timiskaming and Kirkland Lake area, district of Timiskaming; p. 67-72, in Summary of Field Work, 1978, edited by V.G. Milne, O.L. White, R.B. Barlow, and J.A. Robertson, Ontario Geological Survey, Miscellaneous Paper 82, 235p.

_____, 1980. Kirkland Lake-Larder Lake synoptic mapping project, districts of Cochrane and Timiskaming; p. 55-60, in Summary of Field Work, 1980, edited by V.G. Milne, O.L. White, R.B. Barlow, J.A. Robertson, and A.C. Colvine, Ontario Geological Survey, Miscellaneous Paper 96, 201p.

_____, 1981. Archean gold mineralization in the Kirkland Lake-Larder Lake area; p. 59-65, in Genesis of Archean, Volcanic Hosted Gold Deposits, symposium held at the University of Waterloo, March 7, 1980, edited by R.G. Roberts, and E.G. Pye, Ontario Geological Survey, Miscellaneous Paper 97, 175p.

Jensen, L.S., and Langford, F.F., 1985. Geology and petrogenesis of the Archean Abitibi Belt in the Kirkland Lake area, Ontario; Ontario Geological Survey, Miscellaneous Paper 123, 130p.

Jolly, W.T., 1974. Regional metamorphic zonation as an aid in the study of Archean terrains; Abitibi region, Ontario; Canadian Mineralogist, vol. 12, p. 499-508.

_____, 1978. Metamorphic history of the Archean Abitibi Belt, in metamorphism of the Canadian Shield. Geological Survey of Canada Paper 78-10, p. 63-78.

Kerrich, R., and Watson, G.P., 1984. The Macassa mine Archean lode gold deposit, Kirkland Lake, Ontario: geology, patterns of alteration, and hydrothermal regimes; Economic Geology vol. 79, p. 1104-1130.

Malinin, S.D., and Urusov, U.S., 1983. The experimental and theoretical data on isomorphism in the $(BaSr)SO_4$ system in relation to barite formation; Geochemistry International, vol. 20(5), p. 70-80.

Marmont, S., and Corfu, F., 1988a. Timing of gold introduction in the late Archean tectonic framework of the Canadian Shield: evidence from U-Pb zircon geochronology of the Abitibi sub-province; p. 45-50 in Bicentennial Gold 88, extended abstracts and oral program, Geological Society of Australia, no 22.

Marmont, S., and Corfu, F., 1988b. Timing of volcanism, plutonism, and gold introduction: evidence from U-Pb zircon geochronology of the Abitibi greenstone belt, Ontario; p. 3 in, program with abstracts, Ontario Geoscience Research Seminar, Ontario Geological Survey.

Mason, D.R., 1978. Compositional variations in ferromagnesian minerals from porphyry copper-generating and barren intrusions of the western highlands, Papua New Guinea; Economic Geology, vol. 73, p. 878-890.

McInnes, B.I., 1985. Ore petrology and wall rock alteration studies at the Lake Shore gold mine, Kirkland Lake, Ontario; unpublished B.Sc. thesis, McMaster University, Hamilton, 131p.

Nunes, P.D., and Jensen, L.S., 1980. Geochronology of the Abitibi metavolcanic belt, Kirkland Lake area - progress report; p. 40-45 in Summary of Geochronology Studies 1977-1979, edited by E.G. Pye, Ontario Geological Survey, Miscellaneous Paper 92, 45p.

O'Connor, J.T., 1965. A classification for quartz-rich igneous rocks based on feldspar ratios; p. B79-B84 in Geological Survey Research 1965, U.S. Geological Survey, Professional Paper 525-B, 195p.

Ploeger, F.R., 1980. Kirkland Lake gold study, district of Timiskaming, p. 188-190, in Summary of Field Work, 1980, by the Ontario Geological Survey, edited by V.G. Milne, R.B. Barlow, J.A. Robertson, and A.C. Colvine, Ontario Geological Survey, Miscellaneous Paper 96, 201p.

Ploeger, F.R., and Crocket, J.H., 1982. Relationships of gold to syenitic intrusive rocks in Kirkland Lake; p. 69-72 in Geology of Canadian Gold Deposits, Canadian Institute Mining and Metallurgy Special Volume 24, 286p.

Pyke, D.R., 1981. Relationship of gold mineralization to stratigraphy and structure in Timmins and surrounding area; p. 1-15, in Genesis of Archean, Volcanic-Hosted Gold Deposits, symposium held at the University of Waterloo, March 7, 1980, edited by V.G. Milne, O.L. White, R.B. Barlow and J.A. Robertson, Ontario Geological Survey, Miscellaneous Paper 82, 235p.

Pyke, D.R., and Jensen, L.S., 1976. Preliminary stratigraphic interpretation of the Timmins-Kirkland Lake area, Ontario; program with abstracts, Geological Association of Canada, vol. 1, p71.

Ridler, R.H., 1970. Relationship of mineralization to volcanic stratigraphy in the Kirkland Lake-Larder Lake areas, Ontario; proceedings, Geological Association of Canada, vol. 21, p. 33-42.

Ridler, R.H., 1976. Stratigraphic keys to the gold metallogeny of the Abitibi belt; Canadian Mining Journal, vol. 97, No. 3, p. 81-87.

Robert, F., and Brown, A.C., 1984. Progressive alteration associated with gold-quartz-tourmaline veins at the Sigma Mine, Abitibi Greenstone Belt, Quebec; Economic Geology, vol. 79, p. 393-399.

Robert, F., and Brown, A.C., 1986. Archean gold-bearing quartz veins at the Sigma mine, Abitibi Greenstone Belt, Quebec: part II. vein paragenesis and hydrothermal alteration; Economic Geology, vol. 81, p. 593-616.

Roberts, R.G., 1987. Ore deposits model #11: Archean lode gold deposits; Geoscience Canada, vol. 14, no. 4, Geological Association of Canada, p. 37-52.

Rowins, S.M., Lalonde, A.E., and Cameron, E.M., 1989. Geology of the Murdock Creek intrusion, Kirkland Lake, Ontario; in Current Research, Part C, Geological Survey of Canada, Paper 89-1C, p. 313-323.

Streckeisen, A., 1973. Plutonic rocks: clasc ification and nomenclature recommended by the IUGS subcommission on the systematics of igneous rocks; Geotimes, vol. 18, no. 10, p. 26-30.

Sibson, R.H., Robert, F., and Poulsen, K.H., 1988. High-angle reverse faults, fluid-pressure cycling, and mesothermal gold-quartz deposits; Geology, vol. 16, p. 551-555.

Size, W.B., 1972. Petrology of the Red Hill syenitic complex, New Hampshire; Geological Society of America Bulletin, vol. 83, p. 3747-3760.

Theriault, R., 1988. A study of gold mineralization at the Lake Shore gold mine, Kirkland Lake, Ontario; unpublished B.Sc. thesis, University of Ottawa, Ottawa, 83p.

Thomson, J.E., 1946. The Keewatin-Timiskaming unconformity in the Kirkland Lake district; Transactions of the Royal Society of Canada, Ser. 3, vol. 40, p. 113-124.

_____, 1950. Geology of Teck township and Kenogami Lake area, Kirkland Lake gold belt; Ontario Department of Mines, vol. 57, pt. 5, p. 1-53.

Thomson, J.E., Charlewood, G.H., Griffin, K., Hawley, J.E., Hopkins, H., MacIntosh, C.G., Ogrizio, S.P., Perry, O.S. and Ward, W., 1950. Geology of the main ore zone at Kirkland Lake; Ontario Department of Mines, vol. 57, pt. 5, p. 54-196.

Todd, E.W., 1928. Kirkland Lake gold area; Ontario Department of Mines, vol. 37, pt. 2.

Toogood, D., and Hodgson, C.J., 1985. Grant 227 A structural investigation between the Kirkland Lake and Larder Lake gold camps; p. 200-205, in Geoscience Research Grant Program, Summary of Research 1984-1985, edited by V.G. Milne, Ontario Geological Survey, Miscellaneous Paper 127, 246p.

_____, 1986. Grant 227 Relationship between gold and the tectonic framework of the Abitibi Greenstone Belt in the Kirkland Lake-Larder Lake area; p. 89-86, in Geoscience Research Grant Program, Summary of Research 1985-1986, edited by V.G. Milne, Ontario Geological Survey, Miscellaneous Paper 130, 235p.

Tyrrell, J.B., and Hore, R.E., 1926. The Kirkland Lake fault; Transactions of the Royal Society of Canada, 3rd series, vol. 20, pt. 1 section 4.

Watson, G.P., 1984. Ore types and fluid regimes: Macassa gold mine, Kirkland Lake; unpublished Ph.D. thesis, University of Western Ontario, London, 341p.

Wilson, A.D., 1960. A modified scheme for the determination of ferrous iron in rocks; Analyst, vol. 85, p. 823-827.

Wilson, D.B., Andrews, P., Moxham, R.L., and Ramel, K., 1965. Archean volcanism in the Canadian Shield; Canadian Journal of Earth Science, vol. 2, p. 161-175.

Wones, D.R., and Eugster, H.P., Stability of biotite: experiment, theory and application; American Mineralogist, vol. 50, p. 1228-1272.

APPENDIX I

Whole Rock Chemical Compositions

Analytical Methods

Whole rock analyses were completed at the University of Ottawa, Department of Geology, and by Technical Service Laboratories, Mississauga, Ontario.

Analyses completed at the University of Ottawa were carried out using X-ray fluorescence techniques. Powdered samples were fused into glass disks combining 1.300 g of sample with 0.433 g of lithium carbonate and 3.900 g of lithium tetraborate. All sample disks were analyzed once using a Phillips PW 1410 Automated X-Ray Fluorescence Spectrometer. Relative instrument precision for each element is listed in Table A1.1. FeO was determined by titration techniques using metavanadate (Wilson, 1960).

Analyses completed by Technical Service Laboratories were carried out using Inductive Coupled Argon Plasma (ICAP) techniques. Samples were prepared by fusing 0.2 g of sample with 1 g of lithium metaborate flux in graphite crucibles at 1000°C for 20 minutes and dissolving the molten bead in 100 ml of nitric acid. All samples were analyzed once. Detection limits for all major elements are reported to be 0.01% except Na (0.05%). Detection limits for trace elements are 5 ppm.

CIPW normative values were calculated with the aid of an IBM compatible PC system utilizing the Geochemical Program Package (GPP), version 2.0. For samples in which FeO was not determined, FeO/Fe_2O_3 ratios were averaged and extrapolated from similar rock units for which FeO was determined.

Table A1.1 Precision of X-Ray Fluorescence Analyses

Major Elements (values in relative percent)

	Concentration Range					
Element	.1 - 1.	.1 - 2.	1. - 3.	2. - 5.	1. - 20	50 - 100
% SiO2						±1.25
Al2O3	±10		±1.5	±1.5	±1.5	
Fe2O3	± 5.0				±2.0	
MgO	±25				±3.0	
CaO	± 5.0				±2.0	
Na2O		±15		±8.0		
K2O	± 2.0				±1.0	
TiO2	± 2.0		±1.0			
P2O5	±10		±1.0			
MnO	±10					
S	±10					

Trace elements (values in ppm)

	<10	10 - 30	>30
ppm Ba	<10	±50	±10
Cr	<10	±50	±10
Zr	<10	±50	±10
Sr	<10	±50	±10
Rb	<10	±50	±10
Y	<10	±50	±10
Zn	<10	±50	±10
Ni	<10	±50	±10

Table A1.2

Whole Rock Chemical Compositions and CIPW Norms for the Kirkland Lake Intrusive Complex

	009	014	015	016	017	018	019	020	026	027
% SiO2	48.45	65.38	51.93	51.09	60.32	62.03	61.61	64.52	61.80	58.32
Al2O3	15.63	14.57	14.51	13.60	13.93	14.16	14.44	14.84	14.42	13.29
Fe2O3	5.39	2.02	3.22	4.20	1.72	1.52	2.00	1.27	1.23	3.21
FeO*	7.30	1.79	3.78	4.72	2.24	2.29	2.54	1.96	1.73	n.d.
MgO	6.98	2.03	5.07	6.77	2.99	3.11	2.59	1.59	2.41	2.93
CaO	5.91	2.08	5.75	5.86	4.32	3.39	3.67	2.69	3.36	5.23
Na2O	1.84	5.53	3.92	3.35	4.67	4.76	5.45	5.70	4.64	2.75
K2O	3.55	3.13	5.49	5.36	3.92	4.12	3.06	2.67	3.00	3.82
TiO2	0.96	0.42	0.70	0.87	0.41	0.39	0.48	0.32	0.40	0.38
P2O5	0.02	0.21	0.51	0.79	0.36	0.39	0.32	0.21	0.36	0.37
MnO	0.22	0.05	0.12	0.15	0.07	0.07	0.08	0.07	0.07	0.10
S	0.03	0.06	0.06	0.04	0.04	0.05	0.04	0.11	0.05	0.06
LOI	2.82	2.44	3.55	3.04	3.56	2.75	3.41	2.75	5.25	7.70
ppm Ba	1844	1996	1772	1871	2415	2409	1984	2581	948	2230
Cr	204	87	188	272	186	177	136	93	156	160
Zr	92	163	197	156	185	196	182	268	180	168
Sr	1209	747	1130	1058	1538	1738	1168	5623	570	654
Rb	158	62	182	205	113	126	78	70	118	163
Y	23	19	24	23	19	19	25	14	21	20
Zn	83	72	72	94	63	60	66	56	46	53
Ni	101	68	29	57	87	62	38	16	37	52
V	300	44	155	205	83	66	59	31	81	72
% total	99.60	100.09	99.05	100.30	99.11	99.60	100.14	99.73	98.99	98.57

CIPW Norms										
Ap	0.04	0.47	1.18	1.80	0.83	0.89	0.73	0.48	0.85	0.90
Il	1.90	0.82	1.40	1.72	0.82	0.77	0.95	0.64	0.81	0.80
Mt	8.14	3.02	4.93	6.31	2.63	2.30	3.02	1.93	1.92	1.55
Or	21.79	19.02	34.14	32.73	24.39	25.30	18.79	16.46	18.98	24.90
Ab	16.18	48.14	22.95	21.87	41.62	41.87	47.92	50.33	42.04	25.67
An	24.83	5.85	6.08	6.45	5.76	5.30	6.13	7.33	10.34	13.95
Di	4.45	2.66	16.34	14.57	11.48	7.65	8.55	4.21	3.99	9.72
Hy	19.27	4.98			4.63	6.92	5.06	4.33	6.26	7.05
Ol	3.40		6.50	10.53						
Ne			6.48	4.02						
C										
Q		15.02			7.83	9.00	8.85	14.31	14.81	15.46
Hm										
Wo										
% Totals	100.00	100.00	100.00	100.00	100.00	100.00	100.00	100.00	100.00	100.00

n.d. not determined
* FeO determined by metavanadate titration
# Analyses by Induced Coupled Plasma (ICP)
009 - Diabase - pervasive sericite, mild carbonate alteration
014 - Feldspar porphyry - hydrothermal biotite facies
015 - Augite syenite - moderate actinolite, sericite and carbonate alteration
016 - Augite syenite - mild actinolite, sericite and carbonate alteration
017 - Feldspar porphyry - hydrothermal biotite facies
018 - Feldspar porphyry - hydrothermal biotite facies
019 - Feldspar porphyry - hydrothermal biotite facies
020 - Feldspar porphyry - chlorite facies
026 - Feldspar porphyry - phlogopite-hematite facies
027 - Feldspar porphyry - phlogopite-hematite facies

Table A1.2

Whole Rock Chemical Compositions and CIPW Norms for the Kirkland Lake Intrusive Complex

	028	029	030	031	032	033	034	035	036#	037#
% SiO2	62.57	64.35	63.93	63.99	62.12	61.62	61.96	67.28	87.77	77.85
Al2O3	13.71	14.49	14.57	14.43	13.98	14.63	14.36	11.90	3.84	10.85
Fe2O3	1.10	3.23	3.55	1.31	3.40	3.27	3.87	2.67	1.59	3.56
FeO*	2.00	n.d.	n.d.	1.67	n.d.	n.d.	n.d.	n.d.	n.d.	n.d.
MgO	1.73	1.55	1.80	1.66	2.41	2.05	2.07	1.70	0.37	0.75
CaO	3.17	2.75	2.33	2.67	3.37	2.83	2.84	3.09	2.48	0.28
Na2O	4.31	5.34	5.32	4.50	4.53	4.56	3.21	4.12	0.03	0.03
K2O	3.13	3.19	3.13	3.37	3.26	3.46	4.64	3.20	1.26	3.95
TiO2	0.30	0.30	0.31	0.29	0.31	0.34	0.33	0.24	0.09	0.30
P2O5	0.20	0.18	0.21	0.19	0.16	0.21	0.18	0.14	0.04	0.09
MnO	0.08	0.06	0.07	0.08	0.09	0.08	0.07	0.09	0.03	0.01
S	0.09	0.07	0.04	0.08	0.05	0.07	0.05	0.06	n.d.	n.d.
LOI	5.83	3.58	3.36	4.18	5.10	4.62	5.27	4.50	2.01	3.07
ppm Ba	2741	3279	2428	1429	1347	1623	1946	1870	1018	890
Cr	89	94	110	93	191	131	121	85		
Zr	147	161	158	150	146	156	150	111	28	104
Sr	849	1032	860	656	612	645	404	585	304	134
Rb	94	92	78	99	104	108	162	87		
Y	18	17	19	16	17	20	17	12		
Zn	37	42	54	43	43	52	37	23		
Ni	12	16	21	12	44	27	16	10		
V	44	38	45	39	45	60	100	44		
% total	98.68	99.64	99.07	98.71	99.09	98.07	99.20	99.31	99.71	100.87

CIPW Norms								
Ap	0.48	0.41	0.48	0.45	0.37	0.49	0.43	0.33
Il	0.62	0.60	0.62	0.58	0.63	0.70	0.68	0.49
Mt	1.73	1.47	1.62	2.02	1.58	1.53	1.09	0.16
Or	20.03	19.70	19.37	21.14	20.51	21.91	29.42	20.07
Ab	39.51	47.22	47.15	40.44	40.82	41.36	29.15	37.01
An	9.56	6.42	6.94	9.79	8.72	9.90	11.88	4.80
Di	4.94	5.46	3.07	2.39	6.52	3.02	1.63	8.68
Hy	4.89	4.92	7.17	4.99	7.12	7.68	9.25	4.38
Ol								
Ne								
C								
Q	18.24	13.80	13.58	18.19	13.73	13.41	16.48	24.08
Hm								
Wo								
% Totals	100.00	100.00	100.00	100.00	100.00	100.00	100.00	100.00

n.d. not determined
* FeO determined by metavanadate titration
# Analyses by Induced Coupled Plasma (ICP)
028 - Feldspar porphyry - phlogopite-hematite facies
029 - Feldspar porphyry - chlorite facies
030 - Feldspar porphyry - chlorite to phlogopite-hematite facies
031 - Feldspar porphyry - phlogopite-hematite facies
032 - Feldspar porphyry - phlogopite-hematite to fuchsite-sericite-pyrite facies
033 - Feldspar porphyry - phlogopite-hematite facies
034 - Feldspar porphyry - fuchsite-sericite-pyrite facies
035 - Feldspar porphyry - fuchsite-sericite-pyrite facies
036 - North Vein
037 - North Vein

Table A1.2

Whole Rock Chemical Compositions and CIPW Norms for the Kirkland Lake Intrusive Complex

	038#	039	040	041	042#	043	044	060	082	083
% SiO2	82.99	64.54	65.68	64.38	74.61	62.02	61.58	62.52	63.86	64.12
Al2C3	7.35	13.66	14.80	14.53	10.33	17.19	13.50	14.76	14.13	14.55
Fe2O3	4.70	2.95	0.84	0.74	2.36	3.73	3.79	3.41	1.45	1.44
FeO*	n.d.	n.d.	1.88	2.11	n.d.	n.d.	n.d.	n.d.	1.47	1.72
MgO	0.61	1.54	1.51	1.49	1.08	1.81	1.52	2.14	1.57	1.70
CaO	0.26	3.00	2.42	3.21	2.24	1.17	5.55	2.79	2.87	2.70
Na2O	0.01	3.89	4.94	4.42	1.86	4.42	4.77	4.01	4.86	5.22
K2O	2.62	3.11	3.07	3.30	4.07	4.55	2.94	4.03	3.37	2.90
TiO2	0.64	0.29	0.30	0.31	0.23	0.42	0.27	0.46	0.30	0.32
P2O5	0.05	0.16	0.20	0.20	0.13	0.23	0.12	0.21	0.19	0.21
MnO	0.01	0.05	0.04	0.06	0.04	0.03	0.09	0.07	0.08	0.06
S	n.d.	0.09	0.04	0.03	n.d.	0.06	0.04	0.08	0.08	0.11
LOI	1.27	3.30	2.64	3.30	2.43	2.65	5.03	4.81	4.91	2.93
ppm Ba	1047	3057	2436	1621	1007	1405	2262	1212	2404	3199
Cr		98	85	109		115	87	92	83	116
Zr	62	152	161	161	213	167	158	148	191	260
Sr	128	985	981	996	534	594	1073	537	2544	5666
Rb		82	79	87		186	67	131	85	75
Y		15	13	19		23	17	17	18	16
Zn		62	50	65		60	63	49	39	59
Ni		15	16	15		30	17	22	16	14
V		41	30	43		81	42	92	31	45
% total	100.66	97.11	98.81	98.45	99.58	98.59	99.64	99.54	99.77	99.08

CIPW Norms								
Ap	0.38	0.46	0.46	0.52	0.27	0.49	0.45	0.48
Il	0.59	0.60	0.62	0.84	0.52	0.92	0.61	0.64
Mt	1.37	1.28	1.14	1.70	1.69	1.57	2.24	2.20
Or	19.67	18.96	20.58	28.05	17.74	25.15	21.14	18.04
Ab	35.23	43.69	39.47	39.03	41.23	35.86	43.67	46.52
An	11.37	9.55	10.62	4.49	6.89	10.96	7.21	8.12
Di	2.83	1.33	3.96		16.43	1.81	5.29	3.67
Hy	6.03	5.72	4.99	8.62	3.51	8.33	2.86	4.33
Ol								
Ne								
C				3.57				
Q	22.52	18.42	18.16	13.19	11.43	14.92	16.54	16.00
Hm					0.29			
Wo								
% Totals	100.00	100.00	100.00	100.00	100.00	100.00	100.00	100.00

n.d. not determined
* FeO determined by metavanadate titration
# Analyses by Induced Coupled Plasma (ICP)
038 - North Vein
039 - Feldspar porphyry - phlogopite-hematite facies
040 - Feldspar porphyry - phlogopite-hematite facies
041 - Feldspar porphyry - phlogopite-hematite facies
042 - Feldspar porphyry - fuchsite-sericite-pyrite facies - silicified inclusion in the North Vein
043 - Feldspar porphyry - phlogopite-hematite facies
044 - Feldspar porphyry - chlorite to phlogopite-hematite facies
060 - Feldspar porphyry - phlogopite-hematite facies
082 - Feldspar porphyry - chlorite facies
083 - Feldspar porphyry - chlorite facies

Table A1.2

Whole Rock Chemical Compositions and CIPW Norms for the Kirkland Lake Intrusive Complex

	084	085	087	088	089	090	091	092	093	094
% SiO2	59.47	64.21	63.63	62.98	63.85	61.39	64.94	64.29	64.54	64.93
Al2O3	13.64	11.97	14.45	14.45	14.36	13.88	13.94	14.83	14.44	15.04
Fe2O3	4.72	2.71	0.81	1.29	1.75	2.98	3.34	1.25	0.25	0.54
FeO*	n.d.	n.d.	2.03	2.40	1.55	n.d.	n.d.	1.77	2.46	2.16
MgO	3.22	1.78	1.69	1.72	1.48	1.97	1.27	1.57	1.51	1.38
CaO	3.84	3.92	3.68	3.64	3.00	5.05	4.05	3.00	2.98	2.31
Na2O	5.06	3.32	4.82	5.50	4.71	5.44	3.82	5.02	5.37	5.14
K2O	2.38	4.31	3.55	2.56	3.33	2.03	2.74	3.38	3.10	3.64
TiO2	0.39	0.24	0.33	0.38	0.37	0.29	0.33	0.33	0.30	0.31
P2O5	0.32	0.18	0.16	0.30	0.20	0.17	0.15	0.18	0.23	0.22
MnO	0.08	0.09	0.07	0.09	0.08	0.11	0.05	0.07	0.07	0.05
S	0.20	0.04	0.07	0.04	0.08	0.06	0.06	0.08	0.05	0.05
LOI	4.21	5.52	4.73	4.05	4.42	6.52	4.65	4.48	4.36	3.57
ppm Ba	4458	2362	1880	2286	2416	1854	2501	2721	1889	2900
Cr	115	87	110	108	81	94	61	90	83	86
Zr	283	119	165	176	149	150	173	169	162	170
Sr	7220	507	732	905	574	554	1958	675	523	558
Rb	52	92	117	70	108	72	110	110	83	97
Y	11	16	18	18	19	19	24	18	17	18
Zn	77	40	56	63	40	69	61	41	42	51
Ni	47	4	27	35	15	27	18	18	16	10
V	62	53	42	45	46	28	39	44	29	44
% total	98.98	98.67	100.38	99.82	99.58	100.22	99.93	100.71	99.99	99.81

CIPW Norms										
Ap	0.75	0.43	0.37	0.69	0.46	0.40	0.35	0.42	0.54	0.50
Il	0.79	0.50	0.66	0.76	0.74	0.59	0.67	0.66	0.60	0.62
Mt	2.20	1.27	1.24	1.97	2.68	1.39	1.53	1.90	0.38	0.81
Or	15.04	27.39	22.02	15.87	20.78	12.82	17.06	20.87	19.23	22.47
Ab	45.81	30.21	42.83	48.84	42.09	49.20	34.06	44.39	47.71	45.45
An	8.00	5.41	7.68	7.53	8.67	7.97	13.48	8.31	6.45	7.54
Di	8.29	11.66	8.50	7.66	4.53	14.41	5.54	4.87	6.23	2.42
Hy	9.96	2.28	3.06	3.78	2.73	1.68	4.26	3.62	5.01	5.63
Ol										
Ne										
C										
Q	9.15	20.85	13.65	12.91	17.31	11.54	23.06	14.97	13.87	14.57
Hm										
Wo										
% Totals	100.00	100.00	100.00	100.00	100.00	100.00	100.00	100.00	100.00	100.00

n.d. not determined
* FeO determined by metavanadate titration
# Analyses by Induced Coupled Plasma (ICP)
084 - Feldspar porphyry - hydrothermal biotite facies
085 - Feldspar porphyry - phlogopite-hematite facies
087 - Feldspar porphyry - phlogopite-hematite facies
088 - Feldspar porphyry - chlorite facies
089 - Feldspar porphyry - chlorite facies
090 - Feldspar porphyry - phlogopite-hematite facies
091 - Feldspar porphyry - chlorite to phlogopite-hematite facies
092 - Feldspar porphyry - phlogopite-hematite facies
093 - Feldspar porphyry - phlogopite-hematite facies
094 - Feldspar porphyry - phlogopite-hematite facies

Table A1.2

Whole Rock Chemical Compositions and CIPW Norms for the Kirkland Lake Intrusive Complex

	095	096	100	101	105	106#	107#	108#	109#	110
% SiO2	59.02	64.00	48.76	45.84	65.22	91.44	77.98	91.99	86.10	63.13
Al2O3	14.17	14.59	13.29	15.49	16.91	2.95	11.18	1.98	4.95	16.11
Fe2O3	4.62	3.13	3.78	4.46	2.90	1.08	2.38	0.98	1.56	3.12
FeO*	n.d.	n.d.	9.47	9.58	n.d.	n.d.	n.d.	n.d.	n.d.	n.d.
MgO	3.21	1.60	7.37	8.61	1.34	0.35	0.65	0.25	0.65	1.86
CaO	4.17	3.18	5.82	6.07	1.41	0.39	0.31	0.27	1.41	2.40
Na2O	4.46	4.88	3.35	3.27	0.00	0.14	0.05	0.02	0.02	0.00
K2O	2.83	3.46	1.21	1.69	6.20	1.01	4.00	0.75	1.61	5.88
TiO2	0.50	0.31	1.35	1.04	0.35	0.05	0.21	0.04	0.10	0.33
P2O5	0.44	0.21	0.12	0.08	0.27	0.05	0.11	0.06	0.06	0.20
MnO	0.09	0.08	0.19	0.23	0.03	0.02	0.01	0.01	0.03	0.06
S	0.07	0.04	0.04	0.03	0.12	n.d.	n.d.	n.d.	n.d.	0.06
LOI	6.71	4.61	4.44	3.14	4.05	1.37	2.72	1.25	2.52	5.38
ppm Ba	2225	2492	559	1064	856	4742	817	629	1179	801
Cr	196	100	90	133	96	n.d.	n.d.	n.d.	n.d.	105
Zr	209	167	106	99	165	115	166	23	51	163
Sr	396	751	460	1501	138	348	120	180	12267	190
Rb	99	107	38	42	224	n.d.	n.d.	n.d.	n.d.	235
Y	23	18	34	27	24	n.d.	n.d.	n.d.	n.d.	19
Zn	76	42	100	115	62	n.d.	n.d.	n.d.	n.d.	55
Ni	67	39	49	116	15	n.d.	n.d.	n.d.	n.d.	19
V	93	50	360	295	91	n.d.	n.d.	n.d.	n.d.	66
% total	100.69	100.53	99.44	99.95	99.00	99.44	99.72	97.69	100.60	98.74

CIPW Norms							
Ap	1.03	0.48	0.27	0.19	0.61		0.47
Il	1.02	0.61	2.71	2.05	0.70		0.68
Mt	2.15	1.41	5.80	6.72	4.17		2.13
Or	17.82	26.67	7.55	10.35	38.02		37.38
Ab	40.22	42.75	29.93	26.50			
An	10.96	5.21	18.64	23.43	5.43		11.41
Di	6.54	8.00	9.02	5.91			
Hy	10.44	3.64	20.76		3.46		6.43
Ol			5.32	23.66			
Ne				1.18			
C					8.61		6.32
Q	9.83	11.22			38.87		35.18
Hm					0.13		
Wo							
% Totals	100.00	100.00	100.00	100.00	100.00		100.00

n.d. not determined
* FeO determined by metavanadate titration
# Analyses by Induced Coupled Plasma (ICP)
095 - Feldspar porphyry - phlogopite-hematite facies
096 - Feldspar porphyry - phlogopite-hematite facies
100 - Diabase - moderate sericite, mild carbonate alteration
101 - Diabase - moderate sericite, mild carbonate alteration
105 - Feldspar porphyry - fuchsite-sericite-pyrite facies
106 - North Vein
107 - North Vein
108 - North Vein
109 - North Vein
110 - Feldspar porphyry - fuchsite-sericite-pyrite facies

Table A1.2

Whole Rock Chemical Compositions and CIPW Norms for the Kirkland Lake Intrusive Complex

	111	112	115	116	117	118	119	120	121	122
% SiO2	63.19	62.50	50.19	49.92	50.78	65.74	67.13	64.17	66.34	63.70
Al2O3	15.27	15.57	13.56	12.69	12.84	14.56	15.31	13.45	13.45	14.28
Fe2O3	3.24	3.41	3.14	3.50	3.96	2.18	1.13	1.36	1.12	1.03
FeO*	n.d.	n.d.	5.16	5.48	5.55	n.d.	1.11	2.18	1.57	1.83
MgO	1.87	1.86	5.79	6.61	7.07	1.15	1.34	1.83	2.12	1.98
CaO	3.09	2.82	5.68	8.17	7.54	2.60	1.94	3.87	2.75	2.95
Na2O	2.84	2.55	2.78	3.52	3.32	5.80	6.07	3.18	4.00	3.75
K2O	4.02	4.25	5.93	4.56	4.98	2.77	3.08	3.47	3.06	3.36
TiO2	0.33	0.34	0.82	0.90	0.89	0.21	0.21	0.31	0.27	0.29
P2O5	0.19	0.20	0.73	0.75	0.76	0.13	0.15	0.15	0.17	0.20
MnO	0.07	0.07	0.12	0.15	0.16	0.04	0.04	0.06	0.10	0.09
S	0.05	0.04	0.06	0.03	0.06	0.09	0.08	0.07	0.05	0.04
LOI	5.72	5.47	5.15	3.27	1.86	4.10	1.37	4.52	4.62	4.81
ppm Ba	1718	686	2140	1103	1897	3009	2475	1307	992	1419
Cr	95	98	188	243	236	88	90	87	80	88
Zr	160	157	166	156	149	154	194	134	131	146
Sr	351	292	1159	788	756	2238	4291	363	371	481
Rb	153	166	196	172	156	75	77	150	112	132
Y	20	18	23	26	28	10	10	18	14	16
Zn	44	51	86	96	85	41	31	55	26	34
Ni	17	4	30	31	43	14	16	21	15	27
V	73	67	205	204	242	33	41	30	37	33
% total	100.18	99.26	99.61	99.89	100.22	100.02	99.80	98.87	99.82	98.59

CIPW Norms										
Ap	0.45	0.47	1.71	1.71	1.71	0.31	0.34	0.35	0.39	0.47
Il	0.67	0.70	1.66	1.78	1.73	0.42	0.41	0.63	0.54	0.59
Mt	2.15	2.16	4.86	5.29	5.89	1.01	1.68	2.11	1.72	1.61
Or	25.29	26.89	37.32	27.99	30.07	17.34	18.66	21.80	19.04	21.24
Ab	25.59	23.11	18.92	16.41	16.98	52.01	52.67	28.61	35.65	33.95
An	15.00	13.59	7.47	5.57	5.54	5.84	5.57	12.95	10.23	13.07
Di			14.09	25.31	22.17	5.70	2.64	5.22	2.39	0.97
Hy	6.53	6.83				2.68	3.03	4.95	6.19	7.15
Ol			10.65	8.07	9.57					
Ne			3.32	7.88	6.36					
C	1.15	2.28								
Q	23.17	23.97				14.69	15.01	23.39	23.85	20.95
Hm										
Wo										
% Totals	100.00	100.00	100.00	100.00	100.00	100.00	100.00	100.00	100.00	100.00

n.d. not determined
* FeO determined by metavanadate titration
# Analyses by Induced Coupled Plasma (ICP)
111 - Feldspar porphyry - fuchsite-sericite-pyrite facies
112 - Feldspar porphyry - fuchsite-sericite-pyrite facies
115 - Augite syenite - moderate actinolite, carbonate, mild chlorite alteration
116 - Augite syenite - mild to moderate actinolite, carbonate alteration
117 - Augite syenite - mild actinolite, weak carbonate alteration
118 - Feldspar porphyry - phlogopite-hematite facies
119 - Feldspar porphyry - hydrothermal biotite facies
120 - Feldspar porphyry - strong carbonate, sericite, mild chlorite alteration
121 - Feldspar porphyry - strong sericite, mild carbonate alteration
122 - Feldspar porphyry - phlogopite-hematite facies

Table A1.2

Whole Rock Chemical Compositions and CIPW Norms for the Kirkland Lake Intrusive Complex

	123	124	125	126	127	128	129	130	131	132
% SiO2	63.79	63.10	64.27	67.09	76.18	64.14	63.90	63.35	62.98	63.72
Al2O3	13.83	15.06	15.26	13.61	7.07	14.44	14.68	14.46	13.67	14.16
Fe2O3	2.99	1.09	1.09	2.52	2.50	2.83	3.13	3.38	3.47	3.25
FeO*	n.d.	1.72	1.44	n.d.	n.d.	n.d.	n.d.	n.d.	n.d.	n.d.
MgO	1.98	1.98	1.83	1.41	1.17	2.01	1.77	1.68	2.04	1.74
CaO	3.02	2.80	2.44	2.39	2.00	2.76	2.73	2.62	3.25	2.64
Na2O	3.40	3.94	3.71	4.40	0.00	3.35	5.07	5.17	4.21	4.14
K2O	3.23	3.60	4.14	3.33	4.09	4.39	3.33	3.05	3.40	4.39
TiO2	0.29	0.35	0.32	0.28	0.14	0.31	0.34	0.31	0.30	0.31
P2O5	0.24	0.24	0.24	0.19	0.02	0.21	0.22	0.20	0.21	0.16
MnO	0.08	0.07	0.05	0.06	0.06	0.07	0.07	0.07	0.09	0.08
S	0.08	0.07	0.04	0.09	0.20	0.04	0.05	0.06	0.12	0.05
LOI	5.35	5.16	4.30	3.79	3.65	4.83	4.50	4.51	5.09	4.07
ppm Ba	1948	2081	1393	2787	3042	1677	1503	2239	2364	1965
Cr	91	87	96	99	70	100	98	99	108	95
Zr	140	168	158	159	67	157	169	177	187	149
Sr	336	335	364	837	354	394	608	1988	1986	766
Rb	132	158	139	109	111	149	120	91	101	110
Y	16	19	17	17	10	16	18	15	20	15
Zn	43	35	41	26	34	56	37	43	48	33
Ni	15	19	13	17	8	19	11	19	21	20
V	54	80	59	39	46	59	62	44	53	94
% total	98.60	99.53	99.42	99.62	97.52	99.68	100.10	99.62	99.40	99.10

CIPW Norms										
Ap	0.57	0.56	0.56	0.44	0.04	0.49	0.50	0.47	0.49	0.37
Il	0.59	0.71	0.64	0.56	0.29	0.62	0.68	0.63	0.61	0.62
Mt	2.04	1.68	1.67	1.15	1.17	1.30	1.43	1.56	1.61	1.49
Or	20.59	22.64	25.80	20.60	25.85	27.38	20.60	19.08	21.40	27.35
Ab	31.05	35.49	33.11	38.99		29.93	44.94	46.32	37.94	36.94
An	13.96	13.12	11.12	7.91	7.71	12.03	7.81	7.66	8.91	7.47
Di	0.41			2.63	2.28	0.79	3.99	3.89	5.59	4.30
Hy	6.60	7.16	6.21	5.13	5.01	8.01	6.08	6.34	6.69	6.11
Ol										
Ne										
C		0.18	0.85							
Q	24.18	18.44	20.04	22.58	57.64	19.44	13.96	14.07	16.77	15.34
Hm										
Wo										
% Totals	100.00	100.00	100.00	100.00	100.00	100.00	100.00	100.00	100.00	100.00

n.d. not determined
* FeO determined by metavanadate titration
# Analyses by Induced Coupled Plasma (ICP)
123 - Feldspar porphyry - fuchsite-sericite-pyrite facies
124 - Feldspar porphyry - phlogopite-hematite to fuchsite-sericite-pyrite facies
125 - Feldspar porphyry - phlogopite-hematite facies
126 - Feldspar porphyry - phlogopite-hematite facies
127 - Feldspar porphyry - fuchsite-sericite-pyrite facies - silicified inclusion in the North Vein
128 - Feldspar porphyry - phlogopite-hematite facies
129 - Feldspar porphyry - phlogopite-hematite facies
130 - Feldspar porphyry - chlorite to phlogopite-hematite facies
131 - Feldspar porphyry - phlogopite-hematite facies
132 - Feldspar porphyry - phlogopite-hematite facies

Table A1.2

Whole Rock Chemical Compositions and CIPW Norms for the Kirkland Lake Intrusive Complex

	133	134	135	136	137	138	139	153	No 7
% SiO2	62.52	64.48	62.50	63.93	64.22	64.01	61.34	58.58	57.02
Al2O3	14.98	14.78	14.75	14.58	14.54	14.70	14.22	13.53	18.30
Fe2O3	3.13	0.82	1.95	1.71	1.20	1.11	1.77	4.24	0.98
FeO*	n.d.	2.29	1.94	1.93	2.06	2.12	2.13	n.d.	2.67
MgO	1.89	1.83	2.16	1.94	1.95	1.58	3.60	3.19	1.04
CaO	2.71	2.67	3.26	3.08	2.82	2.64	3.74	3.22	1.99
Na2O	3.60	5.61	5.95	5.67	5.56	4.64	5.35	4.50	4.25
K2O	4.37	3.18	2.52	2.94	3.42	4.18	3.54	3.95	7.41
TiO2	0.41	0.33	0.40	0.37	0.33	0.33	0.39	0.39	1.90
P2O5	0.23	0.22	0.31	0.28	0.27	0.15	0.38	0.31	0.23
MnO	0.07	0.05	0.07	0.07	0.05	0.05	0.07	0.06	0.17
S	0.13	0.04	0.16	0.08	0.07	0.05	0.03	0.10	n.d.
LOI	4.69	2.27	2.61	2.02	2.55	2.68	3.21	2.64	4.01
ppm Ba	943	2042	3634	3367	2270	2036	2152	3139	
Cr	102	99	102	85	119	145	196	133	
Zr	173	180	320	252	178	166	206	222	
Sr	426	1365	5791	5014	1521	1250	1266	3600	
Rb	160	74	68	77	84	73	140	127	
Y	19	21	14	13	15	18	17	13	
Zn	50	50	61	63	56	34	70	107	
Ni	22	21	21	18	26	31	86	61	
V	72	49	50	64	48	53	59	63	
% total	98.96	99.02	99.75	99.65	99.52	98.69	100.28	95.59	99.97

CIPW Norms									
Ap	0.53	0.50	0.71	0.64	0.61	0.35	0.87	0.74	0.53
Il	0.83	0.65	0.79	0.73	0.65	0.66	0.77	0.80	3.77
Mt	1.45	1.24	2.95	2.58	1.80	1.68	2.66	2.00	1.48
Or	27.43	19.52	15.54	18.00	20.96	25.82	21.67	25.29	45.63
Ab	32.36	49.31	52.55	49.72	48.80	41.06	46.91	41.26	35.80
An	12.54	5.98	6.37	5.85	4.79	7.26	4.49	5.48	8.72
Di	0.12	5.15	6.72	6.50	6.40	4.54	9.69	7.85	
Hy	8.27	5.41	3.90	3.61	4.36	4.59	6.69	9.63	
Ol									2.93
Ne									0.91
C									0.23
Q	16.46	12.23	10.46	12.37	11.62	14.04	6.25	6.94	
Hm									
Wo									
% Totals	100.00	100.00	100.00	100.00	100.00	100.00	100.00	100.00	100.00

n.d. not determined
* FeO determined by metavanadate titration
# Analyses by Induced Coupled Plasma (ICP)
133 - Feldspar porphyry - fuchsite-sericite-pyrite facies
134 - Feldspar porphyry - hydrothermal biotite facies
135 - Feldspar porphyry - hydrothermal biotite facies
136 - Feldspar porphyry - chlorite facies
137 - Feldspar porphyry - hydrothermal biotite facies
138 - Feldspar porphyry - chlorite facies
139 - Feldspar porphyry - hydrothermal biotite facies
153 - Feldspar porphyry - hydrothermal biotite facies
No 7 - Syenite - least altered, analysis from Thomson, 1950

APPENDIX II

Mineral Compositions

Analytical Methods

Mineral compositions from the feldspar porphyry were obtained by electron microprobe analyses completed at the National Museum of Natural Sciences, Mineral Science Division, in Ottawa, and at the Queens University, Kingston, Ontario.

Electron microprobe analyses of sulphate, phosphate, and biotite sample 018 were completed at the National Museum of Natural Sciences. Analyses were performed on a JEOL model 733 electron microprobe with Tracor-Northern automation. The instrument was calibrated using natural and synthetic standards of known composition. Elements were analyzed for a maximum of 50 seconds utilizing an operating voltage of 15 kv and a beam current of 20 ± 0.02 nA. Beam size was 1/4 μm. Data reduction was performed using ZAF (atomic number X absorption X fluorescence) correction coefficients.

Electron microprobe analyses of feldspar, hornblende, and biotite were completed at Queen's University. Analyses were performed on an ARL model scanning electron microprobe. The instrument was calibrated using natural standards of known composition. Elements were analyzed for a maximum of 200 seconds utilizing an operating voltage of 15 kv and a beam

current of 100 ± 4 nA. Beam size was 1 μm rasterized over an area of 20 μm^2. Data reduction was performed using Bence Albee (BA) correction coefficients.

Electron microprobe analyses of sericite and fuchsite were provided by E.M. Cameron (Geological Survey of Canada).

Table A2.1

Chemical Composition of Feldspars from the Feldspar Porphyry

	153-1a	153-1b	153-1c	153-2	153-3a	153-3b	153-3c
% SiO2	64.21	65.13	76.96	63.26	65.27	64.99	64.95
TiO2	0.15	0.15	0.00	0.08	0.08	0.14	0.05
Al2O3	21.26	20.95	13.83	21.44	19.92	20.35	20.19
Cr2O3	0.00	0.00	0.00	0.00	0.00	0.00	0.00
FeO	0.27	0.21	0.14	0.14	0.00	0.14	0.09
MnO	0.00	0.00	0.00	0.00	0.10	0.00	0.00
MgO	0.00	0.00	0.06	0.00	0.00	0.00	0.00
CaO	2.47	2.03	0.00	2.70	1.28	1.67	1.53
Na2O	9.71	9.77	8.68	9.37	10.21	10.18	10.17
K2O	0.86	1.10	0.08	0.95	0.91	0.84	0.82
Total	98.94	99.35	99.75	97.94	97.76	98.32	97.80
	Number of ions on the basis of 32 (O)						
Si	11.474	11.575	13.167	11.421	11.747	11.652	11.692
Ti	0.020	0.021	0.000	0.011	0.010	0.019	0.007
Al	4.477	4.388	2.788	4.562	4.225	4.300	4.283
Cr	0.000	0.000	0.000	0.000	0.000	0.000	0.000
Fe	0.041	0.031	0.020	0.021	0.000	0.021	0.014
Mn	0.000	0.000	0.000	0.000	0.015	0.000	0.000
Mg	0.000	0.000	0.014	0.000	0.000	0.000	0.000
Ca	0.473	0.386	0.000	0.523	0.247	0.322	0.294
Na	3.365	3.368	2.879	3.279	3.563	3.539	3.551
K	0.197	0.249	0.018	0.219	0.208	0.192	0.189
mol% An	11.72	9.64	0.00	13.01	6.15	7.94	7.29
Ab	83.40	84.14	99.38	81.55	88.68	87.32	88.03
Or	4.88	6.22	0.62	5.45	5.18	4.74	4.69

153-1a - Plagioclase (core) - unaltered to hydrothermal biotite facies
153-1b - Plagioclase (rim) - unaltered to hydrothermal biotite facies
153-1c - Albite from above altered plagioclase rim
153-2 - Plagioclase (core) - unaltered to hydrothermal biotite facies
153-3a - Plagioclase (core) - unaltered to hydrothermal biotite facies
153-3b - Plagioclase (rim) - unaltered to hydrothermal biotite facies
153-3c - Plagioclase (rim) - unaltered to hydrothermal biotite facies

Table A2.1

Chemical Composition of Feldspars from the Feldspar Porphyry

	153-4a	153-4b	153-3a*	153-3b*	153-5	153-6a	153-6b
% SiO2	65.43	66.21	65.71	65.02	65.11	63.79	63.33
TiO2	0.11	0.07	0.11	0.11	0.08	0.10	0.20
Al2O3	20.32	20.48	20.32	20.39	20.34	21.29	20.86
Cr2O3	0.00	0.00	0.00	0.00	0.00	0.00	0.00
FeO	0.14	0.12	0.16	0.15	0.13	0.06	0.23
MnO	0.00	0.00	0.00	0.00	0.00	0.00	0.05
MgO	0.06	0.00	0.00	0.00	0.00	0.00	0.00
CaO	1.44	1.35	1.54	1.65	1.28	2.58	2.44
Na2O	10.06	10.54	10.09	10.09	9.86	9.51	9.65
K2O	0.92	0.55	1.11	0.88	1.53	0.82	0.71
Total	98.47	99.33	99.05	98.28	98.32	98.14	97.47
	Number of ions on the basis of 32 (O)						
Si	11.695	11.715	11.695	11.657	11.685	11.473	11.481
Ti	0.014	0.009	0.015	0.014	0.010	0.013	0.028
Al	4.280	4.303	4.263	4.308	4.302	4.512	4.457
Cr	0.000	0.000	0.000	0.000	0.000	0.000	0.000
Fe	0.021	0.018	0.025	0.022	0.019	0.009	0.035
Mn	0.000	0.000	0.000	0.000	0.000	0.000	0.008
Mg	0.015	0.000	0.000	0.000	0.000	0.000	0.000
Ca	0.275	0.256	0.294	0.318	0.245	0.497	0.475
Na	3.486	3.617	3.481	3.506	3.430	3.314	3.391
K	0.210	0.124	0.253	0.201	0.350	0.189	0.163
mol% An	6.93	6.40	7.30	7.90	6.09	12.43	11.79
Ab	87.79	90.49	86.42	87.11	85.22	82.85	84.16
Or	5.29	3.10	6.28	4.99	8.70	4.73	4.05

153-4a - Plagioclase (core) - unaltered to hydrothermal biotite facies
153-4b - Plagioclase (rim) - unaltered to hydrothermal biotite facies
153-3a* - Plagioclase (core) second analysis
153-3b* - Plagioclase (rim) second analysis
153-5 - Plagioclase (core) - unaltered to hydrothermal biotite facies
153-6a - Plagioclase (rim) - unaltered to hydrothermal biotite facies
153-6b - Plagioclase (core) - unaltered to hydrothermal biotite facies

Table A2.1

Chemical Composition of Feldspars from the Feldspar Porphyry

	153-7a	153-7b	018-1a	018-1b	018-2a	018-2b	018-3a
% SiO2	63.67	63.56	65.11	64.97	64.86	65.31	65.74
TiO2	0.00	0.22	0.09	0.08	0.00	0.13	0.06
Al2O3	21.29	20.68	20.21	20.09	20.05	20.34	20.67
Cr2O3	0.05	0.00	0.00	0.00	0.00	0.00	0.07
FeO	0.15	0.00	0.19	0.08	0.17	0.20	0.11
MnO	0.00	0.00	0.00	0.00	0.12	0.05	0.00
MgO	0.00	0.00	0.00	0.00	0.00	0.00	0.00
CaO	2.70	1.87	1.62	1.35	1.51	1.63	1.65
Na2O	9.63	9.55	10.10	10.01	9.95	9.97	10.18
K2O	0.68	0.74	0.94	1.16	1.05	1.21	0.88
Total	98.17	96.62	98.26	97.75	97.71	98.83	99.36
	Number of ions on the basis of 32 (O)						
Si	11.458	11.573	11.681	11.710	11.703	11.665	11.655
Ti	0.000	0.031	0.013	0.011	0.000	0.018	0.008
Al	4.515	4.437	4.272	4.267	4.264	4.281	4.319
Cr	0.007	0.000	0.000	0.000	0.000	0.000	0.009
Fe	0.023	0.000	0.029	0.013	0.026	0.029	0.016
Mn	0.000	0.000	0.000	0.000	0.019	0.008	0.000
Mg	0.000	0.000	0.000	0.000	0.000	0.000	0.000
Ca	0.521	0.365	0.312	0.261	0.291	0.311	0.314
Na	3.358	3.371	3.511	3.497	3.479	3.452	3.501
K	0.156	0.171	0.215	0.268	0.242	0.275	0.200
mol% An	12.91	9.34	7.73	6.48	7.25	7.70	7.82
Ab	83.22	86.28	86.95	86.86	86.71	85.49	87.20
Or	3.87	4.38	5.32	6.66	6.03	6.81	4.98

153-7a - Plagioclase (core) - unaltered to hydrothermal biotite facies
153-7b - Plagioclase (rim) - unaltered to hydrothermal biotite facies
018-1a - Plagioclase (core) - hydrothermal biotite facies
018-1b - Plagioclase (rim) - hydrothermal biotite facies
018-2a - Plagioclase (core) - hydrothermal biotite facies
018-2b - Plagioclase (rim) - hydrothermal biotite facies
018-3a - Plagioclase (core) - hydrothermal biotite facies

Table A2.1

Chemical Composition of Feldspars from the Feldspar Porphyry

	018-3b	018-4a	018-4b	017-1	017-2a	017-2b	017-3a
% SiO2	65.02	65.72	66.79	65.80	64.62	65.27	63.84
TiO2	0.08	0.17	0.00	0.12	0.10	0.25	0.09
Al2O3	20.73	20.43	19.91	20.60	21.65	20.74	22.00
Cr2O3	0.00	0.14	0.00	0.00	0.00	0.00	0.00
FeO	0.20	0.09	0.08	0.17	0.26	0.22	0.14
MnO	0.00	0.00	0.00	0.13	0.00	0.00	0.11
MgO	0.00	0.00	0.00	0.00	0.00	0.00	0.00
CaO	1.72	1.43	0.98	1.60	2.75	1.77	2.74
Na2O	9.73	10.13	10.59	10.01	9.71	9.70	9.31
K2O	1.28	1.20	1.05	1.10	0.73	1.27	0.98
Total	98.77	99.30	99.40	99.54	99.82	99.23	99.21
	Number of ions on the basis of 32 (O)						
Si	11.619	11.673	11.819	11.660	11.443	11.611	11.381
Ti	0.011	0.023	0.000	0.016	0.013	0.033	0.012
Al	4.366	4.276	4.153	4.302	4.518	4.349	4.622
Cr	0.000	0.019	0.000	0.000	0.000	0.000	0.000
Fe	0.030	0.013	0.011	0.025	0.039	0.033	0.020
Mn	0.000	0.000	0.000	0.020	0.000	0.000	0.016
Mg	0.000	0.000	0.000	0.000	0.000	0.000	0.000
Ca	0.329	0.272	0.187	0.304	0.521	0.338	0.523
Na	3.370	3.487	3.633	3.441	3.332	3.345	3.219
K	0.291	0.271	0.236	0.248	0.165	0.288	0.223
mol% An	8.25	6.75	4.61	7.61	12.97	8.51	13.19
Ab	84.46	86.53	89.57	86.18	82.93	84.24	81.19
Or	7.29	6.72	5.82	6.21	4.11	7.25	5.62

018-3b - Plagioclase (rim) - hydrothermal biotite facies
018-4a - Plagioclase (core) - hydrothermal biotite facies
018-4b - Plagioclase (rim) - hydrothermal biotite facies
017-1 - Plagioclase (core) - hydrothermal biotite facies
017-2a - Plagioclase (core) - hydrothermal biotite facies
017-2b - Plagioclase (rim) - hydrothermal biotite facies
017-3a - Plagioclase (core) - hydrothermal biotite facies

Table A2.1

Chemical Composition of Feldspars from the Feldspar Porphyry

	017-3b	017-4a	017-4b	017-5a	017-5b	055-1a	055-1b
% SiO2	65.09	64.97	64.85	66.35	65.72	67.41	66.64
TiO2	0.20	0.15	0.11	0.00	0.00	0.00	0.04
Al2O3	20.98	20.90	20.83	20.70	20.54	19.31	18.89
Cr2O3	0.00	0.00	0.00	0.00	0.00	0.06	0.00
FeO	0.21	0.13	0.17	0.00	0.23	0.00	0.00
MnO	0.00	0.00	0.00	0.00	0.00	0.00	0.00
MgO	0.13	0.07	0.00	0.00	0.00	0.00	0.00
CaO	1.45	2.02	1.74	1.57	1.25	0.11	0.71
Na2O	9.50	9.93	9.78	10.34	10.06	11.61	11.67
K2O	1.58	1.03	1.34	0.97	1.14	0.08	0.04
Total	99.16	99.21	98.82	99.92	98.95	98.59	98.00
	Number of ions on the basis of 32 (O)						
Si	11.589	11.563	11.591	11.690	11.699	11.953	11.923
Ti	0.027	0.021	0.015	0.000	0.000	0.000	0.006
Al	4.403	4.384	4.388	4.299	4.309	4.035	3.394
Cr	0.000	0.000	0.000	0.000	0.000	0.008	0.000
Fe	0.031	0.020	0.025	0.000	0.040	0.000	0.000
Mn	0.000	0.000	0.000	0.000	0.000	0.000	0.000
Mg	0.035	0.020	0.000	0.000	0.000	0.000	0.000
Ca	0.277	0.386	0.334	0.296	0.239	0.022	0.137
Na	3.280	3.427	3.390	3.531	3.473	3.992	4.408
K	0.360	0.233	0.305	0.217	0.258	0.019	0.008
mol% An	7.07	9.54	8.29	7.32	6.02	0.55	3.01
Ab	83.74	84.70	84.14	87.31	87.48	98.98	96.82
Or	9.19	5.76	7.57	5.37	6.50	0.47	0.18

017-3b - Plagioclase (rim) - hydrothermal biotite facies
017-4a - Plagioclase (core) - hydrothermal biotite facies
017-4b - Plagioclase (rim) - hydrothermal biotite facies
017-5a - Plagioclase (core) - hydrothermal biotite facies
017-5b - Plagioclase (rim) - hydrothermal biotite facies
055-1a - Plagioclase (core) - chlorite facies
055-1b - Plagioclase (rim) - chlorite facies

Table A2.1

Chemical Composition of Feldspars from the Feldspar Porphyry

	020-1a	020-1b	020-2	020-3a	020-3b
% SiO2	62.16	61.83	65.82	64.02	65.03
TiO2	1.14	1.07	0.16	0.17	0.13
Al2O3	18.71	18.61	20.43	21.43	20.63
Cr2O3	0.00	0.00	0.00	0.07	0.00
FeO	0.00	0.00	0.16	0.00	0.14
MnO	0.00	0.07	0.00	0.00	0.00
MgO	0.00	0.00	0.00	0.00	0.00
CaO	0.04	0.00	1.50	2.65	1.85
Na2O	2.76	1.10	10.21	9.46	9.93
K2O	11.19	14.01	1.12	0.79	1.02
Total	96.00	96.70	99.40	98.58	98.73
	Number of ions on the basis of 32 (O)				
Si	11.773	11.760	11.679	11.456	11.619
Ti	0.162	0.153	0.022	0.023	0.018
Al	4.175	4.172	4.272	4.521	4.343
Cr	0.000	0.000	0.000	0.009	0.000
Fe	0.000	0.000	0.023	0.000	0.021
Mn	0.000	0.012	0.000	0.000	0.000
Mg	0.000	0.000	0.000	0.000	0.000
Ca	0.008	0.000	0.284	0.507	0.353
Na	1.013	0.406	3.511	3.281	3.441
K	2.703	3.398	0.254	0.180	0.232
mol% An	0.21	0.00	7.01	12.78	8.77
Ab	27.20	10.67	86.71	82.69	85.47
Or	72.58	89.33	6.27	4.54	5.76

020-1a - Orthoclase (core) - chlorite facies
020-1b - Orthoclase (rim) - chlorite facies
020-2 - Plagioclase (core) - chlorite facies
020-3a - Plagioclase (core) - chlorite facies
020-3b - Plagioclase (rim) - chlorite facies

Table A2.2

Chemical Composition of Biotites, Sericite, and Fuchsite from the Feldspar Porphyry

	017-1	017-2a	017-2b	017-3a	017-3b	017-3c	017-4a
% SiO2	39.83	38.37	37.51	39.86	46.19	38.62	41.11
TiO2	0.62	1.18	2.98	0.84	1.65	2.20	0.60
Al2O3	12.67	13.33	13.53	12.90	12.22	12.00	12.05
Cr2O3	0.86	0.58	0.00	0.58	0.10	0.00	0.21
FeO	8.71	15.09	15.19	13.07	10.93	14.03	12.89
MnO	0.10	0.20	0.17	0.07	0.09	0.13	0.00
MgO	21.53	17.05	16.08	17.68	12.57	16.01	18.75
CaO	0.00	0.00	0.00	0.00	0.00	0.00	0.00
Na2O	0.00	0.00	0.00	0.32	1.06	0.00	0.00
K2O	9.94	9.24	8.76	9.35	8.35	9.09	9.83
F	n.a.	n.a.	n.a.	n.a.	n.a.	n.a.	n.a.
Cl	n.a.	n.a.	n.a.	n.a.	n.a.	n.a.	n.a.
O=F (-)							
Total	94.26	95.03	94.22	94.65	93.16	92.87	95.45
Number of ions on the basis of 22 (O, OH, F)							
Si	5.848	5.747	5.659	5.922	6.735	5.931	6.042
Al iv	2.152	2.253	2.341	2.078	1.265	2.069	1.958
Al vi	0.041	0.100	0.065	0.180	0.834	0.103	0.130
Ti	0.069	0.132	0.337	0.093	0.181	0.254	0.067
Cr	0.099	0.069	0.000	0.069	0.011	0.000	0.025
Fe	1.070	1.891	1.916	1.623	1.333	1.801	1.584
Mn	0.013	0.026	0.022	0.009	0.011	0.016	0.000
Mg	4.713	3.809	3.616	3.915	2.731	3.666	4.109
Ca	0.000	0.000	0.000	0.000	0.000	0.000	0.000
Na	0.000	0.000	0.000	0.091	0.299	0.000	0.000
K	1.863	1.765	1.685	1.772	1.554	1.781	1.843
F							
Fe/Fe+Mg+Mn	0.18	0.33	0.34	0.29	0.33	0.33	0.28

n.a. not analyzed
n.d. not detected
017-1 - Pale green hydrothermal biotite (core)
017-2a - Light to medium green hydrothermal biotite (core)
017-2b - Medium green hyrothermal biotite (overgrowth on 017-2a)
017-3a - Pale green hydrothermal biotite (core)
017-3b - Medium green hydrothermal biotite (overgrowth on 017-3a)
017-3c - Medium green hydrothermal biotite (overgrowth on 017-3a)
017-4a - Pale green hydrothermal biotite (core)

Table A2.2

Chemical Composition of Biotites, Sericite, and Fuchsite from the Feldspar Porphyry

	017-4b	084-1a	084-1b	084-2	153-1a	153-1b	135-2
% SiO2	38.97	39.33	37.74	38.14	37.56	37.26	35.96
TiO2	1.34	1.89	2.55	0.83	3.27	3.15	3.35
Al2O3	12.55	12.89	13.51	13.30	13.07	13.12	14.08
Cr2O3	0.47	0.55	0.38	0.60	0.00	0.00	0.00
FeO	13.46	14.48	15.60	14.94	15.92	15.46	16.93
MnO	0.09	0.00	0.07	0.10	0.09	0.18	0.17
MgO	17.76	17.30	16.91	17.97	14.92	15.29	14.83
CaO	0.00	0.00	0.00	0.00	0.00	0.00	0.09
Na2O	0.00	0.00	0.00	0.00	0.00	0.00	0.49
K2O	9.65	8.99	7.66	8.15	9.23	9.30	8.10
F	n.a.	n.a.	n.a.	n.a.	n.a.	n.a.	n.a.
Cl	n.a.	n.a.	n.a.	n.a.	n.a.	n.a.	n.a.
O=F (-)							
Total	94.29	94.52	94.43	94.02	94.06	93.76	93.50
Number of ions on the basis of 22 (O, OH, F)							
Si	5.846	5.824	5.653	5.735	5.713	5.682	5.512
Al iv	2.154	2.176	2.347	2.265	2.287	2.318	2.488
Al vi	0.064	0.073	0.038	0.091	0.055	0.041	0.056
Ti	0.151	0.210	0.288	0.093	0.374	0.361	0.387
Cr	0.056	0.064	0.046	0.071	0.000	0.000	0.000
Fe	1.688	1.793	1.953	1.879	2.025	1.972	2.171
Mn	0.011	0.000	0.009	0.012	0.012	0.023	0.022
Mg	3.971	3.819	3.777	4.028	3.382	3.475	3.389
Ca	0.000	0.000	0.000	0.000	0.000	0.000	0.000
Na	0.000	0.000	0.000	0.000	0.000	0.000	0.028
K	1.846	1.699	1.464	1.565	1.790	1.809	1.683
F							
Fe/Fe+Mg+Mn	0.30	0.32	0.34	0.32	0.37	0.36	0.39

n.a. not analyzed
n.d. not detected
017-4b - Medium green hydrothermal biotite (overgrowth on 017-4a)
084-1a - Medium green hydrothermal biotite (core)
084-1b - Medium green hydrothermal biotite (rim)
084-2 - Pale green hydrothermal biotite, within miarolitic cavity
153-1a - Deep reddish-brown magmatic biotite (core)
153-1b - Deep reddish-brown magmatic biotite (rim)
135-2 - Deep reddish-brown magmatic biotite

Table A2.2

Chemical Composition of Biotites, Sericite, and Fuchsite from the Feldspar Porphyry

	135-3	014-1	014-2	014-3a	014-3b	014-4	014-5
% SiO2	37.75	36.68	37.84	39.36	38.16	37.97	37.61
TiO2	3.16	3.83	2.09	1.20	1.74	1.77	0.99
Al2O3	12.79	13.10	12.64	12.79	13.29	13.15	13.85
Cr2O3	0.11	0.18	0.72	0.19	0.07	0.10	1.70
FeO	16.31	16.06	13.63	6.58	12.16	10.58	9.93
MnO	0.07	0.16	0.12	0.00	0.07	0.06	0.06
MgO	14.77	14.22	16.72	22.81	18.89	19.98	19.68
CaO	0.00	0.00	0.00	0.00	0.00	0.00	0.04
Na2O	0.00	0.00	0.00	0.00	0.00	0.00	0.00
K2O	9.33	9.04	8.90	9.91	9.64	9.43	9.07
F	n.a.	n.a.	n.a.	n.a.	n.a.	n.a.	n.a.
Cl	n.a.	n.a.	n.a.	n.a.	n.a.	n.a.	n.a.
O=F (-)							
Total	94.29	93.27	92.66	92.83	94.02	93.04	92.92
	Number of ions on the basis of 22 (O, OH, F)						
Si	5.741	5.641	5.776	5.804	5.708	5.694	5.638
Al iv	2.259	2.359	2.224	2.196	2.292	2.306	2.362
Al vi	0.034	0.016	0.049	0.028	0.051	0.019	0.085
Ti	0.362	0.443	0.240	0.134	0.196	0.200	0.112
Cr	0.014	0.022	0.087	0.022	0.008	0.013	0.200
Fe	2.074	2.066	1.740	0.811	1.522	1.327	1.245
Mn	0.009	0.020	0.016	0.000	0.008	0.007	0.008
Mg	3.348	3.261	3.806	5.014	4.213	4.469	4.400
Ca	0.000	0.000	0.000	0.000	0.000	0.000	0.006
Na	0.000	0.000	0.000	0.000	0.000	0.000	0.000
K	1.809	1.774	1.732	1.864	1.840	1.805	1.735
F							
Fe/Fe+Mg+Mn	0.38	0.39	0.31	0.14	0.27	0.23	0.22

n.a. not analyzed
n.d. not detected
135-3 - Deep reddish-brown magmatic biotite
014-1 - Deep reddish-brown magmatic biotite
014-2 - Medium green hydrothermal biotite
014-3a - Pale green hydrothermal biotite (core)
014-3b - Medium green hydrothermal biotite (overgrowth on 014-3a)
014-4 - Medium green hydrothermal biotite
014-5 - Pale to medium green hydrothermal biotite

Table A2.2

Chemical Composition of Biotites, Sericite, and Fuchsite from the Feldspar Porphyry

	139-1a	139-1b	139-3a	139-3b	018-1a	018-1b	018-2a
% SiO2	36.53	36.72	37.85	36.37	40.30	38.58	38.97
TiO2	3.89	3.67	1.65	1.22	0.55	0.70	1.05
Al2O3	13.29	13.34	13.09	13.93	13.88	13.72	13.26
Cr2O3	0.20	0.00	0.40	0.81	1.57	1.23	0.52
FeO	15.83	15.72	13.85	14.64	4.46	14.38	14.19
MnO	0.11	0.11	0.09	0.11	0.06	0.13	0.09
MgO	14.05	14.78	16.88	17.40	25.47	18.49	18.68
CaO	0.00	0.00	0.00	0.00	0.03	0.03	n.d.
Na2O	0.00	0.00	0.00	0.00	0.07	n.d.	0.08
K2O	9.26	9.30	9.58	8.07	9.89	9.31	9.55
F	n.a.	n.a.	n.a.	n.a.	1.13	0.78	0.73
Cl	n.a.	n.a.	n.a.	n.a.	n.d.	n.d.	n.d.
O=F (-)					0.48	0.33	0.31
Total	93.15	93.64	93.39	92.55	96.92	97.06	96.88
Number of ions on the basis of 22 (O, OH, F)							
Si	5.626	5.620	5.753	5.572	5.683	5.673	5.733
Al iv	2.374	2.380	2.247	2.428	2.307	2.327	2.267
Al vi	0.039	0.026	0.099	0.088	0.000	0.051	0.032
Ti	0.450	0.422	0.188	0.141	0.059	0.077	0.116
Cr	0.024	0.000	0.049	0.098	0.175	0.143	0.060
Fe	2.040	2.012	1.760	1.875	0.526	1.768	1.746
Mn	0.015	0.014	0.011	0.015	0.007	0.016	0.011
Mg	3.227	3.373	3.825	3.976	5.355	4.053	4.097
Ca	0.000	0.000	0.000	0.000	0.005	0.005	0.000
Na	0.000	0.000	0.000	0.000	0.019	0.000	0.023
K	1.820	1.816	1.858	1.577	1.779	1.747	1.972
F					0.550	0.400	0.370
Fe/Fe+Mg+Mn	0.39	0.37	0.31	0.32	0.09	0.30	0.30

n.a. not analyzed
n.d. not detected
139-1a - Deep reddish-brown magmatic biotite (core)
139-1b - Deep reddish-brown magmatic biotite (rim)
139-3a - Pale to medium green hydrothermal biotite (core)
139-3b - Pale to medium green hydrothermal biotite (rim)
018-1a - Pale green hydrothermal biotite (core)
018-1b - Pale green hydrothermal biotite (rim)
018-2a - Pale green hydrothermal biotite (core)

Table A2.2

Chemical Composition of Biotites, Sericite, and Fuchsite from the Feldspar Porphyry

	018-2b	012-1	105-1
% SiO2	38.78	50.49	48.30
TiO2	2.39	0.86	0.25
Al2O3	13.40	27.48	29.23
Cr2O3	n.d.	1.07	0.01
FeO	15.51	3.00	3.16
MnO	0.12	0.02	0.00
MgO	17.81	2.39	1.53
CaO	n.d.	0.00	0.05
Na2O	0.08	0.07	0.14
K2O	8.99	10.57	10.74
F	0.90	n.a.	n.a.
Cl	n.d.	n.a.	n.a.
O=F (-)	0.38		
Total	97.71	95.95	93.41
	Number of ions on the basis of 22 (O, OH, F)		
Si	5.677	6.731	6.615
Al iv	2.312	1.269	1.385
Al vi	0.000	3.049	3.334
Ti	0.263	0.086	0.026
Cr	0.000	0.113	0.001
Fe	1.899	0.335	0.362
Mn	0.015	0.002	0.000
Mg	3.887	0.475	0.312
Ca	0.000	0.000	0.007
Na	0.023	0.018	0.037
K	1.679	1.798	1.877
F	0.450		
Fe/Fe+Mg+Mn	0.33	0.41	

n.a. not analyzed
n.d. not detected
018-2b - Medium green hydrothermal biotite (overgrowth on 018-2a)
012-1 - Fuchsite - fuchsite-sericite-pyrite facies
105-1 - Sericite - fuchsite-sericite-pyrite facies

Table A2.3

Chemical Composition of Hornblendes from the Feldspar Porphyry

	153-1	017-1	017-2
% SiO2	45.14	45.40	45.38
TiO2	0.95	1.08	1.17
Al2O3	8.66	7.25	7.53
Cr2O3	0.00	0.28	0.16
FeO	15.83	15.79	15.71
MnO	0.26	0.37	0.33
MgO	10.95	12.12	11.95
CaO	10.01	10.87	10.93
Na2O	3.11	2.45	2.39
K2O	0.72	0.76	0.74
Total	95.64	96.37	96.29
	Number of ions on the basis of 24 (O, OH,)		
Si	7.174	7.183	7.176
Al iv	0.826	0.817	0.824
Al vi	0.797	0.535	0.579
Ti	0.113	0.129	0.139
Cr	0.000	0.036	0.020
Fe	2.104	2.089	2.078
Mn	0.035	0.050	0.045
Mg	2.595	2.858	2.818
Ca	1.704	1.843	1.852
Na	0.959	0.753	0.734
K	0.146	0.152	0.149

153-1 - Hornblende inclusion within plagioclase - unaltered to hydrothermal biotite facies

017-1 - Hornblende inclusion within plagioclase - hydrothermal biotite facies

017-2 - Hornblende inclusion within plagioclase - hydrothermal biotite facies

Table A2.4

Chemical Composition of Sulphates and Phosphates
from the Feldspar Porphyry

	136-1	135-1	084-1*	084-2*	084-3*
% BaO	n.a.	n.a.	15.13	6.82	13.60
CaO	55.54	55.91	0.08	0.30	n.a.
SrO	n.a.	n.a.	44.64	54.08	46.00
P2O5	41.15	41.61	n.a.	n.a.	n.a.
SO3	0.38	0.75	40.22	39.13	40.40
Total	97.07	98.27	100.07	100.33	100.00

n.a. not analyzed
* semi quantitative analyses
136-1 - Magmatic apatite - chlorite facies
135-1 - Apatite inclusion in barian-celestine - hydrothermal biotite facies
084-1 - Barian-celestine - hydrothermal biotite facies
084-2 - Barian-celestine - hydrothermal biotite facies
084-3 - Barian-celestine - hydrothermal biotite facies

APPENDIX III

Location of Samples Used in the Hydrothermal Alteration Study

The location of the six sample suites used in defining the hydrothermal alteration facies are given in Figures A4.1 through A4.4. These suites transected the North and/or South Veins between the 150 and 1200 foot levels from the eastern portion of the mine near the Wright-Hargreaves boundary.

In addition to the suite samples, numerous samples were also collected along the drifts, crosscuts (lesser altered samples), and working stopes (highly altered wall rocks and vein samples) from the crown pillar section between the east and west boundaries as well as the eastern boundary portion down to the 1200 foot level. Hydrothermally altered wall rock samples collected from these areas show similar alteration facies distributions as the suite samples. Figures showing the exact locations of all samples are omitted for simplicity.

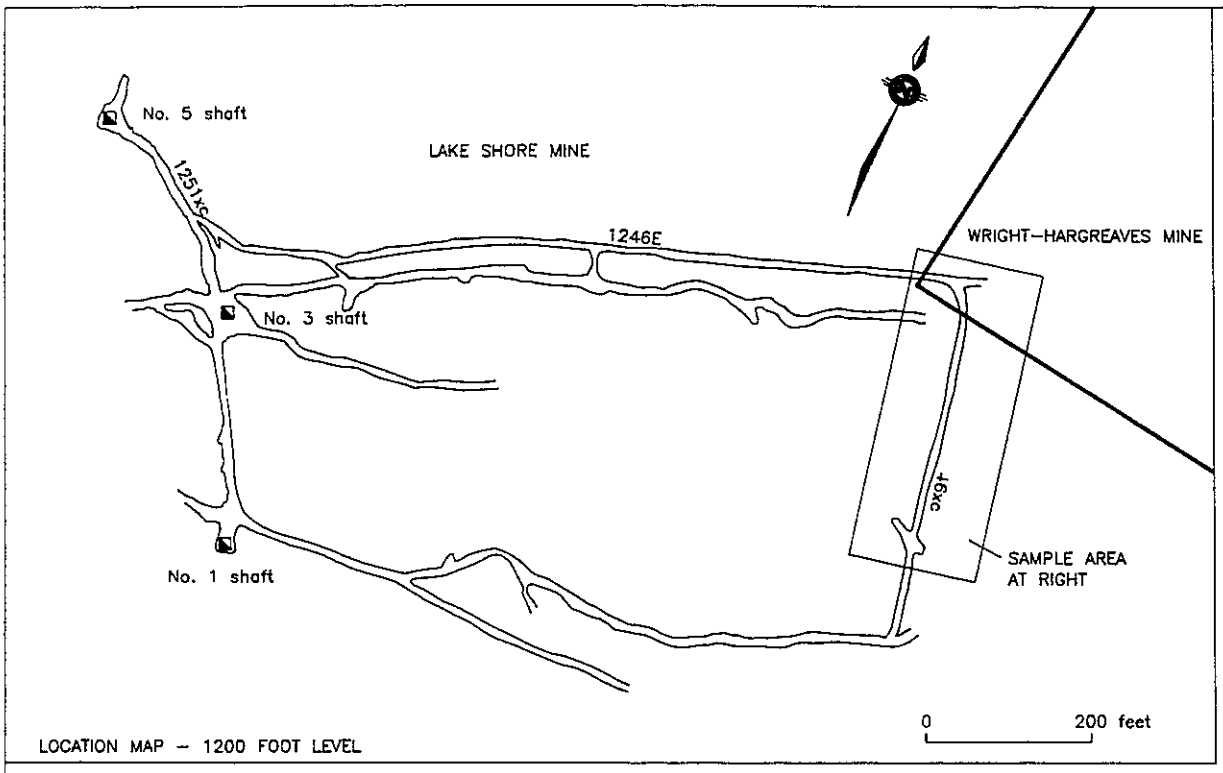

FIGURE A4.1. SAMPLE LOCATION MAP LAKE SHORE MINE 1200 FOOT LEVEL EAST BOUNDARY PILLAR SECTION

LEGEND

- AURIFEROUS VEINS
- X SAMPLE LOCATION WITH NUMBER
- ALTERATION FACIES BOUNDARY (approximate)
- FAULT

ALL ROCK UNITS FOR THIS SAMPLE AREA ARE DEFINED AS FELDSPAR PORPHYRY.

0 40 feet

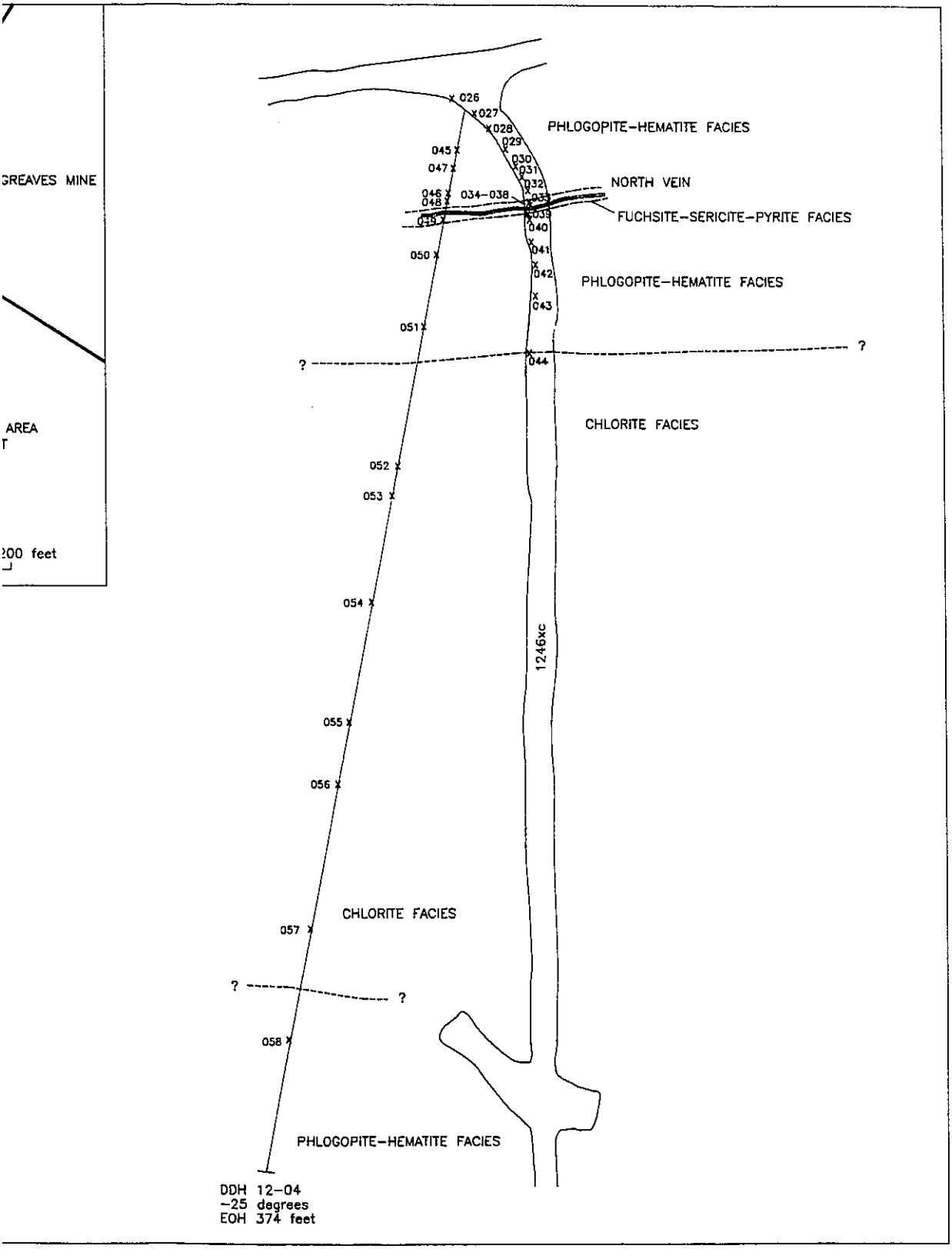
GREAVES MINE
AREA
200 feet
026
027
028
029
030
031
032
033
034–038
039
040
041
042
043
044
045
046
047
048
049
050
051
052
053
054
055
056
057
058
PHLOGOPITE–HEMATITE FACIES
NORTH VEIN
FUCHSITE–SERICITE–PYRITE FACIES
PHLOGOPITE–HEMATITE FACIES
CHLORITE FACIES
1246xc
CHLORITE FACIES
PHLOGOPITE–HEMATITE FACIES
?
?
?
?
DDH 12–04
–25 degrees
EOH 374 feet

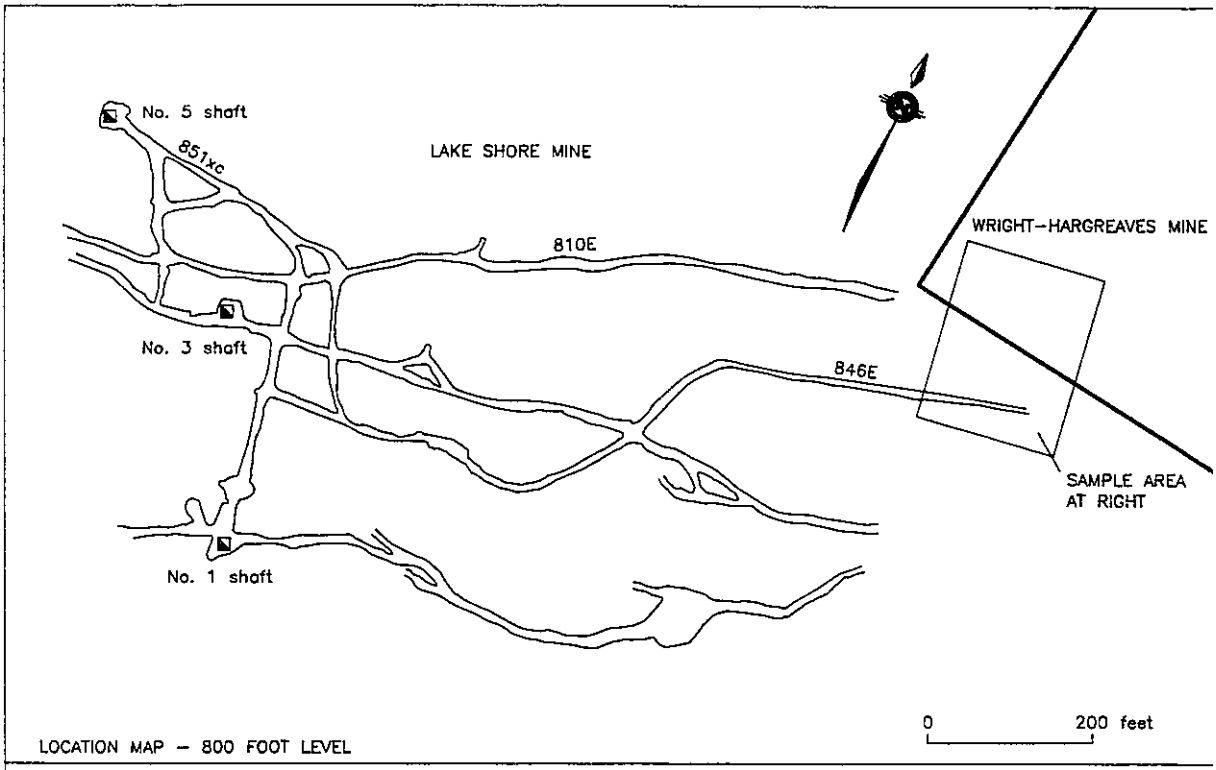

FIGURE A4.2. SAMPLE LOCATION MAP LAKE SHORE MINE 800 FOOT LEVEL EAST BOUNDARY PILLAR SECTION

LEGEND

- AURIFEROUS VEINS
- X SAMPLE LOCATION WITH NUMBER
- ALTERATION FACIES BOUNDARY (approximate)
- FAULT

ALL ROCK UNITS FOR THIS SAMPLE AREA ARE DEFINED AS FELDSPAR PORPHYRY.

0 40 feet

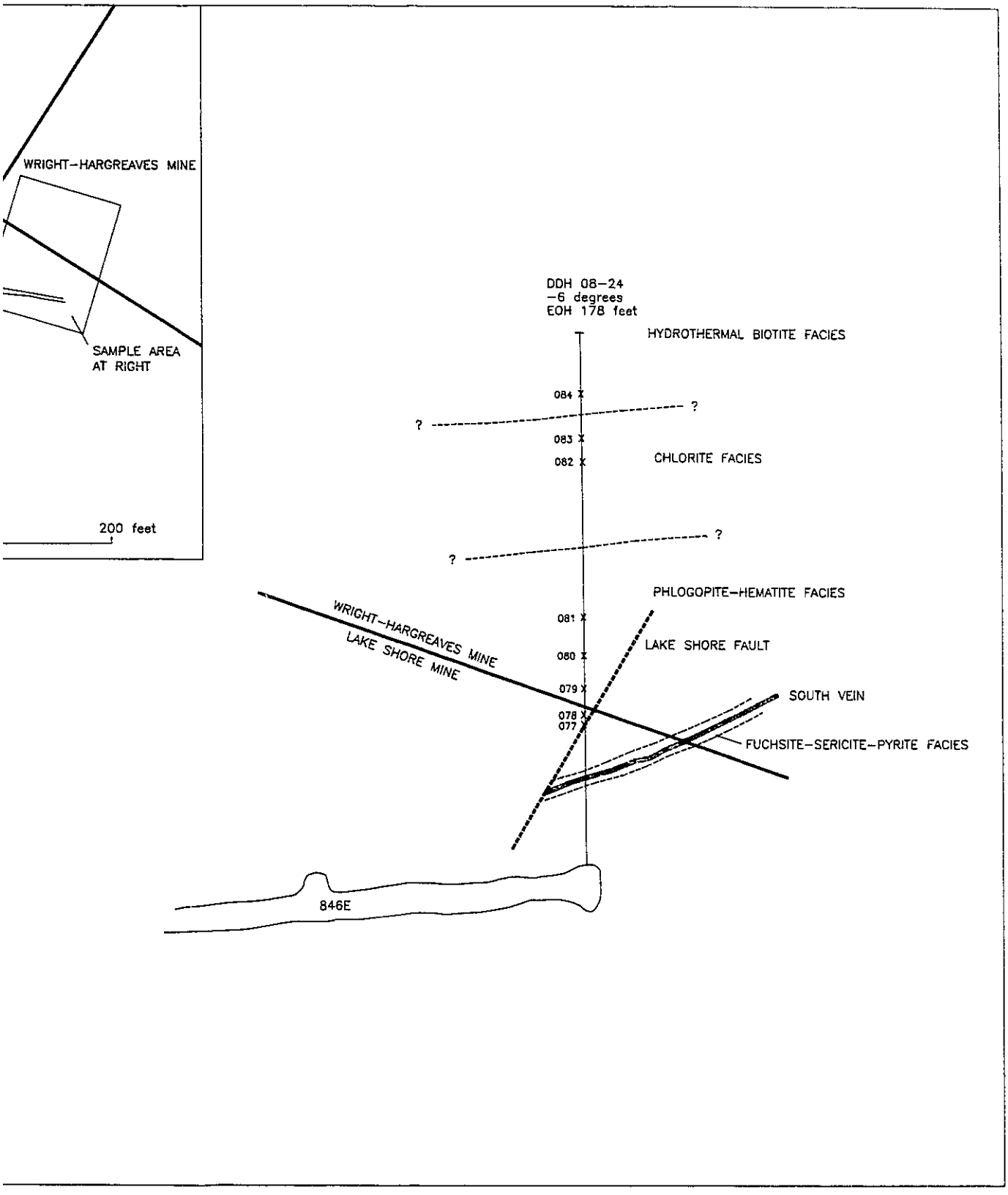
WRIGHT–HARGREAVES MINE
SAMPLE AREA
AT RIGHT
200 feet
DDH 08–24
–6 degrees
EOH 178 feet
HYDROTHERMAL BIOTITE FACIES
084
?
?
083
082
CHLORITE FACIES
?
?
PHLOGOPITE–HEMATITE FACIES
WRIGHT–HARGREAVES MINE
LAKE SHORE MINE
081
LAKE SHORE FAULT
080
079
SOUTH VEIN
078
077
FUCHSITE–SERICITE–PYRITE FACIES
846E

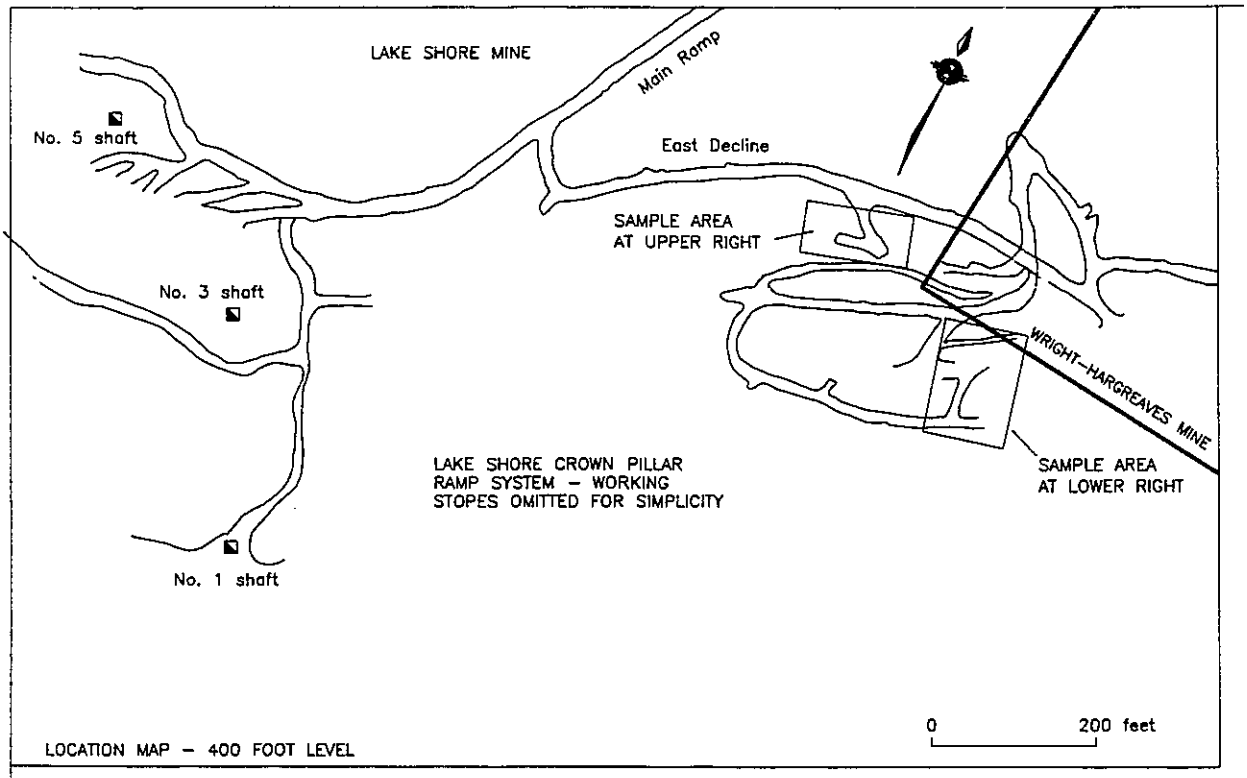

FIGURE A4.3. SAMPLE LOCATION MAP LAKE SHORE MINE EAST CROWN PILLAR SURFACE - 400 FOOT LEVELS

LEGEND

- AURIFEROUS VEINS
- X SAMPLE LOCATION WITH NUMBER
- ALTERATION FACIES BOUNDARY (approximate)
- FAULT

ALL ROCK UNITS FOR THIS SAMPLE AREA ARE DEFINED AS FELDSPAR PORPHYRY.

0 40 feet

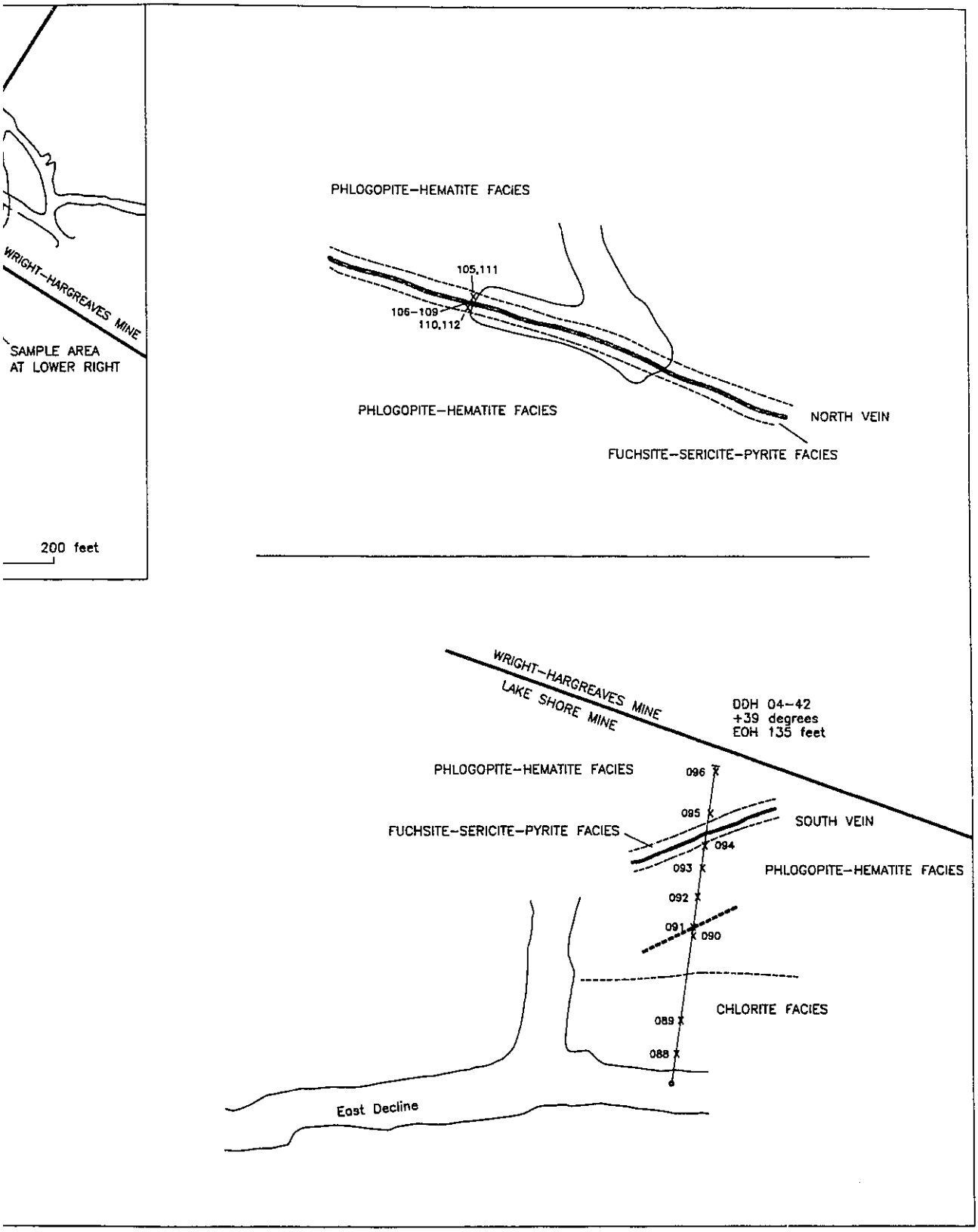
WRIGHT–HARGREAVES MINE
SAMPLE AREA
AT LOWER RIGHT
200 feet
PHLOGOPITE–HEMATITE FACIES
105,111
106–109
110,112
PHLOGOPITE–HEMATITE FACIES
NORTH VEIN
FUCHSITE–SERICITE–PYRITE FACIES
WRIGHT–HARGREAVES MINE
LAKE SHORE MINE
DDH 04–42
+39 degrees
EOH 135 feet
PHLOGOPITE–HEMATITE FACIES
096
095
FUCHSITE–SERICITE–PYRITE FACIES
SOUTH VEIN
094
093
PHLOGOPITE–HEMATITE FACIES
092
091
090
CHLORITE FACIES
089
088
East Decline

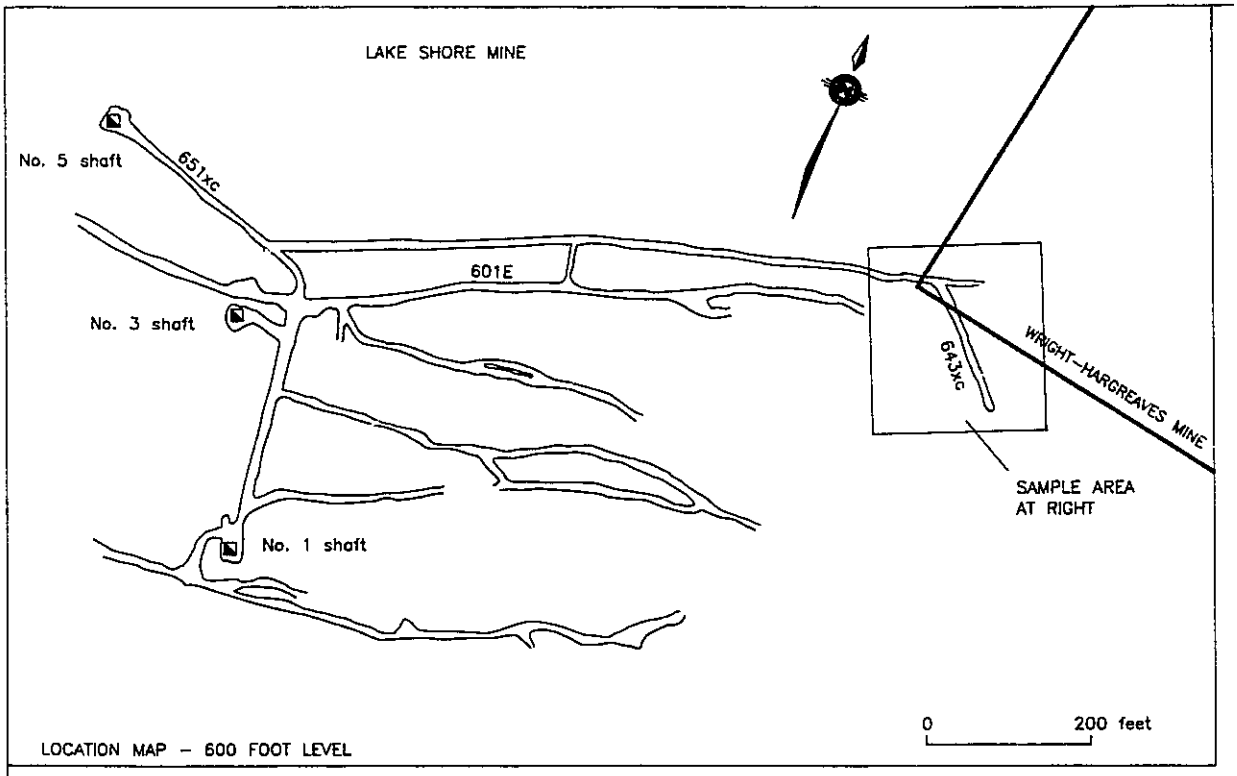

FIGURE A4.4. SAMPLE LOCATION MAP LAKE SHORE MINE 600 FOOT LEVEL EAST BOUNDARY PILLAR SECTION

LEGEND

- AURIFEROUS VEINS
- X SAMPLE LOCATION WITH NUMBER
- ALTERATION FACIES BOUNDARY (approximate)
- FAULT

ALL ROCK UNITS FOR THIS SAMPLE AREA ARE DEFINED AS FELDSPAR PORPHYRY.

0 40 feet

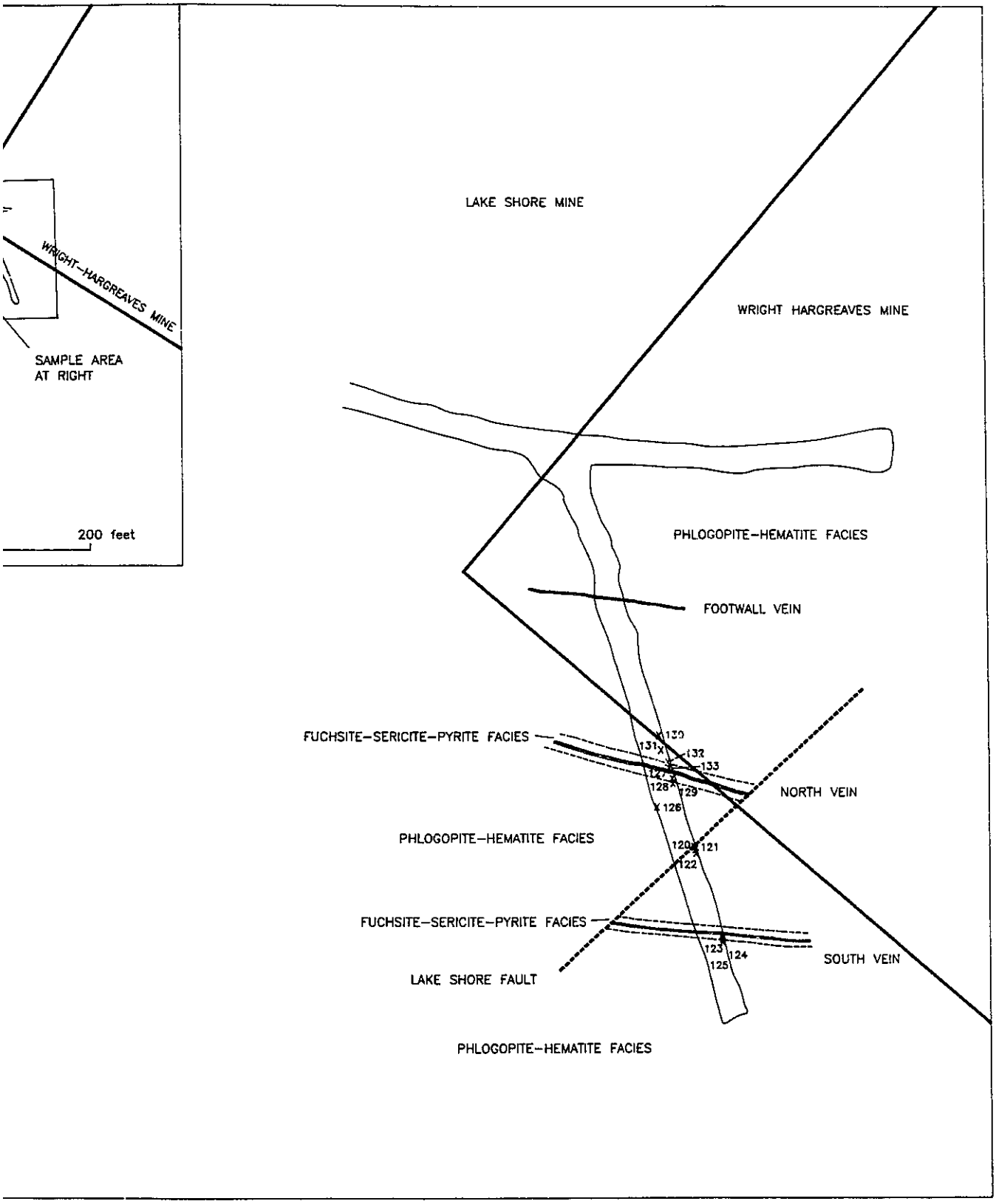
WRIGHT-HARGREAVES MINE
SAMPLE AREA
AT RIGHT
200 feet
LAKE SHORE MINE
WRIGHT HARGREAVES MINE
PHLOGOPITE-HEMATITE FACIES
FOOTWALL VEIN
FUCHSITE-SERICITE-PYRITE FACIES
131
132
133
128
129
126
NORTH VEIN
PHLOGOPITE-HEMATITE FACIES
120
121
122
FUCHSITE-SERICITE-PYRITE FACIES
123
124
125
SOUTH VEIN
LAKE SHORE FAULT
PHLOGOPITE-HEMATITE FACIES